Charge Collection in Silicon Imaging Sensors

Thesis

Charge Collection in Silicon Imaging Sensors

Daniel Philip Weatherill MA MSci (Cantab)

A thesis presented for the degree of

Doctor of Philosophy

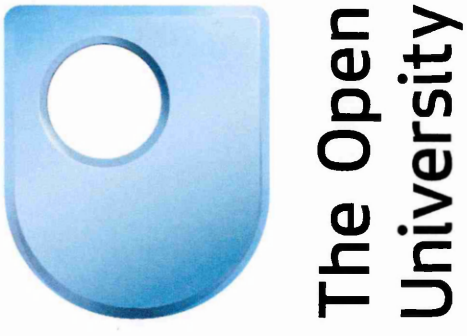

Centre for Electronic Imaging

Space Instrumentation Discipline

Department of Physical Sciences

The Open University

May 2016

ProQuest LLC.
789 East Eisenhower Parkway
P.O. Box 1346
Ann Arbor, MI 48106 – 1346

Abstract

The subject of this thesis is the analysis of instrumental effects caused by the interaction between collected signal charge and electric fields within precision CCD imaging sensors typically used for astronomy. These phenomena cause aberrations in the measured spatial distribution of subsequently collected signal, which may present a major error for upcoming astronomy projects which rely heavily on accurately determining shapes of compact sources. Examples are the Large Synoptic Survey Telescope and the Euclid space telescope. The size of dynamic collection effects may be subtly affected by the operating conditions and design parameters of the device. Dynamic charge collection effects differ in origin from many other errors introduced by imaging detectors in that they are attributable to changes in the confinement of charge carriers during the collection phase of operation, rather than the readout phase. The fact that the exact aberration implied by dynamic charge collection effects depends exactly on the incident light field's spatial distribution also makes them comparatively difficult to correct for.

A method of physically modelling charge collection within the detector using analytical solutions to Poisson's equation is described, which is shown to qualitatively reproduce many features of measured dynamic charge collection effects. Since the model is derived from device physics, it differs in approach in a complementary way from previous efforts which are empirically based. Experimental charge collection measurements from two different CCDs both affected by dynamic collection effects are presented, and shown in large part to be consistent with the predictions from the theoretical model.

Declaration

I hereby declare that no part of this thesis has been previously submitted to this or any other university as part of the requirement for a higher degree. The work described herein was conducted solely by the undersigned except for those colleagues and other workers acknowledged in the text.

Daniel Philip Weatherill

Dedication

To my late father, Donald Weatherill.

Acknowledgements

> Life is and will ever remain an equation incapable of solution, but it contains certain known factors.
>
> Nikola Tesla

The production of this thesis is, I fear, an experience from which it may take my whole life to recover. Any creative work, even one so small as this, is a collaborative effort, and it is traditional to thank those involved but not attributed, and to say that "without them it would not have been possible". Unfortunately, this is an incorrect statement. A related but true statement would be "without them it could not have been done by me". Therefore my words here are insufficient to convey the debt of gratitude I owe each and every person listed, and to many not listed.

First must go to my supervisor Dr Konstantin Stefanov, who has been continuously an enormous help both academically and personally. I wish to thank all members of the Centre for Electronic Imaging past and present for stimulating and illuminating exchanges, and in particular those whom I now also consider to be close personal friends: Mr. Joseph Rushton, Dr. Richard Harriss and Dr. Neil Murray. Colleagues from other institutions have also helped in numerous ways, especially Dr. Doug Jordan of e2v Technologies, and Dr. Ivan Kotov of Brookhaven National Laboratory. Other staff of the Department of Physical Sciences have also helped make my time here more enjoyable, and I will never forget the time I spent especially with the DPS House Band.

My mother Fiona and her partner Russell have been of immense personal support in too many ways to mention, along with my aunt Hilda. Dr. Bill Allison of the Cavendish Laboratory believed I had it in me when nobody else did, including myself. To my close friends Dirk, David, Georgie, Ralph, Matt, Maria, Chris, Jon, Roy and many others (no particular order): I am terrible at keeping in touch, but your friendship has helped me in more ways than I can describe.

Contents

List of Figures

List of Tables

Acronyms

ADC Analogue to Digital Converter

AGN Active Galactic Nuclei

API Application Programming Interface

APS Active Pixel Sensor

AR Anti-Reflection

BFE Brighter-Fatter Effect

BSI Back-Side Illumination

BTE Boltzmann Transport Equation

CCD Charge Coupled Device

CDS Correlated Double Sampling

CIC Clock Induced Charge

CMOS Complementary Metal Oxide Semiconductor

CTI Charge Transfer Inefficiency

DAC Digital to Analogue Converter

DSI Dual Slope Integrator

DSP Digital Signal Processor

ENC Equivalent Noise Charge

FCC Face Centred Cubic

FITS Flexible Image Transport System

FPN Fixed Pattern Noise

FWHM Full Width at Half Maximum

GNUCAP GNU Circuit Analysis Package

GPIO General Purpose Input/Output

GPU Graphics Processing Unit

GSL GNU Scientific Library

HTTP Hyper Text Transfer Protocol

JDOS Joint Density of States

JFET Junction Field Effect Transistor

IR Infra-Red

IP Internet Protocol

LED Light Emitting Diode

LSST Large Synoptic Survey Telescope

MCX Micro Co-Axial

MOS Metal Oxide Semiconductor

MOSFET Metal Oxide Semiconductor Field Effect Transistor

MPI Message Passing Interface

MTF Modulation Transfer Function

NEM Noise Equivalent Modulation

OTF Optical Transfer Function

PCB Printed Circuit Board

PRT Platinum Resistance Thermometer

PSF Point Spread Function

PTF Phase Transfer Function

PTC Photon Transfer Curve

QE Quantum Efficiency

QFL Quasi-Fermi Level

ROI Region Of Interest

RTS Random Telegraph Signal

SIMD Single Instruction Multiple Data

SMD Surface Mount Device

SPICE Simulation Package with Integrated Circuit Emphasis

TCAD Technology Computer Aided Design

TDI Time Delay and Integration

UART Universal Asychronous Receive / Transmit

USB Universal Serial Bus

UV Ultra-Violet

ZIF Zero Insertion Force

Chapter 1

Introduction

"This work contains many things which are new and interesting. Unfortunately, everything that is new is not interesting, and everything which is interesting, is not new."

Lev Landau

1.1 Performance effects of Charge Collection

CCDs and Active Pixel Sensors (APSs) used for detection of electromagnetic radiation in the infra-red through the visible, ultra-violet and soft X-ray regions of the spectrum rely on the injection of free charge carriers into the conduction band of the active material via the photoelectric effect, and the subsequent confinement and measurement of those carriers in a spatially resolved manner. As the accuracy and precision requirements of astronomical observations increase, so too do the constraints on both the resolution and the predictability of imaging detectors. Spatial resolution is determined principally by two factors:

1. The geometric size and separation of the collecting elements (pixels)
2. The spreading of photo-generated carriers in the time between their generation and collection to pixels other than those into which the photons that caused their generation arrived

Factor 1 is essentially limited by semiconductor fabrication and processing technology, whilst factor 2, though it may be mitigated by clever device design and operating conditions, is fundamentally tied to the carrier transport physics of the semiconductor.

In designing a detector for scientific applications, particularly for visible and infra-red wavelength astronomy, an unfortunate but entirely inevitable engineering trade-off must always be made between the device's active thickness and its spatial resolution. Because the photo-generation of carriers is a probabilistic event with a particular wavelength-dependent cross section, in attempting to achieve the maximum Quantum Efficiency (QE) - i.e. in trying to maximise the amount of incoming light which is absorbed and collected - the device thickness should be made as large as possible, and ideally the device should be constructed so that the photons arrive directly at the active silicon, and are not wasted by being absorbed in an oxide or metal layer. Technological advances such as Back-Side Illumination (BSI) and high resistivity deep-depletion construction have enabled very high efficiency sensors to be built. However, the thicker the device, the further that many carriers have to travel before collection; this longer collection time results in the carriers being more affected by thermal diffusion in the lateral direction, and hence spreading to surrounding pixels. The usual strategy for counteracting this is to introduce a large electric field in the collection direction, reducing the drift time of the carriers. This is referred to as "over-depletion".

Recent investigations on thick, fully depleted CCDs [42] have shown that there also exist dynamic charge collection effects in these sensors: the spatial distribution of collected carriers depends on the spatial distribution of those carriers already collected. The exact mechanism for these phenomena was a subject of debate for several years, and though some details are still open for investigation, it is widely agreed that the fundamental cause is the interaction between the stored charge in a pixel and the pixel's electric field. Changing the electric field effectively moves pixel boundaries depending on the exact charge distribution. A brief account of the existing work on what has become known as the Brighter-Fatter Effect (BFE) is given in Section 1.2. The implications of this are significant for several contemporary astronomical missions and observatories, in particular the Large Synoptic Survey Telescope (LSST) and the Euclid mission. Some background on these projects and the specific importance of the BFE in each case are given in Section 1.3 and Section 1.4 respectively.

Another area where charge collection is of direct importance for scientific imaging is in photon counted soft X-ray imaging spectroscopy. An X-ray photon embodies sufficient energy to excite many electrons into the conduction band, so that when the readout rate relative to incident flux is high enough to resolve individual photon interactions (so-called "photon counting" mode) and avoiding the occurrence of multiple interactions within an integration period ("pile-up"), information about the energy of the incident photon is available via the

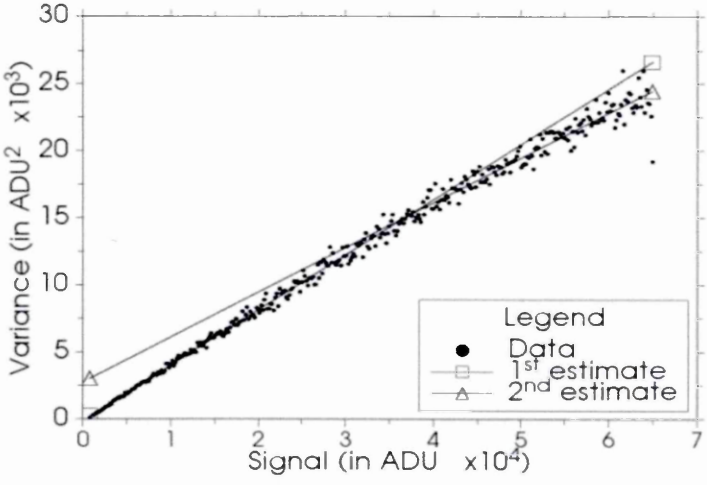

Figure 1.1: First reported non-linearity in the mean-variance curve of a CCD (e2v CCD44-82). Reproduced from Downing et al [27]

number of electrons collected, simultaneously with the spatial information. In addition, if the spread of the cloud of electrons to neighbouring pixels is of a well-known shape, the original interaction position of the photon can be resolved to sub-pixel resolution using appropriately weighted centroiding algorithms [92]. In this case, it may be preferable to encourage more charge spreading, increasing the available amount of information for centroiding. The cost of this is that the resolution of the energy spectra obtained through direct photon counting is degraded: every pixel readout comes with an associated amount of read noise, so the more spreading between pixels, the less accurate is the measurement of the electron number.

The overall aim of this thesis is to develop and validate models for charge collection in imaging sensors, which are able to incorporate dynamic collection effects, and which ultimately are conceptually simple and computationally efficient to evaluate. The utility of such models extends from calculating the expected PSF of a device given its design and operating conditions, to incorporation as part of telescope simulation, and perhaps as part of correction and reconstruction algorithms for scientific images. Though dynamic charge collection is the primary focus, there is a use for computationally cheap calculation of PSF performance in areas where dynamic effects are not a concern, particularly in applications for soft X-ray imaging spectroscopy.

1.2 History of the Brighter-Fatter Effect (BFE)

Signal dependent charge collection processes in thick CCDs were first reported in 2006 [27], and were observed initially as a non-linearity in the PTC (see Figure 1.1 on page 3). A

linear fit to this plot is routinely used as a calibration method for imaging sensors [54]. After eliminating all possible causes of non-linearity arising from the CCD output amplifier circuit and other downstream electronics, analysis of the autocorrelation of pixel values in flat-field illuminated images showed that there was statistical correlation between pixel values: the shot noise assumption that the mean signal over pixels is equal to the variance was invalidated, thus destroying the linearity of the PTC. Those pixels which contained more signal became less likely to accumulate further signal. The physical mechanism suggested in this early work was that electrons may be thermally migrating between pixels after collection. A simple statistical model [94] later showed that electrons migrating between pixels due to lateral drift fields during collection offered a more realistic explanation. Basic quantitative agreement with measurements was subsequently obtained using an electrostatic model, representing the pixel stored charge as a point charge and calculating the resulting change in electron drift trajectories [5]. It was at this time also that the term "Brighter-Fatter Effect" became widely used, as many experimental measurements moved on from measuring statistics on flat-field images to examining projected spots directly. The correlation in this case is observed as a broadening of charge spreading beyond that expected simply from diffusion. The effect is anisotropic: spreading is, in nearly all operating conditions, greater in the CCD's parallel transfer direction than in the serial. This is due to the differing nature of the structures which establish the electric fields in each direction in a CCD.

A framework where the changes in the drift field paths of the electrons are represented as shifts in geometrical boundaries of the pixels themselves was soon advanced [81]. Within this paradigm the scientific implications and possible correction schemes in terms of image processing are readily developed, but it is important to remember that the pixel boundary approach is derived from examination of the field structure of the device. Physically motivated models of dynamic charge collection should therefore concentrate on being able to accurately predict the electric field.

1.3 The Large Synoptic Survey Telescope (LSST)

The LSST is an astronomical sky survey telescope currently in the early stages of construction in the Chilean Andes (see Figure 1.2 on page 6). It is designed to have an étendue (product of primary mirror area and field of view) of $319\,\mathrm{m}^2\mathrm{deg}^2$, which is around an order of magnitude greater than any previous telescope. This property allows the observing strategy of the survey

to be wide (covering a large area of the sky), fast (covering the area very quickly and allowing for frequent repeat pointings at the same area) and deep (able to detect very faint / distant sources) at the same time. Such a survey has the capacity to make progress in many active areas of astronomy and fundamental physics [3]. LSST's instrumentation consists of a single camera, comprised of 189 4k $\times$ 4k format CCDs at the focal plane, with 10 μm pixels, for a total count of 3.2 GPix. The instrument has, as of the time of writing, been described by popular news outlets as "the world's most powerful camera" [71]. The sensors used will be thick, fully depleted, back-illuminated CCDs. The science case for LSST is very broad, encompassing objectives as varied as surveying small bodies in the solar system, observing fast optical transient events occurring at the death of massive stars, and investigating galaxy evolution by cataloguing Active Galactic Nuclei (AGNs). Of most interest in the context of the topic of this thesis is the nature of Dark Energy; in particular, a major component of the cosmological experiments is a weak lensing survey.

It is a consequence of the General Theory of Relativity that the presence of mass in the universe changes the local curvature of space-time, and that this causes the paths of rays of light (which follow paths along space-time geodesics) to alter [47]. The mass density of most of space is very low, but galaxies and galaxy clusters present areas of very high density. The presence of a galaxy cluster between a source and the observing point on Earth can act as a "lens", analogous with classical physical optics, the main difference being that due to the nature of the gravitational potential, maximum deflection occurs at the point closest to the lens centre. This is due to the nature of the gravitational potential. A strongly lensing system therefore deflects light to a ring, rather than focussing to a point. Such a ring is known as an Einstein ring. Strong lensing systems with the fortuitous arrangement to be visible from Earth are rare, and most observed galaxy clusters where the mass distribution is more disperse show only weak lensing, in which case the slight distortions produced by the effect must be measured statistically. These measurements consist of precisely determining the observed shape (specifically, the ellipticity) of many objects [9]. As has been described already (see Section 1.2), the BFE can cause subtle shape-distortion of point sources depending on their brightness. The magnitude of the ellipticity error introduced by the BFE has been shown to be up to several percent in some sensors, and the requirements of next generation weak lensing surveys such as that of LSST require knowledge of the PSF shape at a level two orders of magnitude higher than this, a correction method for the BFE is crucial to ensure that the science goals can be met [42].

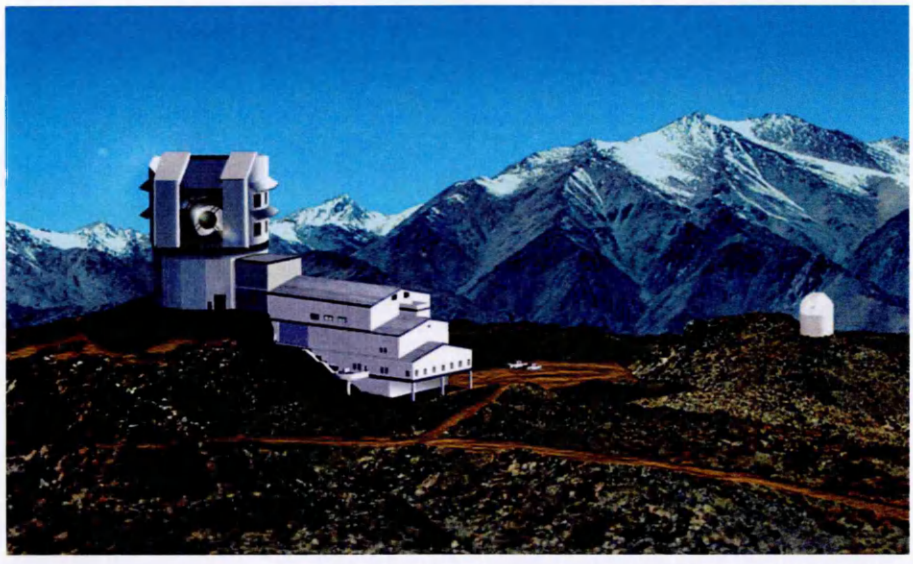

Figure 1.2: Artist's impression of the LSST Telescope. Reproduced with permission of the LSST Corporation from The LSST Science Book [3]

1.4 The Euclid Mission

The ESA Euclid mission aims to address the question of the nature of dark energy, using an observation strategy complementary to that of LSST - a high stability, space based weak lensing survey from the L2 Lagrange point of the Sun-Earth system, due to launch in 2019. The issues arising as a result of the BFE are very similar to those described for LSST in Section 1.3, though the CCD detector used in Euclid's VIS instrument differs in several important respects from that used for LSST, of particular interest when considering the BFE is that it operates without back biasing and is thinner. Nevertheless, significant charge redistribution has been measured in the device during optical characterization [4, 96], and it is certainly a large concern for the delivery of the mission's promise.

1.5 Structure of the Thesis

In Chapter 2, background theory relevant to the modelling of charge transport in silicon devices is briefly presented, beginning from the low level and showing the origins of the drift-diffusion model which is used in general semiconductor modelling. Important parameters such as the silicon mobility and optical absorption coefficient are also explained. Chapter 3 introduces relevant background about imaging sensors, and the specific techniques used to construct thick, back-biased CCDs. Some relevant performance parameters such as QE and MTF are also described. An approach for modelling dynamic charge collection effects is then introduced in Chapter 4, which also includes example calculations from the model which

reproduce qualitatively some results observed in sensors which are subject to the BFE.

Experimental charge collection measurements on a thick, back-illuminated CCD (the e2v CCD261) are presented in Chapter 5, which are then used along with experimental data sets on a second sensor (the e2v CCD250) in Chapter 6 alongside results from finite element modelling to validate some results from the dynamic charge collection model. The thesis is summarised and suggestions for future work are made in Chapter 7.

Chapter 2

Charge Transport in Silicon

> "If you take a bale of hay and tie it to the tail of a mule and then strike a match and set the bale of hay on fire, and if you then compare the energy expended shortly thereafter by the mule with the energy expended by yourself in the striking of the match, you will understand the concept of amplification."
>
> William Shockley

In this chapter the background theory underlying the simulations and models presented in later chapters will be outlined. Brief derivations and justifications are given at each stage (although references are provided for the reader interested in more rigorous treatments). Nevertheless it is useful to recount the origin of the equations and concepts which will be functionally used later, because at each stage to obtain simplicity and tractability, an amount of validity with respect to certain situations is sacrificed.

2.1 Poisson's Equation

Poisson's equation for electrostatics is the fundamental relationship between the quantity of electric potential, Φ, and the charge density $q(\mathbf{r})$. It may be simply derived from Maxwell's

Equations, which can be written in canonical form as:

$$\nabla \cdot \mathbf{D} = q \tag{2.1}$$

$$\nabla \cdot \mathbf{B} = 0 \tag{2.2}$$

$$\nabla \wedge \mathbf{E} = -\frac{\partial \mathbf{B}}{\partial t} \tag{2.3}$$

$$\nabla \wedge \mathbf{H} = \mathbf{J} + \frac{\partial \mathbf{D}}{\partial t} \tag{2.4}$$

where $\mathbf{D}$ is the electric displacement, $\mathbf{B}$ is the magnetic flux density, $\mathbf{E}$ is the electric field, $\mathbf{H}$ is the magnetic field, and $\mathbf{J}$ is the free current density. The operator $\nabla\cdot$ represents the spatial divergence of a vector field, $\nabla\wedge$ represents the spatial curl of a vector field, and $\frac{\partial}{\partial t}$ represents taking the partial derivative with respect to time.

Throughout this work, we will be considering situations only where there is no changing applied magnetic field. (2.3) then implies that $\nabla \wedge \mathbf{E} = 0$, which in turn implies that $\mathbf{E}$ is a conservative vector field. A conservative field may always be written as the gradient of a scalar potential [83, chapter 11], i.e.

$$\mathbf{E} = -\nabla\Phi \tag{2.5}$$

(the minus sign is by convention) and then it follows from (2.1) and the definition of $\mathbf{D}$ that

$$\nabla \cdot (\nabla\Phi) = \nabla^2\Phi = -\frac{q}{\varepsilon_r\varepsilon_0} \tag{2.6}$$

where ϵ_r is the relative permittivity of the material , and ϵ_0 is the permittivity of free space [1]. An especially important property of Poisson's Equation (2.6) for the present work is uniqueness. Consider two potentials ψ_1 and ψ_2, both of which are solutions for(2.6) in a spatial volume Ω , and its enclosing surface $\partial\Omega$. It is clear that:

$$\nabla^2(\psi_1 - \psi_2) = 0 \quad \text{in}\,\Omega \tag{2.7}$$

$$(\psi_1 - \psi_2) = 0 \quad \text{on}\,\partial\Omega \tag{2.8}$$

where we have used the linearity property of the ∇^2 operator, i.e. that:

$$\nabla^2(\psi_1) + \nabla^2(\psi_2) \equiv \nabla^2(\psi_1 + \psi_2). \tag{2.9}$$

[1] We have written Poisson's equation here assuming that the relative permittivity may be regarded as a constant. In fact, it is observed to be a tensor quantity, so the left hand side of equation (2.6) should be written always as $\nabla \cdot (\varepsilon_r\varepsilon_0\nabla\Phi)$. This is, however, unimportant in the present discussion.

It is a simple result of vector field theory [83, chapter 10] that for any scalar field A:

$$\nabla \cdot (A \nabla A) \equiv (\nabla A)^2 + A \nabla^2 A. \tag{2.10}$$

From (2.7) and (2.10), it follows immediately that:

$$\nabla \cdot ((\psi_1 - \psi_2) \nabla (\psi_1 - \psi_2)) = \nabla (\psi_1 - \psi_2)^2 \tag{2.11}$$

and, using the divergence theorem, we then have:

$$\iiint_\Omega \nabla \cdot ((\psi_1 - \psi_2) \nabla (\psi_1 - \psi_2)) \cdot d^3\Omega = \oiint_{\partial\Omega} ((\psi_1 - \psi_2) \nabla (\psi_1 - \psi_2)) \cdot d\hat{\mathbf{S}} \tag{2.12}$$

$$\Rightarrow \iiint_\Omega \nabla (\psi_1 - \psi_2)^2 \cdot d^3\Omega = 0. \tag{2.13}$$

as$\psi_1 - \psi_2 = 0$ on $\partial\Omega$. Since $\nabla (\psi_1 - \psi_2)^2$ cannot be a negative quantity, the only solution satisfying (2.13) is that $\psi_1 - \psi_2 = 0$ over all space, i.e. that the two solutions we began with are identical. This result implies that all solutions to Poisson's equation in some domain satisfying the appropriate boundary conditions are identical. When a solution is evaluated using some particular numerical method, differences in convergence properties and floating point error may become important, but we can be assured that any solution method which is valid will always give the same answer eventually, despite how different they may appear to be when written down. This property will be heavily exploited later in developing analytical solutions to the potential distributions appearing inside CCD sensors.

2.2 The Semi-classical Equations of Motion

The physics of semiconductors, being quantum mechanical systems, are in principle fully described by the Schrödinger equation:

$$\hat{\mathcal{H}} |\Psi\rangle = \hat{i}\hbar \frac{\partial}{\partial t} |\Psi\rangle \tag{2.14}$$

where $\hat{\mathcal{H}}$ is the Hamiltonian operator, $|\Psi\rangle$ is the wave function of the overall system, $\hat{i}$ is the imaginary unit, and $\hbar$ is the reduced Planck constant. The many-body wave function depends on all the degrees of freedom for all the particles (nuclei and electrons) in the semiconductor - including both spatial and spin degrees of freedom. Written out in full for N_e electrons of

mass m_e , charge q_e and positions $\mathbf{r}_i$, N_I ions of masses M_I, charge Z_I and positions $\mathbf{R}_I$ the Hamiltonian operator is:

$$\hat{\mathcal{H}} = \underbrace{\sum_{i=1}^{N_e} \frac{\hat{p}_i^2}{2m_e}}_{\text{e}^- \text{ kinetic}} + \underbrace{\sum_{I=1}^{N_I} \frac{\hat{p}_I^2}{2M_I}}_{\text{ion kinetic}} + \underbrace{\sum_{i>j} \frac{q_e^2}{4\pi\varepsilon_0 |\mathbf{r}_i - \mathbf{r}_j|}}_{\text{e}^- - \text{e}^- \text{ interaction}} + \underbrace{\sum_{I>J} \frac{Z_I Z_J}{4\pi\varepsilon_0 |\mathbf{R}_I - \mathbf{R}_J|}}_{\text{ion}-\text{ion interaction}} - \underbrace{\sum_{i,I} \frac{Z_I q_e}{4\pi\varepsilon_0 |\mathbf{r}_i - \mathbf{R}_I|}}_{\text{ion}-\text{e}^- \text{ interaction}} \tag{2.15}$$

with $\hat{p}_i = -i\hbar\nabla$ being the momentum operator. Of course, since N_e and N_I are extremely large ($\sim 10^{23}$ in macroscopic samples), solving (2.14) directly to obtain the dynamics is completely intractable. In order to obtain problems which can usefully be used to model device behaviour, some very generous assumptions must be made. In the first place, the familiar Born-Oppenheimer approximation is used, allowing the electronic and ionic dynamics to be de-coupled [110, §2.1], resulting in a wave function which can be split into terms governing the nuclear motion $|\Psi_I\rangle$ and a portion $|\Psi_e\rangle$:

$$|\Psi\rangle = |\Psi_I\rangle\,|\Psi_e\rangle \tag{2.16}$$

and a simplified Hamiltonian $\hat{\mathcal{H}}_{\text{BO}}$ which may be written:

$$\hat{\mathcal{H}}_{BO} = \mathcal{H}_{\text{ions}} + \mathcal{H}_{\text{e-ph}} + \sum_{i=1}^{N_e} \frac{\hat{p}_i^2}{2m_e} + \sum_{i>j} \frac{q_e^2}{4\pi\varepsilon_0 |\mathbf{r}_i - \mathbf{r}_j|} - \sum_{i,I} \frac{Z_I q_e}{4\pi\varepsilon_0 |\mathbf{r}_i - \mathbf{R}_I|} \tag{2.17}$$

where $\mathcal{H}_{\text{ions}}$ describes the dynamics of the ion cores reacting to a gas of electrons and $\mathcal{H}_{\text{e-ph}}$ represents the interaction between small displacements in the ion cores and the electrons (the electron-phonon interaction). For the remainder of the discussion we are only interested in the dynamics of electrons, and so drop the parts of the Hamiltonian and wave function which depend only on the fixed ion positions. Equation (2.17) still represents a very difficult problem, in particular because the 4th term (the electron-electron interaction) still depends on multiple electron positions. Yet another major simplification is needed before a solution becomes at all feasible; some kind of single electron approximation provides this. The simplest and most convenient way to perform this reduction is the Hartree-Fock approximation. We start by assuming that the electron wave function may be written as a Slater Determinant

(because electrons are fermions) of single electron wave functions $\psi_i(\mathbf{r}_i)$:

$$|\Psi_e\rangle = \begin{vmatrix} \psi_1(\mathbf{r}_1) & \psi_1(\mathbf{r}_2) & \cdots & \psi_1(\mathbf{r}_{N_e}) \\ \psi_2(\mathbf{r}_1) & \psi_2(\mathbf{r}_2) & \cdots & \psi_2(\mathbf{r}_{N_e}) \\ \vdots & \vdots & & \vdots \\ \psi_{N_e}(\mathbf{r}_1) & \psi_{N_e}(\mathbf{r}_2) & \cdots & \psi_{N_e}(\mathbf{r}_{N_e}) \end{vmatrix}. \tag{2.18}$$

Then , using the Hamiltonian in (2.17), we can calculate the expectation value of the electron energy $\langle\Psi_e|\hat{\mathcal{H}}_e|\Psi_e\rangle$ from the Schrödinger equation as follows:

$$\begin{aligned} \langle\Psi_e|\hat{\mathcal{H}}_e|\Psi_e\rangle &= \sum_i \left(\frac{-\hbar^2}{2m_e}\nabla^2 - \sum_I \frac{Z_I q_e^2}{4\pi\varepsilon_0|\mathbf{r}_i - \mathbf{R}_I|}\right)|i\rangle \\ &+ \frac{q_e^2}{8\pi\varepsilon_0}\sum_{i,j}\left(\left\langle i,j\left|\frac{1}{|\mathbf{r}_i - \mathbf{r}_j|}\right|i,j\right\rangle - \left\langle i,j\left|\frac{1}{|\mathbf{r}_i - \mathbf{r}_j|}\right|j,i\right\rangle\right) \end{aligned} \tag{2.19}$$

where :

$$|i,j\rangle = |\psi_i(\mathbf{r}_i)\rangle \otimes |\psi_j(\mathbf{r}_j)\rangle \tag{2.20}$$

Using the variational principle, we can minimize the electron energy with respect to the $|\psi_i\rangle$ and obtain the Hartree-Fock equations [6, chapter 17], which are now written in terms of the single electron wave functions $|\psi_i\rangle$. In the context of bulk semiconductors operated at finite temperature and where quantum effects are not important, we neglect the last term in (2.19) (the exchange term), and assume that electron interactions can be reduced to a mean field. The resulting time-independent Schrödinger equation is the familiar single-particle form:

$$\frac{-\hbar^2}{2m}\nabla^2|\psi_i\rangle + \mathcal{U}|\psi_i\rangle = \epsilon_i|\psi_i\rangle \tag{2.21}$$

with $\mathcal{U}$ representing the background potential experienced by the electrons, which now contains both mean-field interactions with the rest of the electron cloud, and that with the ion cores, and ε_i is the eigenenergy of the electron state. We next invoke the use of Bloch's theorem:

$$|\psi_k\rangle = e^{\hat{\imath}\mathbf{k}\cdot\mathbf{r}}u_k(\mathbf{r}) \tag{2.22}$$

where $\mathbf{k}$ is the electron wave vector and u_{nk} is a function which has the same periodicity as the crystal lattice.

Following [6, chapter 8], the Bloch wave function can be inserted into the single electron

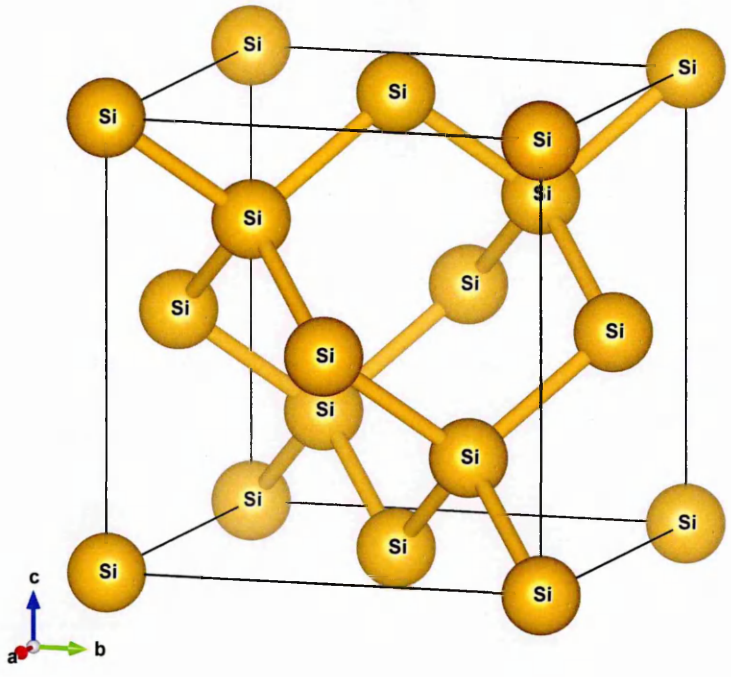

Figure 2.1: Crystal structure of one unit cell of pure silicon

Schrödinger equation, and after some algebra[2], we obtain:

$$\left(\frac{\hbar^2}{2m_e}\left(\frac{1}{i}\nabla + \mathbf{k}\right) + \mathcal{U}(\mathbf{r})\right) u_k(\mathbf{r}) = \epsilon_k u_k(\mathbf{r}) \tag{2.23}$$

which, given the translational periodicity of the crystal lattice, results in an infinite set of discretely spaced energies for any given value of $\mathbf{k}$, which can vary continuously. Labelling these solutions with a so-called "band index" n , the eigensolutions to (2.23) then constitute a family of continuously varying energy bands, $\varepsilon_n(\mathbf{k})$. In some senses, these energy bands may be regarded analogously to a classical dispersion relationship, except that the periodic boundary conditions imply that the quantity $\hbar\mathbf{k}$ (known as the crystal momentum) is not conserved in all situations (since the Bloch functions are not eigenstates of the momentum operator) [90, §5.1].

Energy band dispersion relationships are collectively called the band structure, and in principle depend only on the crystal structure of the lattice, and the manner of the potential induced by the atom cores. Pure mono-crystalline Silicon can be described as having a Face Centred Cubic (FCC) unit cell, with a motif of two atoms (specifically space group number 227), and a lattice parameter $a_0 = 5.43\,\text{Å}$ (illustrated in Figure 2.1).

[2]Full steps are given by Ashcroft and Mermin [6] between their equations (8.30) and (8.49)

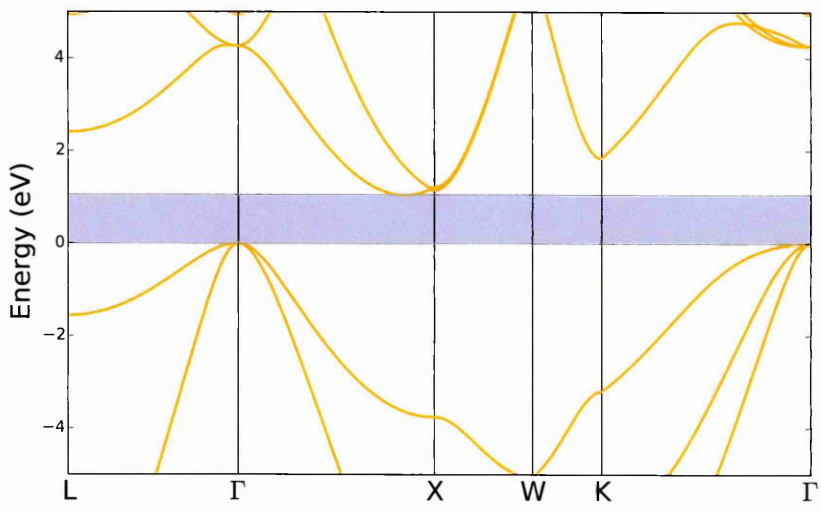

Figure 2.2: Band structure of Si calculated by Empirical Pseudopotential Method. The blue shaded region indicates the band gap.

Calculation of band structure is in itself a huge and complicated subject, and methods exist both completely *ab initio,* or using some experimentally derived data. One of the earliest and simplest methods to implement is the Experimental Pseudopotential Method, primarily developed in the early 1960s [80], which using a very small amount of experimentally measured potential form factors reproduces many of the features of the band structure quite accurately. An example of the band diagram resulting from such a calculation for silicon is shown in Figure 2.2.

The distinguishing feature of a semiconductor, as opposed to a metal or insulator, is that there exists a region with no electron states, whose width is comparable to the thermal energy of the electrons. This region is known as the band gap, and its magnitude in silicon is $E_G = 1.12\,\mathrm{eV}$. Most of the description of electron behaviour in semiconductor and device physics may be ultimately derived from arguments about the band structure. This makes it an extremely useful and simple concept behind which to hide the enormous quantum-mechanical complexity of the solid state.

To move completely into the semi-classical picture, it is necessary to draw some final analogies from classical physics. Consider a wave packet moving through a dispersive medium having a dispersion relationship $\omega(k)$; its overall motion is described by a group velocity v_g given by:

$$v_g = \frac{d\omega(k)}{dk}. \tag{2.24}$$

By comparison, an electron travelling through the band structure has a velocity $\mathbf{v}$ given by:

$$\mathbf{v} = \frac{1}{\hbar}\nabla_{\mathbf{k}}\epsilon_n(\mathbf{k}) \tag{2.25}$$

where $\nabla_{\mathbf{k}}$ represents the gradient operator acting on the dimensions of the wave vector. In the case of an isotropic band structure, the forms of (2.24) and (2.25) become identical. A semi-classical form of Newton's 2nd law can also be constructed [90, §5.2]. If an object subject to a force $\mathbf{F}$ moves at velocity $\mathbf{v}$ in a time interval δt, an amount of work δW is performed, where:

$$\delta W = \mathbf{F} \cdot \mathbf{v}\delta t. \tag{2.26}$$

Substituting in the definition of velocity for electrons (2.25), and using $\delta W = \delta\epsilon_k$, it is found that:

$$\mathbf{F} \cdot \mathbf{v}\delta t = \nabla_{\mathbf{k}}\epsilon_n(\mathbf{k}) \cdot \delta\mathbf{k} = \hbar\mathbf{v} \cdot \delta\mathbf{k} \tag{2.27}$$

$$\Rightarrow \mathbf{F} = \hbar\frac{\partial\mathbf{k}}{\partial t} \tag{2.28}$$

which is compared to the classical definition of Newton's 2nd law as the rate of change of momentum. To cast this into the more familiar form of $\mathbf{F} = m\mathbf{a}$ (with m the mass and $\mathbf{a}$ the acceleration), we simply need to work out the time derivative of the velocity using (2.25):

$$\mathbf{a} = \frac{\partial\mathbf{v}}{\partial t} = \frac{1}{\hbar} \cdot \frac{\partial}{\partial t}\left(\nabla_{\mathbf{k}}\epsilon_n(\mathbf{k})\right) = \frac{1}{\hbar} \cdot \nabla_{\mathbf{k}}\left(\frac{\partial\mathbf{k}}{\partial t} \cdot \nabla_{\mathbf{k}}\epsilon_n(\mathbf{k})\right) \tag{2.29}$$

$$\Rightarrow \hbar^2\mathbf{a} = \nabla_{\mathbf{k}}\left(\mathbf{F} \cdot \nabla_{\mathbf{k}}\epsilon_n(\mathbf{k})\right) \tag{2.30}$$

which in the isotropic band case can be written as:

$$\mathbf{F} = \frac{\hbar^2}{\frac{d^2\epsilon(k)}{dk^2}} \cdot \mathbf{a}. \tag{2.31}$$

The multiplying factor on the right hand side of (2.31) related to the local curvature of the band structure can be seen as the direct analogy of the classical mass, and is named the effective mass, m^*. Unlike the classical mass, the effective mass is a tensor quantity dependent on k-space direction (for an anisotropic band structure), and may be negative where the band structure curvature is negative; these bands are called the valence bands. It is usually the case in semiconductor devices that one is interested in situations where there are only a few

electrons occupying states above the band gap (the conduction band), and therefore an almost completely filled valence band. In this situation, the absence of an electron in the valence band is a much more interesting entity than the electrons filling the majority of states. These absences are constituted as fermionic quasi-particles called "holes", and are taken to have their energy, effective mass, and charge in the opposite sense to electrons (i.e. their energy increases "down" the valence band, and they carry a positive charge).

With the concepts of band structure, holes, and the semi-classical equation of motion (2.31), all the basic tools necessary to study charge carrier transport in semiconductors where truly quantum effects (such as entanglement and spin-spin interactions) are unimportant are in place. For the remainder of this thesis, the entire discussion will take place firmly within the semi-classical domain.

2.3 The Drift - Diffusion Model

Having presented the problem of charge transport semi-classically, the dynamics of electrons and holes could now in principle be addressed by solving the effectively classical equations of motion for each particle, given the forces acting on them, and including events such as ion core scattering and phonon interactions. However, this problem is still computationally formidable even for relatively modestly sized[3] systems. It is necessary to further simplify the picture used in order to effectively treat real world device physics problems of relevant scale. A general way to perform this simplification in many areas is to use the phase space distribution function, $f_i(\mathbf{r}, \mathbf{k}, t)$, which gives the probability of finding a particle of type i (here we represent the distribution of electrons by f_n and that of holes by f_p) at position $\mathbf{r}$, momentum $\hbar\mathbf{k}$ and time t. Since $\mathbf{k}$ and $\mathbf{r}$ for any particular particles are, in the quantum mechanical sense, non-commuting variables, it is clear that no matter how much sophistication is added to the approach, the behaviour of particles as it relates to Heisenberg's Uncertainty Principle cannot be fully captured by this formulation. The fermionic nature of the carriers can be incorporated readily however, by constraining the distribution functions in terms of

[3]Beyond several tens of unit cells

energy to follow the familiar Fermi-Dirac statistics, such that:

$$f_n(\epsilon) = \frac{1}{1+\exp\left(\frac{1}{k_BT}(\epsilon - q_e\phi_{f,n})\right)} \tag{2.32}$$

$$f_p(\epsilon) = \frac{1}{1+\exp\left(\frac{1}{k_BT}(q_e\phi_{f,p} - \epsilon)\right)} \tag{2.33}$$

where k_B is Boltzmann's constant, T is temperature, and $\phi_{f,p}$ and $\phi_{f,n}$ are called quasi-Fermi levels, which allow for non-equilibrium (i.e. biased) conditions[4]. In this case, they are related to the concentrations of electrons and holes (n and p respectively), by:

$$n = N_C \exp\left(\frac{q_e\phi_{f,n} - E_C}{k_BT}\right) \quad p = N_V \exp\left(\frac{E_V - q_e\phi_{f,p}}{k_BT}\right) \tag{2.34}$$

where E_C is the conduction band edge, E_V is the valence band edge (i.e. $E_C - E_V = E_G$) N_C is the effective density of states in the conduction band, and N_V is the effective density of states in the valence band, given by:

$$N_C = 2 \cdot \left(\frac{m_n^* k_B T}{2\pi\hbar^2}\right)^{\frac{3}{2}} \quad N_V = 2 \cdot \left(\frac{m_p^* k_B T}{2\pi\hbar^2}\right)^{\frac{3}{2}} \tag{2.35}$$

which implies that (by multiplying the two equations of (2.34)), the non-equilibrium equivalent of the law of mass-action can be written as:

$$n \cdot p = n_i^2 \cdot \exp\left(\frac{q_e\left(\phi_{f,n} - \phi_{f,p}\right)}{k_BT}\right) \tag{2.36}$$

where n_i is the intrinsic carrier concentration, given by:

$$n_i = \sqrt{N_C N_V} \exp\left(\frac{-E_G}{k_BT}\right) \tag{2.37}$$

An equation for the transport of particles can be very simply derived by considering a volume element of the position-momentum phase space at a particular moment in time t (see Figure 2.3). Between t and a later time $t + \delta t$, particle density may move into and out of the phase space volume via several processes:

- Thermal processes causing stochastic movement of particles; changing their position without changing their average momentum - shown as the horizontal arrows in Figure 2.3.

[4]The inclusion of the electron charge factor q_e is by convention to allow the quasi-Fermi levels to be expressed in voltage units rather than energy units

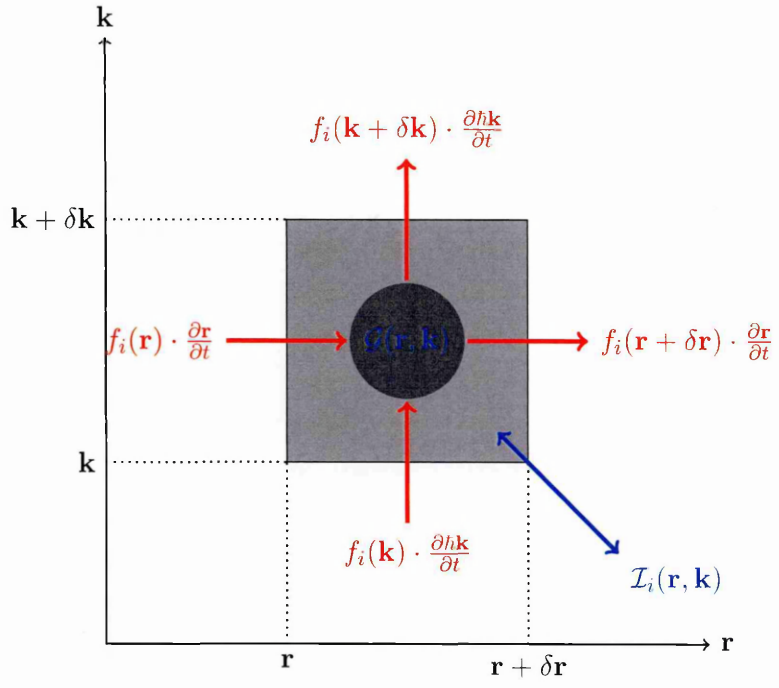

Figure 2.3: Visualising the change in a phase space distribution function f_i due to thermal processes (horizontal arrows), external forcing (vertical arrows), generation and recombination, and scattering.

- External forcing processes which alter the momentum of particles - as shown by the vertical arrows in Figure 2.3.
- Generation and recombination of particles due to traps [74, chapter 7], optical generation (see Section §2.5) or thermal generation. These processes are denoted by $\mathcal{G}$ in Figure 2.3[5].
- Scattering of particles into and out of the volume caused by some collision process with the lattice or with other carriers as shown by the diagonal arrow in Figure 2.3, and denoted by the collision function $\mathcal{I}_{c,i}$

Considering each process in turn and simply summing them to obtain the total change in the distribution function, we find:

$$\delta f_i = \left(\left(f_i\left(\mathbf{r}+\delta\mathbf{r}\right) - f_i\left(\mathbf{r}\right)\right)\cdot\frac{\partial\mathbf{r}}{\partial t} + \left(f_i\left(\mathbf{k}+\delta\mathbf{k}\right) - f_i\left(\mathbf{k}\right)\right)\cdot\frac{\partial\mathbf{k}}{\partial t} + \mathcal{G}\right)\cdot\delta t \quad (2.38)$$

$$\Rightarrow \frac{\delta f_i}{\delta t} = \left(\left(f_i\left(\mathbf{r}+\delta\mathbf{r}\right) - f_i\left(\mathbf{r}\right)\right)\cdot\mathbf{v} + \left(f_i\left(\mathbf{k}+\delta\mathbf{k}\right) - f_i\left(\mathbf{k}\right)\right)\cdot\frac{\mathbf{F}}{\hbar} + \mathcal{G}\right). \quad (2.39)$$

[5]There is no need for a subscript on $\mathcal{G}$, because every generation process will create an electron-hole pair, and every recombination process will annihilate an electron-hole pair.

Taking the limit as the time, space, and momentum intervals to zero, the Boltzmann transport equation emerges:

$$\frac{\partial f_n}{\partial t} = \mathbf{v} \cdot \nabla_{\mathbf{r}} f_n + \frac{\mathbf{F}}{\hbar} \cdot \nabla_{\mathbf{k}} f_n + \mathcal{I}_{c,n} + \mathcal{G} \tag{2.40}$$

$$\frac{\partial f_p}{\partial t} = \mathbf{v} \cdot \nabla_{\mathbf{r}} f_p + \frac{\mathbf{F}}{\hbar} \cdot \nabla_{\mathbf{k}} f_p + \mathcal{I}_{c,p} + \mathcal{G}. \tag{2.41}$$

Nearly all popular device simulation techniques for devices above the nano scale are based on solving simultaneously (2.40) and (2.41) by numerical methods, after having chosen appropriate approximations for $\mathcal{I}_c$ and $\mathcal{G}$.

In recent times, there are semiconductor transport codes which use expensive computational techniques to directly solve the Boltzmann Transport Equation (BTE) [50], or use ensemble Monte-Carlo methods to obtain statistical results on transport properties of devices [100]. Most traditional simulators for device physics, however, rely on further approximations to the BTE resulting from dropping the idea of individual charge carriers altogether.

Making any progress from the BTE requires initially the choice of a collision functional. The simplest sensible approximation [60] is the relaxation time approximation:

$$\mathcal{I}_c(t) = -\frac{f - f_0}{\tau} \tag{2.42}$$

with f_0 as the equilibrium distribution function, and τ representing a characteristic time for a particular scattering mechanism. The relaxation time approximation can in general be extended by using a sum of various scattering times. The approximation corresponds to the distribution function returning exponentially to the equilibrium, in the absence of other forces. To see this simply, consider a situation where the electrons have been given some kind of external "kick", and then all external forces are immediately removed, and all other motion of the particles ceases. Then, neglecting generation/recombination, from (2.40), it can be seen that:

$$\frac{df_n}{dt} = \frac{-f_n - f_0}{\tau} \tag{2.43}$$

$$\Rightarrow f_n(t) = f_0 + \exp\left(-\frac{t}{\tau}\right)(f_n(0) - f_0) \tag{2.44}$$

which in many situations turns out to be a remarkably good approximation to reality. Though

the approximation in principle does not apply when scattering mechanisms are dependent on the momentum of the particle, corrections can be added to the resulting model to somewhat take account of this.

To construct more macroscopic approximations to the BTE, the method of moments is used. The procedure is to multiply the BTE by ascending powers of $\mathbf{v}$ and integrate out the $\mathbf{k}$ dependence of the distribution function, all integrals being taken over all values of $\mathbf{k}$. Starting with the 0th moment :

$$\begin{aligned} \iiint \frac{\partial f_i}{\partial t} d^3\mathbf{k} &= \iiint \mathbf{v} \cdot \nabla_\mathbf{r} f_i \cdot d^3\mathbf{k} + \frac{1}{\hbar} \iiint \mathbf{F} \cdot \nabla_\mathbf{k} f_i \cdot d^3\mathbf{k} \\ &\quad - \iiint \frac{f_i - f_{i,0}}{\tau} \cdot d^3\mathbf{k} + \frac{1}{\hbar} \iiint \mathcal{G} \cdot d^3\mathbf{k} \qquad (2.45) \\ \Rightarrow \frac{\partial}{\partial t} \iiint f_i \cdot d^3\mathbf{k} &= \nabla_\mathbf{r} \cdot \iiint \mathbf{v} f_i \cdot d^3\mathbf{k} + \frac{1}{\hbar} \mathbf{F} \cdot \iiint \nabla_\mathbf{k} f_i \cdot d^3\mathbf{k} + \iiint \mathcal{G} \cdot d^3\mathbf{k}. \qquad (2.46) \end{aligned}$$

The integral in the left hand side term of (2.45) is the distribution function with only its spatial parts; in other words, the spatial carrier density (labelled $n(\mathbf{r})$ for electrons, and $p(\mathbf{r})$ for holes). The velocity in the first term on the right hand side may be moved "inside" the divergence operator because $\mathbf{v}$ is an independent variable to $\mathbf{r}$ (see (2.25)). Using the fundamental vector theorem of calculus, the second term on the right hand side can be re-written as a surface integral:

$$\mathbf{F} \cdot \iiint \nabla_\mathbf{k} f_i \cdot d^3\mathbf{k} \equiv \mathbf{F} \cdot \oiint_{\partial \mathbf{K}} f_i \cdot d^2\hat{\mathbf{s}} \qquad (2.47)$$

which is taken over the surface at the extremum of $\mathbf{k}$-space. As there are a finite number of particles in the system, this surface integral must equate to 0. The terms originating in the collision functional also cancel because any scattering process must conserve total particle number (that is, $\iiint f_i d^3\mathbf{k}$ must equal $\iiint f_{i,0} d^3\mathbf{k}$). The generation - recombination term with only spatial dependence remaining is simply labelled $G(\mathbf{r})$. Finally, a carrier current density ($\mathbf{J}_n$ for electrons, $\mathbf{J}_p$ for holes) is defined in terms of the distribution functions as:

$$\mathbf{J}_i = q_i \iiint \mathbf{v} f_i \cdot d^3\mathbf{k} \qquad (2.48)$$

which leads to the restatement of (2.46) as standard continuity equations:

$$\frac{\partial n}{\partial t} = \frac{1}{q_e}\nabla \cdot \mathbf{J}_n + G \tag{2.49}$$

$$\frac{\partial p}{\partial t} = -\frac{1}{q_e}\nabla \cdot \mathbf{J}_p + G \tag{2.50}$$

which ensure conservation of charge and particle number throughout the volume. Taking the 1st moment of the BTE is a little more involved, and is shown here only for electrons:

$$\begin{aligned}\iiint \mathbf{v}\frac{\partial f_n}{\partial t}d^3\mathbf{k} &= \nabla_\mathbf{r} \cdot \iiint (\mathbf{v}\cdot\mathbf{v})\, f_n \cdot d^3\mathbf{k} + \frac{1}{\hbar}\mathbf{F}\iiint \mathbf{v}\cdot\nabla_\mathbf{k} f_n \cdot d^3\mathbf{k} \\ &\quad - \iiint \frac{f_n - f_0}{\tau}\cdot\mathbf{v}\cdot d^3\mathbf{k} + \iiint \mathcal{G}\cdot\mathbf{v}\cdot d^3\mathbf{k}.\end{aligned} \tag{2.51}$$

To distil (2.51) into a more manageable form, it is first necessary to note that the equilibrium distribution function f_0 (i.e. the Fermi-Dirac energy distribution), is even, in $\mathbf{k}$ space, i.e. $f_0(\mathbf{r},\mathbf{k},t) = f_0(\mathbf{r},-\mathbf{k},t)$, so the integral when multiplied by the odd function $\mathbf{v}$ in the third term on the right hand side of (2.51) vanishes. Using (2.44), it is clear that the same logic applies to the function $\frac{\partial f_n}{\partial t}$, so the left hand side term vanishes also. Assuming that the generation-recombination processes do not depend on momentum, but only the energy of the electrons, the same logic applies to the final term. Finally, the integral in the first term on the right hand side is equivalent to taking a non-normalised weighted average of the squared velocity $\mathbf{v}\cdot\mathbf{v}$ over $\mathbf{k}$-space[6]. This average is denoted $\langle v^2\rangle$. We are then left with:

$$0 = \langle v^2\rangle \nabla_\mathbf{r} \iiint f_n \cdot d^3\mathbf{k} + \frac{1}{\hbar}\mathbf{F}\iiint \mathbf{v}\cdot\nabla_\mathbf{k} f_n \cdot d^3\mathbf{k} - \frac{1}{\tau}\iiint f_n\cdot\mathbf{v}\cdot d^3\mathbf{k} \tag{2.52}$$

$$\Rightarrow 0 = \langle v^2\rangle \nabla_\mathbf{r} n + \frac{1}{\hbar}\mathbf{F}\left(\oiint \mathbf{v} f_n \cdot d\hat{S} - \iiint f_n \cdot \nabla_\mathbf{k}\mathbf{v}\cdot d^3\mathbf{k}\right) - \frac{1}{q_n\tau}\mathbf{J}_n \tag{2.53}$$

where integration by parts has been used. Since the integrals are evaluated over the extrema of populated k-space, by definition the region where the distribution function vanishes, the surface integral term vanishes, and referring back to (2.25), we can then write:

$$0 = q_n\tau_n\langle v^2\rangle \nabla n + \frac{q_n\tau_n\mathbf{F}}{\hbar}\left(\iiint f_n\cdot\nabla_\mathbf{k}^2\varepsilon_n(\mathbf{k})\cdot d^3\mathbf{k}\right) - \mathbf{J}_n. \tag{2.54}$$

[6]The calculation is not normalised in the sense that $\iiint f_i \cdot d^3\mathbf{k} \neq 1$

Substituting in the effective mass approximation (2.30), we arrive at:

$$\mathbf{J}_n = q_n \tau_n \left\langle v^2 \right\rangle \nabla n + \frac{q_n \tau_n \mathbf{F}}{m_n^*} n. \tag{2.55}$$

The external force $\mathbf{F}$ arises entirely from the applied electric field due to the potential Φ:

$$\mathbf{J}_n = q_n \tau_n \left\langle v^2 \right\rangle \nabla n - \frac{q_n^2 \tau_n}{m_n^*} \nabla \Phi \cdot n. \tag{2.56}$$

According to equipartition theorem[7], the square average thermal velocity $\left\langle v^2 \right\rangle = \frac{k_B T}{m^*}$. The quantity $\frac{q_i \tau_i}{m_n^*}$ is given the name mobility, μ_i. Taking the charge on a hole to be $q_p = q$ and therefore the electron charge $q_n = -q$, and using the Einstein-Smoluchowski relations[8] for the mobility and diffusivity $D_i = \frac{\mu_i k_B T}{q_i}$, the final expressions for the current density are:

$$\mathbf{J}_n = - q\mu_n n \cdot \nabla \Phi + q D_n \nabla n \tag{2.57}$$

$$\mathbf{J}_p = - q\mu_p p \cdot \nabla \Phi - q D_p \nabla p. \tag{2.58}$$

These expressions, combined with the continuity equations (2.49) and (2.50), and an appropriate form of Poisson's equation (2.6) constitute the drift-diffusion model, describing the dynamics of carrier motion in the bulk of a semiconductor. From the definitions of the carrier concentrations in terms of the quasi-Fermi levels (2.34), the relevant specific form of Poisson's equation is:

$$\nabla^2 \Phi = -\frac{q}{\varepsilon_r \varepsilon_0} (p - n + N) \tag{2.59}$$

$$\Rightarrow \nabla^2 \Phi = -\frac{q}{\varepsilon_r \varepsilon_0} \left(p_0 \exp\left(\frac{-\Phi}{V_T}\right) - n_0 \exp\left(\frac{\Phi}{V_T}\right) + N \right) \tag{2.60}$$

where N is the net doping, $V_T = \frac{k_B T}{q}$ is the thermal voltage, and n_0 and p_0 are the equilibrium electron and hole concentrations, respectively:

$$n_0 = n_i \exp\left(\frac{\phi_f - \phi_i}{V_T}\right) \qquad p_0 = n_i \exp\left(\frac{\phi_i - \phi_f}{V_T}\right) \tag{2.61}$$

[7]The usual form in 3D is $\left\langle v^2 \right\rangle = \frac{3 k_B T}{m^*}$. The 1D form is justified here (despite the derivation in 3D), because ∇n and ∇p are vectors, so multiplying by the 1D case is equivalent to scaling these vectors isotropically. Implicitly, the assumption that the band structure is completely isotropic is invoked here.

[8]These relations are accurate only for the case when the carrier statistics can be approximated by a Boltzmann distribution, i.e. when the distance of the electron energy from the Fermi level is much greater than the thermal energy: $(\epsilon - q\phi_n) \gg k_B T$ (see 2.32). This condition is well satisfied in Silicon at normal temperatures and operating conditions.

where ϕ_f is the Fermi level and ϕ_i is the intrinsic Fermi level (both in voltage units here). The interdependence of carrier concentration and potential results in a highly non-linear form for (2.60), though all the involved differential operators remain linear. The difficulty of solving this equation is thus significantly increased [100]. In practice, either a linearised form is used, which allows the solution to proceed by an iterative procedure using linear algebra techniques known as Gummel's method [41], or a Newton-Raphson method which solves the continuity and Poisson equations in a coupled fashion.

2.4 Mobility and Resistivity

In Section §2.3 the concept of the mobility μ_i was introduced, as being related to the time constant of scattering processes. From the drift-diffusion equations ((2.57) and(2.58)), the more conventional understanding of the quantity can also easily be justified. Consider a semiconductor with completely uniform doping and temperature throughout: the currents in such a device will be entirely due to the drift component, because ∇n and ∇p are zero:

$$\mathbf{J}_n = -q\mu_n n \cdot \nabla\Phi \equiv q\mu_n n \cdot \mathbf{E} \tag{2.62}$$

$$\mathbf{J}_p = q\mu_p p \cdot \nabla\Phi \equiv q\mu_p p \cdot \mathbf{E}. \tag{2.63}$$

Taking the basic definition of current density (2.48) and now ignoring the details of the distribution function (which are encapsulated by the various simplifications previously described), it is clear that:

$$\mathbf{J}_n = -q \cdot \mathbf{v}_{d,n} \cdot n \tag{2.64}$$

$$\mathbf{J}_p = q \cdot \mathbf{v}_{d,p} \cdot p \tag{2.65}$$

where $\mathbf{v}_d$ is called the drift velocity. Comparing (2.62) and (2.63) with (2.64) and (2.65), the conventional definition for mobility is recovered:

$$\mathbf{v}_{d,n} = -\mu_n \mathbf{E} \tag{2.66}$$

$$\mathbf{v}_{d,p} = \mu_p \mathbf{E}. \tag{2.67}$$

This relationship between a velocity and a force apparently seems to contradict Newton's 2nd law, but in fact arises because the drift velocity is an average velocity over many interaction

events - the collision time τ is in most cases extremely short[9]. Thus $\mathbf{v}_d$ should be thought of as a terminal velocity which is reached very promptly. This emphasizes yet another area in which the drift-diffusion model is a simplification: in any situation where the details of electron motion between individual collisions are important, the model should be used with caution. In practice, some non-idealities caused by this averaging over collisions can be readily incorporated by making the mobility dependent on the factors which affect the collisions. In this thesis, three cases which are particularly important for consideration are the electric field, local doping and temperature. The most widely used and experimentally verified model which incorporates all these factors in a physically motivated semi-empirical fashion is the Klaassen model [64]. This is the model implemented in practically all commercial device simulation programs. For the original solutions and simulations developed in this work, a simpler mobility model is used, since the cases of interest do not generally require coverage of the whole range of applicability of the Klaassen model, due to Caughey and Thomas [25], and the empirical measurements by Canali et al. [15].

The effect of electric field on mobility is also known as "velocity saturation", in that at a certain level of field, an increase in the field does not increase the particle drift velocity. The main cause of this is that extra scattering processes become possible at high carrier kinetic energies: chiefly that at a certain energy, carriers may emit an optical phonon. Although the higher field does increase the instantaneous carrier velocity, the effect of the optical phonon scattering is to reduce the average velocity (i.e. $\mathbf{v}_d$). The expression which is used to calculate the field-dependent mobility $\mu_i(|\mathbf{E}|)$ is given by [25]:

$$\mu_i(|\mathbf{E}|) = \frac{\mu_{i,0}}{\left(1 + \left(\frac{\mu_{i,0} \cdot |\mathbf{E}|}{v_{\mathrm{sat},i}}\right)^{\beta_i}\right)^{\frac{1}{\beta_i}}} \tag{2.68}$$

where $\mu_{i,0}$ is the low field mobility, $v_{sat,i}$ is the saturation velocity and β_i is a dimensionless empirical parameter. Temperature and doping effects are added through making these parameters variable [15]. β_i and $v_{\mathrm{sat,i}}$ are given only temperature dependence:

$$\beta_i = \beta_{0,i} \cdot \left(\frac{T}{T_{\beta,i}}\right)^{\beta_{1,i}} \tag{2.69}$$

$$v_{\mathrm{sat,i}} = \frac{v_{0,i}}{1 + \theta_{v,i} \exp\left(\frac{T}{T_{v,i}}\right)}. \tag{2.70}$$

[9] and indeed is required to be short compared to time scales of interest for the validity of the model to hold

Parameter	Value - electrons ($i = n$)	Value - holes ($i = p$)
$\beta_{0,i}$	1.109	1.213
$\beta_{1,i}$	0.66	0.17
$T_{\beta,i}$	300 K	
$v_{0,i}$	2.4×10^7 cm s^{-1}	
$\theta_{v,i}$	0.8	
$T_{v,i}$	600 K	
$\mu_{i,1}$	55.24 cm^{2}V^{-1}s^{-1}	49.7 cm^{2}V^{-1}s^{-1}
$\mu_{i,2}$	1429.23 cm^{2}V^{-1}s^{-1}	479.37 cm^{2}V^{-1}s^{-1}
$\mu_{i,3}$	-2.3	-2.2
$\mu_{i,4}$	-3.8	-3.7
$\mu_{i,5}$	0.73	0.70
$T_{\mu,i}$	300 K	
$N_{\mu,i}$	1.072×10^{17} cm^{-3}	1.606×10^{17} cm^{-3}

Table 2.1: Empirical Parameters for mobility modelling. Taken from [69, tables 3-41 and 3-66]

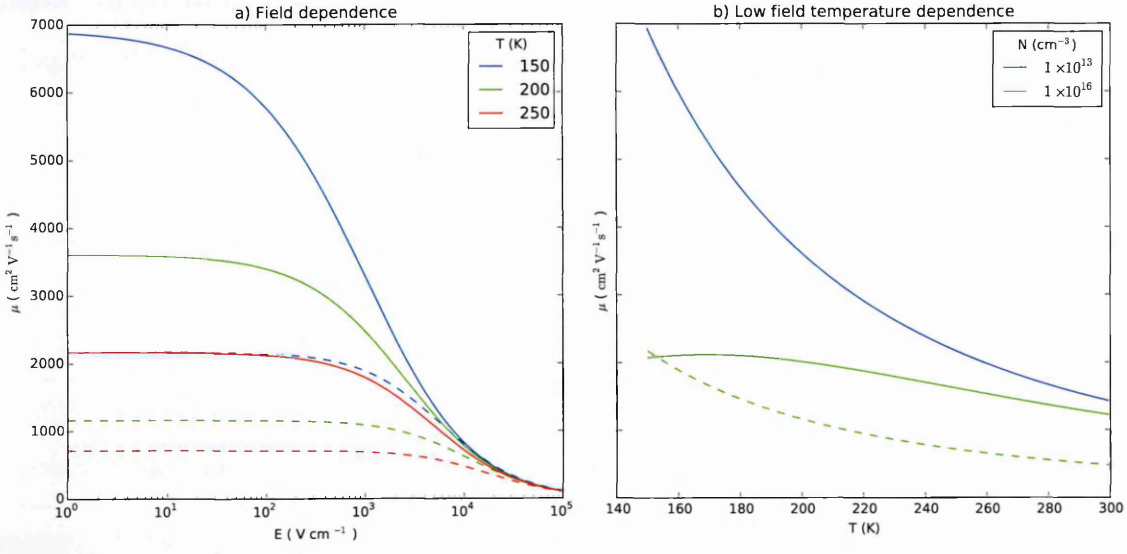

Figure 2.4: Behaviour of the mobility, μ including field, temperature and doping effects. Values for electrons are marked by solid lines, values for holes by dashed lines

Whereas the low field mobility also varies with the net doping :

$$\mu_{i,0} = \mu_{i,1} + \frac{\mu_{i,2}\left(\frac{T}{T_{\mu,i}}\right)^{\mu_{i,3}} - \mu_{i,1}}{1 + \left(\frac{T}{T_{\mu,i}}\right)^{\mu_{i,4}} \cdot \left(\frac{N_D+N_A}{N_{\mu,i}}\right)^{\mu_{i,5}}}. \tag{2.71}$$

The values for all empirical parameters are taken as the defaults used by the ATLAS device simulation program from Silvaco [69], and are reproduced in Table 2.1. Results of the mobility model calculation for relevant field, temperature and doping parameters are shown in Figure 2.4.

The mobility is perhaps the most important material parameter in electron transport

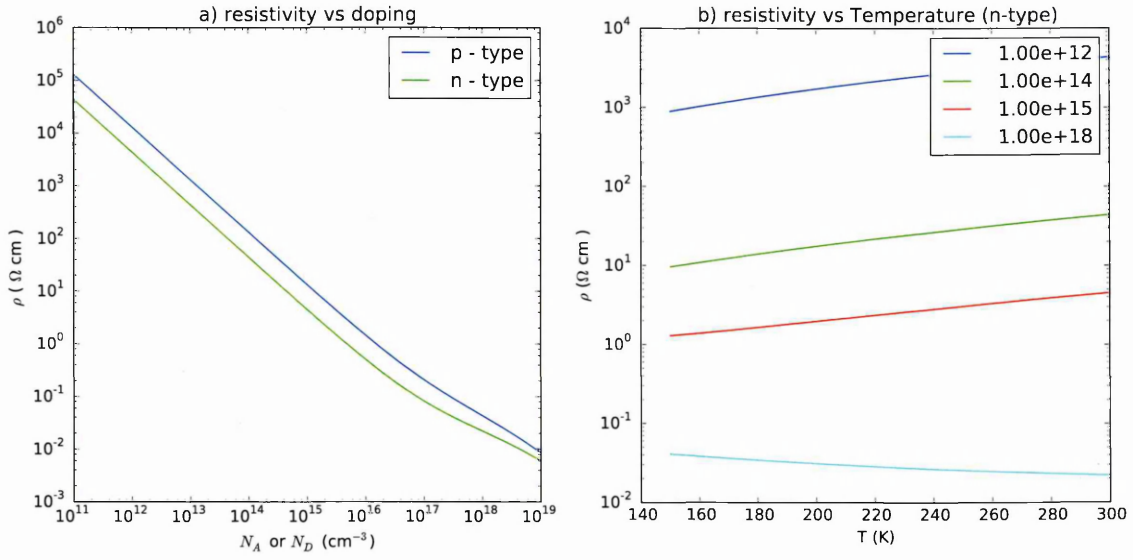

Figure 2.5: Calculated resistivity doping and temperature effects

modelling, but it is also related closely to an extremely significant engineering parameter specified in sensor design: the resistivity ρ, which in turn determines many of the device's performance characteristics. The relationship can be seen by starting from the standard expression for Ohm's law:

$$\mathbf{J} = \sigma \mathbf{E} \tag{2.72}$$

where σ is the conductivity, and $\mathbf{J}$ is the total current, which in the case of a semiconductor must include currents due to both electrons and holes. Taking again the situation where diffusion processes do not contribute an overall net current, from (2.72), (2.62) and (2.63) the conductivity can be written as:

$$\sigma = q\left(n \cdot \mu_n + p \cdot \mu_p\right). \tag{2.73}$$

And for an isotropic material (where the conductivity is not a tensor quantity), the resistivity is given by:

$$\rho = \frac{1}{q\left(n \cdot \mu_n + p \cdot \mu_p\right)}. \tag{2.74}$$

Since both the carrier densities (n and p) and the mobilities (μ_n and μ_p) vary with temperature and doping, the resistivity is also a function of these quantities. In principle, since all the terms in (2.74) also depend on the electric field[10], it is correct in some sense to say that the resistivity itself is field dependent. However, in practice this relationship is rarely used in

[10]Or, to be fully correct, the carrier densities should be said to be dependent on the quasi-Fermi levels rather than the applied field; though these two quantities are clearly closely linked.

a practical sense, because when talking about resistivity in the context of an image sensor, we are mainly interested in questions about the quasi-static characteristics of the device, such as: "how deep will the device's depletion region be, given a certain applied DC bias?".

The behaviour of the resistivity with varying doping environment (calculated from (2.74) assuming total dopant ionization) is shown in Figure 2.5. In this work, the main reference to resistivity will be in extracting estimates for bulk doping parameters - the resistivity is a specified quantity in manufactured devices, but it is the doping that needs to be known in order to construct physically based models. Since the resistivity itself is generally not very precisely known, and with the resistivity being a sensitive function of doping, it is found that these parameters are one of the factors limiting simulation accuracy.

2.5 Optical Excitation

Of particular interest to imaging sensors is optical stimulation. The charge carriers measured at the readout of the sensor consist principally of thermally released carriers, referred to as "dark signal" and ideally minimized in operation; and optically generated carriers[11]. The rate of generation of these carriers in response to stimulus (in this context labelled the "transition rate" $T_{i\to f}$) is at the base level described by Fermi's Golden Rule [32, chapter 3]:

$$T_{i\to f} = \frac{2\pi}{\hbar}\left|\left\langle f\left|qA\mathbf{r}e^{\hat{\jmath}\mathbf{k}\cdot\mathbf{r}}\right|i\right\rangle\right|^2 \cdot g\left(\hbar\omega\right) \tag{2.75}$$

where $\left\langle f\left|qA\mathbf{r}e^{\hat{\jmath}\mathbf{k}\cdot\mathbf{r}}\right|i\right\rangle$ is the quantum mechanical matrix element (in this case a dipole transition for an electromagnetic field of amplitude A) representing the transition between initial state $|i\rangle$ and final state $|f\rangle$; and $g\left(\hbar\omega\right)$ is the density of states available for transition, in this case given by the optical Joint Density of States (JDOS), which accounts for the availability of both an empty electron state in the conduction band, and a filled electron state in the valence band:

$$g\left(\hbar\omega\right) = \iint \frac{\delta\left(\epsilon_f - \epsilon_i - \hbar\omega\right) d^3\mathbf{k}}{\left|\nabla_{\mathbf{k}}\epsilon_n\left(\mathbf{k}\right)\right|} \tag{2.76}$$

where ϵ_i and ϵ_f are the energies of the initial and final states, $\hbar\omega$ is the energy of the incident photon, $\delta\left(\right)$ is the Dirac delta function, and $\epsilon\left(\mathbf{k}\right)$ is the energy band structure, as before. The delta function factor ensures energy conservation. The relative "strength" of optical absorp-

[11] Carriers originating from other mechanisms, including Clock Induced Charge (CIC), delayed trap release, and spurious optical generation from glowing transistors are all important factors to consider in device operation, but are not considered in this work except as possible complicating factors in measurement, where appropriate.

tion is therefore completely determined in principle by the band structure. For convenience, the quantity usually used in calculations of optical absorption is the absorption coefficient $\alpha(\omega)$, which is directly related to $T_{i\to f}$, normalised so as to be measured per unit length of material. For a direct band gap material, and assuming parabolic isotropic band structure, this coefficient is given by [32, eq 3.25]:

$$\alpha_{\text{direct}}(\omega) = \begin{cases} 0 & \hbar\omega < E_G \\ K_{DBG}\sqrt{\hbar\omega - E_G} & \hbar\omega > E_G \end{cases} \tag{2.77}$$

where K_{DBG} is a material constant related to the matrix element. Though a detailed derivation is not given here (an example can be found in [110]), the familiar form of the dependence $\sqrt{\hbar\omega - E_G}$ (being identical to the bulk 3D density of states) can be seen to arise from (2.76). Silicon is, however, not a direct band gap material (see Figure 2.2). In an indirect band gap, transitions must be facilitated by the absorption or emission of a phonon in order to conserve crystal momentum. The absorption coefficient in this case is given by [32, eq 3.36]:

$$\alpha_{\text{indirect}}(\omega) = K_{IDBG}(\hbar\omega - E_G \pm E_{ph})^2 \tag{2.78}$$

where E_{ph} is the phonon energy - the $\pm$ symbol is written because the phonon can be either absorbed or emitted. K_{IDBG} is again a material constant. Since phonon energies follow a spectrum, absorption is possible (though increasingly unlikely) below the indirect band gap. The necessity of a phonon interaction for optical absorption also implies that α_{indirect} must change with temperature, much more strongly than α_{direct}.

The values for α are taken throughout this work from published empirical measurements [37], which include coefficients allowing for temperature modifications. Since the incident light is mostly referred to in terms of wavelength, this is also the way in which α is measured. The data (see Figure 2.6) show a good agreement with a simple fit to (2.78) at the red end of the visible spectrum, and the argument about temperature variation being stronger at lower energies near the indirect band gap than near the direct band gap is clearly supported.

The absorption coefficient is the primary factor determining the QE of a device, though not the only one. Compounding effects include the absorption coefficients in other materials (oxide layers and poly-silicon gate electrodes) particularly for front-illuminated devices, enhanced recombination at semiconductor surfaces and interferometric effects due to device thickness.

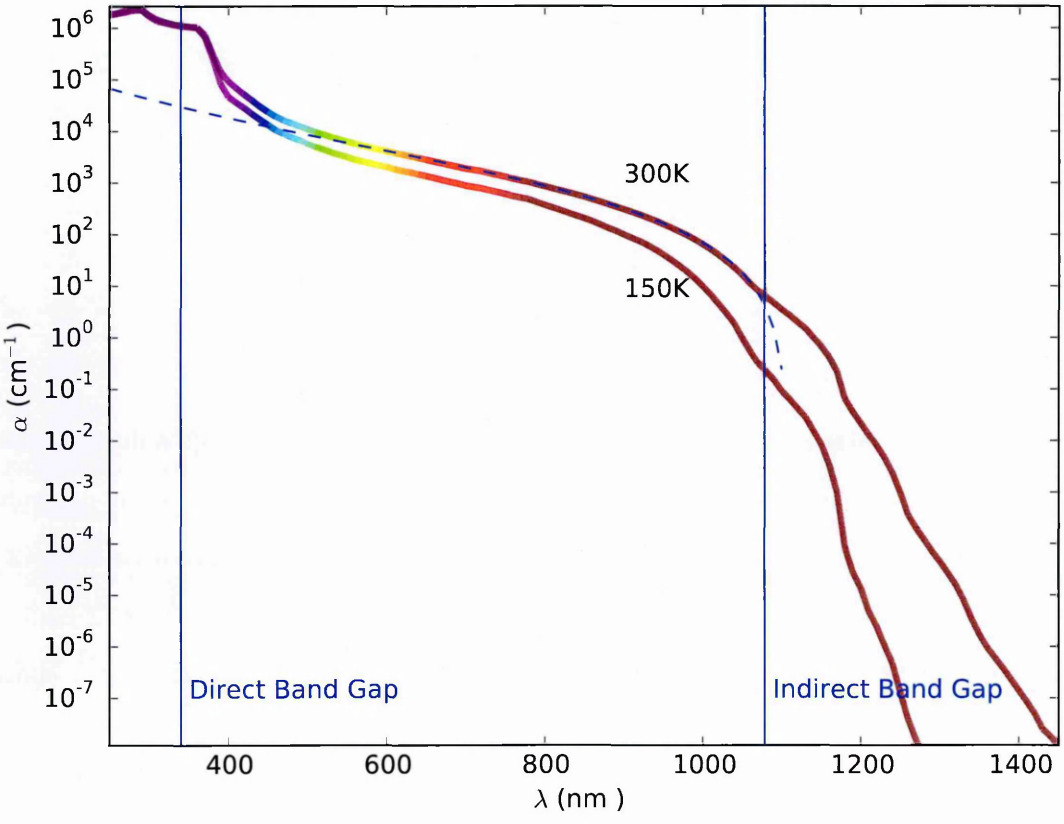

Figure 2.6: The absorption coefficient of silicon, from published tabulated data [37]. Energies of the direct and indirect band gaps are marked. The dashed line shows a basic fit to the expected theoretical behaviour for energies slightly above the indirect band gap (2.78)

For now, the primary purpose is to note that the generation of electrons due to absorption of incident light of a given wavelength follows the Beer-Lambert law:

$$I(z) = I_0 \exp(-\alpha(\lambda) z) \tag{2.79}$$

where I is the remaining photon intensity at depth z , and I_0 is the original intensity. The simple corollary of this expression is that the probability of a given photon having been absorbed after travelling through a certain thickness Z is

$$P(Z) = 1 - \exp(-\alpha(\lambda) Z). \tag{2.80}$$

This expression is used to model electron generation throughout the thesis.

For very high energy photons (e.g. soft X-rays), the properties of the absorption coefficient depend on nuclear, rather than crystal, physics. From the point of view of imaging sensors,

however, the same absorption law applies. Additional considerations are needed when investigating high energy photons, chiefly the Fano effect [31]. A high energy photon releases a high energy primary electron, which in turn has sufficient energy to ionize further silicon cores. This cascade process places a fundamental limit on the energy resolution of a detector which operates by carrier counting, which (due to the correlations introduced into the cascade process by overall conservation of energy) is less than that which would be expected by Poisson statistics (i.e. the mean number of carriers being numerically equal to the variance in the number of carriers). The dispersion between the mean number of carriers eventually released in the cascade and the standard deviation of that number is known as the Fano Factor, F. In silicon, a recently obtained experimental value is $F = 0.06 \pm 0.01$ [23]. A value measured for Argon gas is, for example, $F = 0.20 \pm 0.01$, resulting in the implied energy resolution for a silicon detector being significantly higher than that for the gas detector.

2.6 Finite Element Methods

To obtain practical solutions of drift-diffusion models, finite element numerical methods are used pervasively. Within this work, models are verified against simulations from the commercial Silvaco package [69]. The fine details of the implementation of these solutions are not relevant, though one particular concept is important when comparisons are to be made between the output of finite element simulations and continuously solved models: that of the Scharfetter-Gummel discretization scheme, originally developed in 1969 [87]. The coupled continuity and Poisson's equations are highly non-linear, and a naive interpolation scheme for the relevant quantities leads rapidly to numerical instabilities [100]. Interpolation is needed for any finite element method, because though the solution quantities are obtained at the mesh points, flux quantities must be evaluated at positions between those points. The simplest approach is to interpolate potentials (and, by extension, fields) linearly between mesh points. The Scharfetter-Gummel interpolation then allows the values of the currents J_i and concentrations n and p at points between the mesh points. For simplicity, only the 1 dimensional steady state case is considered ($\frac{\partial n}{\partial t} = \frac{\partial p}{\partial t} = 0$). Throughout, the notation $A^{(i)}$ denotes a quantity A at mesh point i. For electrons, both the continuity equation (2.49) and the current density equation (2.57) must be discretized. The mesh spacing between points (i) and $(i+1)$ is $\Delta^{(i)}$. Starting with (2.49):

$$\frac{J_n^{(i+\frac{1}{2})} - J_n^{(i-\frac{1}{2})}}{\Delta^{(i)}} = -qG. \tag{2.81}$$

To treat (2.57), the potential is assumed to vary linearly, so can be discretized between points, but the concentration is left as a continuous variable, $n(x)$:

$$J_n^{\left(i+\frac{1}{2}\right)} = -q\mu_n^{\left(i+\frac{1}{2}\right)} \cdot n(x) \cdot \frac{\Phi^{(i+1)} - \Phi^{(i)}}{\Delta^{(i)}} + q \cdot D_n^{\left(i+\frac{1}{2}\right)} \cdot \frac{dn}{dx}. \tag{2.82}$$

This expression is then considered as an ordinary differential equation for $n(x)$, with the current J_n as a constant. This problem can be solved using an integrating factor method, with the integrating factor ν given by:

$$\nu(x) = \exp\left(-\int_{x^{(i)}}^{x} \frac{1}{V_T^{\left(i+\frac{1}{2}\right)}} \cdot \frac{\Phi^{(i+1)} - \Phi^{(i)}}{\Delta^{(i)}} \cdot dx'\right) \tag{2.83}$$

$$\Rightarrow \nu(x) = \exp\left(-\frac{1}{V_T^{\left(i+\frac{1}{2}\right)}} \cdot \frac{\left(\Phi^{(i+1)} - \Phi^{(i)}\right)}{\Delta^{(i)}} \left(x - x^{(i)}\right)\right). \tag{2.84}$$

Applying the integrating factor to (2.82) in the usual way:

$$\frac{J_n^{\left(i+\frac{1}{2}\right)}}{qD_n^{\left(i+\frac{1}{2}\right)}} \int_{x^{(i)}}^{x^{(i+1)}} \nu \cdot dx = \nu \cdot [n(x)]_{x^{(i)}}^{x^{(i+1)}} \tag{2.85}$$

$$\Rightarrow \frac{J_n^{\left(i+\frac{1}{2}\right)} \Delta^{(i)} \left(\exp\left(\frac{\Phi^{(i+1)} - \Phi^{(i)}}{V_T^{\left(i+\frac{1}{2}\right)}}\right) - 1\right)}{qD_n^{\left(i+\frac{1}{2}\right)} \frac{\left(\Phi^{(i+1)} - \Phi^{(i)}\right)}{V_T^{\left(i+\frac{1}{2}\right)}}} = \exp\left(\frac{\Phi^{(i+1)} - \Phi^{(i)}}{V_T}\right) \left(n^{(i+1)} - n^{(i)}\right) \tag{2.86}$$

which can be simplified and combined with (2.81) to obtain:

$$J_n^{\left(i+\frac{1}{2}\right)} - J_n^{\left(i-\frac{1}{2}\right)} = \frac{qD_n^{\left(i+\frac{1}{2}\right)}}{\Delta^{(i)}} \left(B\left(\frac{\Phi^{(i)} - \Phi^{(i+1)}}{V_T^{\left(i+\frac{1}{2}\right)}}\right) n^{(i+1)} - B\left(\frac{\Phi^{(i+1)} - \Phi^{(i)}}{V_T^{\left(i+\frac{1}{2}\right)}}\right) n^{(i)}\right) \tag{2.87}$$

where $B(x)$ is the Bernoulli function:

$$B(x) = \frac{x}{\exp(x) - 1}. \tag{2.88}$$

The interpolation rule represented by (2.87) allows the optimal calculation of currents J_n and J_p between finite element cells, given the values of the concentrations n and p and potential Φ at the centre points of those cells. Note that this scheme does not in any significant way help to actually obtain self consistent solutions for the drift-diffusion model, only to avoid numerical instability which otherwise would arise if the currents at the intermediate points

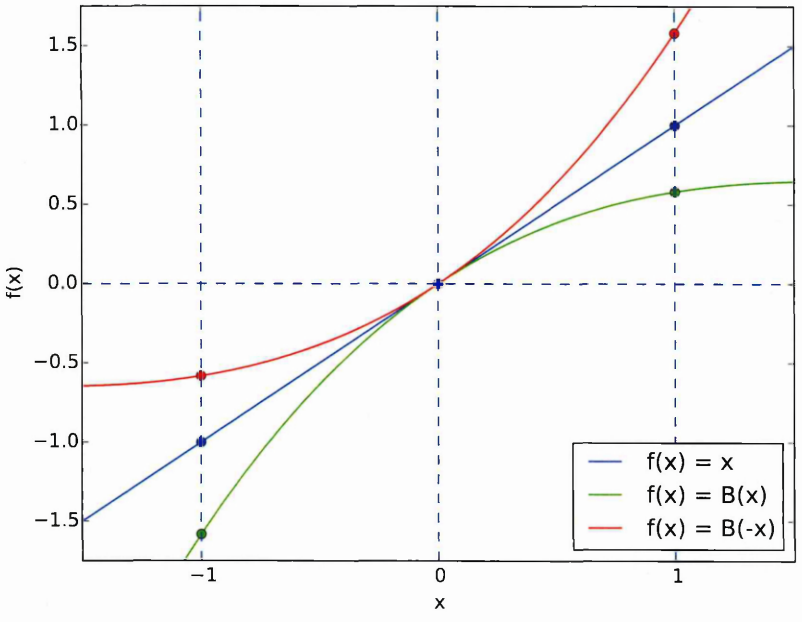

Figure 2.7: Illustration of the difference between linear and Scharfetter-Gummel weighting for interpolation

were obtained by a naive linear interpolation. This allows mesh spacing to be more sparse whilst minimally affecting the accuracy and convergence properties of the solution. The difference of linear weighting as compared with Scharfetter-Gummel weighting is illustrated in Figure 2.7. The model we describe in Chapter 4 can be evaluated at arbitrary co-ordinates.

2.7 Summary

The derivation of some common semiconductor modelling techniques have been described, and some relevance in the context of imaging science has been demonstrated. The computation of models describing charge collection in CCDs will chiefly be performed using the drift-diffusion simulation, with field, doping and temperature dependent mobility. The constants and empirical laws used to calculate these material constants and those for optical absorption which will be used have been given.

Having dealt with the generality of the low level details of charge transport in silicon, it is time to move on to the specific picture of the construction and operation of imaging sensors.

Chapter 3

Image Sensor Design and Construction

> If it's a good idea, go ahead and do it. It is much easier to apologize than it is to get permission.
>
> Rear Adm. Grace Hopper

Imaging sensors are relatively complex devices which generally differ from simpler photosensitive electronic components in two ways:

1. The photosensitive elements (pixels) are arranged in a regular spatial array and are addressable to varying degrees of flexibility, providing spatial information and allowing for numerous readout schemes depending on application.

2. Many (though by no means all) types of sensors operate in an integrating mode: signals arising from incident light are accumulated over a period of time, and are represented by a quantity of charge, rather than instantaneous values of current or voltage.

All the sensors relevant to the work at hand possess these qualities. In the main, the dynamic charge effects considered are most relevant in thick, back illuminated CCDs, and so herein most of the effort is expended in modelling these systems accurately. However, some of the ideas are also very useful in CMOS-APS detectors, especially since some recent APS devices are incorporating properties more traditionally seen in CCDs [49].

This chapter covers the background information about sensor design which are of interest to charge collection investigation, with reference to the performance measurements which are affected. The more intricate details of the performance measurements themselves are given in the later experimental chapters.

3.1 Sensor Architecture

Though the photo-conductivity of silicon junctions had been serendipitously discovered in 1940 by Russel Ohl [84], the development of the earliest practical imaging devices occurred several decades later. In contrast to a "camera-tube" type imaging device, for the construction of an imaging array, photo-conductivity is a necessary but not sufficient property. Having many elements (i.e. pixels) necessarily mandates some readout scheme which consults the signal on only some pixels at the same time - to obtain reasonable sensitivity, the output signal of each element must not be merely related to the momentary incident photon flux, but rather must accumulate based on the fluence since the last readout. Such a device was described in 1967 by Weckler [106]. The photosensitive element in this design is a p-n junction acting as a diode, reverse biased to a reset voltage, and then allowed to float during the integration time. Incident photons allow current to flow through the diode, reducing the voltage at the cathode. The operation of this structure with respect to photo collection will be described in more detail in Section §3.2. After integration, the diode is connected through switching transistors to a charge amplifier. The pixel is then reset by a separate transistor. This kind of array construction is now referred to as a "passive pixel sensor", and is illustrated in Figure 3.1. The passive pixel sensor is extremely sensitive to noise sources coupled in capacitively through the tracks connecting the pixels to the output circuitry; this problem becomes worse the larger the array, because the tracks necessarily become longer. Even for a reasonably sized array, the capacitance represented by the pixel itself is comparable to that of the connecting bus lines [34]. The response to these major limitations was the APS.

3.1.1 Active Pixel Sensor (APS)

As early as 1968 [75], it was suggested to combat the problems with Passive Pixel Sensors by adding buffering circuitry to each pixel. In addition, because the photo diode cannot be reset "through" the buffer, a separate reset transistor is required local to each pixel. The resulting design for the array is shown in Figure 3.2, and the simplest possible design [49] for each pixel (the "three-transistor", or 3T design) is shown in Figure 3.3, consisting of a source-follower Metal Oxide Semiconductor Field Effect Transistor (MOSFET) transistor as the buffer, and an additional MOSFET for reset. These devices have become known as "active pixel sensors" APS. Though they drastically improve the noise and sensitivity performance

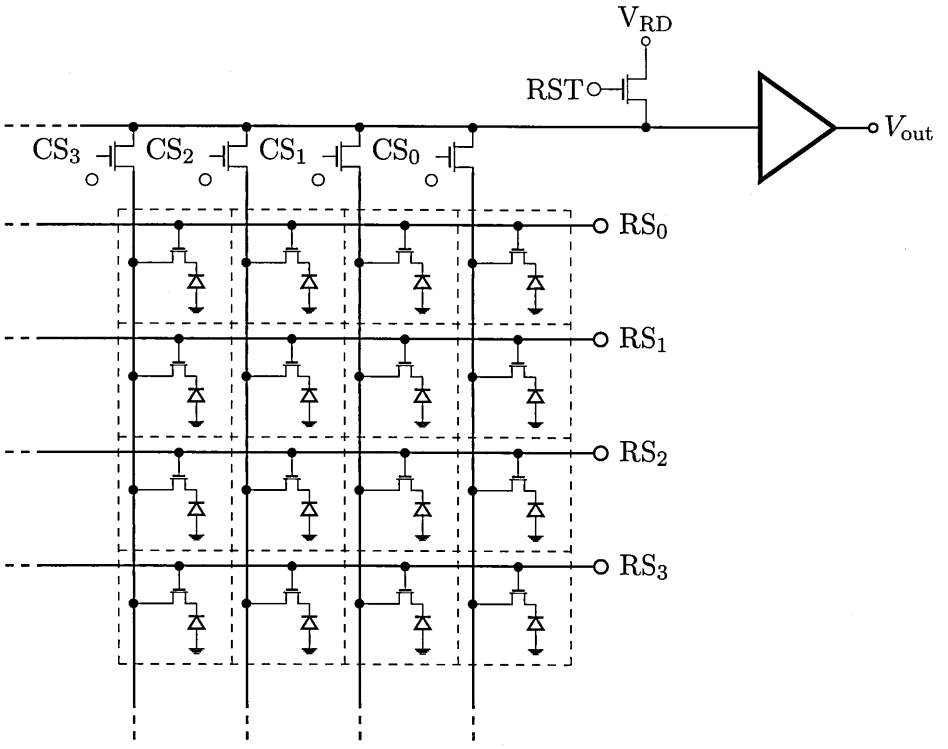

Figure 3.1: Passive Pixel Sensor architecture. The signals RS_i and CS_i are used to select a pixel to readout, which is then connected to the output amplifier. The pixel can be reset to V_{RD} using the RST signal.

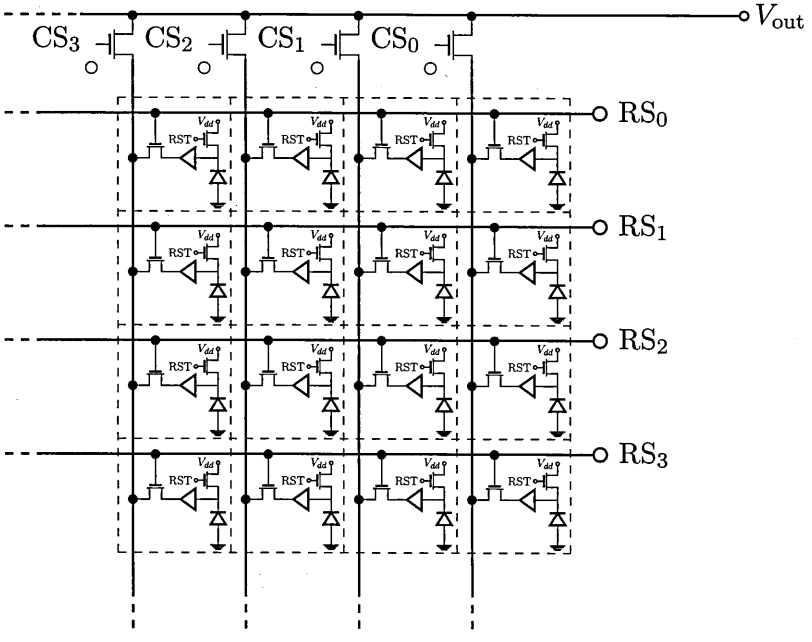

Figure 3.2: Active Pixel Sensor architecture. Each pixel incorporates buffer and reset circuitry.

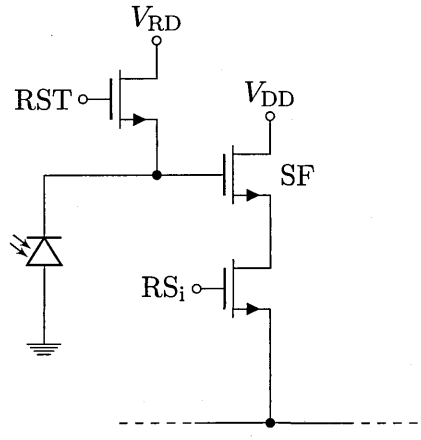

Figure 3.3: 3T pixel design. The source follower transistor is marked "SF"

over the passive device[1] and also offer the possibility of incorporating more features in the pixel (e.g. switchable capacitance, global array reset) by adding more transistors, the practical implementation of useful APS devices was extremely difficult given the available reliability and feature size of semiconductor processing at the time. In recent years APS devices have increased in performance and utility to the point where they can replace CCDs in many applications, though in scientific applications, CCDs still have clear advantages, including noise and linearity performance [49]. In fact, the incorporation of some CCD design features have been incorporated into APS pixel designs in an attempt to leverage the advantages of charge transfer.

3.1.2 Charge Coupled Device (CCD)

Boyle and Smith [11] invented the charge coupled device CCD in 1969. Though the device was primarily intended for use as an electronic delay line, the extension of the concept to imaging arrays was mentioned in the original paper. A CCD is perhaps best thought of as an array of closely spaced MOS capacitors, usually with overlapping gates. Signal charge can be transferred between neighbouring gates by sequentially applying potentials in the appropriate order, a process known as clocking. A simple illustration of this process is shown in Figure 3.4. Gates are connected electrically in sets called phases. Necessity of gate overlap to satisfactory device operation is the main factor causing a difference in the processing and construction between standard Complementary Metal Oxide Semiconductor (CMOS) devices and CCDs. The basic cross-sectional construction of a 3-phase CCD perpendicular to the transfer direction is shown in Figure 3.5.

[1]Indeed, passive pixel sensors are now rarely used for anything but extremely specialized applications, and certainly not in scientific or industrial imaging.

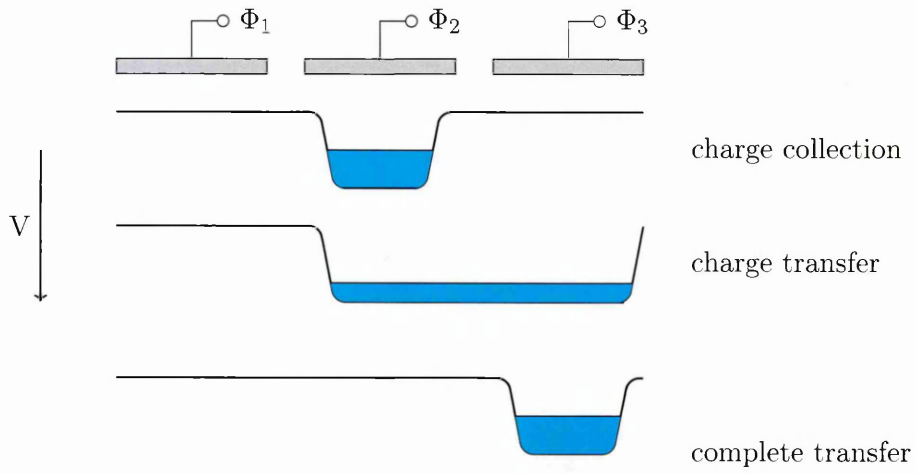

Figure 3.4: Illustration of charge transfer process between neighbouring gates

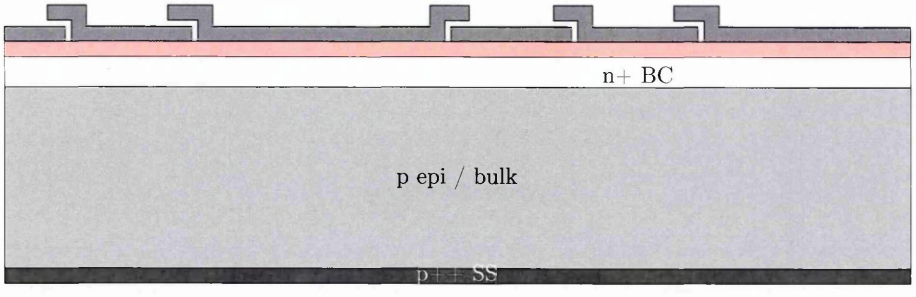

Figure 3.5: 3-phase CCD device cross section. The gate insulation layer (shown in pink in the diagram) is usually a combination of SiO_2 and Si_3N_4. Devices may be constructed from epitaxially grown or bulk Si

An example 2D arrangement of CCD architecture is shown in Figure 3.6. Signal charge from many pixels is read out through the same charge amplifier by clocking rows of the image area into a linear sequence of cells known as the serial register. Phases in the image area are known as image clocks (labelled IΦ1, IΦ2 and so on); those along the serial register are called serial clocks or register clocks (labelled RΦ1, RΦ2 etc). Clocking a row into the register is called parallel transfer, and clocking along the register is called serial transfer. Charge is prevented from "spilling" between pixels during integration and parallel transfer by a p+ implant in the array referred to as the channel stop. One key advantage of the charge transfer architecture is that signals in neighbouring pixels may be summed noiselessly prior to readout, and the difficulty of calibrating the output transfer function of many separate amplifiers to obtain accurate photometric information which is necessary with an APS device is absent. However, reading out the array in this manner is also a slower process than the equivalent APS construction due to the time taken to perform charge transfer. The charge transfer process itself is also not completely efficient, which results in the occasional loss of signal electrons to bulk or surface trapping states. In a modern, high quality scientific device, properly adjusted,

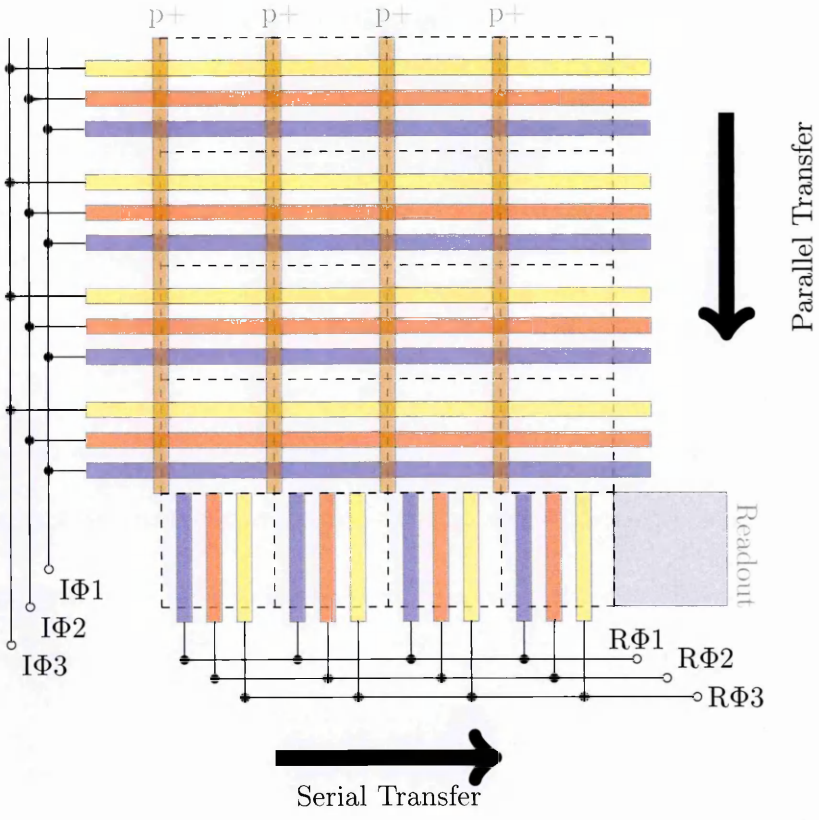

Figure 3.6: Architectural diagram of a 3-phase CCD, showing image clocks, register clocks, and the channel stop implant

the Charge Transfer Inefficiency (CTI) (the fraction of signal charge lost per pixel) is typically below 1×10^{-5}, and is not of importance to the analysis presented in this thesis [54]. In fact, the chief device parameters which affect charge collection are related to the thickness of the device, the geometry of the gates, the operating bias conditions and the details of the buried channel implant, to which we now turn in more detail.

3.2 Collection Elements

Though the CCD is generally thought of as using photo-gates for collection, and the APS is more often associated with photo-diodes, it is perfectly possible to construct a device of either architecture with either collection element - as evidenced by 6T photo-gate CMOS pixels - which use active pixel electronics but collect charge under a photo-gate, and interline transfer CCDs where charge is collected by a reverse biased diode structure before being transferred into the channels used for readout clocking [49].

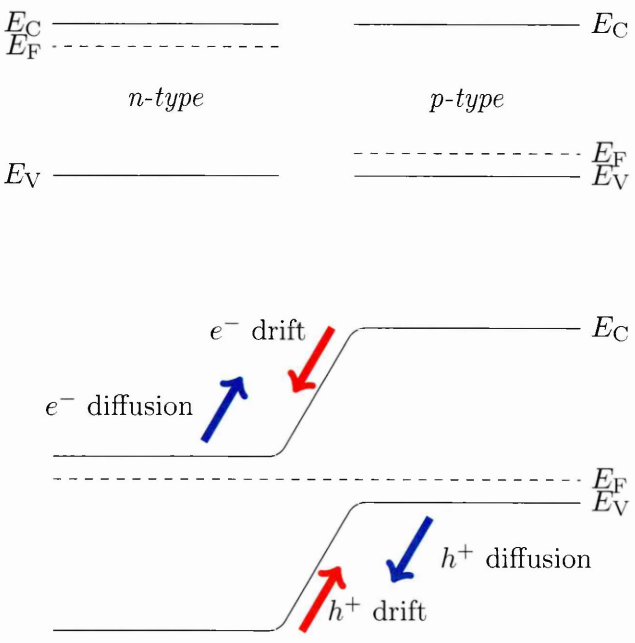

Figure 3.7: Formation of a pn-junction

3.2.1 The pn junction photo-diode

A pn junction is formed when a piece of p-type material (doped with e.g. Boron) is brought into contact with n-type material (doped with Phosphorous or Arsenic). The Fermi level E_f of a semiconductor will always adjust to maintain overall charge neutrality, so in the case of the n-type material, where ionised donor atoms are present, E_f must move towards the conduction band edge. In p-type material, by contrast, E_f must move towards the valence band edge. When the p-type and n-type materials are brought into contact, if the temperature is uniform, the Fermi level must equalise throughout the junction (otherwise electrons simply traversing the junction could gain energy without requiring any input of work). As a result, it is the valence and conduction bands that must "bend" at the junction to satisfy the constraint. This situation is illustrated in Figure 3.7. Carrier concentration differences between the n-type and p-type regions cause diffusion currents to be established for both electrons and holes: holes from p-type towards n-type, and vice-versa for electrons. At the centre of the junction, holes and electrons can meet and recombine, leaving behind unscreened ionised donor impurities on the n-type side, and unscreened ionised acceptor impurities on the p-type side. This volume of unscreened charges is called a depletion region. The existence of these unscreened charges implies an electric field across the junction, directed from the n-type region towards the p-type region, whose magnitude depends on how many unscreened charges are present overall. This field causes a drift current in response; the electrons drift from p-type towards n-type, and

the holes from n-type towards p-type. The directions of these currents oppose the diffusion currents, and hence oppose the expansion of the depletion region. The equilibrium size of the depletion region x_D, therefore, is determined by the point at which the drift currents balance the diffusion currents, and is given by [97]:

$$x_D = \sqrt{\frac{2\varepsilon_{si}\varepsilon_0}{q_e}\left(\frac{N_A + N_D}{N_A N_D}\right)\left(V_{\text{bi}} - \frac{2k_B T}{q_e}\right)} \tag{3.1}$$

where V_{bi} is the "built-in" junction potential. In the case where $N_D \gg N_A$ (as is the case for an n-channel imaging sensor built on high-resistivity p-type substrate), (3.1) reduces to:

$$x_D = \sqrt{\frac{2\varepsilon_{\text{si}}\varepsilon_0}{q_e N_A}\left(V_{\text{bi}} - \frac{2k_B T}{q_e}\right)}. \tag{3.2}$$

Applying a bias voltage to the junction causes electrons and holes to acquire separate quasi Fermi levels $E_{f,n}$ and $E_{f,p}$ (as described in Section §2.3). Reverse biasing enhances the electric field due to the depletion region, whilst forward biasing counteracts it - so that applying a reverse bias to the junction causes the depletion region to expand.

In an APS pixel, the pn junction is reverse biased and then left floating during the integration time. The potential difference across the junction prevents current from flowing, except when a photon absorption causes an electron hole pair to be generated in the depletion region, or when charge is generated within the region by thermal processes (see Section §3.5). In this case, the pair is separated by the electric field; this additional separated charge causes the depletion region width to decrease, and with it the voltage across the junction. Thus, the difference between the original junction bias and the measured voltage after integration is related to the integrated incident photon flux. The process of charge to voltage conversion is hence also performed by the junction diode itself, so the pixel amplifier circuitry (see Section §3.1.1) in the simplest case may consist simply of a single source-follower transistor. There are two disadvantages to this approach:

- Since the size of the depletion region changes with the applied voltage, so does the associated capacitance. The capacitance of the junction therefore changes with signal size, resulting in non-linearity. This non-linearity is generally small, however, compared with that introduced by the amplification transistors themselves [49].

- There is no effective way to cancel reset noise (see Section §3.6.1).

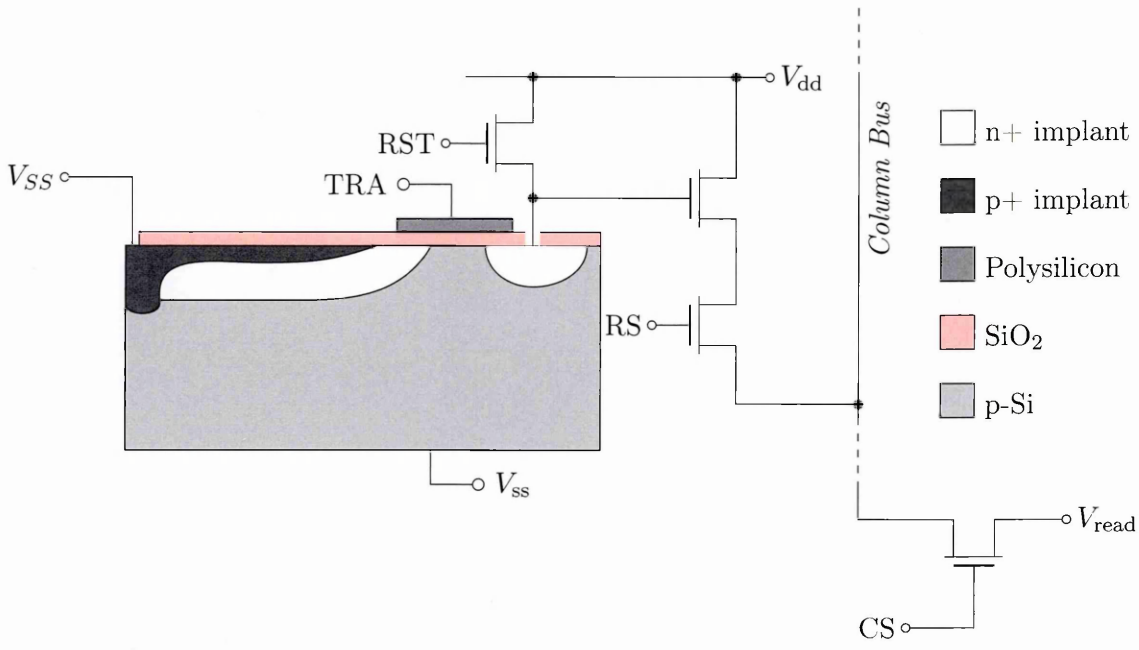

Figure 3.8: 4T readout architecture

Both of these problems are generally eliminated by using a 4T architecture (see Figure 3.8). The structure used for charge collection is called a pinned photo diode [98], and the accumulated charge is transferred through the transfer gate (marked TRA) to a sense node for measurement. This allows elimination of the reset noise through CDS by measuring the sense node voltage after reset (see Section §3.6.1), and also reduces the effect of changing junction capacitance.

3.2.2 The photo-gate

The photo-gate collection structure is essentially a MOS capacitor. The collected charge carriers correspond to the minority carrier type in the substrate. Thus, a photo-gate fabricated on n-type substrate is known as "p-channel" (collecting holes), and one fabricated on p-type is known as "n-channel" (collecting electrons). The performance differences between these devices are rather subtle. The mobility of electrons in p-type silicon is higher than that for holes in n-type silicon (see Section §2.4), implying that for similar conditions, the drift time in n-channel devices should be slightly shorter, and therefore the spatial resolution slightly better. This idea is borne out by some experimental evidence [73]. On the other hand, there is also mounting evidence that p-channel devices may have some other important advantages in terms of radiation damage performance in space environments, due to the differing nature of traps present in n-type as compared with p-type silicon [36].

In the simplest case ("surface channel") the photo-gate structure consists simply of a metal

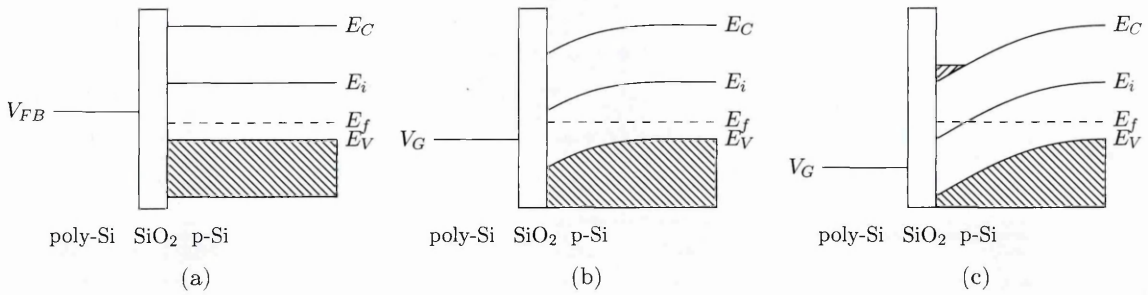

Figure 3.9: Band diagrams for the surface channel MOS capacitor, biased in (a) flat-band, (b) depletion and (c) inversion conditions

or (much more commonly for imaging applications) poly-silicon gate electrode deposited onto an insulating layer (usually SiO_2 and Si_3N_4) which is grown onto either an epitaxial or bulk substrate. Applying a positive bias voltage (above the flat-band voltage) to the gate with respect to the substrate causes holes to be repelled from the semiconductor insulator interface, forming a depletion region (see Figure 3.9). Increasing the bias voltage beyond a point known as the inversion threshold (the point where the intrinsic level E_i crosses the intrinsic Fermi Level E_f), the thermodynamic equilibrium shifts such that electrons will begin to accumulate at the surface - the volume near the surface becoming "inverted" from p-type to n-type: there is in this condition a greater concentration of electrons than holes. However, thermodynamic equilibrium may only be reached given a sufficient supply of electrons. In other devices which use the same construction, for example MOSFETs, the source contact of the device would provide these carriers. The absence of a nearby source in the CCD means that the inversion layer forms very slowly, and the depletion length continues to extend as gate voltage V_G increases, the inversion layer not being present to screen the effect of the increasing voltage. As such, the CCD operates always outside of thermal equilibrium.

Assuming that the concentration of free minority carriers in the depletion region is very low, but that thermodynamic equilibrium applies, the non-linear Poisson Equation (see (2.60)) can be written in one dimension as:

$$\frac{d^2\Phi}{dz^2} = -\frac{q}{\varepsilon_{si}\varepsilon_0}\left(p_0 \exp\left(\frac{-\Phi}{V_T}\right) - N_A\right) \tag{3.3}$$

where N_A is the density of acceptors, and V_T is the thermal voltage. For p-type silicon, neglecting unionised acceptors, $p_0 \approx N_A$, so that:

$$\frac{d^2\Phi}{dz^2} = \frac{qN_A}{\varepsilon_{si}\varepsilon_0}\left(1 - \exp\left(\frac{-\Phi}{V_T}\right)\right) \approx \frac{qN_A}{\varepsilon_{si}\varepsilon_0}\frac{\Phi}{V_T} \tag{3.4}$$

whose solution is:

$$\Phi = \Phi_0 \exp\left(-z \cdot \sqrt{\frac{qN_A}{\varepsilon_{\rm si}\varepsilon_0 V_T}}\right) \tag{3.5}$$

where Φ_0 is the potential at the interface. This shows that the inversion layer screens the gate voltage exponentially with depth into the silicon. However, in the case where no free carriers at all are available, then:

$$\frac{d^2\Phi}{dz^2} = \frac{qN_A}{\varepsilon_{\rm si}\varepsilon_0}. \tag{3.6}$$

If there is no trapped charge in the oxide layer, then the potential in the oxide is linear in form, so that a solution can be written by assuming these forms and matching the boundary conditions at the oxide interface. The solution for the potential can then be written:

$$\Phi(z) = \phi_s + \frac{qN_A}{2\varepsilon_{\rm si}\varepsilon_0}(z_D - z)^2 \tag{3.7}$$

where ϕ_s is the potential at the oxide interface, and z_D is the depletion depth. Assuming no trapped charge in the oxide layer, the voltage drop in the oxide is linear, and the value of ϕ_s can be found from the applied gate voltage V_G by [97]:

$$\phi_s = V'_G + V_0 - \sqrt{2V'_G V_0 + V_0^2} \tag{3.8}$$

$$\text{with} \quad V'_G = V_G - V_{\rm FB} - \frac{d_{\rm ox}Q}{\varepsilon_{\rm ox}\varepsilon_0} \tag{3.9}$$

$$V_0 = qN_A\varepsilon_{\rm si}\varepsilon_0\left(\frac{d_{\rm ox}}{\varepsilon_{\rm ox}\varepsilon_0}\right)^2 \tag{3.10}$$

where Q is the amount of stored charge in the channel. The size of the depletion region z_D can then be obtained by combining (3.8) and (3.7):

$$z_D = \frac{d_{\rm ox}\varepsilon_{\rm si}}{\varepsilon_{\rm ox}}\left(\sqrt{1 + \frac{V'_G}{2V_0}} - 1\right). \tag{3.11}$$

Clearly, z_D decreases as Q increases.

The chief problem with the surface channel MOS capacitor for CCD applications is the presence of surface "trapping" states, which can capture an electron from the signal packet and release it at some time later, resulting in very poor CTI characteristics. The introduction of the buried channel [12] was designed to alleviate this problem: if the stored signal charge can be kept isolated from the surface, the effect of the trapping states is greatly reduced.

This may be achieved by introducing a counter implant at the surface - e.g. for a p-type substrate, a heavily doped n-type implant is used. The effect is to move the position of the potential maximum (and therefore the storage location of the charge packet) away from the surface. As a simple approximation, the buried channel implant can be modelled as an abrupt pn junction.[2] In this case, the equation to be solved to find the potential (in an n-channel device), is :

$$\frac{d^2\Phi}{dz^2} = \begin{cases} -q \cdot N_D & 0 \leq z \leq z_J \\ q \cdot N_A & z_J < z \end{cases} \tag{3.12}$$

where z_J is the junction depth and N_D is the density of donor impurities in the buried channel. In the case of no stored charge, the solution in one dimension can be obtained exactly [109]:

$$\Phi(z) = \frac{q}{2\varepsilon_{si}\varepsilon_0} \cdot \begin{cases} N_D (z - z_m)^2 & z < z_J \\ N_A (z - z_D)^2 & z_J < z < z_D \end{cases} \tag{3.13}$$

$$\text{with} \quad z_m = z_J - \sqrt{\frac{2\varepsilon_{si}\varepsilon_0 N_A V_m}{qN_D (N_A + N_D)}} \tag{3.14}$$

$$V_m = \left(1 + \frac{N_A}{N_D}\right)\left(V_G + V_1 + V_2 - \sqrt{V_2^2 + 2V_2 (V_G + V_1)}\right) \tag{3.15}$$

$$V_1 = \frac{qN_D z_J^2}{2\varepsilon_{si}\varepsilon_0}\left(1 + \frac{2\varepsilon_{si} d_{ox}}{\varepsilon_{ox} z_J}\right) \tag{3.16}$$

$$V_2 = \frac{qN_A z_J^2}{\varepsilon_{si}\varepsilon_0}\left(1 + \frac{\varepsilon_{si} d_{ox}}{\varepsilon_{ox} z_J}\right)^2 . \tag{3.17}$$

When a stored charge is included, the exact solution for the potential cannot be obtained analytically, though a numerical solution using the Successive Over-Relaxation approach is possible [62]. It is found by Yin and Cooper [109] that a simple approximation which allows the potential to still be calculated analytically with reasonable accuracy is to assume a charge packet with constant density equal to N_D. This model is used to simulate charge storage in modelling the BFE in Chapter 4.

In contrast to the surface channel device, where the lack of an electron source/sink at the surface will result in a long time elapsing before thermodynamic equilibrium is achieved, in a buried channel the counter-doped region provides a source of signal carriers, since they are the majority carriers in that region. Thus, to achieve sustained deep depletion conditions and operate the device for imaging, the buried channel region must itself be depleted of carriers.

[2] In a real device, the buried channel is normally formed by diffusion or implantation, so the abrupt junction is physically unrealistic. However, by adjusting the depth, behaviour similar to realistic conditions can be achieved

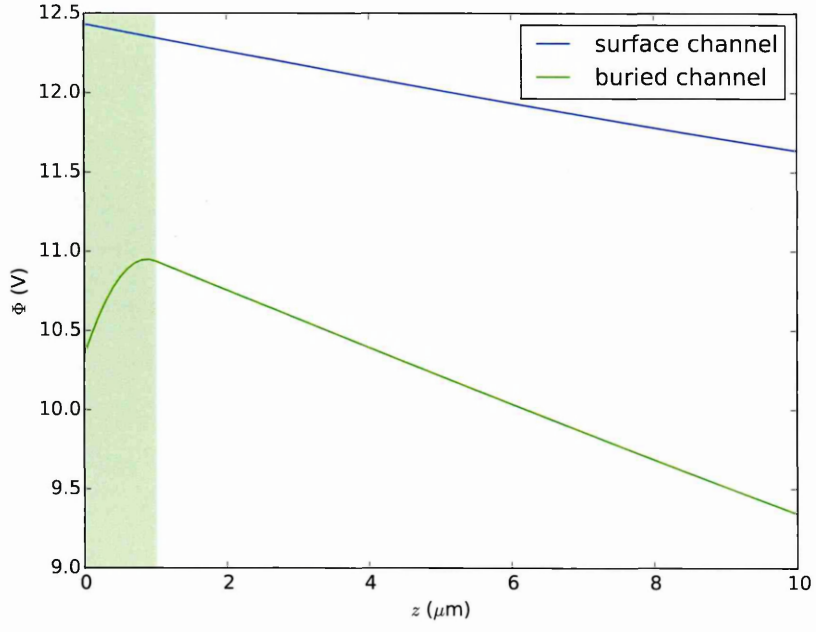

Figure 3.10: Potential vs depth for surface channel and buried channel devices, with $N_A = 1 \times 10^{12}\,\mathrm{cm}^{-3}$, $V_G = 10\,\mathrm{V}$, $N_D = 1 \times 10^{15}\,\mathrm{cm}^{-3}$, $z_J = 1\,\mu\mathrm{m}$. The buried channel region is shaded in green.

This is usually achieved by clocking several full frames out of the whole device - the electrons are ultimately drained through the output node, leaving the buried channel depleted.

Buried channel construction significantly decreases CTI [54], but the full-well capacity of the device is reduced compared to a surface channel CCD. The comparison in the potential shapes for the two device types (calculated using (3.7) for the surface channel case and (3.13) for the buried channel case) are illustrated in Figure 3.10.

3.3 Back Side Illumination

In a conventional CCD, incident light must pass through the poly-silicon gates and insulation layers before reaching the active silicon. Such a construction is called "front illuminated". This is a particular problem for the QE at short wavelengths, because the absorption length in the gate layers is very short. This means many photons are lost before reaching a photo-sensitive area. A solution which has been adopted in both CCDs and APS detectors [102] is to flip the wafer after manufacturing, so that the light arrives at the back surface of the device, and hence almost immediately at active silicon (see Figure 3.11). Back-Side Illumination (BSI) is a highly effective technique for the improvement of blue QE. However, the delicate extra processing steps needed during manufacture make it difficult to successfully carry out [55],

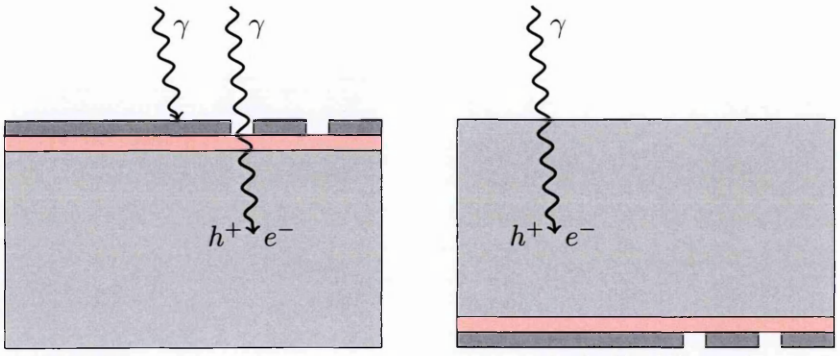

Figure 3.11: Front illumination (left) compared with back illumination (right)

and there is always some trade-off between the improvement of QE and the degradation of the Modulation Transfer Function (MTF) (see Section §3.7).

A formula for the approximate QE of a device can be derived starting from the absorption probability of a photon (2.80). For a front illuminated device, QE is reduced by photons being absorbed in the poly-silicon or insulating layers, and also by reflections from the surface. The resulting formula is [49]:

$$QE_{FI} = (1 - R(\lambda))\, e^{-\alpha(\lambda) d_{\text{poly}}} \left(1 - e^{-\alpha(\lambda) z_T}\right) \tag{3.18}$$

where d_{poly} is the thickness of the poly-silicon gates, z_T is the device's active thickness and $R(\lambda)$ is the reflectance of the surface. For a back-illuminated device, losses in the gates are eliminated:

$$QE_{BI} = (1 - R(\lambda)) \left(1 - e^{-\alpha(\lambda) z_T}\right). \tag{3.19}$$

The reflectance of silicon is plotted in Figure 3.12. It is calculated from the refractive index by [32]:

$$R = \frac{(n-1)^2 - k^2}{(n-1)^2 + k^2} \tag{3.20}$$

where the detector is assumed to be in a vacuum (unity refractive index), and n and k are the real and imaginary parts of the refractive index, respectively. The values for $R(\lambda)$ are calculated from published tabulated data [37]. Assuming that the reflectance for poly-silicon is identical to that for silicon, theoretical QE results for both front and back illuminated devices are presented in Figure 3.13.[3] As can be seen, the performance at short wavelengths for a front illuminated device is dominated by the gate thickness, whilst for a back illuminated

[3] a native oxide layer will form on the bare silicon surface of a back-illuminated device during processing, reducing the QE slightly from that shown in Figure 3.13, which does not include any oxide layer in the back-illuminated calculation.

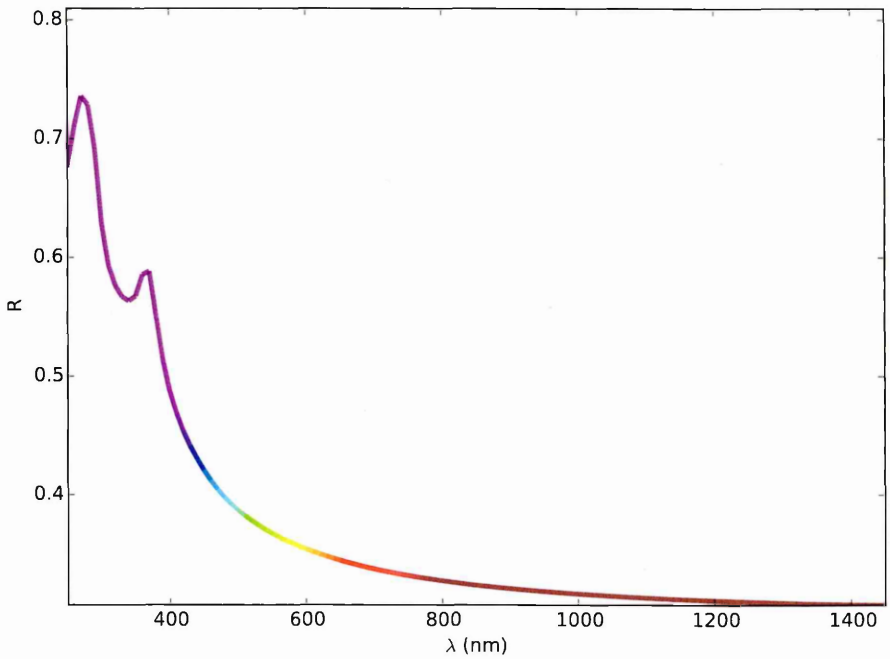

Figure 3.12: Reflectance of silicon vs wavelength (using published data [37])

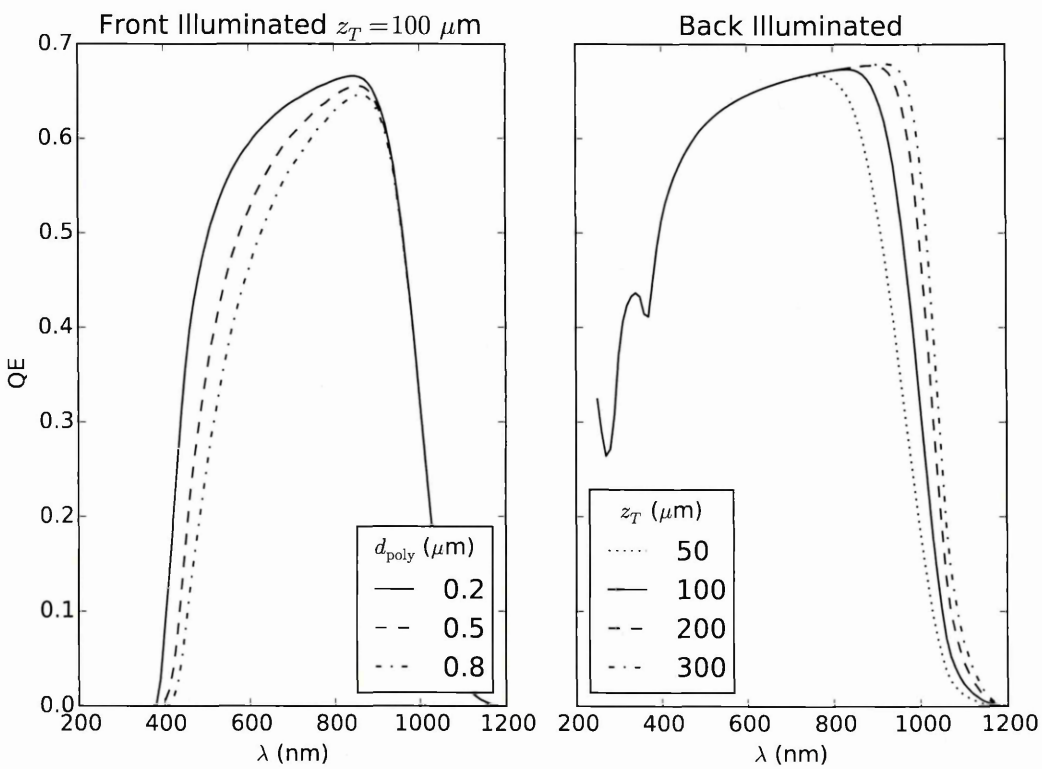

Figure 3.13: Theoretical Quantum Efficiency curves for front and back illuminated devices, varying gate thickness and active thickness

device it is most affected by the peaks in silicon reflectance. Typically, specialised coatings (known as a Anti-Reflection (AR) coatings) are applied to devices in an attempt to mitigate the effects of these peaks for devices where Ultra-Violet (UV) QE is of particular importance [43].

As seen from Section §2.5, the absorption depth $\alpha(\lambda)$ is temperature dependent, which in turn means that QE varies with operating temperature. In fact, α increases significantly as temperature decreases, especially for longer wavelengths (especially near Infra-Red (IR)). Low operating temperatures are desirable to reduce dark current (see Section §3.5) but come at the expense of some QE reduction. It is noted by Janesick [54] that the QE can change by a factor of $\sim$3.5 over an operating temperature difference of 100 °C.

3.4 Deep Depletion

To achieve high QE at the red end of the spectrum, a sensor should be fabricated as thick as possible (see Figure 3.13), due to the high absorption length for low energy photons (see Section §2.5). However, in a thick, back-illuminated device, charge which is generated near the back surface must drift a long way before collection. During this time, it is subject to thermal diffusion (see Section §2.3). The thicker the device, the more opportunity for lateral diffusion and hence degradation of the spatial resolution and the PSF. This can be mitigated by reducing the drift time, i.e. by applying an increased electric field. A backside contact is typically added to thick devices so that a negative voltage (for n-channel) can be applied, increasing the total applied bias, and also allowing full depletion of the device to be achieved.

As described in Section §3.2.2, the depletion depth of a CCD is proportional to the square root of the gate voltage, and inversely proportional to the square root of the substrate doping. From Section §2.4, this implies that higher resistivity silicon will increase depletion depth. There are practical limits on the resistivity of silicon available [54], and very high resistivity silicon may have a value around $\rho \approx 1 \times 10^4\,\Omega\,\mathrm{cm}$. Such devices have been fabricated successfully using n-type bulk silicon substrates [30].

It is impractical to achieve full depletion of a thick device by simply making the gate operating voltages more positive (or equivalently making the substrate potential more negative) - application of a very large reverse bias to the pn junctions contained in the output circuitry of the device will result in them exceeding the avalanche breakdown threshold [97], leading to unwanted and possibly damaging current flows. The approach adopted by thick e2v CCDs

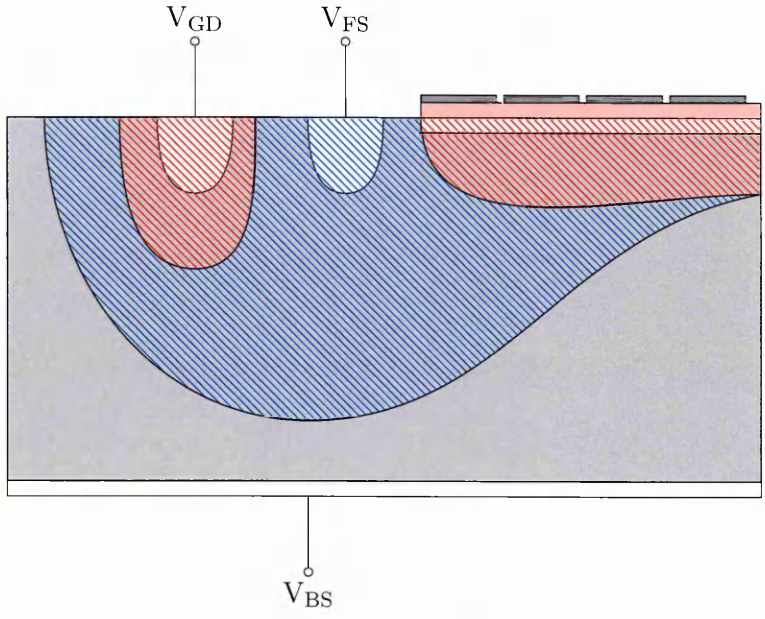

Figure 3.14: Guard diode structure illustration. The hatched areas indicate depletion regions formed when V_{GD} is insufficiently positive (red) allowing leakage currents to flow from the back substrate contact to the front. When V_{GD} is sufficiently positive (blue), the depletion region prevents leakage current from flowing between the front and back substrates

(referred to as "high-rho technology") is to operate the back substrate contact at a negative voltage, and the front substrate contact at the normal ground reference level [58]. In this way, all the components relying on the front substrate reference operate as normal, but the back substrate provides a large bias voltage to increase the drift field. Using this scheme, there still remains the problem that leakage current will flow from the back substrate contact to the front. The leakage currents are eliminated by adding an extra guard diode contact at the edge of the device. Biasing this contact to a sufficiently positive value V_{GD} causes the formation of a depletion region which extends over the front substrate contacts (see Figure 3.14) and merges with the depletion regions created by the gate biases, preventing leakage current from flowing. This protective voltage must be applied before taking V_{BS} negative, so the power on sequence of the device is important. The e2v CCD261 (used for experiments in Chapter 5) and the e2v CCD250 (analysed in Chapter 6) both use this approach.

3.5 Dark Signal

Dark signal refers to any process which causes signal carriers to be generated and collected by a sensor, even in the complete absence of optical stimulus. In a CCD there are two major contributors to dark signal - the Si/SiO_2 surface and the depleted volume. Dark current may also be generated in undepleted detector volume and by the back surface in a BSI device, but

these contributions are generally much smaller [54].

The conceptually simplest mechanism for dark signal generation is the direct band-to-band generation of electrons and holes. In silicon, due to the large scale of the band gap with respect to phonon energies, this process is extremely rare [6]. The overwhelming majority of dark signal is generated by the Shockley-Read-Hall mechanism - a defect level whose energy E_t resides within the band gap facilitates the emission of electron-hole pairs. Under some simplifying assumptions, the generation/recombination rate G_{SRH} is given by [97]:

$$G_{\text{SRH}} = \frac{\sigma_t v_{\text{th}} \left(np - n_i^2\right) N_t}{n + p + 2n_i \cosh\left(\frac{E_t - E_i}{k_B T}\right)} \tag{3.21}$$

where v_{th} is the thermal velocity of electrons, σ_t is the cross section of the process, N_t is the volume density of the trapping centre, n_i is the intrinsic carrier density and E_i is the (intrinsic) Fermi level (see Section §2.3). To find the dominant trapping centres responsible for dark signal, consider the derivative $\frac{\partial G_{\text{SRH}}}{\partial E_t}$:

$$\frac{\partial G_{\text{SRH}}}{\partial E_t} \propto \frac{\sinh\left(\frac{E_t - E_i}{k_B T}\right)}{\left(n + p + 2n_i \cosh\left(\frac{E_t - E_i}{k_B T}\right)\right)^2} \tag{3.22}$$

it can be seen that the maximum generation rate is produced by traps whose energy is near E_i, which is near the centre of the band gap. These are so-called "deep level" traps. In a depletion region (in either n-type or p-type material), we may assume that $n = p = 0$ (the majority carriers are depleted, and minority carriers are swept away by the electric field). Therefore, (3.21) reduces to:

$$G_{\text{SRH}} = \frac{-\sigma_t v_{\text{th}} n_i N_t}{2 \cosh\left(\frac{E_t - E_i}{k_B T}\right)}. \tag{3.23}$$

By assuming a uniform distribution of trapping energies[4], (3.23) can be integrated between the valence band edge E_V and the conduction band edge E_C (see [55, sec 7.1.1.4]). Assuming a fully depleted device of thickness z_T, the resulting dark current density J_{dark} is:

$$J_{\text{dark}} = \frac{1}{2} q n_i z_t \sigma v_{\text{th}} \pi k_B T N_t. \tag{3.24}$$

The analysis for surface dark current proceeds in exactly the same way, though substituting

[4]there is no suggestion that this is a particularly realistic assumption - in reality a few trap species with specific activation energies likely dominate. The action of integrating equation (3.23) to obtain an estimate of the total dark signal is acknowledged to be a rather coarse procedure.

the density of surface trapping states N_s for N_t. In high quality silicon, typically $N_s > N_t$, so that the surface dark current is the largest component. From (2.35) and (2.37), it is found that the temperature relationship of n_i goes as:

$$n_i(T) \propto T^{\frac{3}{2}} \exp\left(\frac{-E_G}{2k_BT}\right) \tag{3.25}$$

and since $v_{\text{th}} \propto \sqrt{T}$, the overall temperature dependence of J_{dark} may be written:

$$J_{\text{dark}} = K_{\text{dark}} T^3 \exp\left(\frac{-E_G(T)}{2k_BT}\right) \tag{3.26}$$

where K_{dark} is a constant collecting those in (3.24). The band gap energy E_G itself also varies with temperature, according to the Varshni relationship [99]:

$$E_G(T) = E_{G0} - \frac{A_0 T^2}{T + A_1} \tag{3.27}$$

where $E_{G0} = 1.166\,\text{eV}$, $A_0 = 4.73 \times 10^{-4}\,\text{eV K}^{-1}$ and $A_1 = 636\,\text{K}$ are empirical constants. The relationship (3.26) differs from that reported by Widenhorn et al. [107] only in that the assumed temperature dependence of v_{th} (and therefore also the diffusivity) is made explicit here. However, in agreement with the literature, (3.26) does lead to a Melder-Neldel relationship [6]. At low temperatures, the behaviour of dark current is chiefly determined by the exponential behaviour of (3.26).

Operation at low temperatures to reduce dark current is desirable both in order to increase the available well capacity for use by photo-generated charge (particularly important for long integration times), and (more importantly) to reduce the overall noise in the image; dark signal, being composed of electrons, is subject to shot noise (see Section §3.6.3).

3.6 Noise Sources

3.6.1 Reset Noise

The output circuit of a CCD consists of a charge to voltage conversion stage followed by an on-chip pre-amplifier. The charge conversion stage is formed by a "floating diffusion" called the sense node, into which the signal charge is transferred (illustrated in Figure 3.15). This process results in the decrease of the voltage on the sense node with respect to the substrate, by an amount determined by the capacitance associated with the sense node, C_N. Measuring

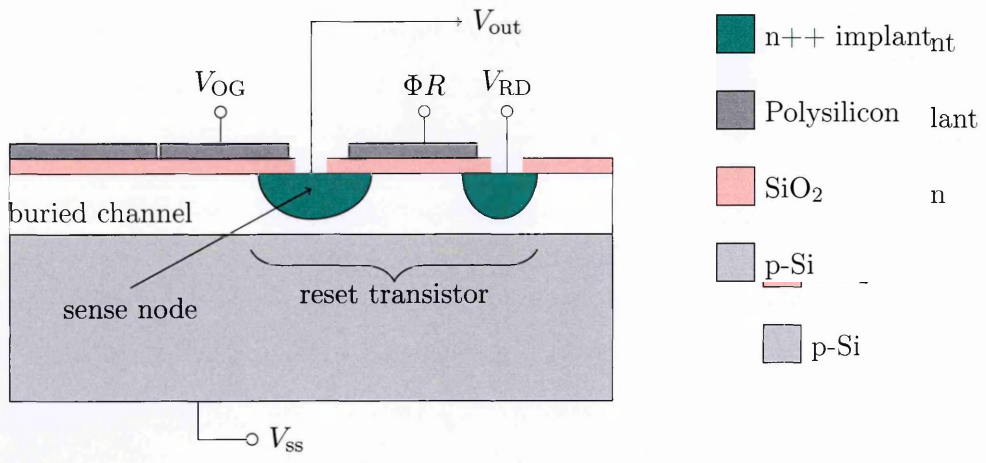

Figure 3.15: Buried Channel CCD output and reset circuitry

the voltage at the sense node gives a value proportional to the number of signal electrons, provided that the capacitance of the sense node does not change with charge. Since the sense node is simply a pn junction, it is subject to the effects described in Section §3.2.1 - that is, the capacitance does change with voltage. However, with proper design, the doping of the sense node is set such that there is very little change over the range of the pixel full well capacity [54, §6.2.8.1].

After a measurement is taken, the sense node must be reset to be ready for the next pixel's charge to arrive. This is achieved using a MOSFET whose gate is clocked by the ΦR signal. When ΦR is high, electrons from the sense node are drained into the reset drain, which is held at voltage V_{RD}. Since the reset MOSFET channel has an associated resistance, the voltage to which the sense node is reset is subject to thermal Johnson-Nyquist noise [76] with magnitude σ_{reset}:

$$\sigma_{\mathrm{reset}} = 2\sqrt{k_B T B R} \tag{3.28}$$

where R is the channel resistance and B is the signal bandwidth. In the case of the reset transistor, the bandwidth B is set by the RC circuit formed by the channel resistance and the sense node, whose transfer function $|H_{RC}|^2$ is [52]:

$$|H_{RC}(\omega)|^2 = \frac{1}{1 + (\omega RC)^2} \tag{3.29}$$

where $\omega = 2\pi f$ is the angular frequency. The noise bandwidth of the circuit is found by integration of (3.29):

$$B = \int_0^\infty |H_{RC}(2\pi f)|^2 \, df = \frac{1}{4RC}. \tag{3.30}$$

In turn, this means that (3.28) can be written as:

$$\sigma_{\text{reset}} = \sqrt{\frac{k_B T}{C_N}}. \tag{3.31}$$

Using the identity $Q = CV$, the reset noise can be written in units of signal electrons:

$$\sigma_{\text{reset}}\left[e^-\right] = \frac{\sqrt{k_B T C_N}}{q_e}. \tag{3.32}$$

For a typical value of $C_N = 100\,\text{fF}$ in a scientific CCD, the reset noise at $T = 150\,\text{K}$ may be as large as $\approx 50\,\text{e}^-$ rms. Note that the size of the reset noise is independent of the value of the channel resistance of the reset MOSFET. All amplification transistors downstream of the reset also add Johnson noise to the signal, but their bandwidth is set by external components. The value of C_N is critical to both sensitivity and linearity of the sensor output, so given a desired value of those parameters, the reset noise is an inevitable consequence. Without any form of correction, this would constitute by far the largest noise source in a CCD sensor. However, reset noise can be entirely cancelled by measuring the value of the sense node before transferring signal electrons and then again afterwards. The difference between these two levels is the signal voltage with the reset noise removed. The filter used to achieve this cancellation is called a Correlated Double Sampling (CDS) circuit. There are many possible practical designs (discussed in detail by Hopkinson and Lumb [51]), but all share the basic property of this subtraction. The process is shown conceptually in Figure 3.16. Practically, the reset and clocking feed-through transients must be allowed to settle for a reasonable time before the reset and pixel levels are sampled. In the simplest case, the output voltage of the CDS circuit is given by:

$$V_{\text{out}}(t) = V_{\text{in}}(t) - V_{\text{in}}(t - \tau_{\text{cds}}) \tag{3.33}$$

where τ_{cds} is the time between the reset and signal samples. To derive the transfer function of the basic CDS circuit, we take the Fourier Transform of (3.33):

$$\hat{V}_{\text{out}}(\omega) = \hat{V}_{\text{in}}(\omega) - \int_{-\infty}^{\infty} V_{\text{in}}(t - \tau_{\text{cds}})\, e^{-\hat{i}\omega t} dt \tag{3.34}$$

where $\hat{V}(\omega)$ is the time domain Fourier Transform of $V(t)$. Making the substitution $t' =$

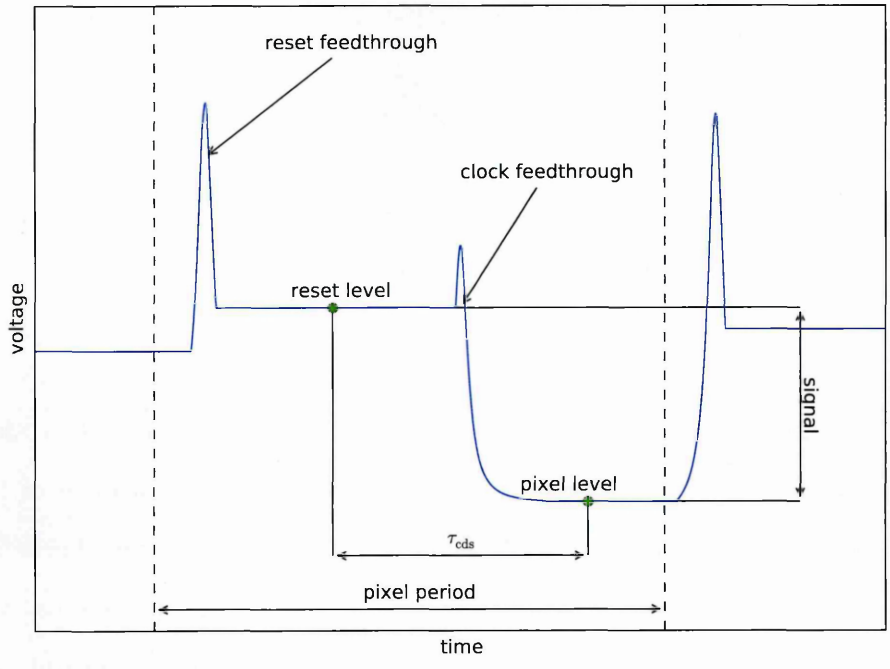

Figure 3.16: CCD output signal diagram

$t - \tau_{\text{cds}}$:

$$\hat{V}_{\text{out}}(\omega) = \hat{V}_{\text{in}}(\omega) - \int_{-\infty}^{\infty} V_{\text{in}}(t')\, e^{-\hat{i}\omega(t'+\tau_{\text{cds}})} dt' \tag{3.35}$$

$$\Rightarrow \hat{V}_{\text{out}}(\omega) = \hat{V}_{\text{in}}(\omega)\left(1 - e^{-\hat{i}\omega\tau_{\text{cds}}}\right) \tag{3.36}$$

from which the transfer function $|H_{\text{CDS}}|^2$ can be derived:

$$|H_{\text{CDS}}(\omega)|^2 = \frac{\left|\hat{V}_{\text{out}}(\omega)\right|^2}{\hat{V}_{\text{in}}(\omega)} \tag{3.37}$$

$$\Rightarrow |H_{\text{CDS}}(\omega)|^2 = \left(1 - e^{-\hat{i}\omega\tau_{\text{cds}}}\right)\left(1 - e^{\hat{i}\omega\tau_{\text{cds}}}\right) \tag{3.38}$$

$$\Rightarrow |H_{\text{CDS}}(\omega)|^2 = 4\sin^2\left(\frac{\omega\tau_{\text{cds}}}{2}\right). \tag{3.39}$$

This function is plotted in Figure 3.17. The CDS circuit also has the advantage of attenuating low frequency noise.

3.6.2 Read Noise

Read noise is a term that generally refers to all remaining on-chip noise sources after reset noise has been eliminated. This noise arises from thermal effects, carrier trapping and fluctuation in semiconductor parameters within the output amplifier components. As discussed in (3.6.1), all

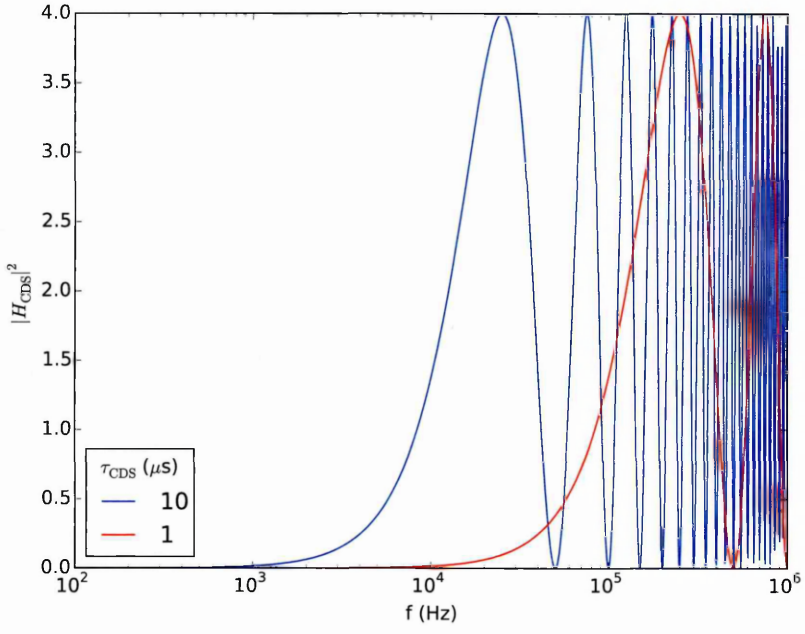

Figure 3.17: CDS transfer function

resistive electronic components operating at finite temperature are subject to thermal noise, which, being a random uncorrelated process results in a power spectrum with constant density. Such a spectral density is referred to as "white". Johnson noise is very closely modelled as having a Gaussian probability distribution [52]. The other major noise component is known as "flicker" noise, or $\frac{1}{f}$ noise, which has a power spectrum of the form:

$$S(f) = \frac{1}{f^{\gamma}}. \tag{3.40}$$

When $\gamma = 1$, the noise is specifically referred to as "pink" noise, having an equal total power when integrated over any frequency decade. This type of noise is observed almost universally across many physical systems, and though no conclusive reason why this should be the case has been established, a compelling case is made by Kendal and Jorgensen [61] that the Tweedie Convergence Theorem (a related effect to the Central Limit Theorem) provides a reason for many classes of physical processes to exhibit $\frac{1}{f}$ noise spectra. In the case of MOSFETs channels, such as those used for image sensor output amplifiers, a specific physical mechanism of flicker noise is known: trapping of charge carriers at the interface of the channel exhibits a correlated Random Telegraph Signal (RTS) noise, having a Lorentzian power spectral density [103]. Summation of many trapping states with different energy levels results in a $\frac{1}{f}$ noise spectrum.

Taken together, the white and flicker noise components give the total noise spectrum for the CCD output:

$$|S(f)|^2 = N^2_{\text{white}}\left(1 + \frac{f_c}{f}\right) \tag{3.41}$$

where we have assumed a perfect pink noise spectrum for the flicker noise ($\gamma = 1$). The frequency f_c is called the corner frequency and characterises the operating frequency at which the low frequency $\frac{1}{f}$ noise begins to dominate over the white noise. The corner frequency may be affected by the operating biases of the output amplifier circuitry [49], but in general it sets the limit for the minimum noise achievable in a CCD [54].

3.6.3 Shot Noise

Shot noise is the variation that arises from any system governed by a Poisson probability distribution, which ultimately is true for any process that results from the movement of quantised values. Since both electric current and luminous flux fall into this category (arising from electrons and photons, respectively), any system measuring these phenomena must experience shot noise, except in the case where the emission of the discrete packets is statistically correlated, as in non-classical forms of light emission [33]. Shot noise represents the lowest achievable noise limit for any imaging system, and is used to calibrate an imaging device in physical units (see Chapter 5).

3.7 Resolution

Resolution in an optical system is a quantity which in general does not have a firm technical definition. The important question in determining performance is to describe how the measured spatial distribution of incident radiation is related to the true spatial distribution. The analysis differs substantially between optical systems dealing with coherent and incoherent light sources [13] - for spatially or temporally coherent light sources, interferometric effects related to wave amplitude summation are possible, whilst for incoherent sources, only intensity may be summed. Imaging systems principally deal with incoherent illumination sources, which is the only case we consider in this work. Continuous, linear optical systems (such as lenses or mirrors) are described using a quantity called the Point Spread Function (PSF), and its Fourier Transform, the Optical Transfer Function (OTF). Consider an optical component illuminated by a perfect point source (represented by a Dirac δ function) - if the component is

linear, its action on an incident light field to produce an image $I(x, y)$ can always be described by a convolution:

$$I(x, y) = (h * \delta)(x, y) \tag{3.42}$$

where $h(x, y)$ is called the PSF, and describes what is known in signal processing as the impulse response of the system. Since it is impossible to generate perfect point source illumination, the PSF is usually inferred from measurements of its Fourier Transform pair [108], which is named the OTF. Since the PSF is a real quantity, the OTF is in general complex. Its magnitude (called the MTF) describes the amplitude response to spatial frequencies in the incident image, and its argument (the Phase Transfer Function (PTF)) represents image distortions. The MTF is often used to describe spatial resolution - in particular because separate contributing components may be multiplied rather than convolved (c.f. the convolution theorem).

For a pixellated detector there are complications to the theory describing spatial resolution in a continuous optical system. In the first place, the detector is obviously not perfectly shift-invariant: illumination that has high spatial frequency components compared to the pixel pitch will produce very different detector outputs depending on its position with respect to the array. This is partly accounted for by introducing a "sampling" component into the MTF. In the ideal case, the detector can perfectly average over the irradiance in each pixel, so that the contribution for a pixel size α is:

$$\mathrm{MTF}_{\mathrm{sampling}}(s) = \mathrm{sinc}(\alpha s) \tag{3.43}$$

corresponding to the convolution of the PSF with a top-hat. In the case of detectors with fill-factor of less than 1, the situation is further complicated by the fact that integration does not occur over the whole pixel area [49]. Aliasing is also possible for spatial frequencies above the Nyquist limit of the system. For these reasons, when measuring PSF directly it is best to ensure illumination at the centre of a pixel, such that asymmetries caused by the non shift-invariance are cancelled. For accurate measurements of PSF and MTF in a pixellated detector, for comparison with the classical optics definitions, the method of measurement must involve some average over many images at different positions - the results of such measurements are known as the "pseudo-MTF" [28].

In the context of spatial resolution, a CCD may also not be considered to be perfectly

linear - each pixel is subject to a random amount of additive noise. The effect is that even for spatial frequencies below Nyquist, distortions may be added for low signal levels. The level of read noise ultimately sets the limit at which modulations may be resolved rather than the spatial extent of the pixels. This limit is known as the Noise Equivalent Modulation (NEM) [10]. Since the noise level is not actually related to the spatial distribution of the light field, it is affected mostly by the gain of the various system electronic components - in practice, measurements must simply be taken at high enough signal levels that the Noise Equivalent Modulation (NEM) limit is not approached.

Apart from the constraints imposed by electrical noise and the finite pixel size, the main factor affecting the spatial resolution of a detector is the level of lateral diffusion experienced by photo-generated carriers in the time between their conversion and collection. The detailed modelling of these effects in thick, fully depleted CCDs is the subject of Chapter 4.

Taking the case of a front-illuminated CCD, a theoretical analysis was initially performed by Crowell and Labuda [19] for silicon diode array vidicon tubes, and refined for the CCD by Seib [89]. Starting from a sinusoidal illumination, the generation rate of carriers in the active silicon is:

$$G(x,z) = \frac{I_0}{2}(1 - R(\lambda))\,\alpha(\lambda)\,e^{-\alpha(\lambda)d_{\text{poly}}}e^{1-\alpha(\lambda)z}(1 + \cos(kx)) \tag{3.44}$$

which can be seen to be closely related to the expression for QE_{FI} in (3.18), and where I_0 is the incident intensity, and k is the spatial frequency. The resulting MTF for a front illuminated device of infinite thickness is found to be [89]:

$$\text{MTF}_{\text{FI}}(\text{k}) = \frac{1 - \frac{\exp(-\alpha z_D)}{1+\alpha\tilde{z}}}{1 - \frac{\exp(-\alpha z_D)}{1+\alpha\tilde{z}_0}} \tag{3.45}$$

where $\tilde{z}_0$ is the diffusion length of electrons, and:

$$\frac{1}{\tilde{z}^2} = \frac{1}{\tilde{z}_0^2} + k^2. \tag{3.46}$$

Note that for a thick, fully depleted device the value of $\exp(-\alpha z_D) \approx 0$ so that the diffusion MTF is predicted to be near unity. The expressions for a back illuminated device are much more complicated, and involve contributions for interference effects at long wavelengths [89]. However, for either very thick devices, or those with no appreciable field-free regions, the expressions all reduce to near unity. This is due to the authors assuming that any carrier arriving in a depleted region is collected without further diffusion - indeed, compared to the

lateral diffusion in a field-free region, the spreading during collection in a depletion region is very small. However, neglecting this spread in a device which is fully depleted is inadequate for modelling - the expressions provided by the literature cannot be used in this case. The simplest possible assumptions for the spreading in a depleted region are considered in Chapter 4 before moving on to develop more detailed models.

Chapter 4

Models for Dynamic Charge Collection Effects

> I have tried to improve telescopes and practised continually to see with them. These instruments have play'd me so many tricks that I have at last found them out in many of their humours.
>
> William Herschel

In this chapter, simplified approaches for modelling dynamic charge collection effects at the device level are developed. The approach is "simplified" in the sense that the aim is to avoid using full-blown transient finite element simulations to obtain pixel signal values. Dynamic charge collection effects imply a feedback cycle between the electric field structure within the device and the collected charge distribution: photo-generated electrons are collected under the pixel gates; the field caused by this stored charge distribution then affects the collection of further charge and so on. It is certainly possible in principle to calculate all the collection properties of the device using finite element methods, but the computational time required for these calculations is high. Moreover, as a matter of utility in astrometric image correction, the user is interested only in observed signals in pixels. Opportunities abound to produce models which can beat finite element methods for speed and efficiency but which are nonetheless still useful.

Some of the material in this chapter has been published before in two papers, by Weatherill et. al [104, 105].

Before moving on to specifics, it is helpful to emphasize some general points about the approach. In the first place, for the purposes of astronomical imaging at least, we may

completely ignore interaction between electrons as they are collected. From simple semiconductor physics reasoning, it is clear that for distant electrons, field interactions are completely screened by the Thomas-Fermi mechanism. Consider a typical deep depletion CCD having $10\,\mu$m pixels, operated at cryogenic temperature $T = 150$K, with net doping density of e.g. $N = 1 \times 10^{13}\mathrm{cm}^{-3}$ in the bulk. The Debye length L_D in such a device is given by [6]:

$$L_D = \sqrt{\frac{\varepsilon_{\mathrm{si}}\varepsilon_0 k_B T}{q_e^2 N}} \approx 0.91\,\mu\mathrm{m} \tag{4.1}$$

which is much smaller than a single lateral pixel spacing, but large enough that one might think local electron interaction may be important in the fine detail of a single pixel. However, being generous in saying that a scientific CCD may have a full well of $\sim 2 \times 10^5\,\mathrm{e}^-$, and imagining a situation where a bright point source saturates this pixel in an exposure of 15 s (which might be roughly the case for some LSST science frames [3]), the pixel experiences an electron arriving every $\sim 7.5 \times 10^{-5}$ s. A back-biased CCD with thickness $z_T = 100\,\mu$m might operate with an effective collecting voltage of $V_{\mathrm{coll}} = 70\,\mathrm{V}$, the collection time t_{coll} will then approximately be:

$$t_{\mathrm{coll}} = \frac{z_T^2}{\mu V_{\mathrm{coll}}} \approx 1.4\,\mathrm{ns} \tag{4.2}$$

where the value of $\mu = 1000\,\mathrm{cm}^2\mathrm{V}^{-1}\mathrm{s}^{-1}$ which includes temperature dependence and field dependence has been used (see Section §2.4 for details). Thus, on average, electron collection is effectively instantaneous, a fact which allows a complete de-coupling between field calculations and electron trajectory computation. Working out the associated diffusion length r_{diff} associated with this collection time is:

$$r_{\mathrm{diff}} = \sqrt{2Dt_{\mathrm{coll}}} = \sqrt{\frac{2\mu k_B T}{q_e} \cdot t_{\mathrm{coll}}} \approx 2.8\,\mu\mathrm{m} \tag{4.3}$$

so that an ideal point source will still produce a Gaussian cloud with 3σ radius of $\sim 8\,\mu$m, assuming no confinement from lateral fields. Unless the point source is positioned close to the geometric centre of the pixel, the hypothetical saturating point source will still likely result in a measurable amount of signal charge being collected in surrounding pixels. The theoretical minimum PSF is a useful quantity to consider, and compare measured values to, which we

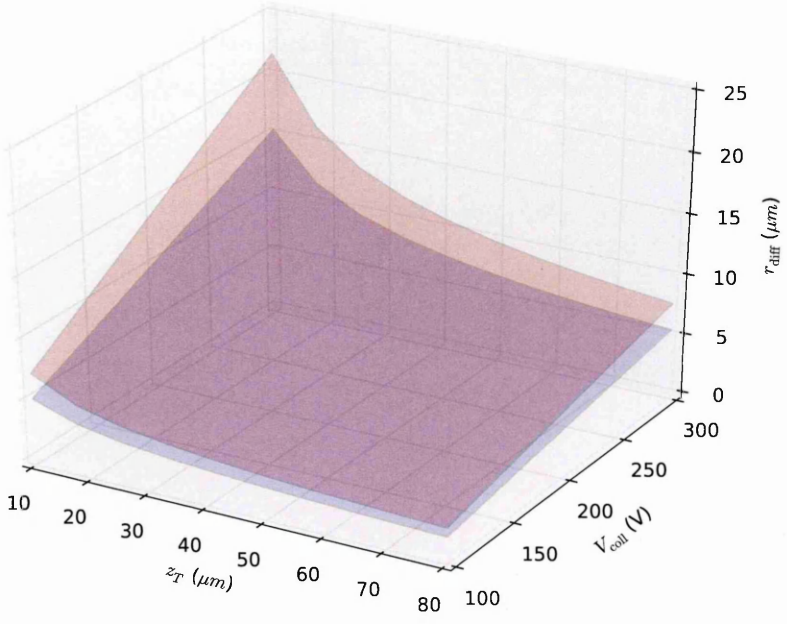

Figure 4.1: Theoretical minimum PSF size for varying collection voltage V_{coll} and thickness z_T. The red plane shows the result for $T = 300\,\text{K}$, the blue plane for $T = 150\,\text{K}$

will define as the quantity x_{diff} from equation (4.3). Combining (4.2) and (4.3), we find:

$$r_{\text{diff}} = z_T \sqrt{\frac{2k_B T}{q_e V_{\text{coll}}}} \tag{4.4}$$

which is illustrated as a function of temperature, device thickness and collecting voltage in Figure 4.1. Before refining calculations of PSF, we must first turn to a method of finding the potential structure of a pixel.

4.1 Calculating Potential

The potential in a CCD is obtained by solving Poisson's equation (see Section §2.1), which in the full non-linear form solved by finite element simulations is given by (2.60) and (2.61). It will be shown in this section that a solution in analytic form can be constructed for the linear version of Poisson's equation, and that this solution is a good approximation to the non-linear solution in the case of a fully depleted device. Incomplete depletion will also be considered, but the accuracy of the solution there is much more limited. Though this is somewhat frustrating from an intellectual point of view, all scientific CCDs in use will be operating in full depletion. The geometry of the device used for the rest of this section is shown in Figure 4.2, and the meanings of all geometric quantities and constants are given in Table 4.1. The stored charge

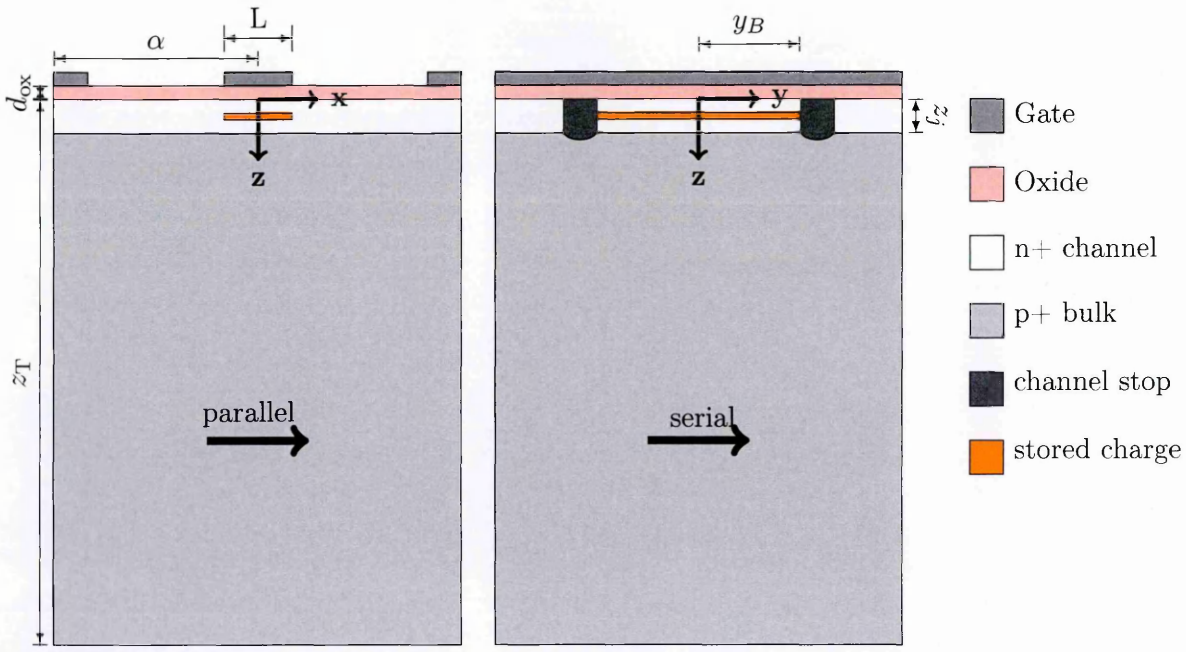

Figure 4.2: 3D geometry of an idealised CCD pixel. The coordinate origin is at the centre of a pixel, the x and y directions being aligned with parallel transfer and serial transfer respectively. The z dimension origin starts at the $\mathrm{Si} - \mathrm{SiO_2}$ boundary and increases with depth.

is assumed to be cuboid in shape (as opposed to a more realistic "used soap bar"), and the same holds for the buried channel and channel stop implants. The channel stop implants are additionally assumed to have the same depth as the buried channel[1]. All implants and the stored charge are assumed to have constant density. All junctions are assumed to be perfectly abrupt (also known as the depletion-layer approximation).

We start by asserting that the linearity and uniqueness properties of Poisson's equation (see Section §2.1) allow us to write the total device potential as a sum of contributing potential components:

$$\Phi(x,y,z) = \Phi_H(x,z) + \Phi_B(x,z) + \Phi_P(x,z) + \Phi_C(x,y,z) + \Phi_S(y,z) \tag{4.5}$$

where the components have the following meanings:

- $\Phi_H(x,z)$ - "Homogeneous Gate Potential", the potential due to the applied voltage at the collecting gates (including the gates which are held low). This component is obtained by solving Poisson's equation for the case of a device with zero doping but obeying proper boundary conditions.

[1] In fact we will mostly consider the channel stop to be a lack of buried channel, rather than an additional implant

Symbol	Name	Simulation Value	Description
α	pixel pitch	$15\,\mu$m	Distance between centres of adjacent pixels
y_B	channel stop position	$7\,\mu$m	distance from centre of pixel to channel stop inner surface
d_{ox}	oxide thickness	200 nm	Thickness of gate oxide including SiO_2 and Si_3N_4 (equal thickness, each 100 nm)
L	gate width	$3\,\mu$m	width of collecting gate
z_j	junction depth	$0.6\,\mu$m	distance from oxide interface to edge of buried channel implant
z_T	device thickness	$100\,\mu$m	distance from oxide interface to device back surface
N_D	donor density	$1 \times 10^{14}\text{cm}^{-3}$	volume density of donors in the buried channel n-layer
N_A	acceptor density	$1 \times 10^{12}\text{cm}^{-3}$	volume density of acceptors in the bulk
ε_{si}	silicon relative permittivity	11.7	
ε_{ox}	SiO_2 relative permittivity	3.4	
ε_{Ni}	Si_3N_4 relative permittivity	7.0	

Table 4.1: Description of quantities used in modelling

- $\Phi_B(x,z)$ - "Back Side Bias Potential", which is due to the backside substrate contact.
- $\Phi_P(x,z)$- "Particular Potential", the potential due to the doping concentration, obtained by solving Poisson's equation for zero boundary conditions but including depth charge distribution.
- $\Phi_C(x,y,z)$- "Charge Potential", the potential due to the stored charge packet. We find this using a Green's function method.
- $\Phi_S(y,z)$ - "Channel Stop Potential", the potential due to the channel stop implants, again found using a Green's function.

In the next sections, derivations of suitable functions for calculating each component will be presented. Unless otherwise mentioned, values for all the geometric quantities used in calculations and simulations are taken from Table 4.1. Equations indicating important results are boxed.

4.1.1 Homogeneous Potential Components

At first glance, Φ_H seems to be the most challenging part to write down. Note that to find Φ_H, the problem to be solved is:

$$\nabla^2 \Phi_H (x, z) = 0 \tag{4.6}$$

subject to the boundary conditions:

$$\Phi_H (x, z = -d_{\text{ox}}) = \begin{cases} V_G & |x| > \frac{L}{2} \\ V_T & |x| < \frac{L}{2} \end{cases} \tag{4.7}$$

where V_G is the collecting gate high voltage, and V_T is the collecting gate low voltage. The case where two gates are used during integration is handled simply by increasing L by the requisite amount and always defining the centre of the pixel as the centre of the collecting gate. Any effects due to incomplete gate overlap would therefore be ignored by this solution.

Computing the potential distribution in a CCD has been of interest since the invention of the device. The earliest attempt to construct an analytic 2D solution to the problem found by the author was presented by Carnes et al. in 1972 [16]. Their purpose was to model the efficiency and speed of charge transfer, for which aim a semi-infinite depletion layer was assumed. This condition is not compatible with investigations (such as the present) where the back side of the device is of interest. More general approaches were taken by McKenna and Schryer [70] and full inclusion of finite device thickness was performed in the solution by Hanneman and Esser [44], though as later pointed out by De Meyer and Declerck [21], the solution proposed did not satisfy the boundary condition that the potential at the depletion depth be equal to that of the substrate. De Meyer and Declerck's solution satisfies all the required boundary conditions, but was still written as an infinite sum of trigonometric functions, due to the method of images approach used. Several years after De Meyer and Declerk, in 1984 Lester and Pulfrey [66] presented an elegant solution which agreed with De Meyer and Declerck, but was written in a fully closed form way. We reproduce the necessary steps to obtain the solution here, in a manner slightly less terse than limited publication space afforded the original authors.

Consider a co-ordinate transformation from the system (x, z) to (x', z') where:

$$x' = x,\ z' = z + d_{\text{ox}} \tag{4.8}$$

which changes the boundary conditions 4.7 to:

$$\Phi'_H\left(x', z' = 0\right) = \begin{cases} V_G & |x'| > \frac{L}{2} \\ V_T & |x'| > \frac{L}{2} \end{cases}. \tag{4.9}$$

Next, define complex numbers u and w, given by:

$$u = x' + \hat{i}z' \tag{4.10}$$

$$w = \ln\left(\frac{u - \frac{L}{2}}{u + \frac{L}{2}}\right) \tag{4.11}$$

where $\hat{i}$ is the imaginary unit. w can also be written in terms of its real and imaginary parts, given by :

$$w = x'' + \hat{i}z''. \tag{4.12}$$

The transformation $(x, z) \rightarrow (x'', z'')$ constitutes a conformal map, which transforms all points where $\Phi_H = V_G$ to the plane $y'' = 0$, and all points $\Phi_H = V_T$ to the plane $y'' = \pi$. The transformation is visualised in Figure 4.3. Having performed this transformation, the solution to the problem in (x'', z'') is analogous to that of a simple parallel plate capacitor (see Figure 4.4) . The solution is then given by:

$$\Phi_H\left(x'', z''\right) = V_T + \frac{(V_G - V_T)}{\pi} \cdot z''. \tag{4.13}$$

The solution in the original space can be obtained by applying the inverse conformal map to the solution in the transformed space. Using the definition of the natural logarithm of a complex number $a + \hat{i}b$:

$$\ln\left(a + \hat{i}b\right) \equiv \ln\left(\sqrt{a^2 + b^2}\right) + \hat{i} \cdot \tan^{-1}\left(\frac{b}{a}\right) \tag{4.14}$$

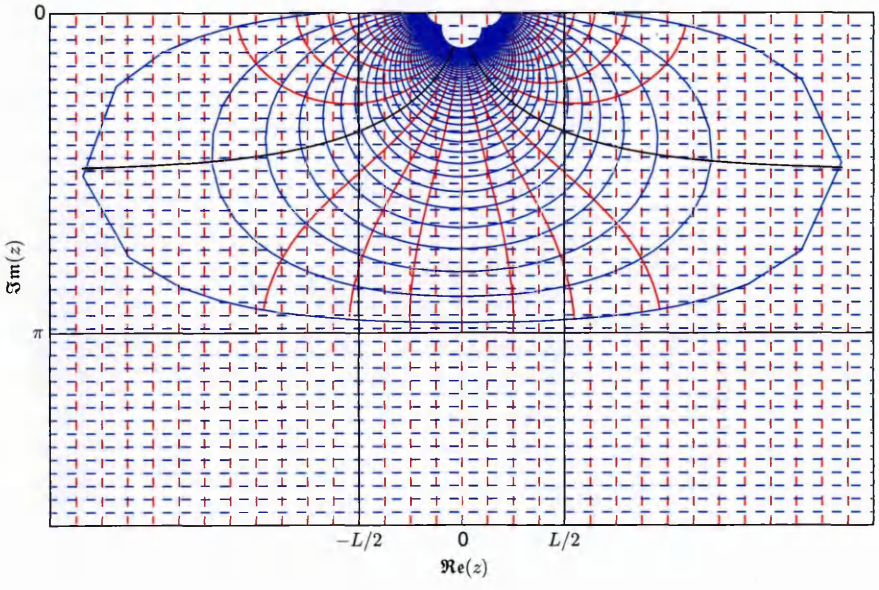

Figure 4.3: Argand diagram visualization of grid lines in the co-ordinate spaces defined by u (dashed lines), and w (solid lines). The curved black lines show the grid lines at $u = \frac{L}{2}$ and $u = -\frac{L}{2}$ in the transformed co-ordinate space

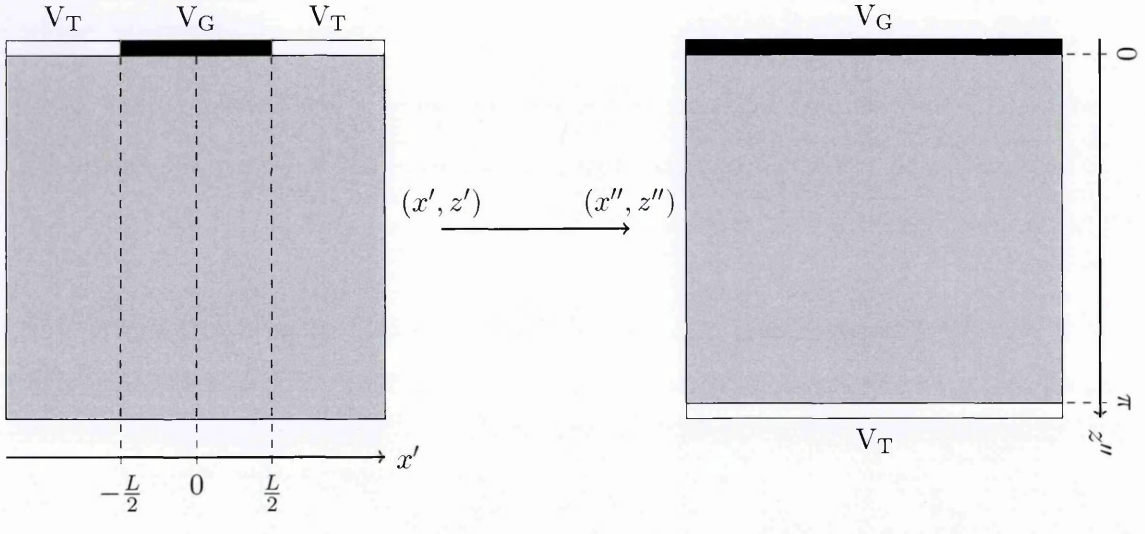

Figure 4.4: Illustration of Φ_H problem domain and boundary conditions before (left) and after (right) conformal mapping

it follows from equation (4.11) and equation (4.12) that:

$$z'' = \Im\mathfrak{m}\left(\ln\left(\frac{x' - \frac{L}{2} + \hat{i}z'}{x' + \frac{L}{2} + \hat{i}z'}\right)\right) \tag{4.15}$$

$$\Rightarrow z'' = \Im\mathfrak{m}\left(\ln\left(x' - \frac{L}{2} + \hat{i}z'\right) - \ln\left(x' + \frac{L}{2} + \hat{i}z\right)\right) \tag{4.16}$$

$$\Rightarrow z'' = \tan^{-1}\left(\frac{z'}{x' - \frac{L}{2}}\right) - \tan^{-1}\left(\frac{z'}{x' + \frac{L}{2}}\right) \tag{4.17}$$

$$\therefore z'' = \tan^{-1}\left(\frac{z + d_{\text{ox}}}{x - \frac{L}{2}}\right) - \tan^{-1}\left(\frac{z + d_{\text{ox}}}{x + \frac{L}{2}}\right) \tag{4.18}$$

and, substituting equation (4.18) into equation (4.13) it is found that:

$$\boxed{\Phi_H(x,z) = V_T + \frac{(V_G - V_T)}{\pi} \cdot \left(\tan^{-1}\left(\frac{z + d_{\text{ox}}}{x - \frac{L}{2}}\right) - \tan^{-1}\left(\frac{z + d_{\text{ox}}}{x + \frac{L}{2}}\right)\right)}. \tag{4.19}$$

The electric field associated with this potential can then be found by differentiation:

$$\mathbf{E}_H(x,z) = \begin{pmatrix} E_{H,x} \\ E_{H,z} \end{pmatrix} = -\begin{pmatrix} \frac{\partial}{\partial x}\Phi_H \\ \frac{\partial}{\partial z}\Phi_H \end{pmatrix} \tag{4.20}$$

$$E_{H,x}(x,z) = \frac{(V_G - V_T)}{\pi} \cdot \left(\frac{d_{\text{ox}} + z}{\left(x + \frac{L}{2}\right)^2 + (d_{\text{ox}} + z)^2} - \frac{d_{\text{ox}} + z}{\left(x - \frac{L}{2}\right)^2 + (d_{\text{ox}} + z)^2}\right) \tag{4.21}$$

$$E_{\text{H},z}(x,z) = \frac{(V_G - V_T)}{\pi} \cdot \left(\frac{x - \frac{L}{2}}{\left(x - \frac{L}{2}\right)^2 + (d_{\text{ox}} + z)^2} - \frac{x + \frac{L}{2}}{\left(x + \frac{L}{2}\right)^2 + (d_{\text{ox}} + z)^2}\right). \tag{4.22}$$

A plot of Φ_H for the centre of a single pixel is shown in Figure 4.5. Note that all the surface plots of potential distributions in this section are plotted with the ϕ axis reversed, so that electrons would "roll downhill".

At this point, a detour from the solution of Lester and Pulfrey is needed in order to incorporate the extra boundary conditions arising from the back substrate contact, held at V_{BS}. Note in particular from Figure 4.5 that the value of Φ_H at large values of z does not decay to 0 V. This is a problem both for the extension to multiple pixels and matching the back side boundary conditions. A correcting potential is therefore necessary: this correction was included by Lester and Pulfrey in their particular integral component, but since we must also constrain the solution to include back side biasing it makes sense to correct Φ_H at this stage as well.

Assuming the device thickness to be constant, the problem to solve for the back bias

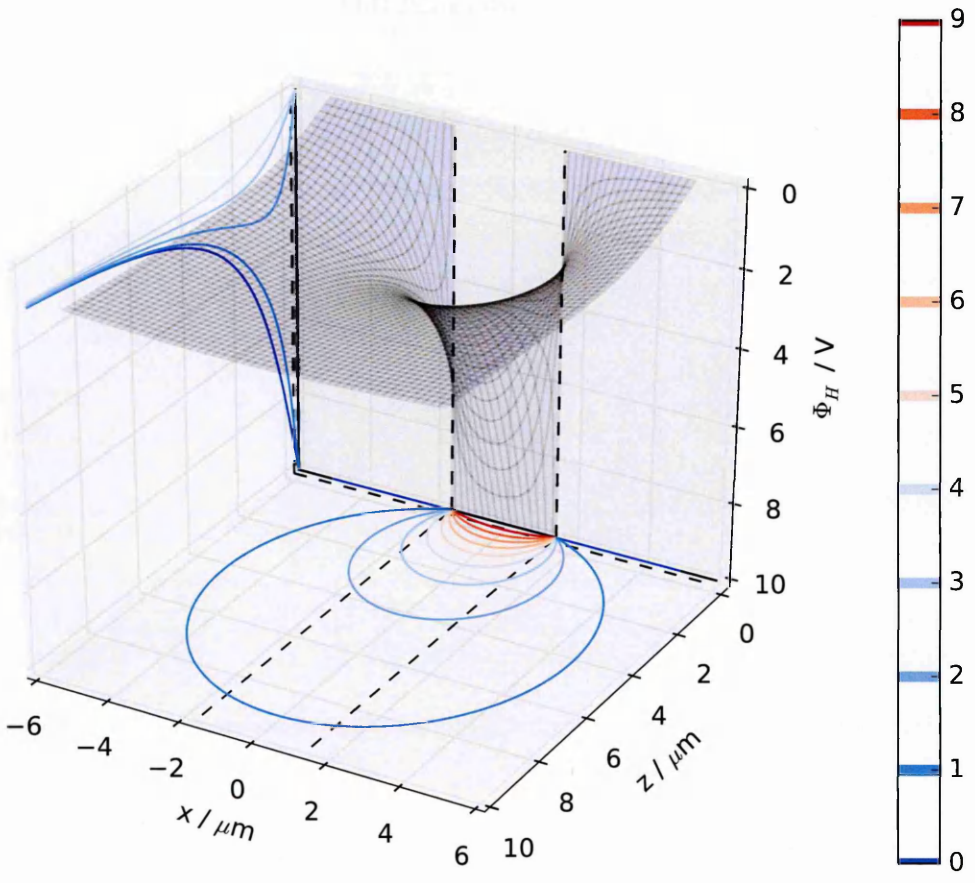

Figure 4.5: Visualisation of Φ_H with $V_G = 10\,\mathrm{V}$, $V_T = 0\,\mathrm{V}$. Dashed lines show the location of the gate edges and oxide interface

potential Φ_B is simply:

$$\frac{\partial}{\partial z}\left(\varepsilon(z)\frac{\partial}{\partial z}\Phi_B\right) = 0 \tag{4.23}$$

subject to boundary conditions:

$$\Phi_B(x, z = z_T) = V_{\mathrm{BS}} - \Phi_H(x, z) \tag{4.24}$$

$$\Phi_B(x, z = -d_{\mathrm{ox}}) = 0 \tag{4.25}$$

where the second term in the right hand side of (4.24) is added explicitly to cancel the residual Φ_H potential. Apart from this term, the rest of the problem is entirely one-dimensional. To deal with the change in permittivity from the oxide layer to the silicon[2], the solution is split into two parts $\Phi_{B,\mathrm{ox}}$ and ,$\Phi_{B,\mathrm{si}}$, which are matched at the interface. The equations and

[2]Since the actual sensor construction consists of both oxide and nitride layers below the gate electrodes, a further change in ε from the nitride to the oxide should really be included. The exact relative thicknesses of the insulation layers (nitride and oxide) are not known, but we assume equal thicknesses of 100 nm each (see Table 4.1), and model the structure as a single layer having effective permittivity of $\varepsilon = \frac{\varepsilon_{\mathrm{Ni}}+\varepsilon_{\mathrm{ox}}}{\varepsilon_{\mathrm{Ni}}\varepsilon_{\mathrm{ox}}}$

boundary conditions arising are:

$$\frac{\partial^2 \Phi_{B,\mathrm{si}}}{\partial z^2} = 0 \qquad \frac{\partial^2 \Phi_{B,\mathrm{ox}}}{\partial z} = 0 \tag{4.26}$$

$$\Phi_{B,\mathrm{si}}(x, z=0) = \Phi_{B,\mathrm{ox}}(x, z=0) \tag{4.27}$$

$$\varepsilon_{\mathrm{si}} \left.\frac{\partial \Phi_{B,\mathrm{si}}}{\partial z}\right|_{z=0} = \varepsilon_{\mathrm{ox}} \left.\frac{\partial \Phi_{B,\mathrm{ox}}}{\partial z}\right|_{z=0} \tag{4.28}$$

$$\Phi_{B,\mathrm{si}}(x, z=z_T) = V_{\mathrm{BS}} - \Phi_H(x, z_T) \tag{4.29}$$

$$\Phi_{B,\mathrm{oxR}}(x, z=-d_{\mathrm{ox}}) = 0. \tag{4.30}$$

The solution to the 1D Laplace equation (4.26) is straightforward:

$$\Phi_{B,\mathrm{si}} = A \cdot z + B + f(x) \cdot z + g(x) \tag{4.31}$$

$$\Phi_{B,\mathrm{ox}} = C \cdot z + D + h(x) \cdot z + k(x) \tag{4.32}$$

where A, B, C, D are constants to be found, and $f(x), g(x), h(x), k(x)$ arise from integrating a partial derivative. Boundary conditions (4.27) and equation (4.28) immediately give

$$B + g(x) = D + k(x) \tag{4.33}$$

$$\varepsilon_{\mathrm{si}} \cdot (A + f(x)) = \varepsilon_{\mathrm{ox}} \cdot (C + h(x)) \tag{4.34}$$

and realizing that these equations must be true $\forall x$ leads to:

$$g(x) = k(x); \qquad B = D \tag{4.35}$$

$$\varepsilon_{\mathrm{si}} f(x) = \varepsilon_{\mathrm{ox}} h(x); \qquad \varepsilon_{\mathrm{si}} A = \varepsilon_{\mathrm{ox}} C. \tag{4.36}$$

Including (4.30) then implies that:

$$B = \frac{\varepsilon_{\mathrm{si}}}{\varepsilon_{\mathrm{ox}}} d_{\mathrm{ox}} A \tag{4.37}$$

$$g(x) = \frac{\varepsilon_{\mathrm{si}}}{\varepsilon_{\mathrm{ox}}} d_{\mathrm{ox}} f(x). \tag{4.38}$$

Finally, (4.29) gives:

$$A = \frac{V_{\mathrm{BS}}}{z_T + \frac{\varepsilon_{\mathrm{si}}}{\varepsilon_{\mathrm{ox}}} d_{\mathrm{ox}}} \tag{4.39}$$

$$f(x) = \frac{-\Phi_H(x, z_T)}{z_T + \frac{\varepsilon_{\mathrm{si}}}{\varepsilon_{\mathrm{ox}}} d_{\mathrm{ox}}} \tag{4.40}$$

leading to the full solution of Φ_B as:

$$\boxed{\Phi_B(x,z) = \left(\frac{V_{\mathrm{BS}} - \Phi_H(x, z_T)}{z_T + \frac{\varepsilon_{\mathrm{si}}}{\varepsilon_{\mathrm{ox}}} d_{\mathrm{ox}}} \right) \cdot \begin{cases} \frac{\varepsilon_{\mathrm{si}}}{\varepsilon_{\mathrm{ox}}} (z + d_{\mathrm{ox}}) & z < 0 \\ \left(z + \frac{\varepsilon_{\mathrm{si}}}{\varepsilon_{\mathrm{ox}}} d_{\mathrm{ox}} \right) & z > 0 \end{cases}} \tag{4.41}$$

The sum $\Phi_B + \Phi_H$ is hereafter referred to as the "Homogeneous Potential", and is visualised in Figure 4.6. As can be seen, the variation in the x direction beyond a few μm depth is very small, and indeed it is tempting for computational reasons to drop the x dependence entirely from (4.41). However, when evaluating effective pixel boundaries (which is crucial to the calculation of both PSF and the Brighter-Fatter effect), the resulting small deviation from boundary condition (4.29) results in the field lines at the back surface not being perpendicular to the boundary. The fringing field (i.e. the field in the x direction) at the back surface must vanish, or the pixel boundaries, being almost entirely determined by the magnitude of this fringing field, will erroneously curve at the back surface, resulting in an exaggerated dependence on quantities such as wavelength and device thickness, which are critically affected by the back surface environment. As with Φ_H, the electric field components may again be found from differentiation :

$$E_{B,x}(x,z) = \frac{E_{H,x}(x, z_T)}{z_T + \frac{\varepsilon_{\mathrm{si}}}{\varepsilon_{\mathrm{ox}}} d_{\mathrm{ox}}} \cdot \begin{cases} \frac{\varepsilon_{\mathrm{si}}}{\varepsilon_{\mathrm{ox}}} (z + d_{\mathrm{ox}}) & z < 0 \\ \left(z + \frac{\varepsilon_{\mathrm{si}}}{\varepsilon_{\mathrm{ox}}} d_{\mathrm{ox}} \right) & z > 0 \end{cases} \tag{4.42}$$

$$E_{B,z}(x,z) = \frac{V_{\mathrm{BS}} - \Phi_H(x, z_T)}{z_T + \frac{\varepsilon_{\mathrm{si}}}{\varepsilon_{\mathrm{ox}}} d_{\mathrm{ox}}} \cdot \begin{cases} -\frac{\varepsilon_{\mathrm{si}}}{\varepsilon_{\mathrm{ox}}} & z < 0 \\ -1 & z > 0 \end{cases} . \tag{4.43}$$

4.1.2 Particular Integral Component

The particular integral Φ_P is used to model the contribution from the doping within the device. The solution presented is somewhat analogous to that of Lester and Pulfrey [66], but note that since Φ_B has already been obtained, there are slight differences. Assuming the

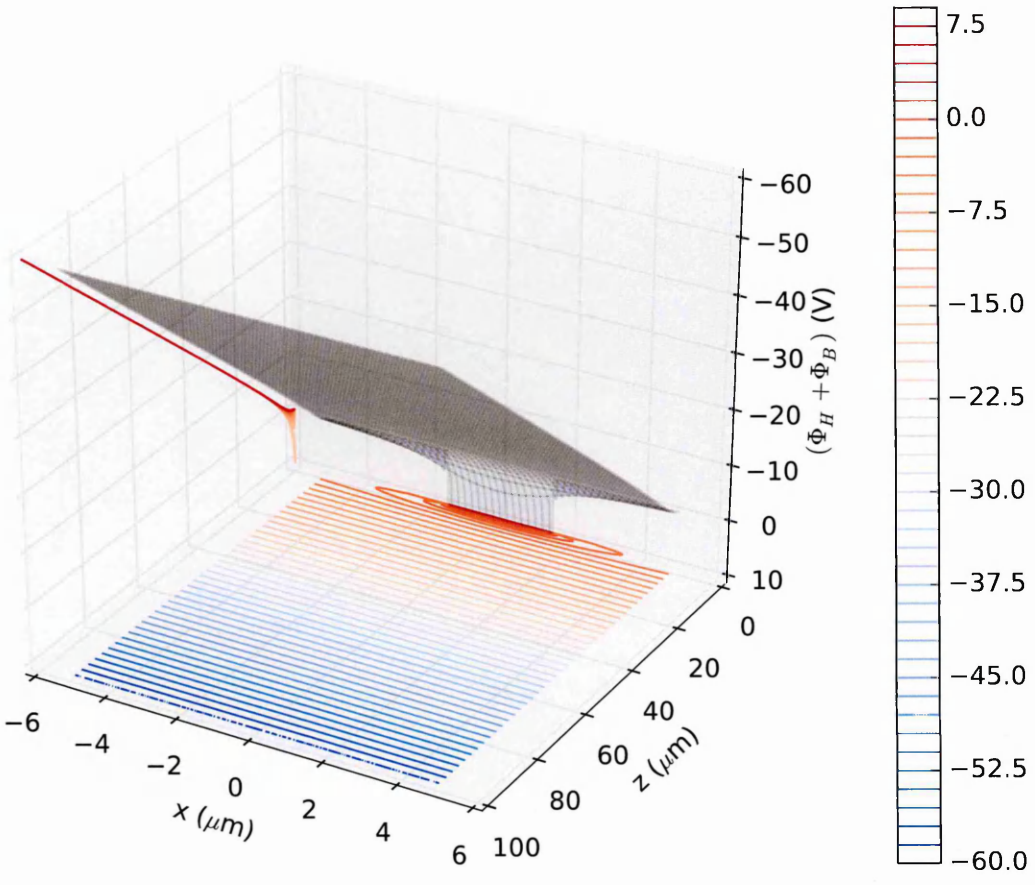

Figure 4.6: Visualisation of $\Phi_H + \Phi_B$ with $V_G = 10\text{V}$, $V_T = 0\text{V}$, $V_{\text{BS}} = -60\text{V}$

doping only depends on depth, and having dealt with the x direction variation due to the gates in Φ_H and Φ_B, the symmetry of the problem to solve for Φ_P is entirely one dimensional:

$$\frac{d^2\Phi_P(z)}{dz^2} = \frac{N(z)}{\varepsilon(z)} \tag{4.44}$$

where $N(z)$ is the net doping function given by:

$$N(z) = q_e\left(N_D(z) - N_A(z)\right) + \rho_{\text{ox}}(z) \tag{4.45}$$

where N_D is the concentration of ionised donors,N_A is the concentration of ionised acceptors and $\rho_{\text{ox}}(z)$ is the density of trapped charge in the oxide layers. Φ_P is made compatible with Φ_H and Φ_B by imposing the boundary conditions:

$$\Phi_P(z = -d_{\text{ox}}) = 0 \tag{4.46}$$

$$\Phi_P(z \geq z_d) = V_{\text{BS}} - \Phi_H(x,z) - \Phi_B(x,z) \tag{4.47}$$

where z_d is the depletion depth. x direction dependence has been re-introduced here by the need to match the boundary conditions. The problem posed by (4.44) can be solved using integration by parts:

$$\Phi_P(x,z) = z\int_{-d_{ox}}^{z}\frac{N(t')}{\varepsilon(t')}dt' - \int_{-d_{ox}}^{z}t'\frac{N(t')}{\varepsilon(t')}dt' + P(x,z)\cdot z + Q(x,z) \tag{4.48}$$

where t' is a dummy variable and P and Q are functions to find. For simplicity, we assume that there is no oxide trapped charge (i.e. $\rho_{ox} = 0$), which reduces (4.48) to :

$$\Phi_P(x,z) = \frac{1}{\varepsilon_{si}\varepsilon_0}\left(z\int_0^z N(t')\,dt' - \int_0^z t'N(t')\,dt' + P(x)\cdot z + Q(x)\right). \tag{4.49}$$

Applying boundary conditions (4.46) and (4.47), we find:

$$Q(x) = 0 \tag{4.50}$$

$$\Rightarrow P(x) = \int_0^{z_d}\left(\frac{t'N(t')}{z_d} - N(t')\right)dt' - \varepsilon_{si}\varepsilon_0\left(\frac{(\Phi_H+\Phi_B)(x,z_d) - V_{BS}}{z_d}\right). \tag{4.51}$$

As yet, we have not assumed full depletion (i.e. in general, $z_d \neq z_T$). In fact, it is perfectly possible to continue the solution without that assumption. However, without full depletion, there is nothing to "force" the boundary condition (4.47) to hold. In this case, the depletion depth z_d must be found by solving the equation:

$$P(x; z_d) = 0. \tag{4.52}$$

Clearly, though this may be possible for some choices of $N(z)$, the general case is not soluble analytically. For now we proceed with the analytically tractable solution by assuming $z_T = z_d$. Since, by construction, $\Phi_H(x,z_T) + \Phi_B(x,z_T) = V_{BS}$, the final term in (4.51) vanishes, and with it all x variation in Φ_P. The full depletion solution for Φ_P is therefore given by:

$$\boxed{\Phi_P(z) = \frac{1}{\varepsilon_{si}\varepsilon_0}\left(z\int_{z_T}^{z}N(t')\,dt' - \int_0^z t'N(t')\,dt' + \frac{z}{z_T}\int_0^{z_T}t'N(t')\,dt'\right)} \tag{4.53}$$

which in some ways is a peculiar result - it seems that since no constraints (other than integrability) have been placed on the net doping function $N(z)$, that sharp edges have not been assumed. This is only partly true - indeed it is possible to use any reasonable function for $N(z)$ and not resort to abrupt changes in doping at a pn junction, for example. However, in

obtaining the solution using the boundary condition (4.47), the depletion layer approximation was implicitly used; without assuming a sharp depletion edge, the full non-linear Poisson equation and drift-diffusion equations would have had to have been involved in the solution. So, we should consider that Φ_P may be quite inaccurate in cases of either partial depletion of the device, or for values $z \approx z_T$ even in full depletion. Note that this does not introduce the same problem for pixel boundaries as inaccuracy of Φ_H or Φ_B at $z \approx z_T$, because there is no x dependence in Φ_P, but does potentially impact on the accuracy of models depending on exact values of fields in the z direction, such as PSF calculation.

We proceed to explicitly write down Φ_P for the simplest relevant case of $N(z)$ - that of the abrupt step pn junction, which will be used as the basis for modelling all buried channel CCDs in this work - given by:

$$N(z) = \begin{cases} -q \cdot N_D & 0 \leq z \leq z_J \\ q \cdot N_A & z_J < z \leq z_T \end{cases} \tag{4.54}$$

where z_J is the junction depth. Substituting (4.54) into (4.53) it is found that:

$$\Phi_P(z) = \frac{q_e}{\varepsilon_{\text{si}}\varepsilon_0}\left(zK_P + \zeta(z)\right) \tag{4.55}$$

$$\text{with} \quad \zeta(z) = \begin{cases} \frac{N_D z^2}{2} - z\left(N_A\left(z_J - z_T\right) - N_D\left(z - z_J\right)\right) & 0 \leq z \leq z_J \\ N_A z\left(z - z_T\right) + \frac{1}{2}\left(N_A\left(z_J^2 - z^2\right) + N_D z_J^2\right) & z_J < z \leq z_T \end{cases} \tag{4.56}$$

$$\text{and} \quad K_P = \frac{1}{2z_T}\left(N_A z_T^2 - \left(N_A + N_D\right) z_J^2\right). \tag{4.57}$$

Examples of Φ_P depth profiles for different substrate doping are shown in Figure 4.7 for $z_J = 1\,\mu\text{m}$.

Having calculated all the static components of the potential distribution relevant for parallel transfer, the sum $\Phi_H + \Phi_B + \Phi_P$ may be validated against finite element simulations (this is performed in Chapter 6). The analogous situation for serial transfer must use the sum $\Phi_H + \Phi_B + \Phi_P + \Phi_S$. However, we leave the description of Φ_S until after considering the stored charge potential Φ_C, because their method of calculation is nearly identical.

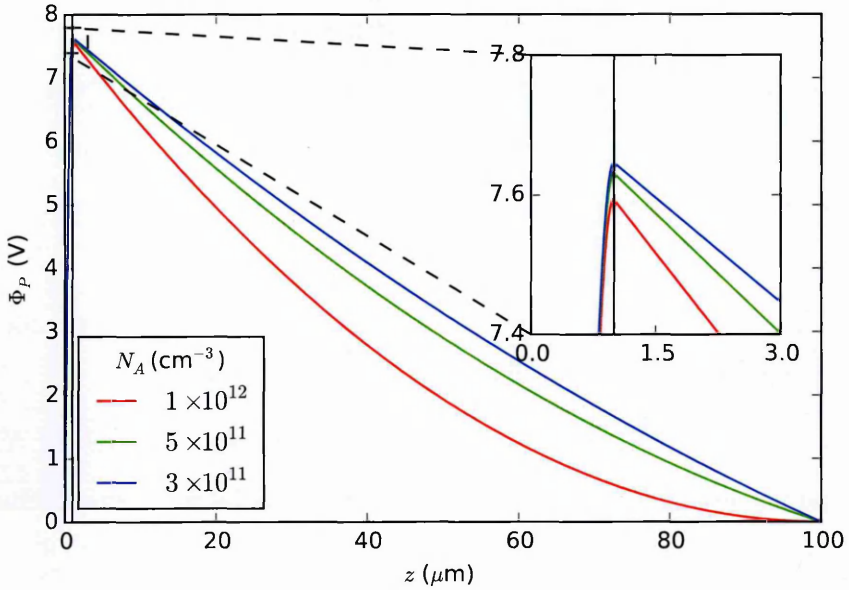

Figure 4.7: Depth plot of Φ_P for block doping model (4.55). z_J is indicated by a solid black line

4.1.3 Potential Due to Stored Charge

In this section, we will describe the solution for Φ_C, the potential component due to stored charge. All of the components considered until this point are static for a given device condition, and therefore when simulating, for example, a filling electron well, they need only be calculated once. Φ_C on the other hand changes throughout, so it is the most critical to optimize from a computational standpoint. Unfortunately, this component is also intrinsically the most expensive to compute, because it can only be written as the sum of an infinite series. The approach used is the Green's function method.

Given a linear differential operator $\mathcal{L}$, the Green's function $G(\mathbf{x}, \mathbf{x}')$ is defined by the equation:

$$\mathcal{L}\{G(\mathbf{x}, \mathbf{x}')\} = \delta(\mathbf{x} - \mathbf{x}') \tag{4.58}$$

where $\delta(\mathbf{x})$ is the Dirac delta function [83]. Given a differential equation of the form:

$$\mathcal{L}\{u(\mathbf{x})\} = v(\mathbf{x}) \tag{4.59}$$

where $u(\mathbf{x})$ and $v(\mathbf{x})$ functions, we can obtain a solution using Green's function and the

properties of the delta function as follows:

$$\iiint \mathcal{L}\left\{G\left(\mathbf{x},\mathbf{x}'\right)v\left(\mathbf{x}'\right)\right\}d^3\mathbf{x}' = \iiint \delta\left(\mathbf{x}-\mathbf{x}'\right)v\left(\mathbf{x}'\right)d^3\mathbf{x}' = v\left(\mathbf{x}\right). \tag{4.60}$$

Using (4.59) it then follows that:

$$\mathcal{L}\left\{u\left(\mathbf{x}\right)\right\} = \iiint \mathcal{L}\left\{G\left(\mathbf{x},\mathbf{x}'\right)v\left(\mathbf{x}'\right)\right\}d^3\mathbf{x}'. \tag{4.61}$$

The linearity of $\mathcal{L}$ is then used to bring it outside the integral:

$$\mathcal{L}\left\{u\left(\mathbf{x}\right)\right\} = \mathcal{L}\left\{\iiint G\left(\mathbf{x},\mathbf{x}'\right)v\left(\mathbf{x}'\right)d^3\mathbf{x}'\right\} \tag{4.62}$$

which finally leads to:

$$u\left(\mathbf{x}\right) = \iiint G\left(\mathbf{x},\mathbf{x}'\right)v\left(\mathbf{x}'\right)d^3\mathbf{x}' \tag{4.63}$$

and, if $\mathcal{L}$ is translation invariant (as is the case for the Laplacian operator ∇^2 appearing in Poisson's equation), $G\left(\mathbf{x},\mathbf{x}'\right)$ is able to be written as a convolution operator:

$$u\left(\mathbf{x}\right) = \iiint G\left(\mathbf{x}-\mathbf{x}'\right)v\left(\mathbf{x}'\right)d^3\mathbf{x}'. \tag{4.64}$$

The Green's function is general to each differential operator - once it is known, solutions to specific problems can be obtained using (4.64) and boundary condition constraints. Considering, for now, the solution in 2 dimensions, the Green's function for the 2D Laplacian operator $G_2\left(x,z;x',z'\right)$ is given by [63]:

$$G_2\left(x-x',z-z'\right) = \frac{1}{4\pi}\ln\left(\left(x-x'\right)^2+\left(z-z'\right)^2\right)+\kappa \tag{4.65}$$

where κ is a constant used to satisfy boundary conditions. For the modelling of CCDs stored charge, we simplify the charge distribution into a sharp block with finite extent from $(-x_0, z_0)$ to (x_0, z_1), and having constant charge density ρ_0, which will be adjusted according to how much charge is stored in the well. The unconstrained solution for Φ_C can then be written:

$$\frac{\varepsilon_{si}\varepsilon_0\Phi_C\left(x,z\right)}{\rho_0} = \int_{-x_0}^{x_0}\int_{z_0}^{z_1} G_2 dz'dx'. \tag{4.66}$$

The double anti-derivative of G_2, can be found analytically:

$$\begin{aligned} 4\pi \iint G_2 dz'dx' &= (z-z')(x-x')(G_2-2) + 2x'(z-z') - (z-z')^2 \tan^{-1}\left(\frac{z-z'}{x-x'}\right) \\ &\quad - (x-x')^2 \tan^{-1}\left(\frac{x-x'}{z-z'}\right) - \frac{\pi x^2}{2} + fx' + g + \kappa x'z' \qquad (4.67) \\ 4\pi \iint G_2 dx'dz' &= (z-z')(x-x')(G_2-2) + 2z'(x-x') - (z-z')^2 \tan^{-1}\left(\frac{z-z'}{x-x'}\right) \\ &\quad - (x-x')^2 \tan^{-1}\left(\frac{x-x'}{z-z'}\right) - \frac{\pi y^2}{2} + ly' + m + \kappa x'z' \qquad (4.68) \end{aligned}$$

where $f(x,y)$, $g(x,y)$, $l(x,z)$, $m(x,z)$ are functions to be found, and we have used the fact that:

$$\tan^{-1}\left(\frac{A}{B}\right) + \tan^{-1}\left(\frac{B}{A}\right) \equiv \tan^{-1}\left(\frac{\frac{A}{B}+\frac{B}{A}}{1-\frac{A}{B}\cdot\frac{B}{A}}\right) = \frac{\pi}{2}. \qquad (4.69)$$

The functions f, g, m, n can be found by demanding that Φ_C be physical, and therefore that

$$\frac{\partial^2 \Phi_C}{\partial z \partial x} = \frac{\partial^2 \Phi_C}{\partial x \partial z} \qquad (4.70)$$

and (after some algebra), this leads to the physical double anti-derivative of G_2, which we label Υ_2:

$$\boxed{4\pi\Upsilon_2(x,z) = xz(4\pi G_2(x,z) - 2) - \left(x^2 \tan^{-1}\left(\frac{x}{z}\right) + z^2 \tan^{-1}\left(\frac{z}{x}\right)\right)} \qquad (4.71)$$

. The functions G_2 and Υ_2 are visualised in Figure 4.8.

At this point, it should be acknowledged that the operator used in Poisson's equation is not ∇^2, but $\nabla \cdot (\varepsilon(\mathbf{x})\nabla)$, which in the case of non-constant ε is not identical. However, using standard vector calculus identities, we find that, for a general scalar field Ψ [83]:

$$\begin{aligned} \nabla \cdot (\varepsilon(\mathbf{x})\nabla\Psi) &\equiv \varepsilon(\mathbf{x})\nabla\cdot(\nabla\Psi) + (\nabla\Psi)\cdot(\nabla\varepsilon(\mathbf{x})) \qquad (4.72) \\ \Rightarrow \nabla \cdot (\varepsilon(\mathbf{x})\nabla\Psi) &= \varepsilon(\mathbf{x})\nabla^2\Psi + \frac{\partial\Psi}{\partial z}\cdot\frac{d\varepsilon(z)}{dz} \qquad (4.73) \end{aligned}$$

where in (4.73) we have used the fact that ε varies only in one direction. For the abrupt slab model used in this work, the second term on the right hand side of (4.73) vanishes everywhere except exactly at the semiconductor-insulator interface, $z = 0$. If we consider the solution domain to only include the silicon for the purposes of stored charge (which we also acknowledge means that from this point forward, fields and potentials calculated within

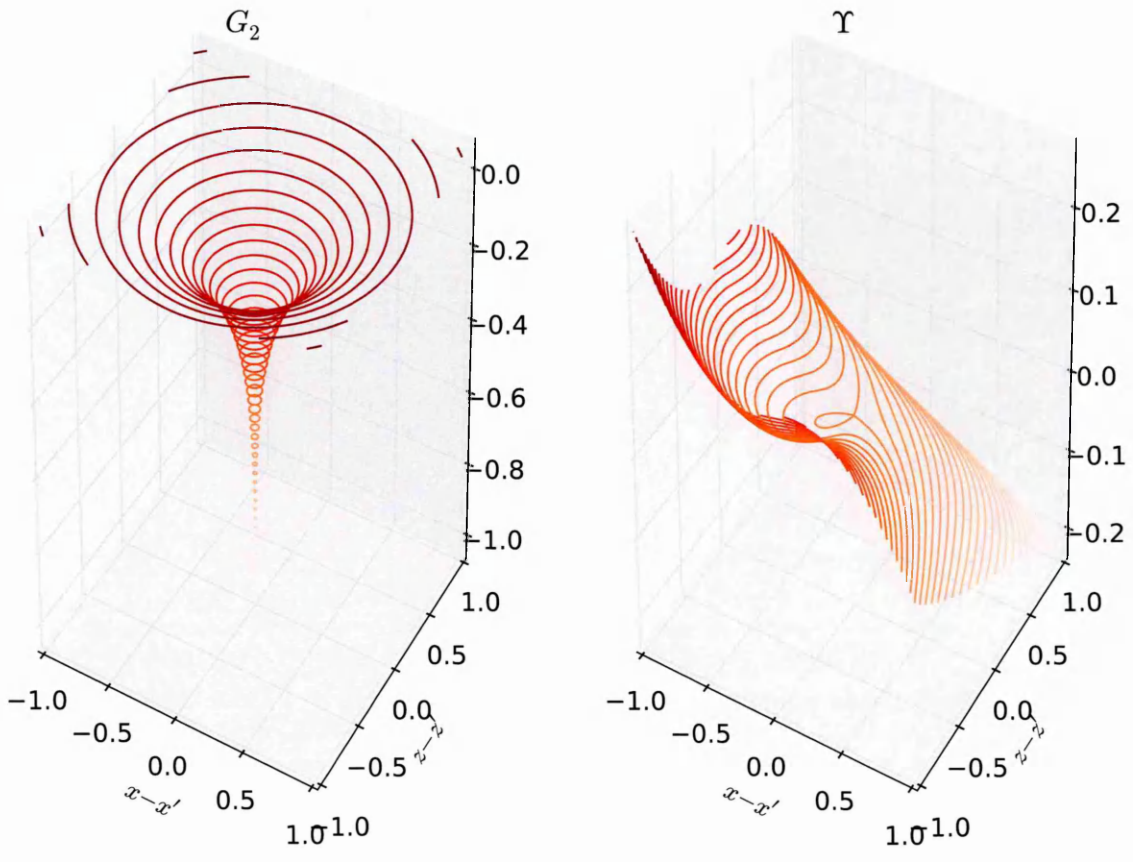

Figure 4.8: Visualising G_2 and Υ

the oxide layer may be invalidated) and assume a perfectly insulating oxide layer, then the boundary condition at the semiconductor - insulator interface is of Neumann type [53]:

$$\left.\frac{\partial \Phi_C}{\partial z}\right|_{z=0} = 0 \tag{4.74}$$

so that the problematic term vanishes completely and it becomes valid to use (4.64) in the charge storage solution. The other boundary condition that Φ_C must satisfy is the Dirichlet conditions that at the back surface $z = z_T$:

$$\Phi_C\left(z = z_T\right) = 0 \tag{4.75}$$

$$\left.\frac{\partial \Phi_C}{\partial x}\right|_{z=z_T} = 0 \tag{4.76}$$

$$\left.\frac{\partial \Phi_C}{\partial y}\right|_{z=z_T} = 0. \tag{4.77}$$

Satisfying (4.76) and (4.77) in the present context is particularly crucial, for the same reasons as described in Section §4.1.1: if these conditions do not hold, the effective pixel

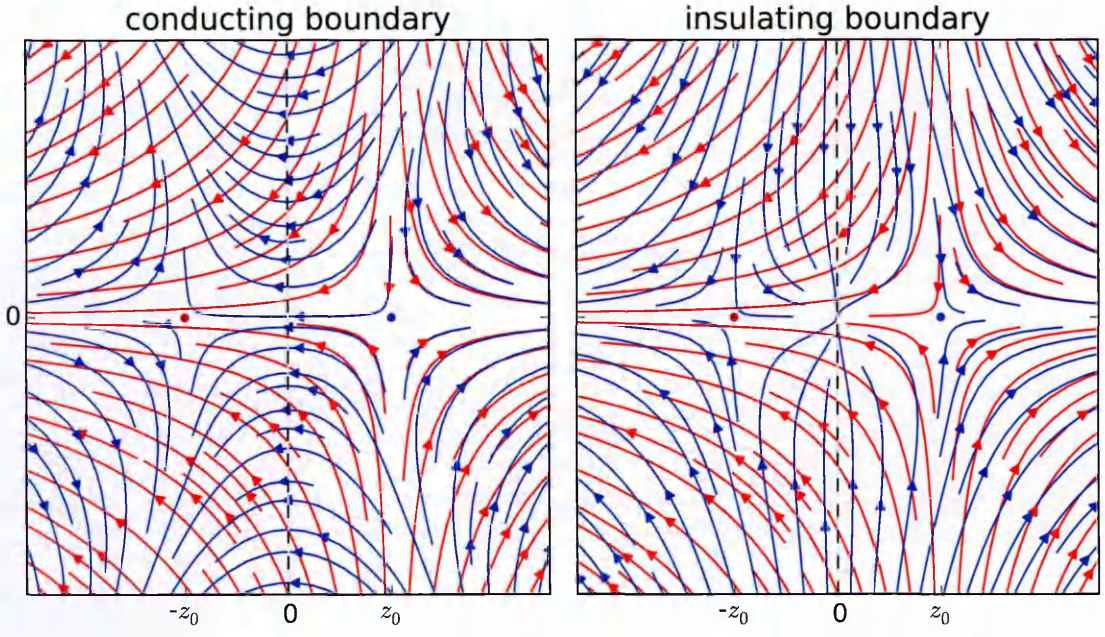

Figure 4.9: Method of Images used to satisfy boundary conditions at $z = 0$. The red lines show the electric field calculated using only the "true" charge at z_0, the blue lines include also the "image" charge at $-z_0$, for a conducting boundary (left panel) and insulating boundary (right panel).

boundary will spuriously be found to "bend" at the back surface. The condition is imposed using the familiar "method of images"; the uniqueness theorem (see Section §2.1) implies that the correct potential may be obtained by treating the plane $z = z_T$ as a mirror and creating a fictitious charge with opposite polarity to the real charge behind the mirror. This method is illustrated for a simple point charge example in Figure 4.9. The principle extends trivially to any charge distribution: for a charge density $\rho(\mathbf{x})$ at position $z = z_0$, we create a fictitious charge distribution $-\rho(\mathbf{x})$ shifted to position $z = 2z_T - z_0$. In fact, the same method can be used to satisfy the condition imposed by (4.74), except that in this case we have the mirror at position $z = 0$, and the fictitious charge distribution is identical to the original, rather than opposite. Unfortunately, using the method of images for both (4.74) and (4.76) sets up a situation akin to the "mise en abyme" effect experienced in a hall of mirrors (see - Figure 4.10); each mirror must reflect not only the original object, but also the entire image produced by the opposite mirror. Clearly the result must be written as some form of infinite series to be fully valid. A closely analogous problem is considered in [101, pp.130-131], but using two conducting planes. For a charge at z_0, image charges must be placed at every point $2n \pm z_0$ with n ranging from $-\infty$ to ∞. Diagrammatic representations of the necessary image charge positions for the problem solved by Wallace [101], and the modified version required here to

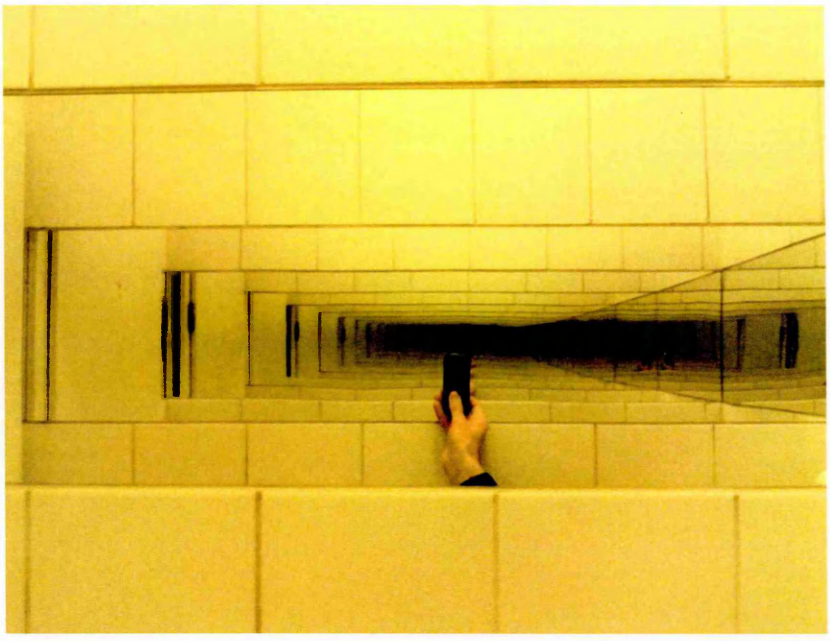

Figure 4.10: "Mise en abyme" effect experienced between two parallel mirrors. Reproduced from [1] under CC BY-SA 2.0 license

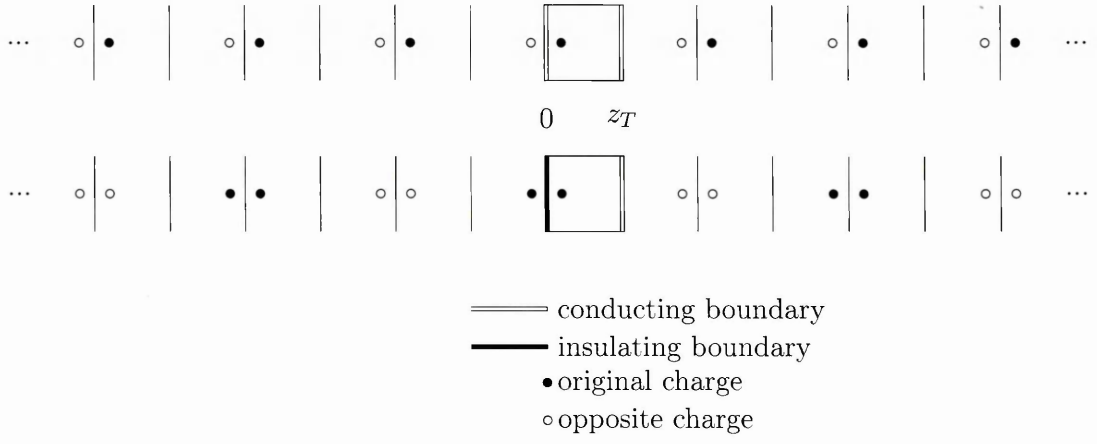

Figure 4.11: Diagrams showing arrangement of charges for the infinite method of images sum, in the case of two conducting boundaries (upper), and one conducting one insulating boundary (lower).

solve for the insulating boundary, are shown in Figure 4.11.

We now define the function $\zeta(z_a, z_b)$, which is simply the evaluation of the double integral on the right hand side of (4.66):

$$\zeta(z_a, z_b) = \left[\left[\Upsilon_2(x - x', z - z')\right]_{x'=-x_0}^{x'=x_0}\right]_{z'=z_a}^{z'=z_b}. \tag{4.78}$$

The x, z and x_0 dependencies of ζ are not included in the parameters for brevity.

Using Figure 4.11, we begin constructing the series U for solving Φ_C:

$$\begin{aligned} U &= \zeta(z_0, z_1) + \zeta(-z_1, -z_0) - \zeta(2z_T - z_1, 2z_T - z_0) \\ &\quad -\zeta(2z_T + z_0, 2z_T + z_1) - \zeta(-2z_T + z_0, -2z_T + z_1) \\ &\quad -\zeta(-2z_T - z_1, -2z_T - z_0) + \zeta(4z_T - z_1, 4z_T - z_0) \\ &\quad +\zeta(4z_T + z_0, 4z_T + z_1) - \zeta(-4z_T + z_0, -4Z_T + z_1) \\ &\quad -\zeta(-4z_T - z_1, -4z_T - z_0) + \dots . \end{aligned} \tag{4.79}$$

Noting that $\zeta(z_0, z_1) = -\zeta(z_1, z_0)$, the sequence can be written in pairs:

$$\begin{aligned} U &= \zeta(z_0, z_1) - \zeta(-z_0, -z_1) \\ &\quad +\zeta(2z_T - z_0, 2z_T - z_1) - \zeta(2z_T + z_0, 2z_T + z_1) \\ &\quad +\zeta(-2z_T - z_0, -2z_T - z_1) - \zeta(-2z_T + z_0, -2z_T + z_1) \\ &\quad +\zeta(4z_T + z_0, 4z_T + z_1) - \zeta(4z_T - z_0, 4z_T - z_1) \\ &\quad +\zeta(-4z_T + z_0, -4z_T + z_1) - \zeta(-4z_T - z_0, -4z_T - z_1) \\ &\quad +\dots \end{aligned} \tag{4.80}$$

so that the total series for Φ_C is:

$$\frac{4\pi\varepsilon_{si}\varepsilon_0}{\rho_0}\Phi_C(x, z) = \sum_{n=-\infty}^{\infty}\left((-1)^n\left(\Xi_n^+(z_0, z_1) - \Xi_n^-(z_0, z_1)\right)\right) \tag{4.81}$$

$$\text{with} \quad \Xi_n^{\pm}(z_a, z_b) = \zeta(2nz_T \pm z_a, 2nz_T \pm z_b). \tag{4.82}$$

The sequence in (4.81) has the property that if only a finite number of terms N are evaluated, the boundary conditions will not be satisfied, since the image charges at that instant do not balance each other. It is impossible in any part of the finite sum to simultaneously perfectly satisfy all boundary conditions - but the sum can be written such that it perfectly satisfies either the conducting boundary at $z = z_T$ or the insulating boundary at $z = 0$ for all values of N, depending on which surface is made the "centre" of the series. Then, the number of terms to evaluate can be chosen based on the accuracy of the other boundary condition. To prioritise the insulating boundary, the series is:

$$\frac{4\pi\varepsilon_{si}\varepsilon_0}{\rho_0}\Phi_C(x, z) = \sum_{n=0}^{\infty}(-1)^n\left(\Xi_n^+ - \Xi_{-n}^- + \Xi_{n+1}^- - \Xi_{-(n+1)}^+\right) \tag{4.83}$$

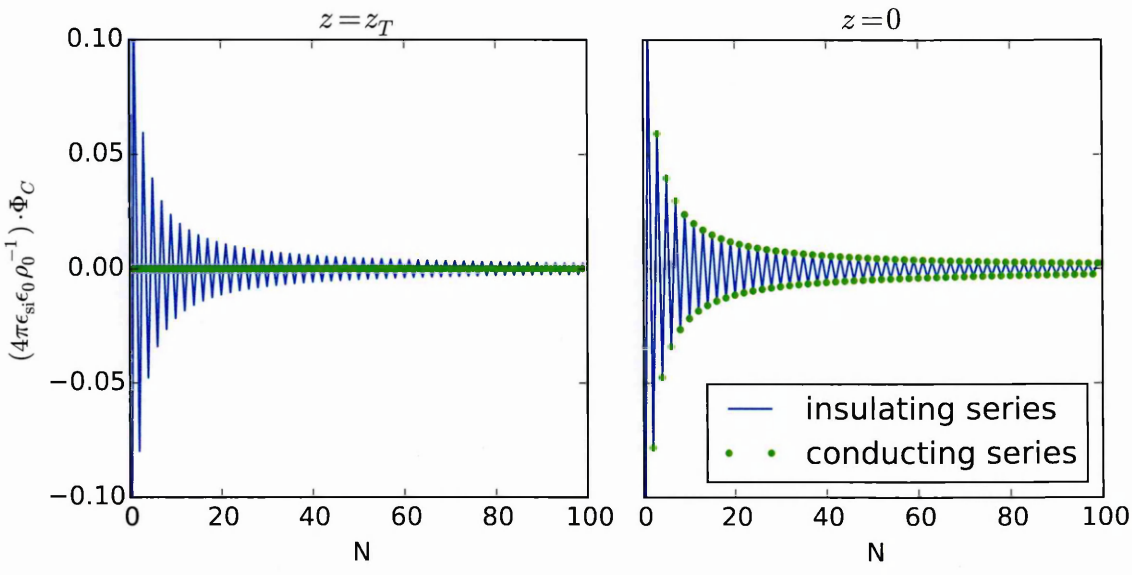

Figure 4.12: Convergence properties of series for Φ_C at the conducting boundary (left panel) and the insulating boundary (right panel). The values of parameters used were $x_0 = 1.5\,\mu$m, $z_0 = 0.5\,\mu$m, $z_1 = 1.0\,\mu$m.

whilst to keep the conducting boundary intact, the series is:

$$\frac{4\pi\varepsilon_{si}\varepsilon_0}{\rho_0}\Phi_C(x,z) = \sum_{n=0}^{\infty}(-1)^n\left(-\Xi^-_{-n} + \Xi^+_{-n} + \Xi^-_{n+1} - \Xi^+_{n+1}\right). \tag{4.84}$$

The importance of (4.75) for correctness mean that (4.84) is generally preferred to (4.83). The computed values of $\Phi_C(x=0, z=0)$ and $\Phi_C(x=0, z_T)$ for varying number of terms N are shown in Figure 4.12. This convergence behaviour is quite common in Green's function methods - each additional term over-corrects for the previous one, but by an exponentially-damped amount. Computationally, we find that using around $N = 10$ terms and a Levin acceleration [67] (further described in Section §4.6) gives adequate accuracy of potentials (relative error within 1×10^{-6}).

The electric field $\mathbf{E}_c$ can be found by differentiating Φ_C - which results in an identical series to equation (4.84), but with Υ_2 replaced by its appropriate partial derivatives:

$$4\pi\frac{\partial\Upsilon_2(x,z)}{\partial x} = \frac{z^3 + x^2 z(2\pi - 1)}{(x^2+z^2)} + z(4\pi G_2 - 2) - 2x\tan^{-1}\left(\frac{x}{z}\right) \tag{4.85}$$

$$4\pi\frac{\partial\Upsilon_2(x,z)}{\partial z} = \frac{x^3 + xz^2(2\pi - 1)}{x^2+z^2} + x(4\pi G_2 - 2) - 2z\tan^{-1}\left(\frac{z}{x}\right). \tag{4.86}$$

In principle, the process can also be extended to 3 dimensions, by replacing the 2d Green's

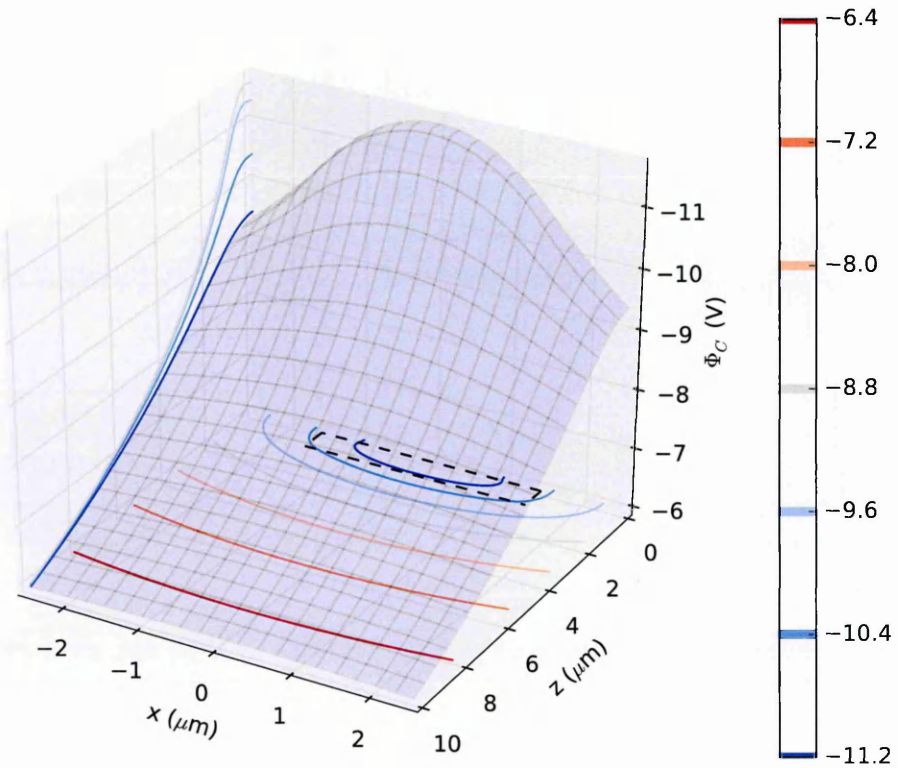

Figure 4.13: Visualisation of stored charge potential Φ_C for $x_0 = 1.5\,\mu$m, $z_0 = 0.2\,\mu m$, $z_1 = 1.0\,\mu m$, $\rho_0 = N_D$

function G_2 by its 3D equivalent, G_3, given by :

$$G_3 = \sum_{i=0}^{\infty} \frac{r^l}{r^{l+1}} P_l\,(cos\theta) \tag{4.87}$$

$$r = \sqrt{(x-x')^2 + (y-y')^2 + (z-z')^2} \tag{4.88}$$

where P_l are the Legendre Polynomials. There exists no simple-form anti-derivative of this function in the case where the potential is not cylindrically symmetric [83]. The true 3D solution of Φ_C is not considered further in this work. Those results which are presented involving 3D calculations consist of two separate 2D simulations for the (x, z) and (y, z) planes. This means, in particular, that our calculations are likely to have substantial errors at the pixel corners. Examples of the potential components for different amounts of charge are shown in Figure 4.13. The calculation of the values z_0 and z_1 depend on the storage volume model in use, and are described in Section §4.2.

4.1.4 Channel Stop Potential

The channel stop potential Φ_S is derived following exactly the same method as for the stored charge potential (Section §4.1.3), but translating the origin of the y axis to the centre of the channel stop. The density of the charge in the channel stop is simply taken to be exactly equal to the buried channel density N_D, with opposite charge, and with a depth equal to the buried channel depth z_J. In effect, the treatment of the channel stop is as a "lack of buried channel" rather than an extra implant, which reflects the manufacturing steps of many sensors [54].

The depth integration limits of the channel stop potential are taken to be $z_0 = 0$, $z_1 = z_J$. Since we take the co-ordinate origin as the centre of a pixel, the channel stops are implemented by translating the y co-ordinate to y' where:

$$y' = y - \frac{\left(\frac{\alpha}{2} + y_B\right)}{2}. \tag{4.89}$$

The integration limit constant y_0 is then:

$$y_0 = \frac{\left(\frac{\alpha}{2} - y_B\right)}{2}. \tag{4.90}$$

The width of each channel stop implant (see Figure 4.2) is $\alpha - 2y_B$. In each pixel, the "inner" halves of the channel stop implant in each direction from the centre is included. In this way, the potentials for a grid of pixels remains balanced for any number of pixels.

4.1.5 Total Potential

The total potential for a single pixel is calculated simply by the sum of all the relevant components (4.5), and the field components are obtained in exactly the same way. This process is illustrated in Figure 4.14.

The overall structure of a CCD device is assembled by adding translated copies of the "background" potentials (Φ_H, Φ_B, Φ_P,Φ_S). Since the stored charge potential is specific to the pixel (because each pixel may contain a different amount of charge), a single evaluation of the solution cannot simply be "tiled" in two dimensions. Rather, an individual copy of Φ_C must be maintained for every pixel.

Having assembled an appropriate set of solution potentials, our implementation of the potential calculation can either calculate the potential on demand at arbitrary co-ordinate values (useful for accurately evaluating a few electron tracks), or pre-calculate the potential

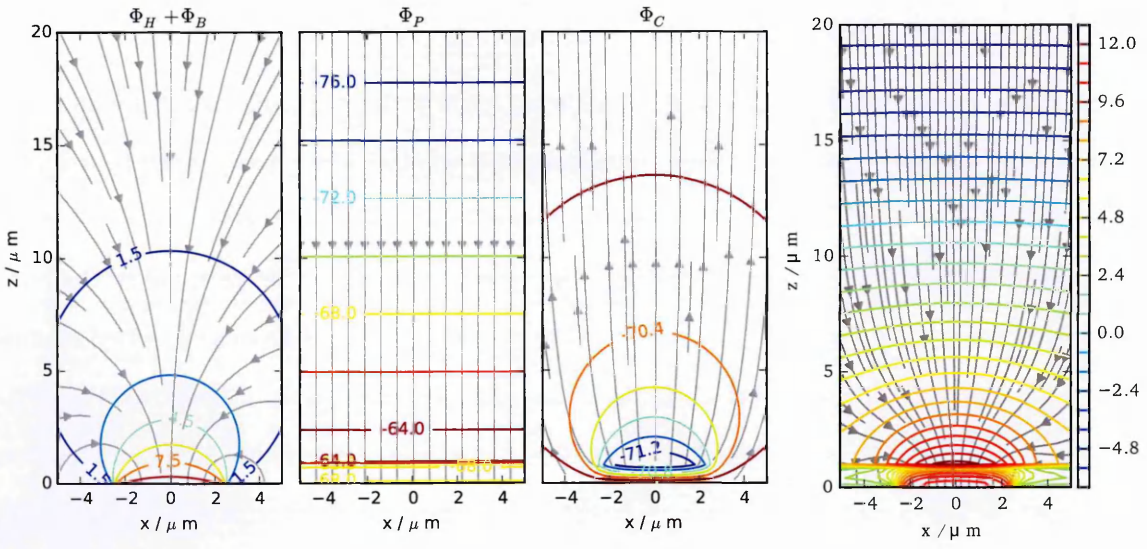

Figure 4.14: The homogeneous, particular and charge potential components of a pixel, and the resultant total potential.

on a grid of points and interpolate between them. The potential scalar and field vector values can be exported in a structured grid format suitable for visualisation using the ParaView program which is part of the Visualisation tool-kit [88]. This output can be particularly useful for visualising the shapes of electron trajectories. An example for a biased but empty pixel grid is shown in Figure 4.15.

4.2 Charge Storage Volume

For the potentials and field calculated in Section §4.1.3 to hold, the density of the stored charge in the channel stop must be constant across the spatial extent of the charge packet. As described in Section §3.2.2, even in one dimension the solution of the non-linear Poisson equation including stored charge is not possible analytically, but numerical solutions show that the stored charge density in reality is not constant [62]. A simplified analytical solution assuming constant density does, however, provide a fairly good approximation to the true solution [109]. That the depletion layer approximation is a reasonably accurate model in a buried channel CCD has been justified on both computational and theoretical grounds in the literature [20]. The varying density of stored charge at different signals in CCDs is critical in modelling radiation damage effects, and has been observed to follow a power-law relationship [17]. It is possible that using a combination of a constant density approximation and a power law for the density at various signal levels could provide improved fidelity, but is not explored further in this work.

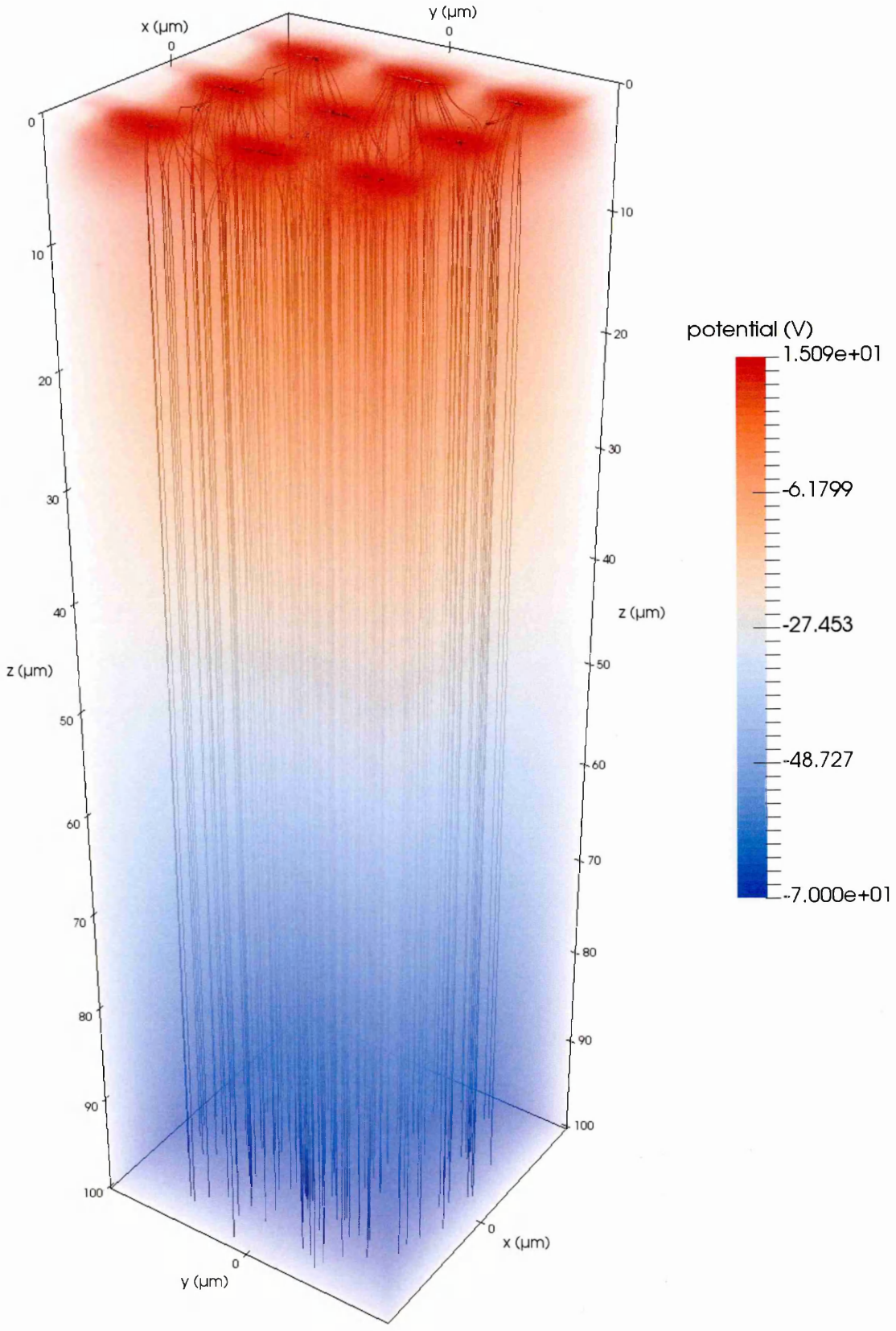

Figure 4.15: Volume rendering of total potential for 9 neighbouring pixels - the black lines show the streamlines of the resultant electric field

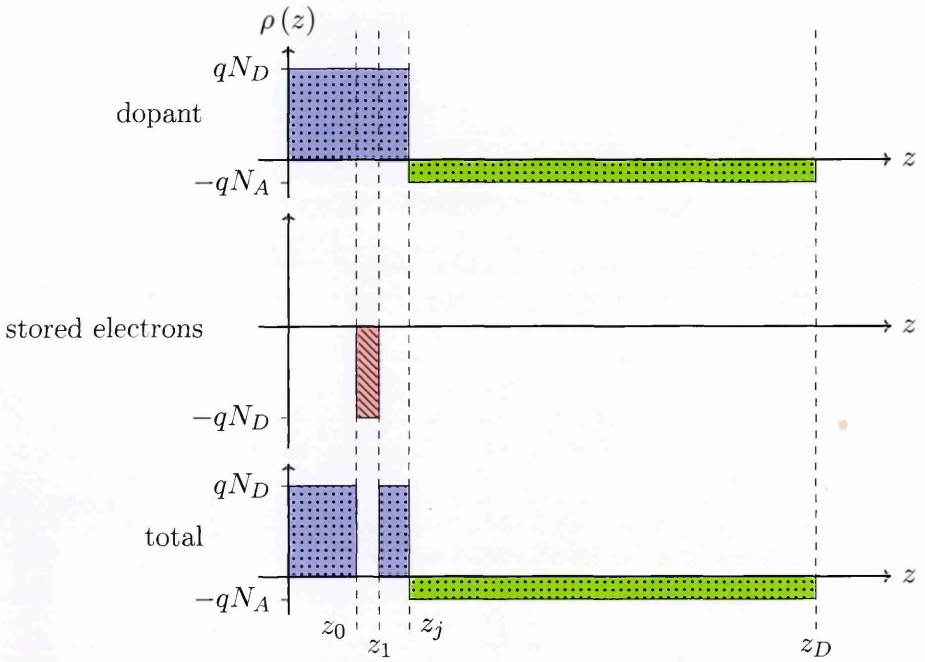

Figure 4.16: Charge distribution using the 1D constant density approximation

The stored charge is approximated as a perfectly rectangular block, extending the same width as the collecting gates in the parallel direction (i.e. $x_0 = \frac{L}{2}$), and between the inside edges of the channel stops in the serial direction (i.e. $y_0 = y_B$). The charge distribution in the z direction is modelled as shown in Figure 4.16. The analytical solution for this model proceeds similarly to that described in Section §3.2.2, except also matching potential boundary conditions at both edges of the charge packet. The solution is described in detail (and compared to Kent's method [62]) by Yin and Cooper [109]. Minor modifications must be made to include the back-biased substrate [105]. The edges of the charge packet, z_0 and z_1 are found to be:

$$z_0 = z'_J - \sqrt{\frac{2\varepsilon_{\rm si}\varepsilon_0 N_A V_m}{q_e N_D (N_A + N_D)}} \tag{4.91}$$

$$z_1 = z_J - \sqrt{\frac{2\varepsilon_{\rm si}\varepsilon_0 N_A V_m}{q_e N_D (N_A + N_D)}} \tag{4.92}$$

where the potential maximum V_m is given by:

$$V_m = \left(1 + \frac{N_A}{N_D}\right)\left(V_G + V_1 + V_2 - \sqrt{V_2^2 + 2V_2 (V_1 + V_G)}\right) \tag{4.93}$$

$$\text{with} \quad V_1 = \frac{q_e N_D (z'_J)^2}{2\varepsilon_{\rm si}\varepsilon_0}\left(1 + \frac{2\varepsilon_{\rm si} d_{\rm ox}}{\varepsilon_{\rm ox} z_t}\right) \tag{4.94}$$

$$V_2 = \frac{q_e N_A (z'_J)^2}{\varepsilon_{\rm si}\varepsilon_0}\left(1 + \frac{\varepsilon_{\rm si} d_{\rm ox}}{\varepsilon_{\rm ox} z_t}\right)^2. \tag{4.95}$$

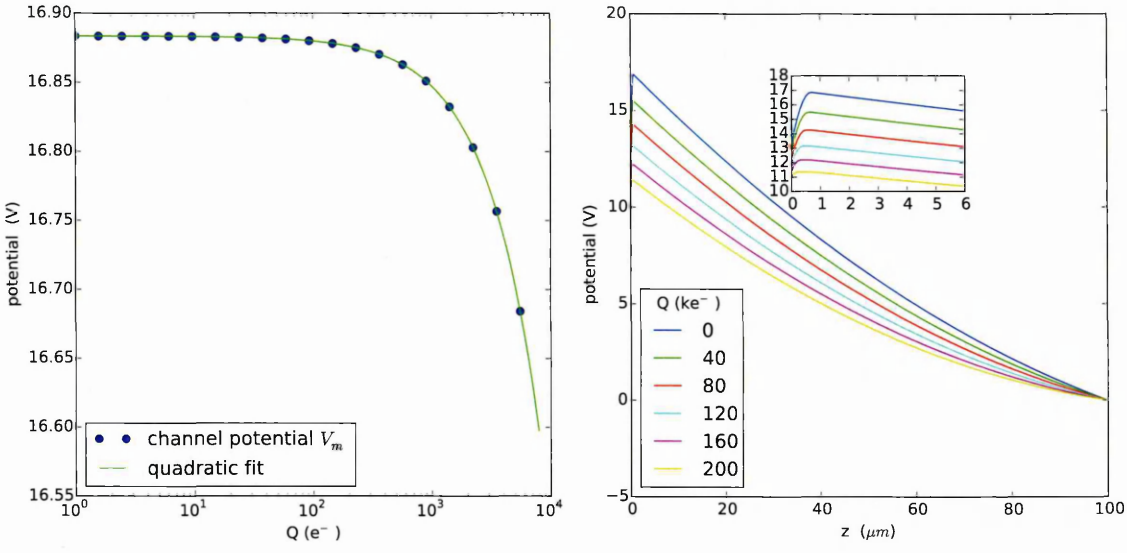

Figure 4.17: Potentials calculated using analytical 1D storage model.

The modified junction depth z'_J is given by:

$$z'_j = z_J - \frac{Q}{2N_D y_B L} \tag{4.96}$$

where Q is the stored charge measured in electrons. The term $\frac{Q}{2N_D y_B L}$ is thus the charge density as seen in the 1D model. The constant densities used for calculating 2D stored charge potentials (see Section §4.1.3) are then given by :

$$\rho_{\text{ser}} = \frac{Q}{N_D L} \qquad \rho_{\text{par}} = \frac{Q}{2N_D y_B}. \tag{4.97}$$

Example potentials calculated using the 1D storage model are shown in Figure 4.17. The surface full well capacity of a device in this model is found by solving the equation $z_0 = 0$ (i.e. when the charge packet contacts the device surface), a property which is used to calibrate the storage modelling (in particular the junction depth z_J) against experimental data (see Section §5.4.3 and Chapter 6).

It is important to appreciate the limitations imposed by the charge storage model. In the first place, assuming that the charge packet is always as wide as the channel stop spacing in one direction, and as wide as the collecting gate in the other implies that the charge packet may only grow in the z direction. This approximation has been shown using finite element modelling to be accurate for large signals, but breaks down at very low signals [17]. Secondly, since the width of the charge packet in the (x, y) plane does not change, the phenomena

of blooming cannot occur in our model, which is a significant limitation for various types of modelling. However, for a correctly optimised CCD, the blooming full well is set (by optimisation of gate voltages) to be the same as the surface full well [54], so that provided we operate within the limits of the surface full well predicted by our calculations, modelling the BFE in a properly operated device is still possible without blooming. The third and perhaps most serious approximation is the constant charge density itself. Whilst it has been discussed that good approximations to the channel potential maximum and potential shape are achieved by the constant density model, details of the potentials and fields very close to the actual charge packet itself will be inaccurate. In addition, the onset of surface full-well is likely to be overestimated somewhat. It is expected, however, that in general the constant density rectangular block charge model should provide at least a slightly closer approximation to reality than the (already extremely successful) point charge storage model used in previous BFE modelling approaches, in particular that of Antilogus et al. [5].

At this stage, it is already possible to estimate the magnitude of some part of the BFE: this is the isotropic excess diffusion, identified previously in the literature [105, 42]. If a pixel contains stored charge, the collection field in the bulk silicon is slightly reduced overall, so that the collection time increases (see equation (4.2)). Using Yin and Cooper's model, assuming constant mobility, the collection time can be calculated explicitly by integrating the electric field from the collection depth z_{coll} to the charge packet [105]:

$$t_{\text{coll}} = \frac{\varepsilon_{\text{si}}}{q_e \mu_e N_A} \ln\left(\frac{z_m - z_J + A}{z_m - z_{\text{coll}} + A}\right) \tag{4.98}$$

$$\text{with} \quad z_m = z_J + \sqrt{\frac{2\varepsilon_{\text{si}}\varepsilon_0 N_D V_m}{q_e N_A (N_A + N_D)}} \tag{4.99}$$

$$A = \frac{-q_e N_A (z_m - z_T)^2}{2\varepsilon_{\text{si}}\varepsilon_0 \left(\frac{\varepsilon_{\text{ox}}}{\varepsilon_{\text{si}}} z_T + d_{\text{ox}}\right)}. \tag{4.100}$$

The dependency on stored charge is introduced through V_m (see (4.93)). The Full Width at Half Maximum (FWHM) diffusion radius of collected charge can then be calculated using (4.3). Results are shown in Figure 4.18. Increased stored charge clearly increases diffusion radius, though the degree of change between empty and full wells is significantly reduced by a large back bias voltage, in addition to the total diffusion radius. Though excess diffusion produces a broadening of point sources as stored charge increases, it should be almost perfectly isotropic in nature. Thus, it cannot account for the anisotropic increase in point source width

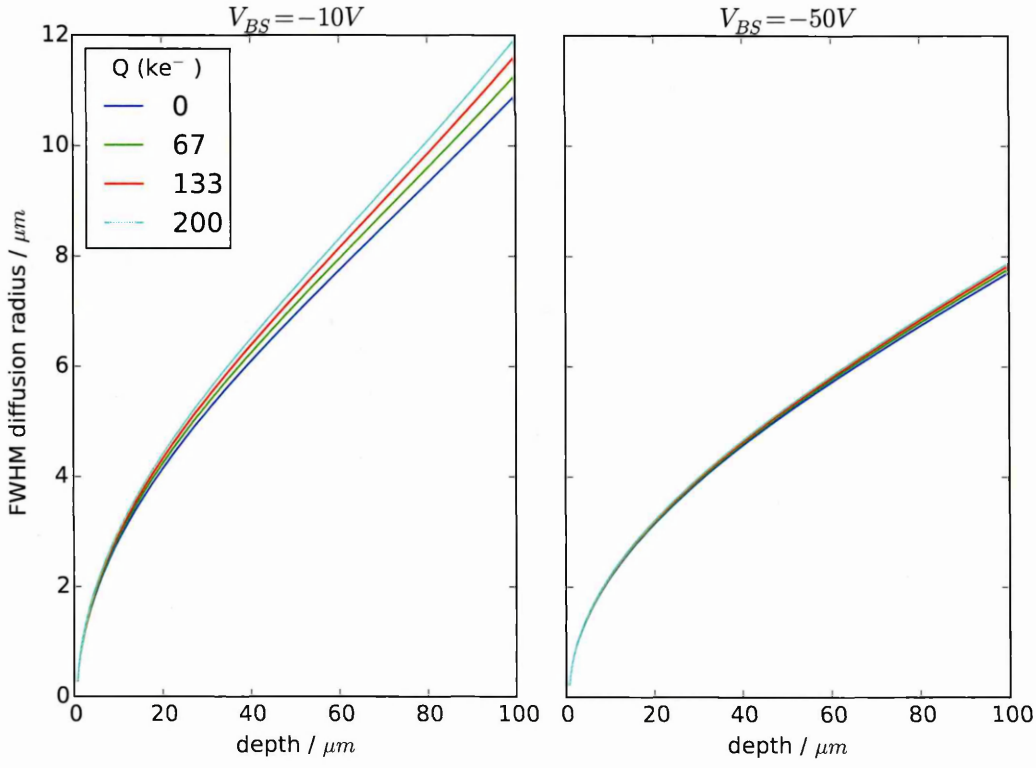

Figure 4.18: Excess diffusion for varying conversion depths

due to the BFE. Additionally, the total effect is very small in comparison to the observed boundary changes in measured devices [42].

4.3 Point Spread Function

The BFE has been referred to as a "signal dependent PSF" [68]. Whilst this terminology in some ways captures conceptually the behaviour resulting from the BFE, in other ways it introduces confusion. In order for a PSF to be properly defined for an optical system, it must meet the requirements of shift-invariance and linearity [108].[3] These conditions allow the PSF to be defined as one of the functions in a convolution operation, mapping the source light field to the measured. If the pixel boundary shifts caused in a pixel by the BFE depend on the charge collected in many nearby pixels (which current evidence suggests strongly that they do [5]), then the effect itself cannot be represented by a convolution operation. It could well be the case that for point sources, correction strategies for the BFE using de-convolution may nevertheless be useful. The question is not explored in the current work, though the modelling approach we present may be an asset in exploring this problem in future work.

[3] which in fact are already invalidated for all pixellated sensors, though useful "pseudo" proxies can be calculated - see Section §3.7

Two methods for charge collection calculations have been investigated, both being based on directed random walks: these are referred to as the full Monte Carlo random walk, and the fast Monte Carlo random walk. The simulations are performed in discrete time steps, δt. At each time step, the position (x_i, y_i, z_i) of an electron is updated in a drift step:

$$\begin{pmatrix} x_{i+1} \\ y_{i+1} \\ z_{i+1} \end{pmatrix} = \begin{pmatrix} x_i \\ y_i \\ z_i \end{pmatrix} - \mu(\mathbf{E}) \begin{pmatrix} E_x \\ E_y \\ E_z \end{pmatrix} \delta t \tag{4.101}$$

where the electric field $\mathbf{E}$ is calculated from the appropriate potential ($\Phi_H + \Phi_B + \Phi_S + \Phi_P$ for an empty well) as described in Section §4.1. In the full random walk, a diffusion step is also performed, and the positions are again updated:

$$\begin{pmatrix} x_{i+1} \\ y_{i+1} \\ z_{i+1} \end{pmatrix} = \begin{pmatrix} x_i \\ y_i \\ z_i \end{pmatrix} + \sqrt{D\delta t} \begin{pmatrix} \sin\left(\tilde{\theta}\right) \sin\left(\tilde{\phi}\right) \\ \cos\left(\tilde{\theta}\right) \sin\left(\tilde{\phi}\right) \\ \cos\left(\tilde{\theta}\right) \cos\left(\tilde{\phi}\right) \end{pmatrix} \tag{4.102}$$

where the angles $\tilde{\theta}$ and $\tilde{\phi}$ are chosen at each step uniformly over the intervals $[0, 2\pi]$ and $[0, \pi]$ respectively. Even in the 2D simulations mostly used for the collection simulations (i.e. in the (x, z) or (y, z) planes) it is very important to select both angles, so that the behaviour of the random walk is not changed [65]. Steps are performed until the desired end condition is reached, which typically is that the z co-ordinate of the electron has reached a position where its collection in its current pixel is inevitable - at some point just deeper than the already collected charge packet z_1, or the junction depth z_J in the case of an empty well. Setting this limit too low causes the random walk to continue indefinitely until a step limit is reached, because the charges simply move diffusively around the collection region. A choice must be made about the back surface conditions, otherwise diffusion may carry electrons beyond the device thickness, giving rise to erroneous results. Since in a real device construction the back surface is passivated using a high-dose p++ implant intended to reduce the surface recombination velocity [56], in this work a perfectly reflecting back surface has been implemented - if the z component chosen by a diffusion step would take an electron beyond the back surface, the direction of that component is simply reversed.

For the fast random walk, no diffusion step is performed; rather, a single random lateral offset selected from a Gaussian distribution scaled by the total diffusion length $\sqrt{Dt_{\text{coll}}}$ is

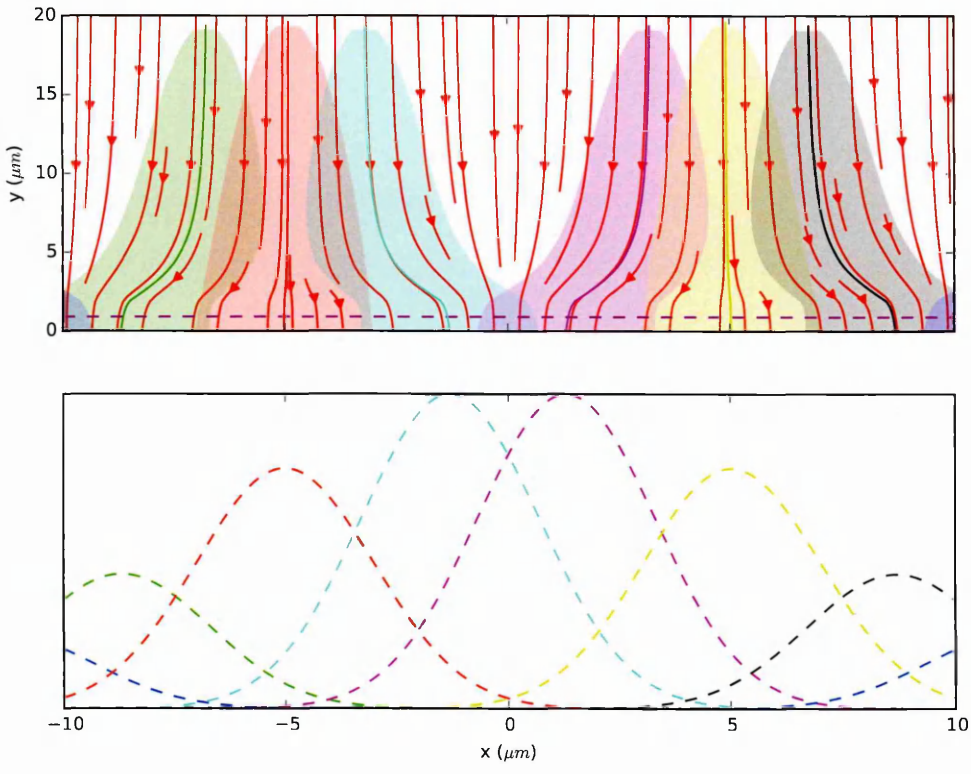

Figure 4.19: Illustration of the "fast" random walk procedure. The trajectories are computed from drift field lines alone, and Gaussian diffusion scaled by the collection time is added at the end.

added in each dimension. This approach is conceptually illustrated in Figure 4.19. Taking any given trajectory, the computational advantage of the fast method is very limited, since the vast majority of the time is spent calculating the field components themselves. Over many trajectories sharing the same potential environment, however, endpoints for trajectories with starting points nearby to previous calculations can be found simply by using the existing cached result and selecting a new pair of random angles, thus eliminating the need to perform many trajectory traces entirely. The disadvantages are that:

1. When simulating many trajectories using the fast random walk, the exact field environment at each step is not calculated. Therefore, the field-dependent mobility cannot be correctly applied to calculate the diffusion coefficient to apply to the Gaussian generator at the endpoint. A field average calculated over the original trajectory must be used.

2. In a case where pixel boundaries change rapidly over short distances, it is possible that diffusion process might affect the collection statistics, which are lost using the fast Monte Carlo approach. The extremely large statistics required to test this prediction combined

with the increasing computational effort required by the full random walk led to this question not being explored in this work. It should be a priority for verification in future efforts, however.

In the naive implementation of the simulation so far created by the author, the most significant computational burden by far is the calculation of the field values at each electron position, which must be performed once per time step, rather than the propagation of electron trajectories. A more advanced implementation using caching and interpolation of pre-calculated field values might change this situation somewhat. For this reason, and the obvious trivial parallelisation of the procedure (especially in the empty well case), the simulations presented in the remainder of this chapter all use the full random walk method.

The chief parameter requiring adjustment in all random walk based calculations is the time step between each step δt. The smaller this value, the longer each random walk takes to calculate, because it consists of more steps. Therefore, a value as large as possible whilst maintaining reasonable realism is desired. If δt is too large, the spatial resolution of the simulation is degraded, and changes in electric field magnitude over relevant distances are ignored. From a theoretical perspective, the largest sensible value to consider for the time step is the time taken for an electron to move by the Debye Length L_D (see (4.1)). Assuming an average electric field of $0.8\,\mathrm{V}\,\mu\mathrm{m}^{-1}$ (a total bias potential of 80 V through a device of $100\,\mu\mathrm{m}$ thickness), doping of $N_A = 1 \times 10^{12}\,\mathrm{cm}^{-3}$ and operating temperature of 150 K, and that the drift component of each step is larger than the diffusion, this corresponds to a maximum value of $\delta t \approx 1 \times 10^{-11}\,\mathrm{s}$ including field dependent mobility (see Section §2.4). Figure 4.20 shows the number of simulation steps required for an electron starting at the centre of an empty pixel to reach collection for varying δt values at $T = 150\,\mathrm{K}$ and $V_{\mathrm{BS}} = -70\,\mathrm{V}$, and also compares field dependent mobility and constant mobility calculations. If the total time to collection t_{coll} remains constant (which it should for the simulations to be physical), we expect an inversely proportional relationship between the number of steps N_{steps} and δt, which is well followed by the observed relationship, until roughly the expected maximum allowed value of δt. The remaining simulations in this chapter are carried out at $T = 150\,\mathrm{K}$, so we choose a δt value of $\delta t = 10^{-12}\,\mathrm{s}$. As expected, the number of time steps required for constant mobility is significantly lower than that for the field dependent mobility, which is a simple consequence of velocity saturation increasing the collection time. We also verify that the t_{coll} remains consistent at this time step as compared with a very small time step -

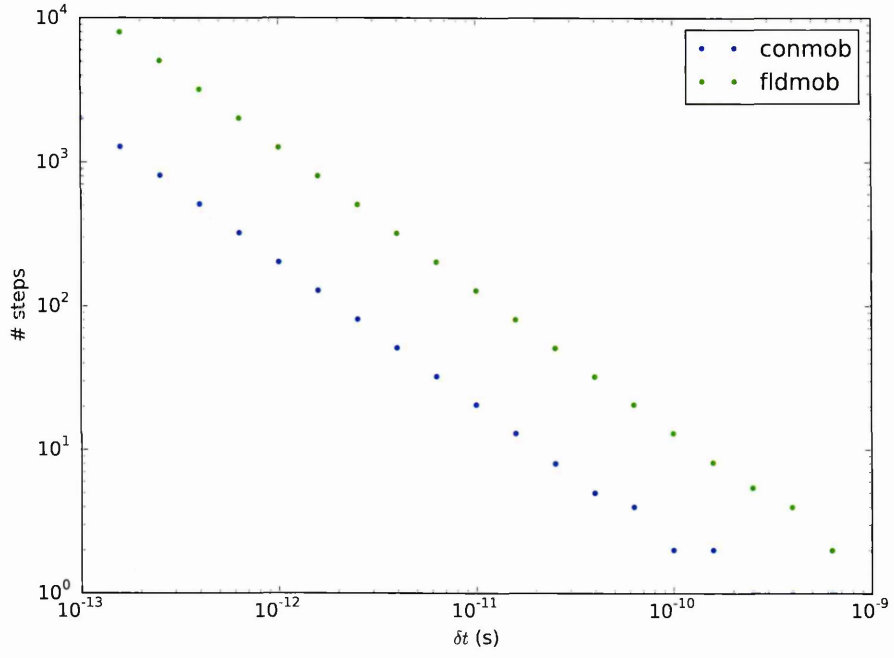

Figure 4.20: Number of steps to collection against simulation time step δt. Each point is an average of 1000 random walk simulations.

this is shown in Figure 4.21. Again, we see as expected that constant mobility calculations are much faster, even though the calculation of the mobility term itself at each time step is computationally inconsequential compared to all other operations. The collection time found in the constant mobility case is (re-assuringly!) very close to that predicted from the simple estimation equation (4.2).

At this point we proceed to calculate the PSF. Though the response of the device to a perfect point source may be an interesting situation to simulate, for comparison to any practically realisable measurement, a pseudo-PSF must actually be calculated (see Section §3.7). Random walk simulations are repeatedly performed over a set of Gaussian distributed initial positions. The mean of the distribution is shifted at each step, from the centre of the pixel to the edge, constructing a probability distribution for each initial position using the histogram of end points. To simulate wavelength dependence, the initial z positions for each random walk are selected from an exponential distribution whose parameter is the absorption coefficient at the desired wavelength (see Section §2.5). The individual probability distributions are then shifted, summed and normalised to yield the PSF measurement. Examples of individual end point histograms for the x direction are shown in Figure 4.22, and the resulting pseudo-PSF shapes obtained are shown in Figure 4.23, along with a Gaussian fit. The simulated results for the PSF width in both directions are shown against varying back bias voltage in Figure 4.24.

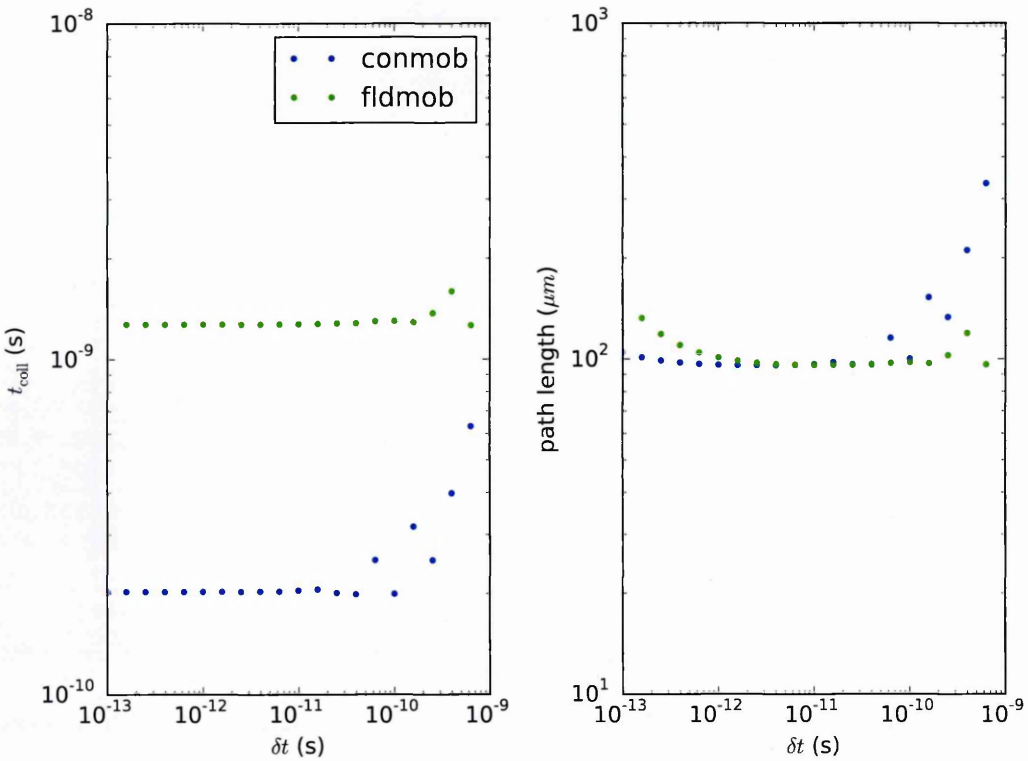

Figure 4.21: Time to collection and path length against time step δt.

4.4 Pixel Boundaries

As described earlier in this work, and by several authors in the literature [5, 7, 81, 82], the BFE can be well understood conceptually by regarding pixel boundaries as dynamically shifting due to stored charge. The definition of "boundary" in this case is regarded as that plane which divides electron trajectories whose endpoint is in one pixel from trajectories whose endpoint is in another. In the empty well case, without any pixel to pixel differences in gate potential or geometry, this clearly corresponds to the centreline between two pixel centres. The introduction of charges which differ between pixels will shift the boundary. Recalling from Section §2.4 the relationship between electron velocity and electric field (2.66), it is clear that in the case of constant mobility, and without diffusion, the trajectories followed by electrons will be given by the streamlines of the electric field[4]. Field dependent mobility can be readily incorporated into this picture by regarding the mobility as a non-linear scaling of the electric field vector. Depending on the model used for the mobility, this may or may not change boundary positions: in the more advanced models of field dependent mobility, μ depends not only on field magnitude but also field direction with respect to the crystal axes [100]. In

[4]To be precise, given the negative charge on the electron, the trajectories will be in the opposite direction to the electric field streamlines

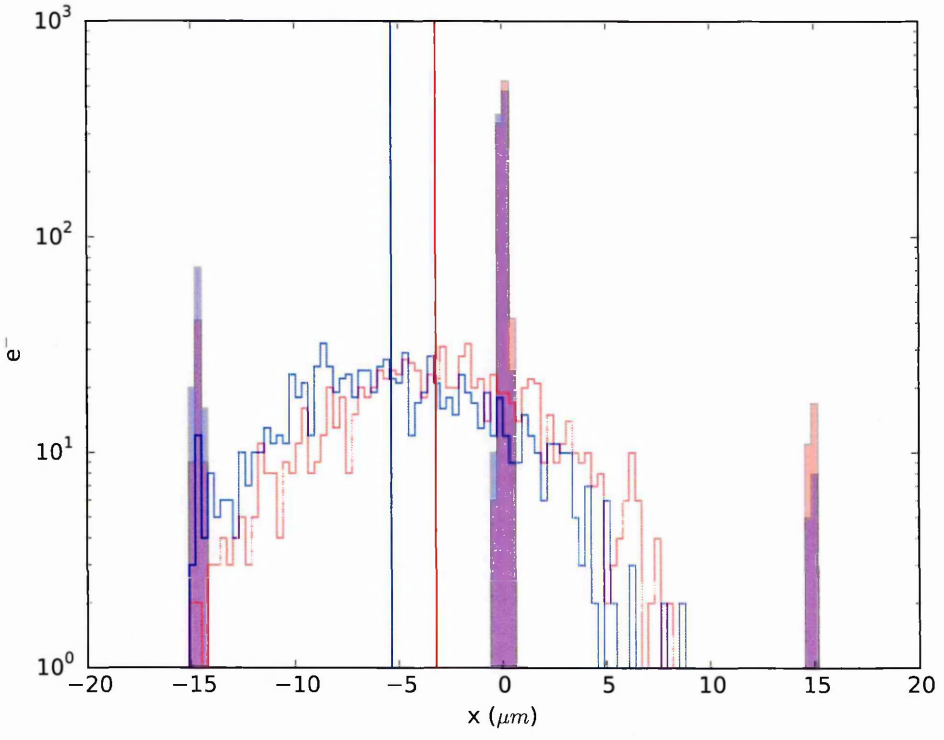

Figure 4.22: Individual collection histograms used to simulate a pseudo-PSF experiment. The unfilled histograms show the initial electron positions in the x direction, and the filled histograms show the final positions. The vertical lines indicate the mean position of the incident electron distribution. The red and blue colours indicate initial electron positions of $x = -3\,\mu$m (red) and $x = -6\,\mu$m (blue).

this case, the shape of the boundaries necessarily change. In the simple Caughey-Thomas model which has been described in this thesis, which is scaled only with the magnitude of the field, the directions of streamlines are not changed; hence, neither are the pixel boundaries. Two dimensional streamlines for an empty pixel and a pixel containing charge are shown in Figure 4.25.

An important point about the determination of dynamic pixel boundaries which has not been greatly emphasised in the literature is that to find the pixel boundary given the electric field, it is not sufficient to find the zero crossing of the fringing component (E_x or E_y depending on the direction). This can be clearly seen by examination of the streamline shape near the boundary in Figure 4.25. Many trajectories whose endpoints are in one pixel nevertheless experience some "bending" in the direction of the neighbouring pixel due to the charge distribution. This is true even in simpler models using only point charges (evident in the simulations performed by Antilogus et al [5]), except if the charge is stored at the device surface - which effectively is the case in the transformed co-ordinate system used to qualitatively

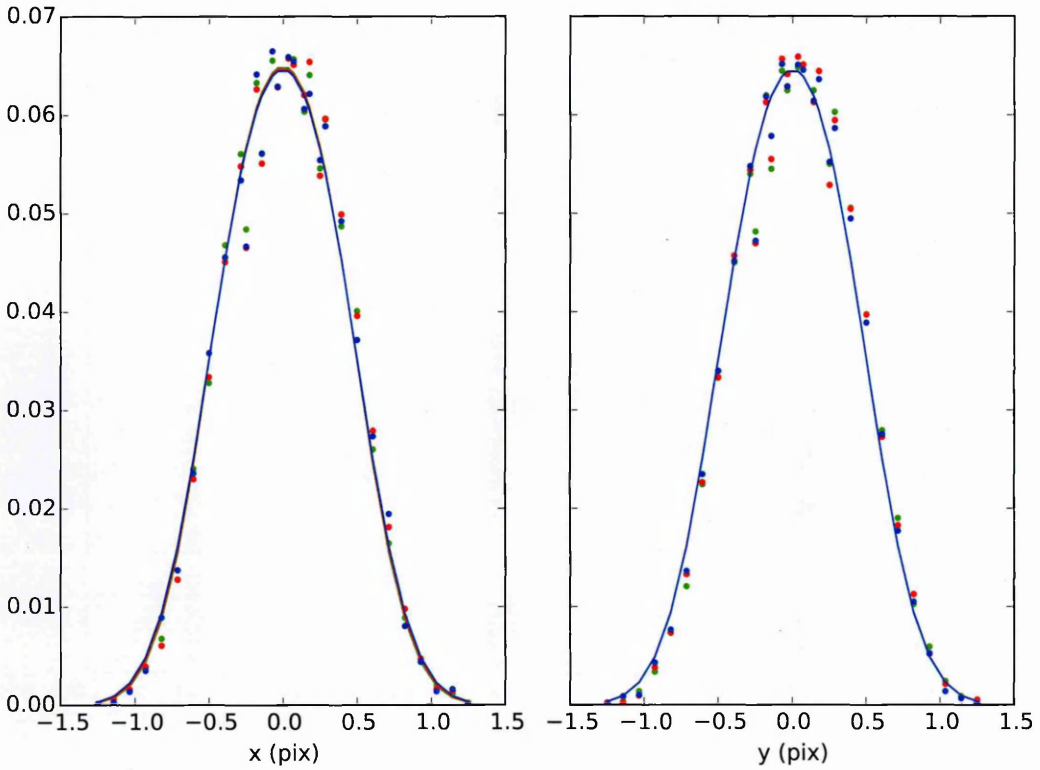

Figure 4.23: Simulated pseudo-PSF measurement at $V_{BS} = -70\,\mathrm{V}$. The colours of the points and fitted lines indicate simulated wavelengths of $\lambda_{\mathrm{red}} = 650\,\mathrm{nm}$, $\lambda_{\mathrm{green}} = 550\,\mathrm{nm}$, $\lambda_{\mathrm{blue}} = 450\,\mathrm{nm}$. As expected, no difference is seen in the centroids of the distributions

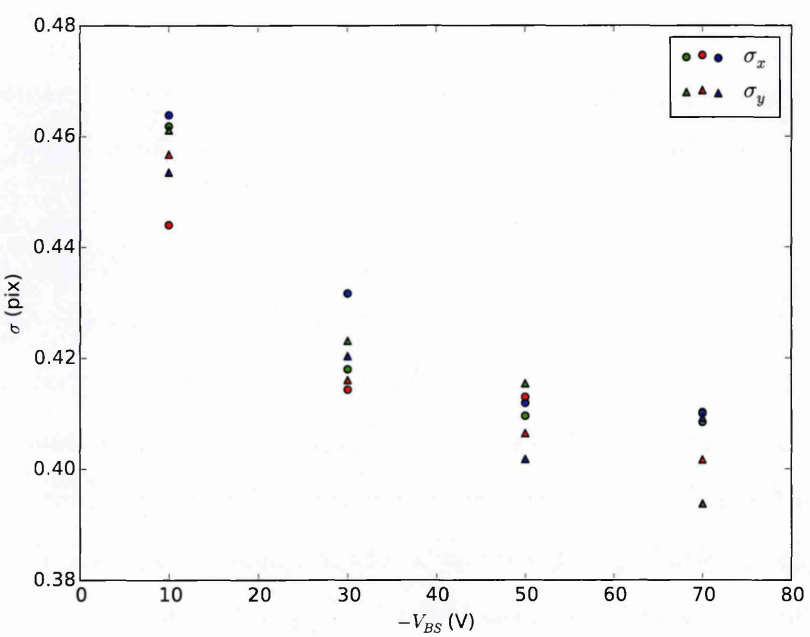

Figure 4.24: Simulated pseudo-PSF width against V_{BS}. The colours of points indicate the simulated wavelengths $\lambda_{\mathrm{red}} = 650\,\mathrm{nm}$, $\lambda_{\mathrm{green}} = 550\,\mathrm{nm}$, $\lambda_{\mathrm{blue}} = 450\,\mathrm{nm}$

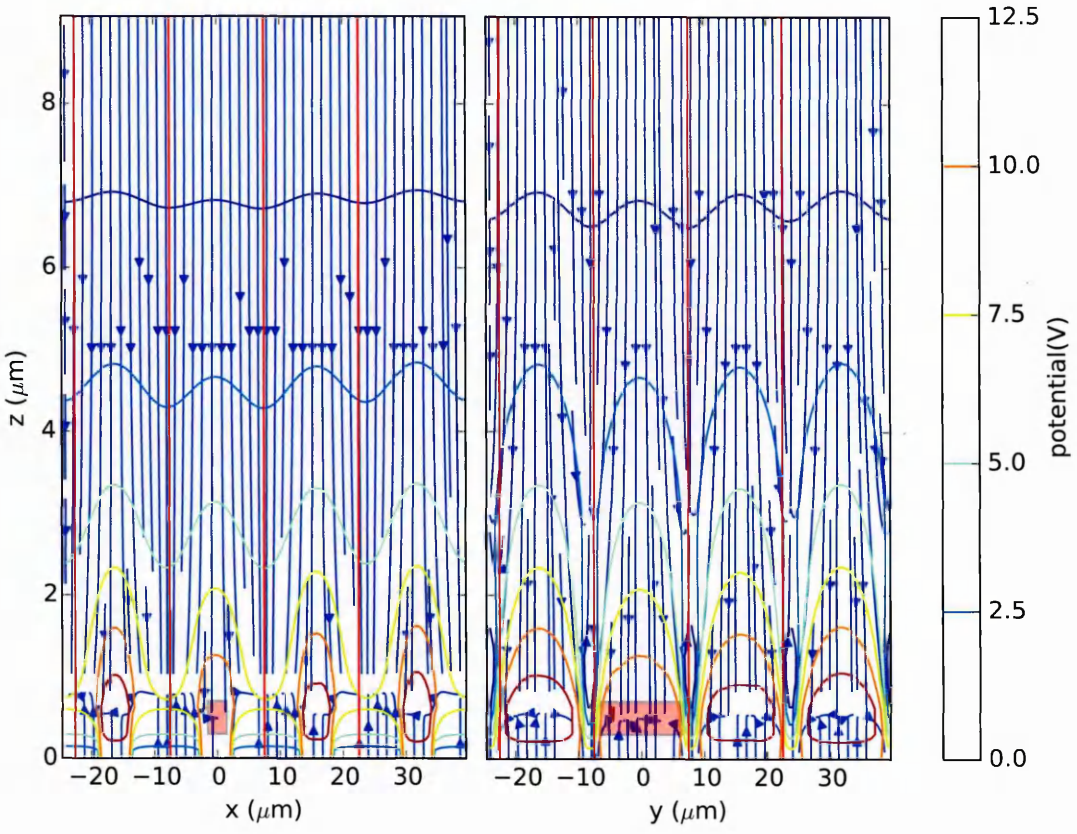

Figure 4.25: Electron trajectory streamlines near a pixel containing 100 ke$^-$ signal charge. The charge storage region is indicated by the shaded red area.

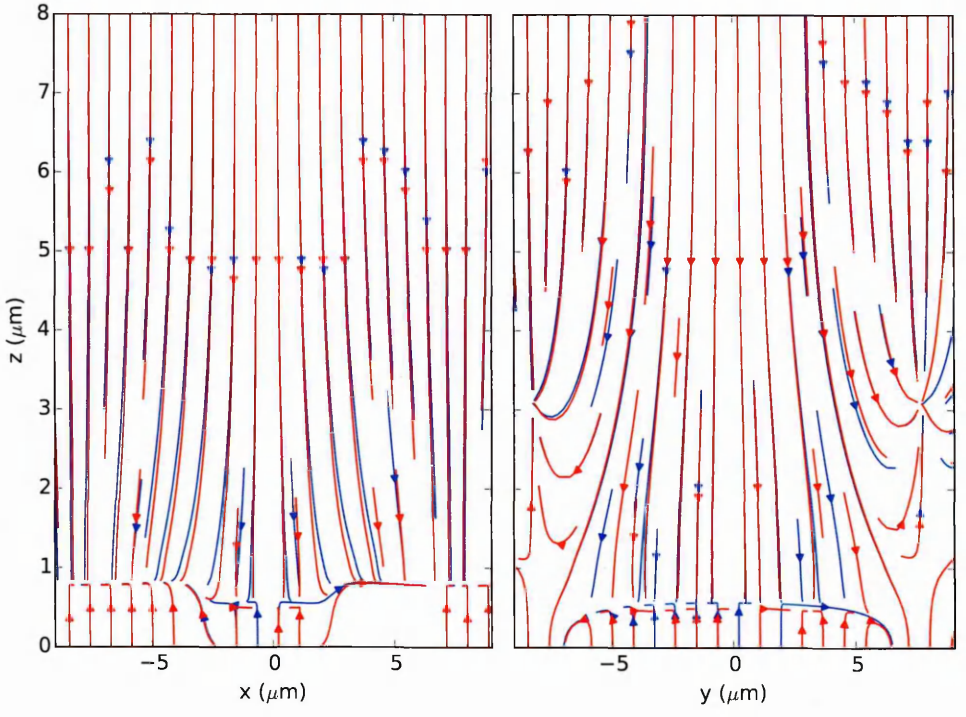

Figure 4.26: Change in trajectory streamlines between empty and filled pixels. The red streamlines show an empty pixel, the blue streamlines show the pixel filled with 100 ke$^-$.

model the pixel boundary shift in Weatherill et al [105]. Unfortunately, a simple mathematical statement about the properties required by a particular streamline to determine which pixel will be its endpoint is, after much consideration, still not clear to the author. Consider a streamline (for simplicity in the (x, z) plane) whose path is parametrically given by:

$$x = X(\Gamma); \quad z = Z(\Gamma). \tag{4.103}$$

The explicit trajectory is found by solving the differential equation [29]:

$$\frac{dx}{dz} = \frac{E_x}{E_z}. \tag{4.104}$$

And then, the position of the electron in the lateral direction when it reaches the collection depth $(x_{\rm ep}, z_1)$ given a particular starting point (x_s, z_s) must be found by the path integral:

$$x_{\rm ep} = \int_{z=z_s}^{z_1} X(\Gamma)\, d\Gamma \tag{4.105}$$

which certainly cannot be evaluated analytically. Instead, we simply find endpoints by tracing trajectories as described in Section §4.3 without diffusion. The boundary position must then be found using Brent's minimization procedure [22].

Pixel boundaries are found to substantially vary laterally only in the first few μm near the collection region, which as noted previously gives justification for the observed lack of wavelength dependence in the BFE [5]. In the model presented here, this is a clear consequence of the boundary conditions (4.76) and (4.77), constraining the electric field vector to be parallel to the back surface normal. The degree to which this boundary condition holds will likely depend on the nature of the back surface treatment applied to the CCD during manufacture. An interesting avenue for future study is therefore to investigate whether the back surface passivation affects the wavelength dependence of the BFE. This would serve only to increase understanding, since there is seemingly no technologically desirable outcome for precision astronomy in increasing chromaticity!

Since the chromaticity for the BFE is very low, for most purposes the boundary shift implied by a stored charge is simply taken to be the lateral boundary position at the back surface. The result of such a calculation for a single central pixel containing charge, and completely empty surrounding pixels, is shown in Figure 4.27. In accordance with previous investigations, we find that pixel boundary shifts can occur over a distance of several pixels

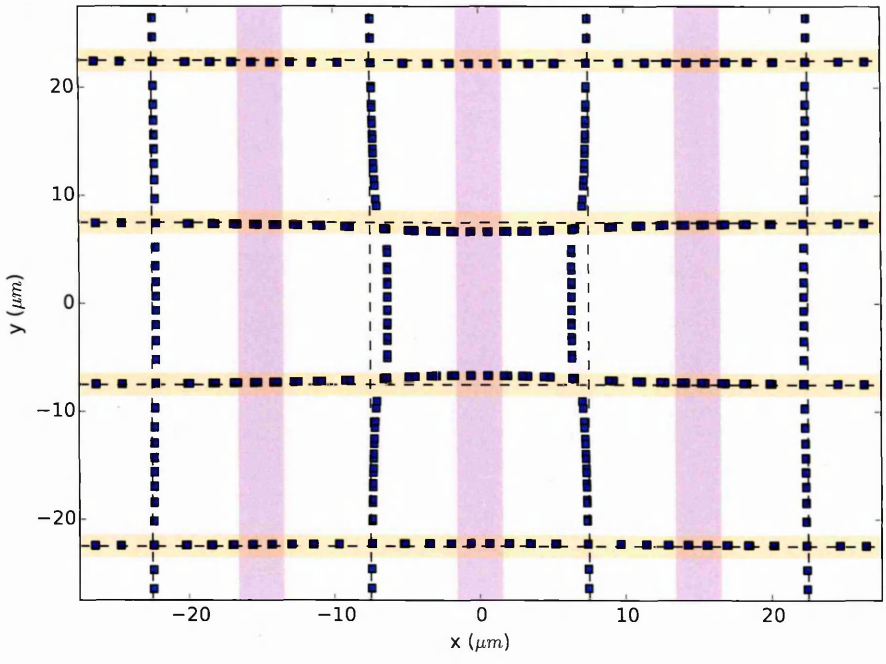

Figure 4.27: Pixel boundary positions shifting with stored charge. The central pixel contains 100 ke$^-$, all other pixels are empty. The orange shaded areas show the channel stops, and the purple shaded regions indicate the collecting phases

from the stored charge [42]. Theoretical values for the ancillary pixel data coefficients required for the correction strategies described by Guyonnet et al [42] may also be derived from this boundary calculation procedure, which offers future possibilities for directly simulating scientific images for given CCD designs and operating conditions. This procedure is discussed further in Section §6.4.

The boundary calculation is also very useful in investigating the effect of gate width (which can be varied experimentally by collecting under a different number of gates) and pixel pitch. A 10 μm pixel was simulated at two different gate widths: $L = 3\,\mu$m and $L = 6\,\mu$m. The results are shown in Figure 4.28. A much larger shift in the parallel transfer direction is found for the wider gate than the narrower, and a slightly reduced shift in the serial direction. Since Φ_H only varies in the parallel direction, the serial boundary shifts must be a secondary effect caused by the fact that with a higher gate width comes a smaller depth range over which the charge is stored, and an effective decrease in the charge storage density as seen along the serial direction (the same total number of electrons is now stored in a larger area - see (4.97)).

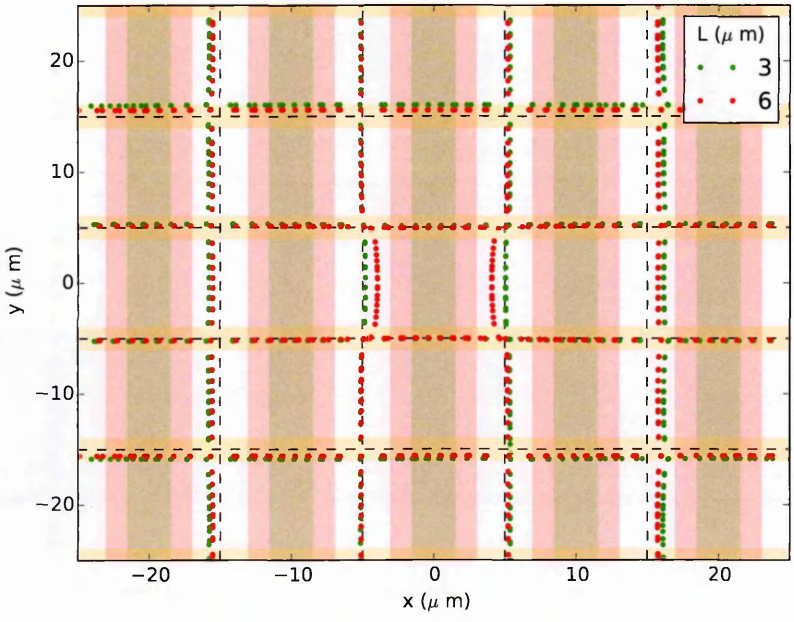

Figure 4.28: Comparison of boundary shifts for a pixel with varying gate widths. The shaded regions represent the geometric gate widths.

4.5 Brighter - Fatter Effect

Simulation of the BFE proceeds according to the following procedure:

1. Choose spatial distribution of incident photons (for example: uniform flat field, Gaussian spot), and generate starting depths according to the wavelength.

2. Propagate electrons to endpoints via random walk simulations.

3. Identify the pixel associated with the endpoint and update device status accordingly. Record appropriate statistics (e.g. mean, variance, width of spot, etc.)

4. Calculate new stored charge potential components using the charge volume storage model

5. Repeat steps 2 - 4 as necessary.

Using this scheme, most experimental results associated with the BFE (mean-variance curves, spatial autocorrelation coefficients and spot anisotropy) can be simulated. More detailed explanations of the mean-variance analysis of imaging sensors is given in Section §5.6.

During work on simulating mean-variance curves, it was observed that when evaluating trajectories without diffusion, the exact charge state of the device (and thus the boundary

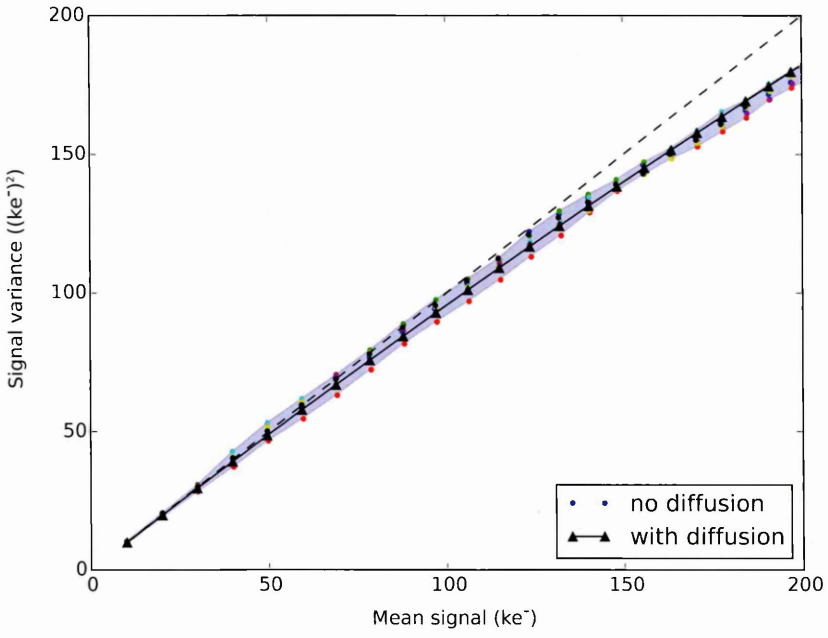

Figure 4.29: Comparison of mean-variance curves with and without diffusion. The same photon arrival positions are used in all cases, but with different ordering for each of the "no diffusion" cases. The blue shaded area represents the span of 9 simulations with different ordering.. The coloured points show some individual mean-variance curve simulations using different photon arrival ordering.

shifts, and the collection statistics) at any given stored charge value varied significantly from simulation to simulation. This property held even for identical lists of initial electron positions, but with shuffled ordering. Examples of the mean-variance curves obtained by this process for several simulations are shown in Figure 4.29. Averaging over several simulations for each charge level restores the expected smooth properties for the mean variance curve. However, in real experiments, it is found that such a mean-variance curve can be generated by taking a single pair of exposures at each signal level. This seems to indicate that even for a single process of filling a device's potential wells, the brighter-fatter effect should not depend on the exact ordering of the electron arrivals. We find that performing random walks with diffusion steps included indeed recovers the observed behaviour, without averaging over simulations (represented by the curved black line in Figure 4.29). If it were true that the effect of the BFE depended not only on signal level, but on the exact history of the arrival of signal charges, it would become essentially impossible to design a reliable correction algorithm, since for an individual image there is no way in any CCD type detector to gain this information. Thankfully, successful correction strategies have begun to be demonstrated [7], and as such the dependence on ordering must not be exhibited in reality. We therefore conclude that

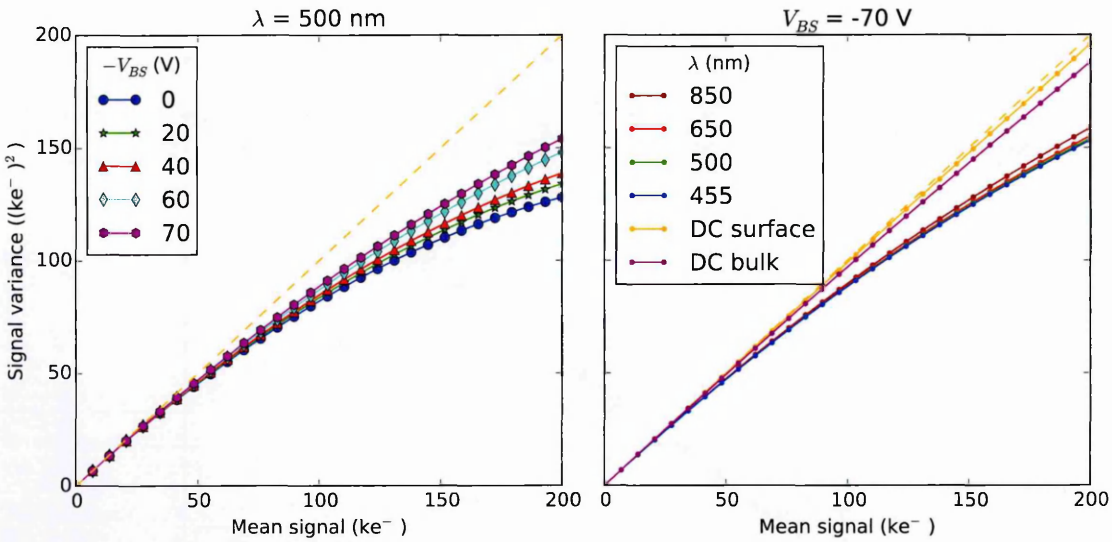

Figure 4.30: Simulated mean-variance curves at varying V_{BS} (left panel), and varying wavelength (right panel)

though the diffusion in sensors itself might contribute only a very small portion of the BFE (see Section §4.2), it is nonetheless a physically important part of understanding the effect.

Simulated mean-variance curves for varying V_{BS} and λ are shown in Figure 4.30. Taking the backside bias voltage more negative clearly decreases the non-linearity of the mean-variance curve as observed in experimental data (see Chapter 5), and shorter wavelengths are found to produce slightly more non-linear mean-variance curves, which is expected from a theoretical viewpoint: the shorter wavelengths have a shorter absorption depth, so that for a backside illuminated device, electrons generated from a shorter wavelength illumination will, on average, have to travel slightly further to reach collection. This trend would be expected to reverse for a front illuminated device, which has been reported experimentally [94]. Simulations were also performed where the initial depth of carriers was taken to be at the insulator interface, and uniform throughout the active depth, in order to model the collection of surface dark current and bulk dark current, respectively. In both cases, the non-linearity of the mean-variance curve is drastically reduced, which is confirmed qualitatively by experiment (see Chapter 5), though matching an experimental result quantitatively to a simulation would require good knowledge of the ratio of the surface dark current generation rate to that of the bulk dark current. As mentioned in Section §3.5, the surface dark current generation rate in typical scientific CCDs tends to exceed the bulk generation rate substantially.

The observed relationship between V_{BS} and non-linearity has some subtleties which deserve further discussion. In our model, the degree of non-linearity decreases monotonically

with more negative V_{BS}. This coincides with published experimental results [42] and those presented in Chapter 5. In the language of our analytical model, the change in pixel boundaries is caused directly by the perturbing stored charge potential Φ_C, which affects the field streamlines near the front surface. The more bias applied to the back surface, the more the collection behaviour is dominated by the back bias potential Φ_B, reducing the relative influence of Φ_C. Thus, it is reasonable that a more negative back bias recovers linearity. Consider, though, the case of a device without any applied bias (back side or gate): in this case the device would not be fully depleted, so the electron transport would be dominated by diffusion - there may be some drift contribution from the dopant charge in the buried channel (depending on whether the channel itself is depleted or not). In such a situation, forgetting for a moment that without any gate potential there is no confinement in the parallel transfer direction at all, logically there must be no correlated collection, since the diffusion follows a random walk. If the back surface is completely reflective, the charges will nevertheless at some point reach the front surface, disregarding recombination. The effect of incomplete diffusion, therefore, must be to reduce correlation. Since the model results presented in Figure 4.30 do not take into account the presence of a field-free region even at equilibrium bias conditions, it is not surprising that we do not see this "recovery" of linearity for low biases. Slightly less obvious is why experimental results do not seem to strongly present evidence for the effect. To justify this, consider that the very high resistivity substrates typically used in the devices in question mean that a very large portion of the device's overall depth is depleted with the application of just the gate potential V_G, without any extra back-bias (see Section §5.4.2 and [85]). Full depletion typically occurs at a value somewhere near $V_{\mathrm{BS}} = -10\,\mathrm{V}$ (see Chapter 5 and Chapter 6). Hence, in all tests yet reported including this work it would be unlikely that significant effects due to incomplete depletion would be evident.

As a final point, we note that the observed pixel histograms of correlated flat-fields in the model are found to be well fitted by Gaussian functions. It again seems slightly counter-intuitive that the probability distribution of a set of values (the individual pixel signals) which has been arrived at via a physical process which explicitly involves correlation should be Gaussian. A possible explanation is arrived at via analogy with a familiar effect in CCDs: the Fano effect [23]. When a high energy photon interacts inside a CCD, it releases a high energy primary electron, which in turn causes many secondary ionisations. The distribution of the total number of electrons released is found to be very well characterised by a Gaussian, yet significantly narrower than suggested by the assumption that the cascade process producing

the secondary electrons with random, independently chosen values of energy. In other words, there is a correlation between individual secondary electron ionisations. In the case of the Fano effect, this correlation is very significant: the dispersion co-efficient between variance and mean (known in this area as the Fano Factor) is $F \approx 0.1$ in silicon. A simple and pleasing model of the Fano effect was delivered by Jordan et al [57]. They find that any system with a conservation law for some quantity (in the case of X-ray detectors, the quantity is the total energy of the incident photon) exhibits a Fano effect due to the implicit correlation implied by the necessity of conserving that quantity. Furthermore, they show that the well known Central Limit Theorem applies to all such systems, such that independent of the distribution of the underlying process, the measured overall results show a Gaussian probability distribution. In the system composed of correlated collecting pixels, a similar conservation law is clear: the conservation of total collecting area. The movement of an effective pixel boundary reduces the collecting area of one pixel by precisely the same amount that it increases that of the neighbouring pixel. Ultimately, this fact means that the conditions stated by Jordan et al [57] apply to the correlated collection process, and we therefore expect that the flat-field histogram will be near-perfectly Gaussian (for a device with a reasonable number of total pixels) even in the absence of any readout noise or other broadening effects.

To conclude our theoretical treatment of the BFE, we summarize in turn the most important parameters which are thought to affect the magnitude of dynamic charge collection processes, drawing on insight from our model and previous results. The examination of some of these areas is expanded in Chapter 6.

- Bias conditions - clearly the operating voltages of V_G, V_T and V_{BS} are directly related to the magnitude of observed non-linearity in charge collection. This is backed by multiple observational studies ([5, 26, 42] and see Chapter 5 and Chapter 6) and by the modelling presented in this chapter. The BFE is caused by the electric field changes arising from charge stored in the pixel's buried channel (Φ_C). If the static fields in the device (Φ_H, Φ_B, Φ_S, Φ_P) can be made larger compared to these dynamic fields, their boundary distorting effect is lessened. From a practical standpoint, it is most important to examine very carefully the effect of the chosen back bias voltage V_{BS}. Even though the boundary distortions are much larger near the front surface, and therefore likely to respond better to changing V_G, there are two significant reasons why adjusting the back bias is preferable. Firstly, the chosen value of V_G is constrained by many other

considerations than just the BFE, in particular, the full well capacity (see Section §5.4.3). Secondly, there is in a conventional CCD no way (after manufacture) to affect the confining potential due to the channel stops (Φ_S), which is governed by the details of the channel implant. Adjusting V_G may be useful to change the anisotropy observed between spreading in the parallel and serial transfer directions (see Chapter 5 and Chapter 6), but if an overall reduction in the observed non-linearity is required, it is a safer choice to vary V_{BS}. Users of these devices may have to be prepared to make undesirable trade-offs (e.g. full-well capacity for isotropy), and should be aware that the selection of operating bias conditions is highly important in this regard. As argued above, it is likely that a device with a large field-free region would suffer much less due to dynamic charge collection effects, so that there may be a point below the full depletion voltage where applying additional back-bias actually makes the non-linearity worse. It is unlikely in the extreme that any possible benefit to scientific imaging that might be obtained by operating a back-biased device with a field-free region would outweigh the disadvantages (principally a much larger overall PSF), given that the whole point of introducing back-biased contacts to scientific CCDs was to allow for fully depleted operation in thick silicon.

- Wavelength - In general, experimental studies of the BFE have found little evidence of its chromaticity. Previous theoretical modelling based on point charges [42] and fully numerical calculations of the Green's function [82] (both approaches sharing much in common with that we have taken here), has suggested that the variation of the BFE with incident wavelength should be small. This result is corroborated by our work here. Small, however, is not the same as non-existent. The change in the optical absorption coefficient with wavelength means that lower energy photons will, on average, be absorbed further into the device, and for a back-illuminated device this means that they will experience a lower probability of being collected in a different pixel to that which their geometric position would imply. The effects of excess diffusion, that is to say the extra lateral diffusion caused by longer collection time experienced by a carrier due to the reduction in the longitudinal field from the stored charge work in the same direction, but are also very small. It is still the author's opinion that a sufficiently precise experiment would reveal chromaticity in the effect. Indeed, in some tests the data presented later in this work (Chapter 5) does show systematically higher spot anisotropy for higher energy

photons. Due to fairly large uncertainty, we cannot claim to have entirely settled this matter. Previous studies have also seen a wavelength dependence in other devices, however [94]. It is entirely plausible that at the level of correction likely to be required by LSST [81], wavelength consideration may be necessary in correcting for the BFE. Logically, it is certainly the case that the magnitude of correlated charge collection must depend on wavelength at some level. The open question is simply whether this effect is strong enough to be of import in sensors relevant for LSST.

- Temperature - The operating temperature of scientific CCDs is generally selected in order to minimise dark current (see Section §3.5). A fortuitous side-effect is that, due to the decrease in absorption co-efficient and increase in carrier mobility (see Section §2.4), both the QE and MTF of the sensor also generally improve (we discussed this effect in Section §3.3) . In this chapter, we have remarked that the electron mobility μ might be an important factor affecting the BFE, on the dual grounds both that it changes the diffusion properties of carriers (so can enhance or subdue excess diffusion) and that it changes the relationship between drift velocity and electric field. The model we have presented, in its present form, is unable to represent any possible effect due to the latter contribution (which is likely the larger), since our mobility model is isotropic: the mobility depends only on the magnitude of the electric field, not its direction with respect to the crystal axes. This is not true of some more complex and modern mobility models [100], and indeed is not tenable theoretically due to the origin of the mobility from the effective mass, itself a tensor-valued quantity. If there is an effect, it is likely that higher operating temperatures actually make the BFE less pronounced, since anisotropic mobility models tend to predict less difference between crystal directions at higher temperatures [100]. Given the magnitudes of the changes involved, however, what is clear is that there would never be a good reason to change operating temperature solely to alleviate dynamic charge collection effects: large increases in dark signal inflicted by raising the operating temperature, in particular, are unlikely to be a price worth paying. Simulations showing whether mobility modelling has an effect on the BFE should, however, be a focus for future work, because they might offer insight into future device design.

- Pixel geometry - In some ways it is a reasonably legitimate argument to say that the BFE is similar in some manner to more traditional "crosstalk" effects which are a concern

mainly in APS imagers [39]: both cause spatial correlations in measured pixel signals, and both are affected by device geometry. Unlike capacitive crosstalk (which is caused by a parasitic capacitive coupling between neighbouring collection and/or readout elements) however, the BFE is caused by the changes in the shape of the collecting fields in response to stored charge, and has a strong signal dependence. The relationship between pixel geometry and capacitive crosstalk is indirect in that the geometry may affect the size of the parasitic capacitance. With the BFE, the geometric effect is direct: the perturbing fields decay with distance from the stored charge, and as such if the collecting elements are placed further apart the pixels will (for the same collecting fields and stored charge amounts) experience less correlated collection. We present comparative experimental and simulation results supporting this theory in Chapter 6.

- Doping - From the point of view of our model (and likely in this case it is a good approximation to reality), changing the doping parameters of the substrate itself only really matter indirectly through the effect on Φ_P, and thus the collection fields. The effect should be identical to changing V_{BS}. If changing mobility has an impact, then there may be a very small secondary effect from doping change, since mobility also depends on doping. We find this highly unlikely, since the substrate is uniformly doped. Changing the doping of the channel has, again, an indirect effect, but a much more important one. The storage depth of the charge does change the magnitude of the BFE - deeper storage depths tend to increase the effect. In our model, an inspection of the form of the series (4.81) shows mathematically the reasoning for this: the closer the stored charge is to its fictitious "image" charges, the less the field lines of its potential spread laterally. We have not covered this effect in detail, chiefly because it has been examined already quite thoroughly in the literature (by Antilogus et al [5]). We do note, however, that their series is constructed from two equipotential planes, as opposed to our conception of a single conducting plane (the back surface) and a single insulating plane (the front surface). The difference in the resulting series is subtle (see Figure 4.11), but we suggest that it may be the reason why the value for the channel depth these authors obtain when finding a fit for their model (they find $z_T = 2.5\,\mu\mathrm{m}$) seems rather high for a realistic CCD device.

- Gate width - The argument about whether changing the collecting gate width (and the channel stop distance) is somewhat more subtle than that for changing the total pixel

pitch. On the one hand, increasing the gate width does increase the volume of the device containing stored charge, in principle making Φ_C a greater contributor to the boundary position. However, increasing gate width also decreases the effective 2D density of charge storage (see (4.2)), which is part of the pre-factor in (4.81). Thus, while the edge of Φ_C would be closer to a position where it could impact the pixel boundary, its overall magnitude would be smaller. Our simulation model shows emphatically that a greater gate width should result in increased boundary shifts, and hence greater dynamic effects (see Section §4.4). There have not been, to the author's knowledge, any studies examining this parameter experimentally, which should be a priority for future work.

4.6 Implementation Details

The dynamic charge simulations are all coded in the C++11 programming language [95], and compiled using the GCC compiler, version 4.8. Object oriented design techniques were used to improve modularity of the software - the classes for performing random walks are completely de-coupled from those for calculating potentials and fields, for instance. During performance testing of the program, it was found that the major bottleneck was the repeated evaluation of certain numerical functions, in particular the arctangent and logarithm. Very large performance enhancements were obtained by manipulating the algebraic forms such that fewer of these expensive operations had to be carried out. For instance, re-writing (4.19) so that the right hand side only contained a single arctangent operation yielded immediately a speed increase of around 20% in some test cases. A similar result was found when considering (4.71). Though in isolation the number of expensive evaluations cannot be reduced, this function is nearly always calculated within the context of the double integral equation (4.78). Expanding all 8 terms algebraically allows for the collection of some arctangent functions. Using the GCC "-ffast-math" option also provided a speed increase, as measured using statistical profiling. A very large optimisation was also discovered when examining the series sum equation (4.81): the identical nature of arithmetic operations performed on translated copies of the co-ordinates in each term was extremely well suited to implementation using Single Instruction Multiple Data (SIMD) processor instructions, supported on many modern processors. Inspection of the compiler-generated assembly code for the function as naively written revealed that the compiler had not performed this optimisation, and manually writing some arithmetic operations using SIMD directives increased the speed of this critical code

path by around 30%. At a value of $\delta t = 5 \times 10^{-12}$ s, the current implementation is able to trace around 100 electron tracks per second using a single core of an AMD FX-6200 processor. Statistical profiling indicates that over 90% of the execution time is still spent evaluating trigonometric and logarithmic functions, so improved interpolation or caching schemes could likely be implemented to great effect.

Special mathematical functions were provided by the GNU Scientific Library (GSL) [35]. In particular, for summing infinite series, extensive use was made of the implementation of the Levin u-transform series acceleration algorithm [67].

The simulation of random walks is a trivially parallelisable algorithm, because it is an entirely data-parallel problem for calculations which do not involve shared state (e.g. finding empty well PSF). We leverage the Message Passing Interface (MPI) implementation provided by the Boost libraries [38] to provide scalability across either multiple processor cores on a single machine, or between a cluster of machines. For the dynamic charge collection simulations, shared state between random walkers is inevitable because the charge storage must be calculated after tracing electrons. In practice, we are still able to achieve a reasonable degree of parallelisation by performing multiple random walks between the re-calculation of charge storage. In practice, running around 10^3 electron trajectories between storage updates seems to have no appreciable effect on the results. The data parallel nature of the algorithm, and the fact that the calculations themselves rely heavily on trigonometric function evaluation imply that implementation of the model on Graphics Processing Unit (GPU) hardware might be very efficacious.

4.7 Summary

The implementation of a physical model of dynamic charge collection in CCDs was described. A solution to Poisson's equation within the CCD was developed which consists of individual components corresponding to the applied gate biases (Φ_H and Φ_B) , the buried channel and bulk doping (Φ_P), the channel stops (Φ_S) and the potential due to stored charge (Φ_C). It was shown that linear summations of these potentials, appropriately translated in space, can be used to construct an array of CCD pixels.

Simulation of charge collection is achieved by coupling the Poisson solution with a stored charge density model and electron trajectory tracing. The model for stored charge was derived and justified based on a simple one-dimensional constant density approach. The tracing of

electron trajectories is achieved through biased random walks based on the drift-diffusion approximation.

We have shown how, using the model, several quantities of interest can be extracted, including the static low signal PSF, the location of the dynamic pixel boundary, and the mean-variance curve of the detector in electron units.

The predictions of these quantities from our model all agree at least qualitatively with both experimental measurements and other numerical simulations described in the literature. We have discussed the evidence from our model and from the literature the likely effect of various operating parameters on the magnitude of the observed correlation effects in imaging sensors.

Chapter 5

Experimental Tests on the e2v CCD261

> I just hope... that you will find someday that, after all, it isn't as horrible as it looks
>
> Richard Feynman

In this chapter, charge collection related experimental tests performed at The Open University on the e2v technologies CCD261 device will be described. The focus is principally on experimental details and brief discussion of results. More detailed evaluation of the data and comparison of the experimental tests with the modelling approach described in Chapter 4 are left to Chapter 6 and Chapter 7.

5.1 Device Details

The CCD261 is a full frame scientific image sensor fabricated on high resistivity bulk silicon. It is available in several thicknesses from 100 μm to 300 μm, and in back-illuminated and front-illuminated variants. The sensor has 4104 rows and 2048 columns in the image area, with an additional 50 pre-scan elements at each end of the serial register, which is split and has two outputs. Both of the outputs were connected, but only one was used for the experiments presented, since the imaging area in one output was observed to have a large number of cosmetic defects. The clocking scheme is three-phase, with the image area being split into two sections which can be parallel clocked separately to facilitate frame transfer operation if needed. A diagram showing the optical format of the CCD261 is shown in Figure 5.1. The pixel size is 15 μm square. Apart from its back-biased construction, the

sensor has several parameters which make operation slightly challenging (see Table 5.1). The responsivity of the output amplifier is very high (values quoted ranging between $7.5\,\mu\mathrm{V}\,(\mathrm{e}^-)^{-1}$ and $10\,\mu\mathrm{V}\,(\mathrm{e}^-)^{-1}$), and this combined with the high full-well capacity means an output range of up to 2.5 V at full-scale, demanding a high input range Analogue to Digital Converter (ADC). Relatively high phase capacitance also presents issues for the drive circuitry to minimise spurious voltage spikes in the clock signals (see Section §5.4.4). The CCD output circuitry is a 2-stage amplifier (diagram in Figure 5.2) with an optional Junction Field Effect Transistor (JFET) buffer which was not used in the experiments described here, and is not shown in Figure 5.2. Of particular note is that the transfer gate clock (used to transfer charge from the image area into the serial register) is internally connected to the signal marked TGA in the output, which resets the second stage output amplifier to correct for any long term drift. It is ergo impossible to manually reset the second stage amplifier without energising the transfer gate. The device is usually supplied with an anti-reflection coating to improve QE but the specific device used in these experiments was uncoated. Indeed, the appearance of the device surface is rather mirror-like (see Figure 5.3). As has been recognised in the literature [40], thick CCDs are inherently prone to collection of large numbers of cosmic rays, and the CCD261 used here proved to be no exception. Figure 5.4 shows a region of the detector exposed in dark conditions for 45s, indicating the high density of cosmic rays. Note that the pixel readout rate of 150 kHz (see Section §5.2.3) implies that to read out the entire device takes around 60 s. Readouts used for most experiments (partial device area) took around 30 s per image. Many cosmic rays therefore arrive during readout as opposed to integration. The observed rate seems still rather high as compared with accepted sea level cosmic ray incidence [45]. It is therefore likely that an additional source of radiation is present, likely the borosilicate glass optical window of the cryostat. These additional "cosmic rays" may be contributing to the long tail peak observed in the read noise spectrum (see section 5.2.4).

5.2 Experimental Setup

5.2.1 Camera Head

The CCD camera head was constructed from a sheet of copper forming a cold bench, with mounting holes drilled appropriately so that the existing mount points of the CCD261 handling jig could be attached. The custom Zero Insertion Force (ZIF) socket which mates to the back of the device was mounted on the pre-amplification headboard, and passed through the cold

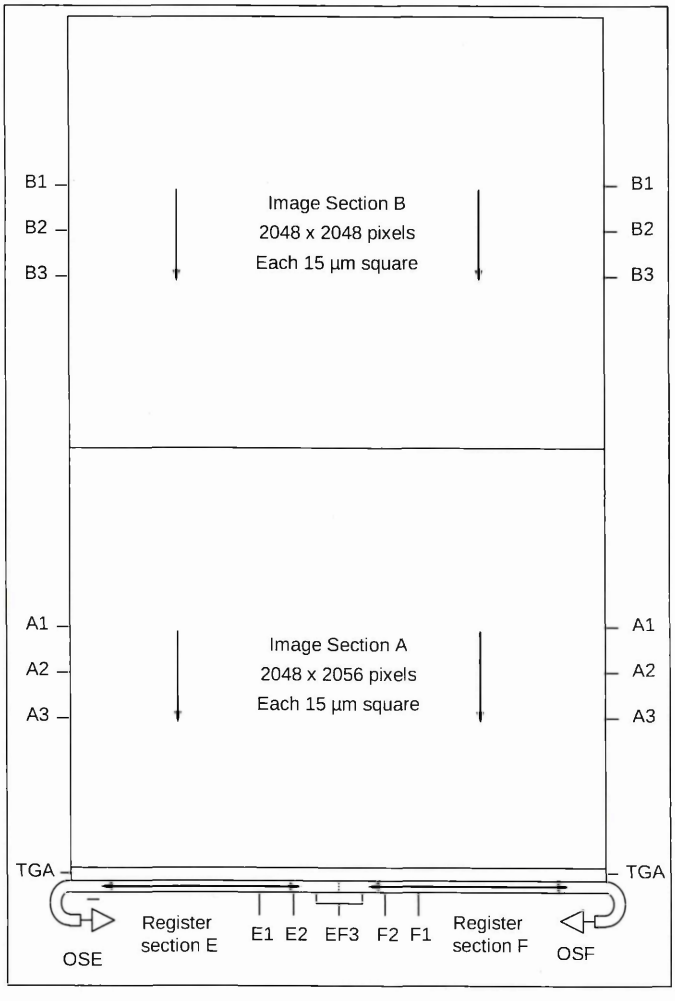

Figure 5.1: Plan layout of the CCD261 (reproduced from e2v data sheet with permission)

Parameter	typical specified value	units
Full well (image section)	230 000	e^-
Full well (register)	500 000	e^-
node capacity	300 000	e^-
output responsivity	7.5-10	$\mu V\,(e^-)^{-1}$
read noise	2.5	e^- r.m.s. (at 100 kHz)
Dark signal (at 153 K)	0.5	$e^-\,pix^{-1}\,s^{-1}$
Inter-phase capacitance	22	nF
Phase-substrate capacitance	10	nF
Electrode series resistance (A)	30	Ω
Electrode series resistance (B)	50	Ω
Pixel pitch	15	μm
Thickness	100	μm

Table 5.1: Selected relevant specified performance parameters for CCD261.

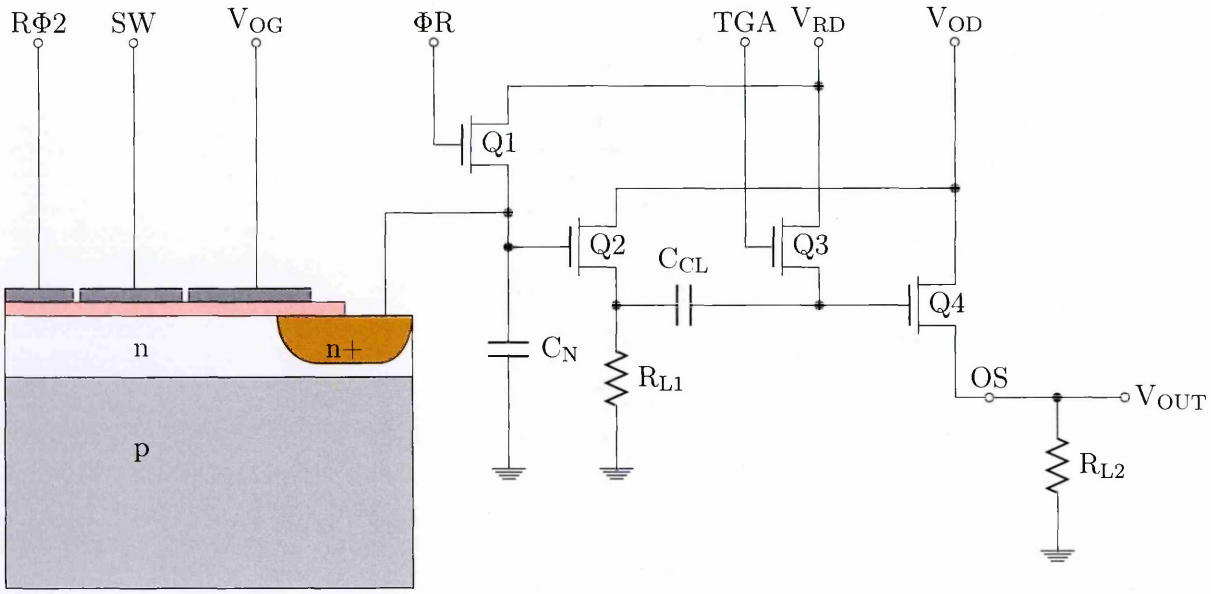

Figure 5.2: 2-stage CCD output circuit. The capacitor C_N represents the sense node capacitance. The components Q1, Q2, Q3, Q4, C_{CL} and R_{L1} all reside on chip. The second stage load R_{L2} is part of the external readout circuitry.

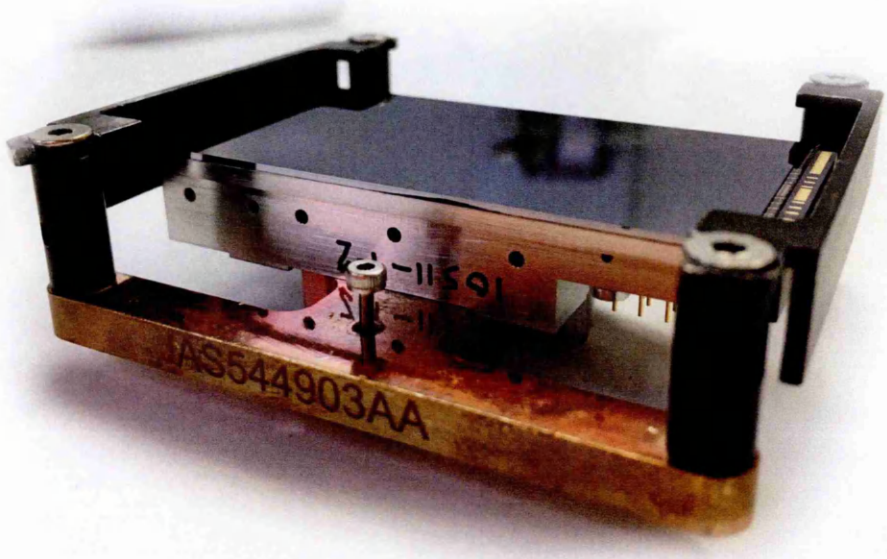

Figure 5.3: Photograph of uncoated CCD261 device

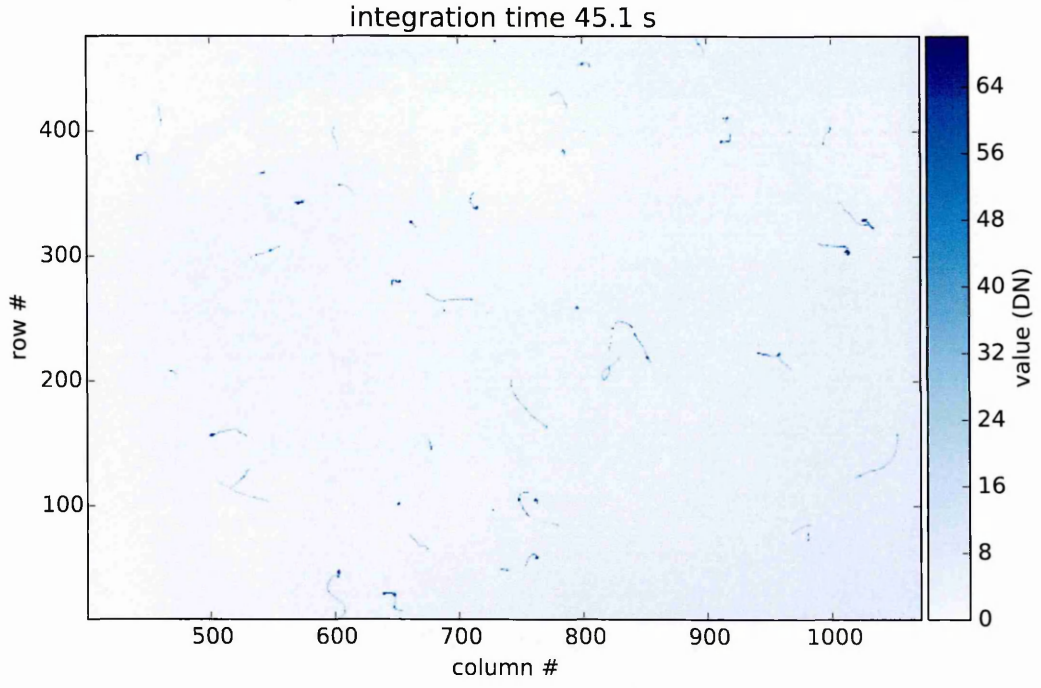

Figure 5.4: 45 second integration time dark frame showing cosmic rays

bench by means of a cut out area. Both the cold bench and the headboard were attached on to 110 mm spaced ⌀M4 studding using nylon spacers and aluminium machine nuts. The studding in turn was threaded into the vacuum chamber flange. The video output signals (carried on co-axial cable), the bundle of clock signals and bias levels, and the sense connections for the Platinum Resistance Thermometer (PRT) penetrated the flange through separate panel mount Fischer connectors. Figure 5.5 depicts a photograph of the assembled camera head, ready for insertion into the vacuum chamber. Throughout the experiment, the chamber was held at a pressure of 1.2×10^{-6} bar.

5.2.2 Headboard

The CCD261 headboard was designed around the Analog Devices AD829 high speed video op amp [24] for pre-amplification. The headboard also provides low-pass filtering on bias lines, serial resistors for termination matching on the clocking lines, and the CCD output load resistors. The schematic for the headboard is shown in Figure 5.6 and Figure 5.7. The op amp compensation capacitor (labelled C30 in Figure 5.7) and feedback load capacitor (labelled C31 in Figure 5.7) are chosen such that the bandwidth of the circuit is 71 MHz, with a slew rate of 38 V μs^{-1} (values are chosen using a selection table in the AD829 datasheet [24,

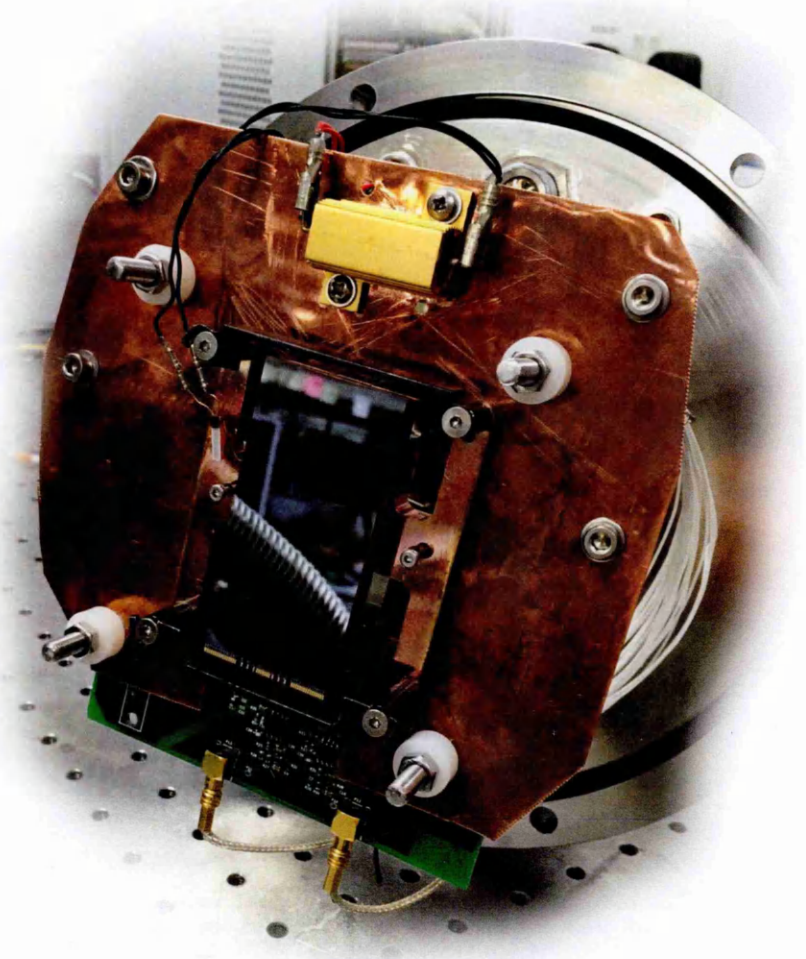

Figure 5.5: CCD261 camera head assembly

Table 4]). The feedback resistors set the gain to 2 (the high output sensitivity of the CCD261 means that only a small amount of amplification is required to match the full well input scale of the ADC). Board artwork for the headboard is shown in Figure 5.8. The headboard was manufactured on 4-layer FR4 circuit board, and features isolated ground planes separating the sensitive analog signal ground from the power ground which experiences transient currents due to high speed clock switching. The ZIF socket which interfaces with the pins of the CCD package is a custom part made by Tactic Electronics [2]. Bias and clock connections arrive to the board via a high density D-sub connector, and the co-axial output signals leave via right angle board mount Micro Co-Axial (MCX) connectors. Surface Mount Device (SMD) passive components were used throughout, taking care that those parts subjected to high voltage differences (chiefly filtering on the V_{BS} bias path) were selected to be suitable for high voltage operation.

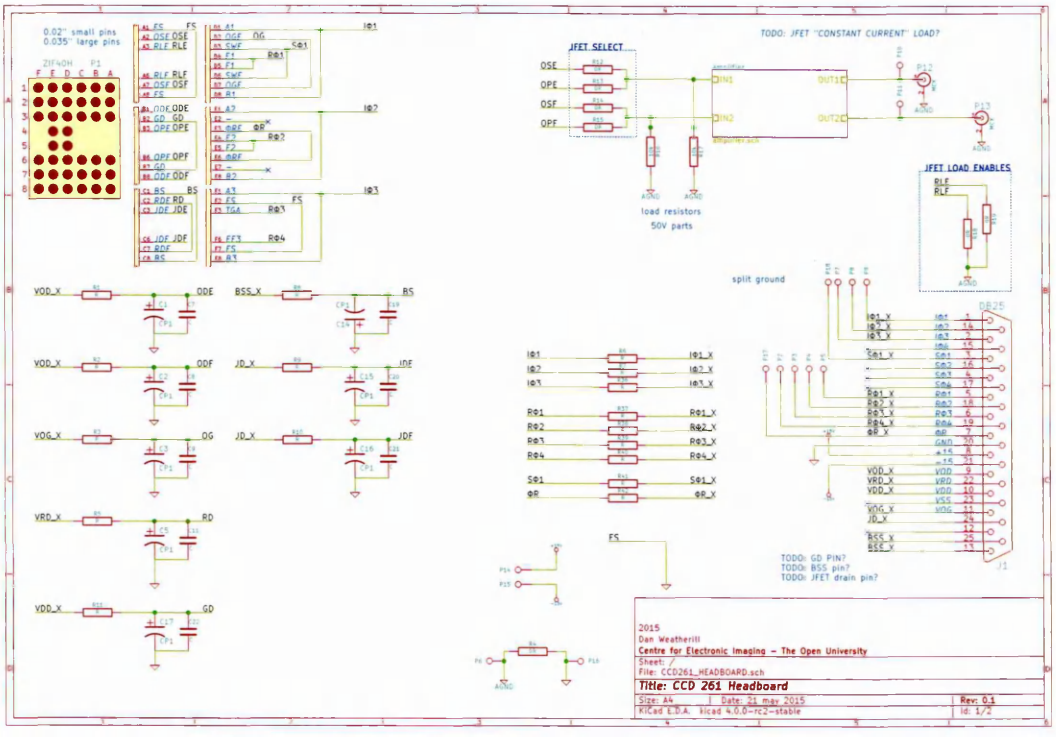

Figure 5.6: Schematic of the CCD261 headboard (overview)

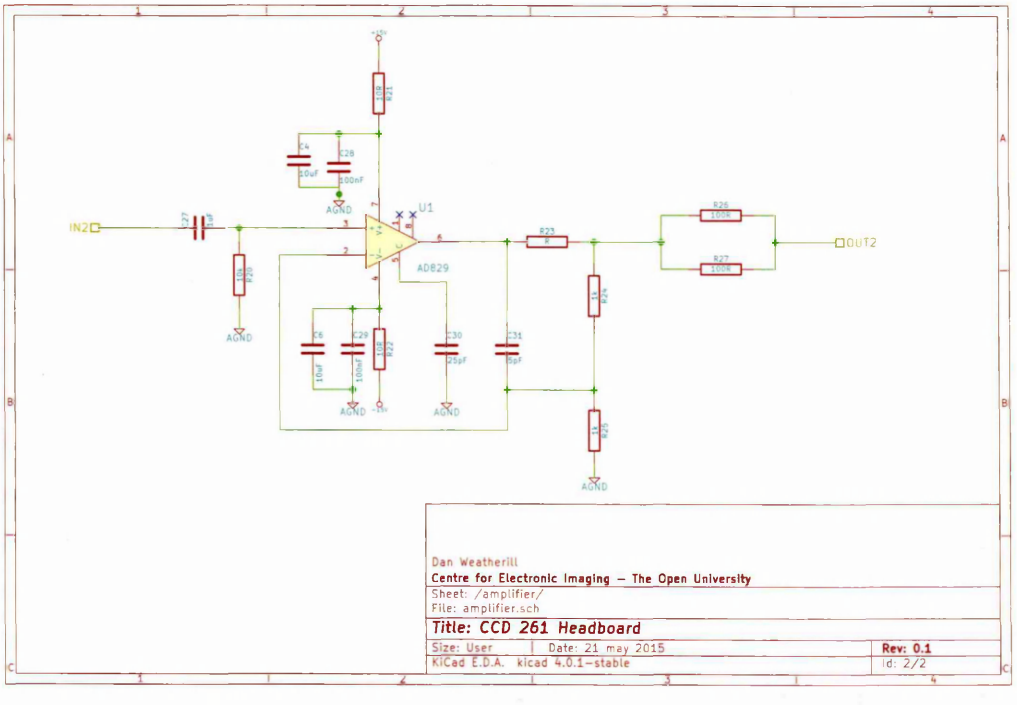

Figure 5.7: Schematic of the CCD261 headboard (pre amplifiers)

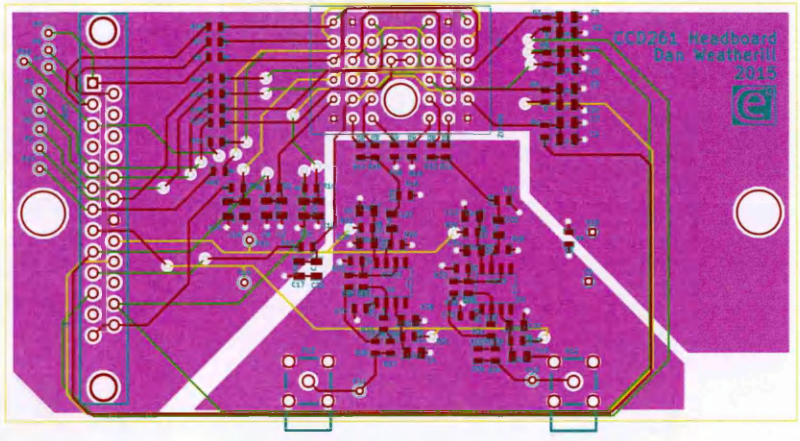

Figure 5.8: PCB artwork for the CCD261 headboard

5.2.3 CDS and Digitization

Drive signals and data conversion for the CCD were provided by an XCAM USB2REM camera unit. The system provides CDS functionality, specifically in the form of a Dual Slope Integrator (DSI) circuit. A basic schematic for implementing this type of CDS is shown in Figure 5.9. During the CCD reset feed-through, the CLAMP and RESET switches are closed, which forces both the voltage after the capacitor C_{IN} and the output voltage V_{OUT} to ground. CLAMP and RESET are then released, at which point amplifier U3 begins acting as an integrator. The switch INT_+ is then closed during the CCD reset period, such that the noise on the reset level is averaged by U3. After an integrating period τ_{int}, INT_+ is then opened, and the register is clocked forward, so that the pixel output signal reaches the output. Switch INT_- is then closed, routing the signal through inverting amplifier U2 for the duration of the integrating period. After INT_- is opened, the signal at V_{OUT} is the difference between the reset and output levels. All CDS circuits cancel correlated white noise sources common to both reset and signal periods, with the DSI circuit having the advantage over simpler CDS implementations that uncorrelated white noise is also strongly attenuated, with the cancellation increasing as τ_{int} increases. As mentioned in Section §3.6.1, all electrical systems are subject also to $\frac{1}{f}$ ("flicker") noise, which becomes the dominant noise source below a certain frequency, f_c. The CDS circuit is unable to cancel flicker noise, (but can suppress it to some degree [93]) and as such below f_c, there are diminishing returns from further increasing τ_{int}. A more detailed description of the operation of the DSI circuit is given in [54, 6.5]. The CDS timing signals and CCD output as measured from an oscilloscope trace for the experimental system are shown in Figure 5.10.

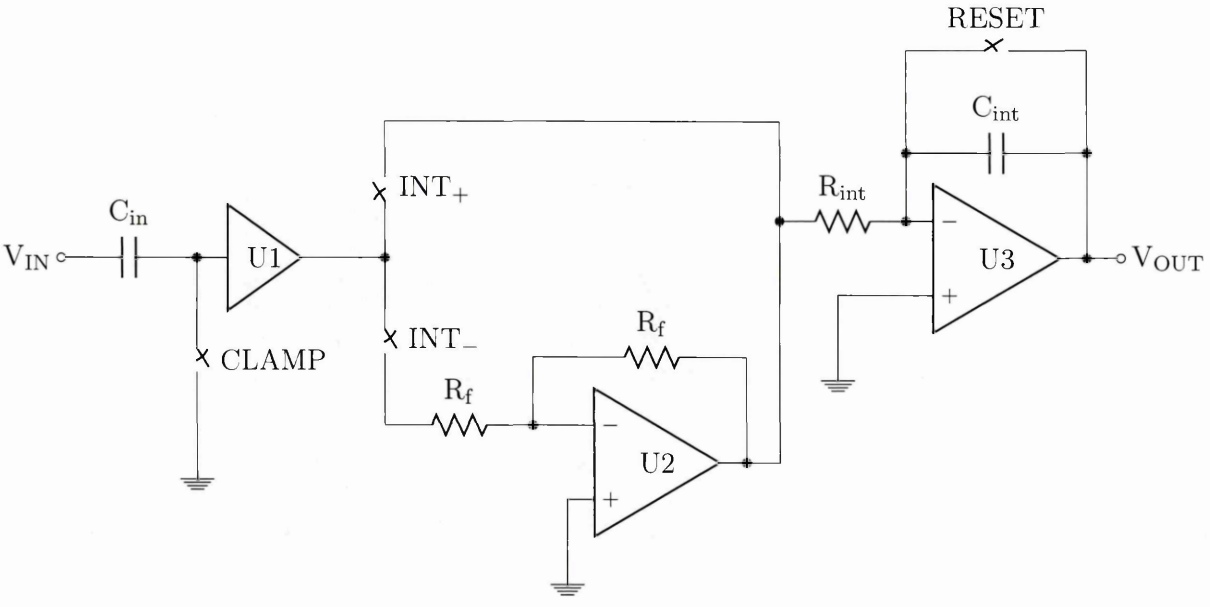

Figure 5.9: Dual Slope Integrator circuit schematic

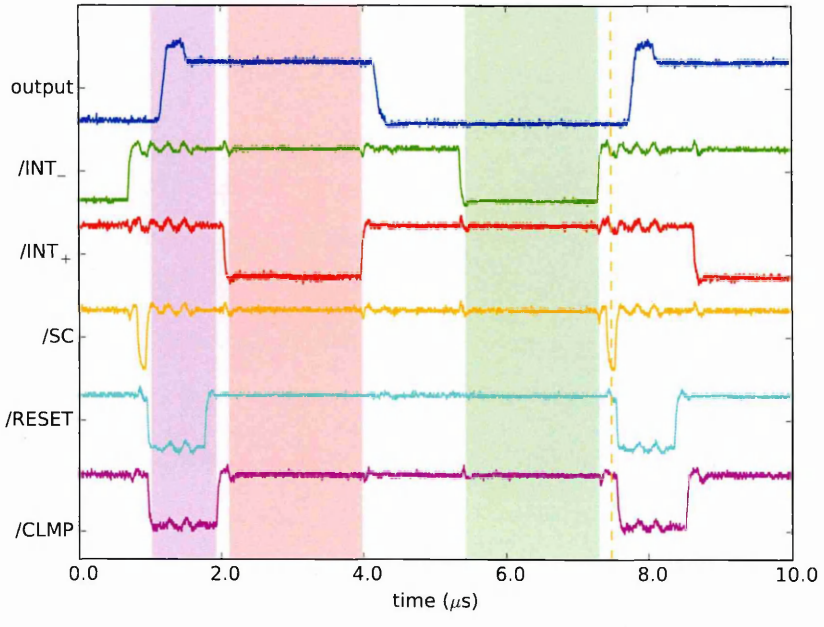

Figure 5.10: Measured output waveform and CDS signals. The reset and signal integration periods are shaded in red and green, respectively. The CDS reset period is shaded in purple, and the ADC conversion strobe time is indicated by the dashed orange line.

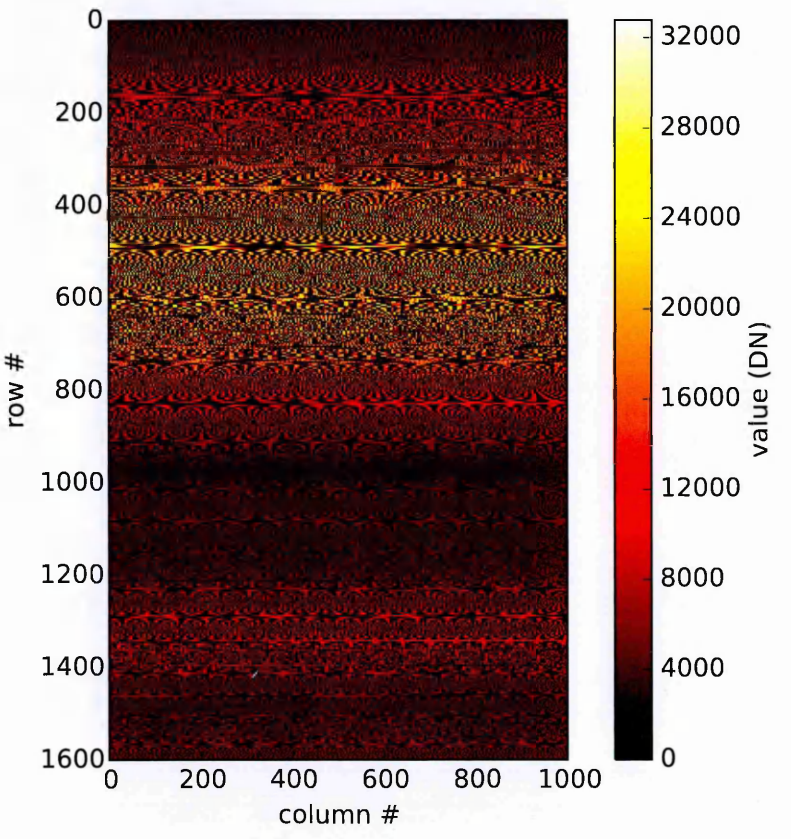

Figure 5.11: Example of frequency chirp image used to measure the CDS transfer function.

Theoretically, the frequency response of the DSI circuit is given by:

$$|H_{\mathrm{DSI}}(f)|^2 = \frac{4\sin^4(\pi f \tau_{\mathrm{int}})}{(\pi f \tau_{\mathrm{int}})^2} \tag{5.1}$$

which can also be shown to be a matched filter for a CCD output signal with only white noise [93]. A basic test was performed to compare the true transfer function of the XCAM electronics to $|H(f)|^2$. A signal generator (Rigol model DG1022U) was set to output a geometric chirped sine wave, the frequency sweeping logarithmically from 50kHz to 7MHz over a period of 21s, with the start of the frequency sweep synchronised to the beginning of the XCAM electronics readout sequence. The readout sequence was setup to perform only CDS operations with minimum delay between readouts (i.e. there were no clocking signals included). The amplitude was adjusted to provide a large signal after digital conversion. An example of an image obtained from this process is shown in Figure 5.11. Such images were obtained for several values of τ_{int}. The images were processed by taking the difference between the maximum and minimum of each row. Though the frequency of the sine wave

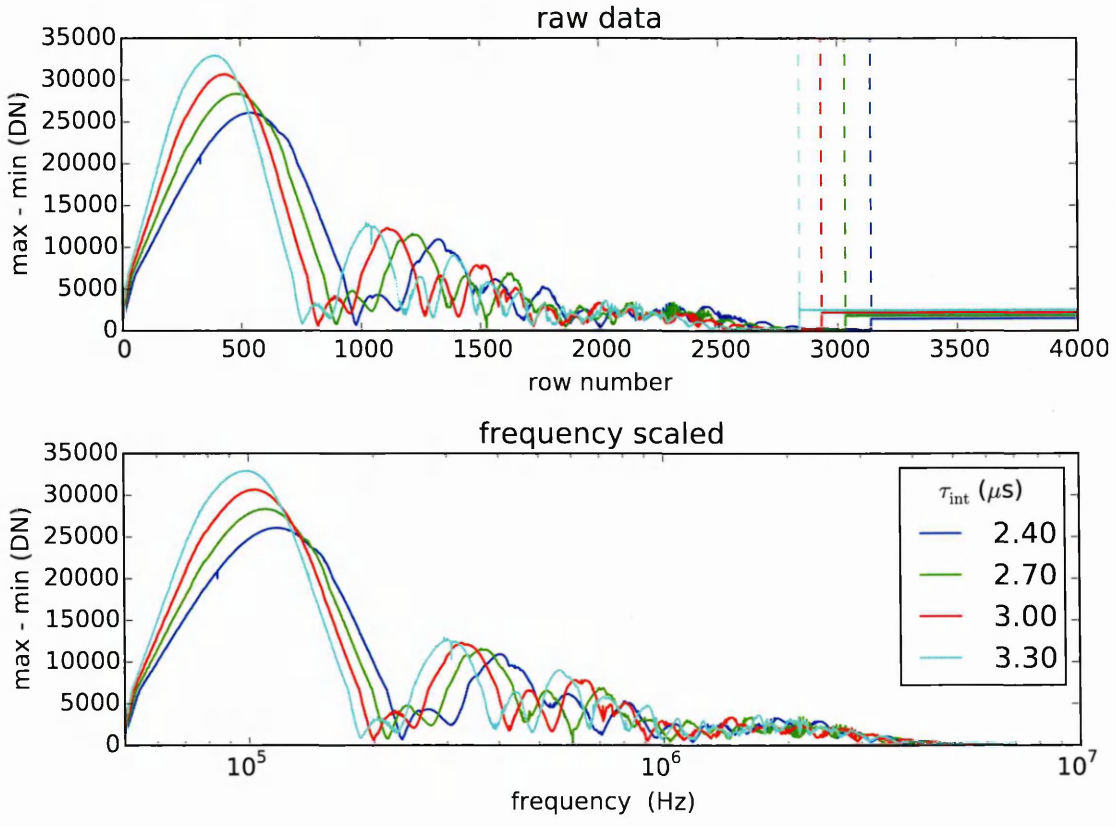

Figure 5.12: CDS Transfer function measurement for different integration times. The raw data (upper panel) is scaled to frequency (lower panel) by identifying the end points of the frequency sweep (shown as dashed lines)

was changing during each row, the effect of this processing is to obtain an estimate of the relative response at a frequency of an average value within the row. Since the total real time duration of the readout sequence changes with τ_{int}, the resulting data must be scaled to real frequencies separately for each image. At the end of each chirp, the signal generator returns abruptly to outputting a constant frequency sine wave, and this point is easily identifiable in the processed data (see dashed lines in the upper panel of Figure 5.12), allowing re-scaling of the data to absolute frequencies (see lower panel of Figure 5.12). Comparison of $|H_{DSI}|^2$ to the measured transfer function after normalization of both (see Figure 5.13) shows reasonably good agreement with the main peak, with lower response at low frequencies likely due to the input clamp acting as a high pass filter. The overall envelope at high frequencies shows an extra "bump" in response around 2MHz, whose cause is not known. There are also several extra peaks evident in the measured response which are not in locations near those in $|H_{\text{CDS}}|^2$. The positions of the principal minima in the measured transfer functions are close but not identical to those predicted by $|H_{\text{CDS}}|^2$. This could be due to timing delay introduced by the analog switching circuitry in the DSI circuit.

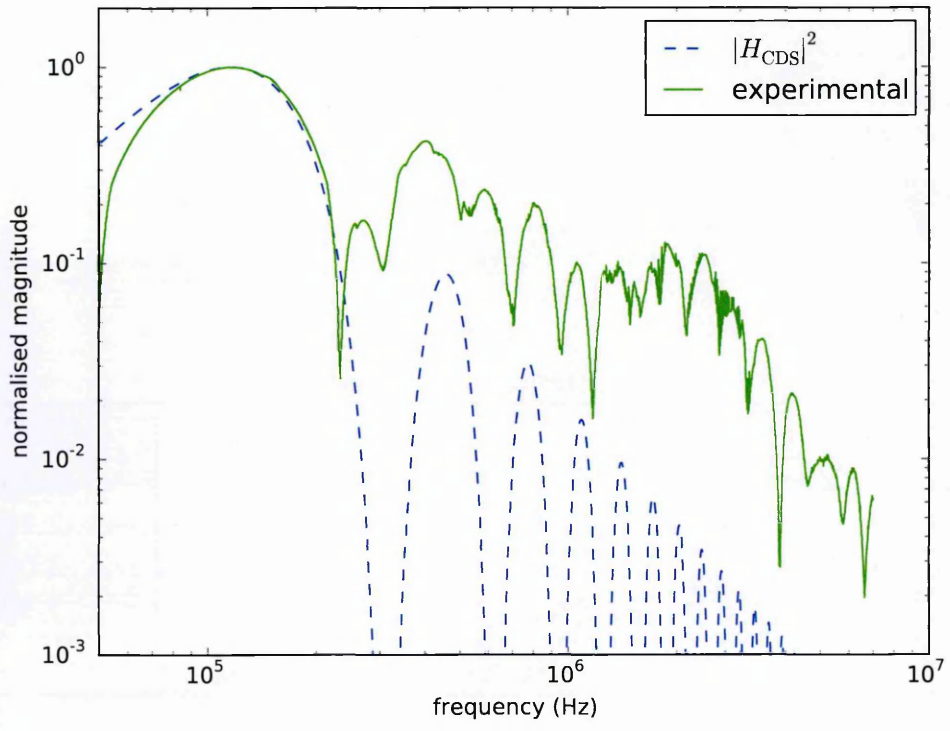

Figure 5.13: Comparison of measured and theoretical CDS transfer functions for $\tau_{\mathrm{int}} = 2.40\,\mu$s

5.2.4 Read Noise

The read noise of the device was measured using the signal variance of the clock over-scan regions. In general, it would be preferable to measure read noise using either the low signal part of a PTC, or using bias frames taken at zero integration time. Without changing the gain of the CDS circuit, the first method was unavailable in this work due to the very high output sensitivity of the CCD261 (as can be seen from e.g. Figure 5.28, even at very low mean signal values, the shot noise regimen has already been reached). Stray light issues and instabilities in the XCAM electronics sequencing at zero integration time caused issues with the second method in the CCD261 experiments, though this is the method which we use to determine the read noise of the CCD250 (see Section §6.3). Given that a large number of frames - in total, 862 suitable images - were taken to construct the analysis for flat-field photon transfer (see Section §5.6), a reasonable estimate of read noise can still be made using the overscan regions of these images. After gain calibration for each PTC, the standard deviation of the over-scan values of the two raw (non differenced) images were collected. Multiplying this number by the camera gain K_G gives an estimate of the read noise in e^- rms Equivalent Noise Charge (ENC). Images which were clearly above full well illumination (where the

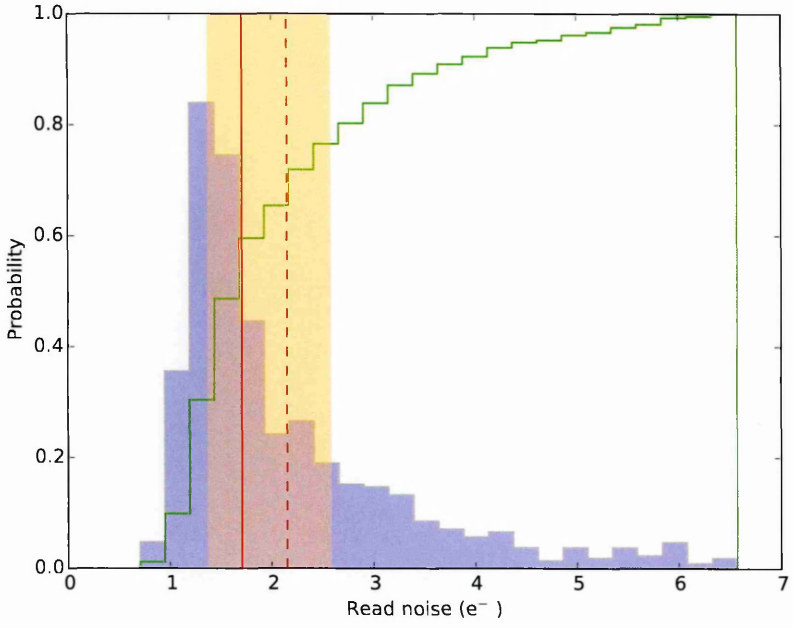

Figure 5.14: Read noise measurement histogram for the CCD261. The green line shows the cumulative histogram, the orange shaded region the inter-quartile range of measurements, the solid red line the median, and the dashed red line the mean value.

collected signal charge generally "spills" beyond the array into the overscan) were discarded. The distribution of these individual read noise measurements can be used to make a fairly sound estimate of the true read noise. The results are shown in Figure 5.14. The distribution of measured read noise values shows a long tail to high values, but the modal value is around $\sigma_r = 1.3\,\mathrm{e}^-$, lower than the data sheet specified value of $\sigma_r = 2.5\,\mathrm{e}^-$ rms (see Table 5.1). Taking instead the mean value, and using the standard error of the measurements as an error estimate, we find that $\sigma_r = (2.15 \pm 0.01)\ \mathrm{e}^-$, still comparable with the data sheet specified read noise. No de-glitching procedure to eliminate cosmic rays was applied to the read noise measurement data, so cosmic rays may contribute a significant fraction of the high measured values.

5.2.5 Temperature Control and Cooling

The CCD camera head is actively cooled using a Brooks Polycold Compact Cooler: a closed loop gas mix compressor-based cryo system. This system provides around 20 W of cooling power operating at 153 K [8]. Inside the vacuum chamber, the cold head is connected via 4 flexible metal braids to a cold bench consisting of a copper plate, to which the CCD package attaches. The plate is designed to mount the CCD including its copper handling jig, which

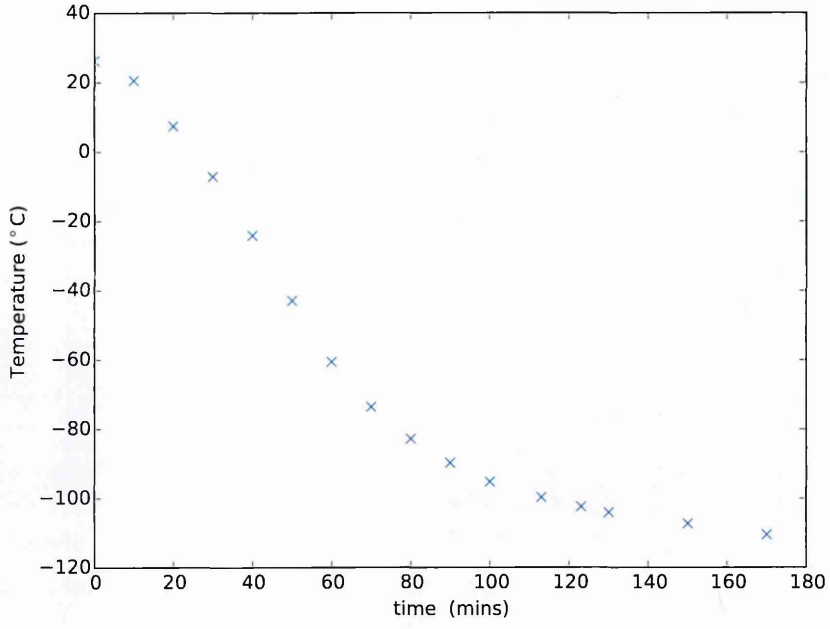

Figure 5.15: Cooling curve of experimental setup after cryo cooler activation

minimizes handling risk. A plate of TUFNOL 10G epoxy laminate material [18] is mounted behind the cold bench, and nylon spacers are inserted into the mounting holes for the main mechanical connections to the vacuum chamber studding. These measures help to reduce the thermal load on the cooling system.

Temperature at the sensor is monitored by a PT1000 PRT attached directly to the CCD handling jig. The temperature at the PRT T is related to the resistance R using the ITS-90 linearisation equation [14]:

$$R = R_0 \left(1 + \kappa_A T + \kappa_B T^2 + \kappa_C \left(T - 100\,^\circ\mathrm{C}\right) T^3\right) \tag{5.2}$$

where the values of the constants R_0 and κ_i are given in Table 5.2. To calculate temperature from resistance, a measured value for R is substituted into equation (5.2), and the real root of the resulting quartic equation is found numerically. The experiment reaches a usable temperature of 158 K approximately 3 hours after turning on the cryo system, as shown in Figure 5.15. After 6 hours of operation, the temperature was found to be 153 K, which remained stable to ± 1 K (according to occasional checks) for the duration of the experiment.

constant	value	units
κ_A	3.85×10^{-3}	$(°C)^{-1}$
κ_B	-5.775×10^{-7}	$(°C)^{-2}$
κ_C	$\begin{cases} -4.183 \times 10^{-12} & T < 0\,°C \\ 0 & T > 0\,°C \end{cases}$	$(°C)^{-3}$
R_0	1.000	$k\Omega$

Table 5.2: PT1000 calibration constants

colour	specified λ (nm)	measured λ (nm)	specified $\Delta\lambda$ (nm)	measured $\Delta\lambda$ (nm)
red	650	655 ± 2	28	22 ± 4
green	525	522 ± 2	30	40 ± 4
blue	470	470 ± 2	25	34 ± 4

Table 5.3: Measured LED wavelengths and line widths

5.2.6 Light Source

For both flat field and point source illumination, 5mm tricolour common cathode LED light sources were used, emitting specified peak wavelengths of $\lambda_r = 650\,\text{nm}$, $\lambda_g = 525\,\text{nm}$, $\lambda_b = 470\,\text{nm}$ with FWHM line widths of $\Delta\lambda_r = 28\,\text{nm}$, $\Delta\lambda_g = 30\,\text{nm}$ and $\Delta\lambda_b = 25\,\text{nm}$. A simple hand-held spectrometer was used to check these values for the actual LED being used for flat field illumination, the results being given in Table 5.3. The central wavelengths were found to agree quite well with specified values, but the FWHM line widths for green and blue illumination were not consistent with the specified values. The blue LED also exhibited significantly higher brightness than either the green or red, though the sensor used in the spectrograph is uncalibrated, so quantitative results for this are not possible. The flat field LED was mounted in a holder attached to a short lens tube enclosure, at the other end of which was mounted an engineered diffuser. The point source LED was directed into a small integrating sphere whose interior was coated with Barium Sulphate, and the output port of which was directed into a lens tube. A 5 μm diameter pinhole was positioned in the lens tube, followed by an achromatic doublet lens. Both lens tubes were attached to the breadboard platform of a 3-axis moveable positioning stage within a large dark enclosure. A black plastic baffle was installed around the mouth of the lens tubes in an attempt to reduce spurious stray light. Between the dark enclosure and the sensor vacuum chamber window a ⌀72 mm IR and UV cut filter was installed. Unfortunately, the interferometer used within the positioning stages introduces a significant amount of stray IR emission, which along with imperfections in the dark enclosure, was a limiting factor in some experiments and was not completely eliminated by the filter.

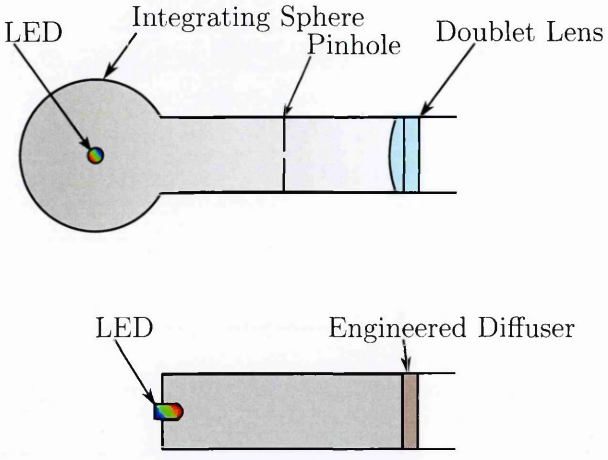

Figure 5.16: Schematic diagrams of point source (above) and flat field (below) light sources

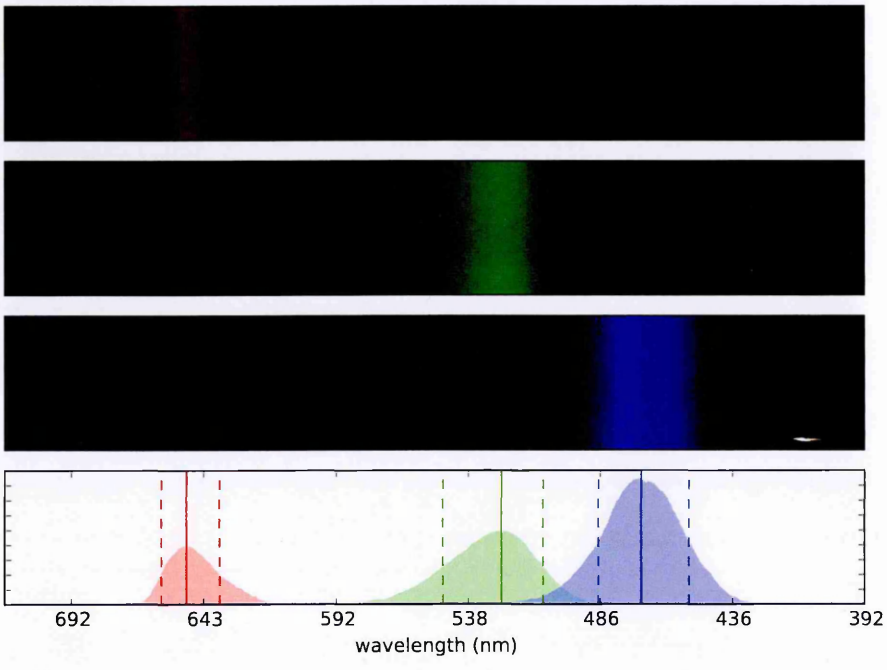

Figure 5.17: Measured spectrograms of the LED light sources

The readout sequencing program running on the Digital Signal Processor (DSP) chip of the XCAM readout electronics has access to a General Purpose Input/Output (GPIO) line which is used to synchronise the activation of the light source. A small microcontroller-controlled circuit[1] was constructed to allow for multiple outputs and DSP brightness to be selected by the computer. The analog part of this circuit is shown schematically in Figure 5.18. The microcontroller was connected to the SYNC signal and the signals CR, CG and CB using GPIO pins, and it provided an analog output from its 10-bit Digital to Analogue Converter (DAC) which is buffered to provide the reference voltage to a current mirror. The experimental computer is interfaced to this microcontroller via a Universal Serial Bus (USB) connection.

[1]The specific chip used was an NXP LPC1768

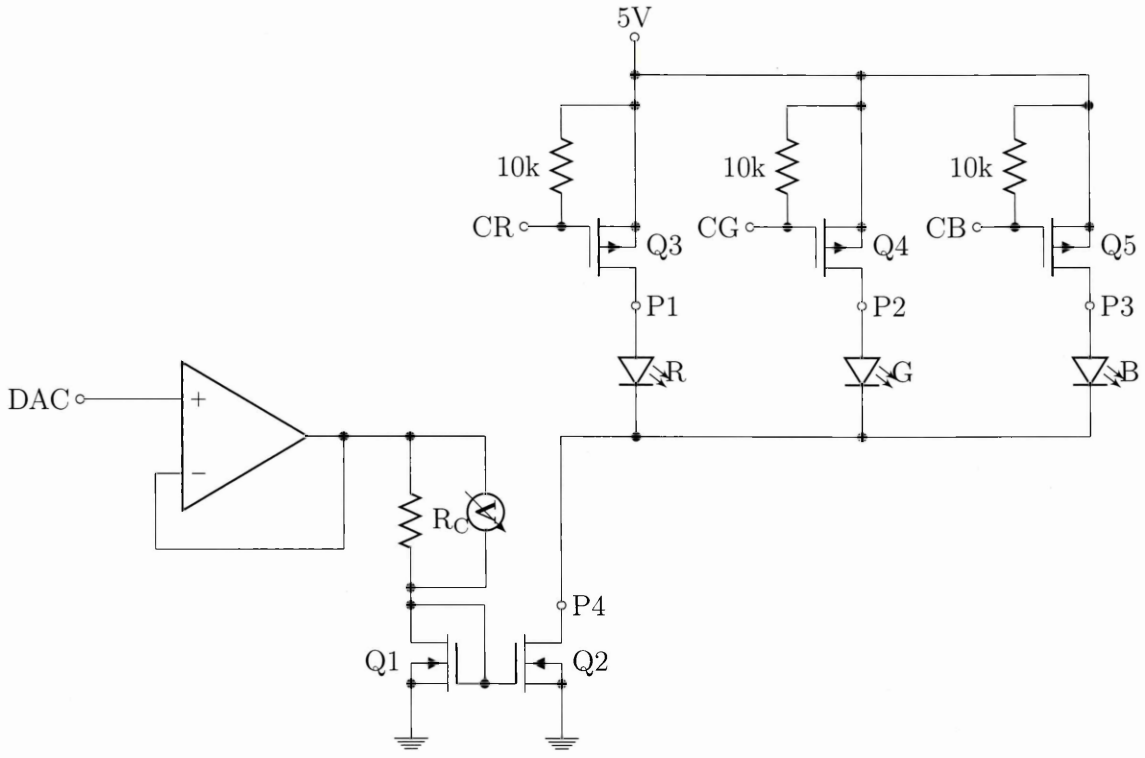

Figure 5.18: LED Drive circuit

The computer can then select an active output and choose an LED current. In this way, experiments using different illumination levels and wavelengths can be automated. The delay between the SYNC signal and the microcontroller processing an interrupt and activating the selected output line was measured as a consistent 1 μs, which is negligible compared to the integration times used in experiments (typically varying between 200 ms and 60 s).

5.2.7 Software and Control

To the greatest extent possible, all parts of the experiment were set up to be automated from the Python programming language. To this end, a wrapper library was written for the shared library provided with the XCAM camera electronics. As described already (see Section §5.2.6), the LED light source was connected to the same computer using a Universal Asychronous Receive / Transmit (UART) over USB connection, easily accessible from the Python environment after a small library was written for convenience. The Newport XPS series motion controller connects to the computer via a standard Internet Protocol (IP) network, and exposes a well documented Application Programming Interface (API) over Hyper Text Transfer Protocol (HTTP) to control and report on all operations. Interoperation with Python was therefore also very simple. Unfortunately, a remotely programmable high voltage power supply to provide the bias voltage V_{BS} was unavailable, so this voltage had to be set

manually. More detailed characterisation of most of the effects investigated here could be obtained if this part of the experiment were also amenable to automation.

A small set of components were written to perform the various types of experiments, organised in an object oriented fashion so that different experimental procedures could be constructed using reusable modules. All data was saved using the Flexible Image Transport System (FITS) format, with the header of the file containing all relevant meta data about the experimental state, including all bias voltages and timings. The ADC of the XCAM electronics has a 16-bit resolution, but due to the fact that the FITS format does not natively support unsigned 16-bit data, the standard convention of storing the data as 16-bit signed, and setting the FITS header parameters BSCALE=1 and BZERO=32768 was used.

5.3 Optical System Optimisation

5.3.1 Spot Focussing

In attempting to measure the PSF or any other properties related to point source illumination, it is crucial that the point source be well focussed. Focussing is therefore the first optimisation performed when setting up the optical system for point source illumination. Due to chromatic aberration, for any given lens, the focal point varies with wavelength. Focussing must therefore be performed separately for each colour of light, and the translation stage must be repositioned every time the incident wavelength is changed. This requirement is the principal reason why the power to the translation stages was not removed after focussing while performing each subsequent experiment, even though doing so would have eliminated the IR emissions observed during initial commissioning of the system (see Section §5.2.6). Keeping the stages powered during experimentation allowed for a much greater degree of automation in the data collection.

In the discussion that follows, the co-ordinate system used is referenced to that we have previously used throughout to describe the detector geometry (the x axis being along the parallel transfer direction, the y axis being the serial transfer direction, and the z axis being a normal to the detector plane), and with the CCD being mounted with its longest dimension vertical such that the readout register was horizontally situated, the "horizontal" direction along the laboratory bench is actually the y axis, and the vertical direction normal to the bench is the x axis. The position of the origin is arbitrary, though was chosen to be quite near the serial register, which allowed most experiments to be performed whilst reading out only several hundred rows of the sensor, giving prompt readout speeds even at the comparatively

low pixel rate employed.

After manually finding a rough position where a spot was visible in the image output for each wavelength, the translation stage Z position was systematically scanned through an appropriate range for each wavelength, and a spot image with 10s integration time was recorded at each step. Each row was over-scanned by 26 elements, the first step in the processing of every image being the row-wise subtraction of the median of the overscan pixels. A square Region Of Interest (ROI) 10 pixels on a side was selected to include the projected spot, and the median value was subtracted column-wise in an attempt to remove dark current baseline and spurious flat field illumination sources. For each spot image I, the image moments M_{ij} defined by [72] :

$$M_{ij}(I) = \sum_x \sum_y I(x,y)\, x^i y^j \tag{5.3}$$

were computed. An estimate of the centroid position of the spot $(\bar{x}, \bar{y})$is then given by:

$$\bar{x} = \frac{M_{10}}{M_{00}} \qquad \bar{y} = \frac{M_{01}}{M_{00}} \tag{5.4}$$

and the spread of the spot in both directions is characterised by the covariance matrix $\mathbf{s}$ defined by:

$$\mathbf{s} = \begin{bmatrix} \sigma_{xx}^2 & \sigma_{xy}^2 \\ \sigma_{xy}^2 & \sigma_{yy}^2 \end{bmatrix} \tag{5.5}$$

$$\sigma_{xx}^2 = \frac{M_{20}}{M_{00}} - \bar{x}^2 \tag{5.6}$$

$$\sigma_{yy}^2 = \frac{M_{02}}{M_{00}} - \bar{y}^2 \tag{5.7}$$

$$\sigma_{xy}^2 = \frac{M_{11}}{M_{00}} - \bar{x}\bar{y}. \tag{5.8}$$

The results are shown in Figure 5.19. It is not completely clear why the differences in focus position for the various wavelengths are so large. Possible contributing factors include chromatic aberration in the doublet lenses, misalignment of the optical system leading to non co-planarity of the projection source and detector, and wavelength dependent effects in the cryostat viewport. The first encouraging sign is that the values of σ_{xy} are near zero throughout, so there is comparatively little covariance between the perpendicular directions, or equivalently stated: the eigenvectors of $\mathbf{s}$ are roughly equal to $\mathbf{e_1} = \begin{pmatrix} 1 \\ 0 \end{pmatrix}$ and $\mathbf{e_2} =$

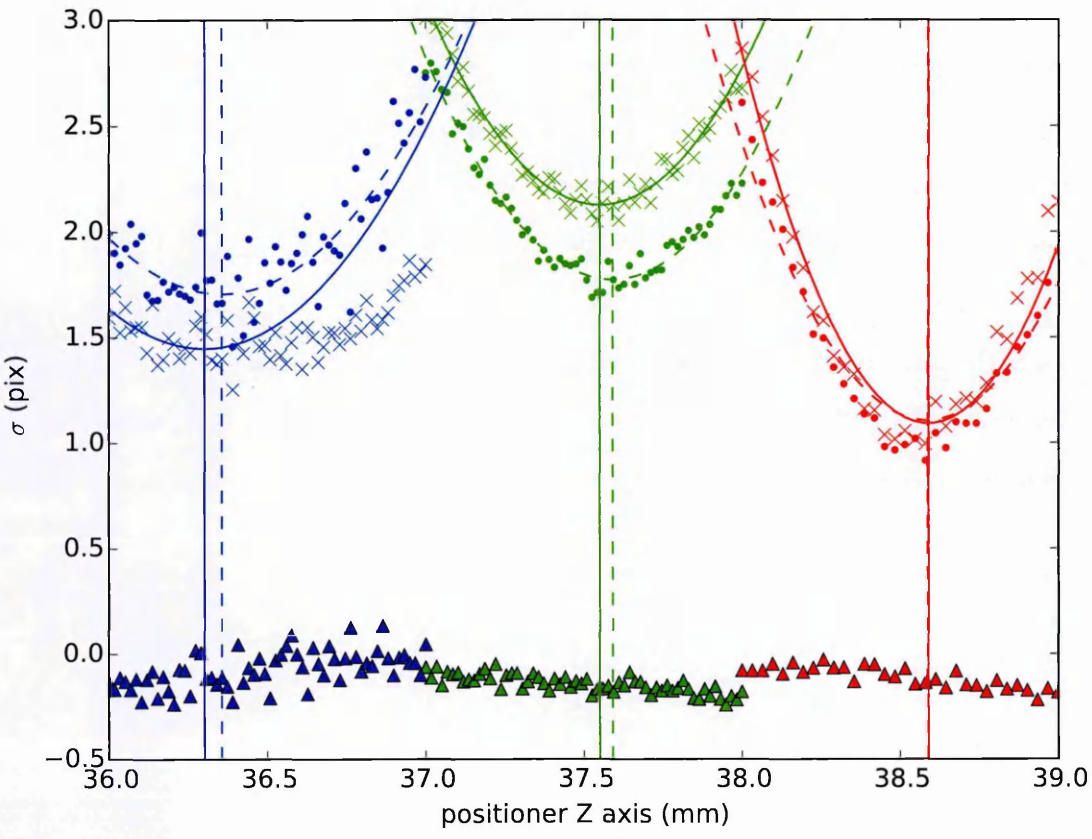

Figure 5.19: Focussing point sources using image moments. Dots show horizontal measurement (σ_y), crosses show vertical measurement (σ_x), triangles show σ_{xy} . Continuous lines show quadratic fits, vertical lines show located focus positions. Colours indicate illumination wavelengths (see Table 5.3).

Light Colour	Horizontal optimum (mm)	vertical optimum(mm)	chosen value (mm)
red	38.512 ± 0.009	38.51 ± 0.01	38.51
green	37.550 ± 0.001	37.591 ± 0.002	37.55
blue	36.35 ± 0.07	36.30 ± 0.02	36.32

Table 5.4: Positioning stage focus points

$\begin{pmatrix} 0 \\ 1 \end{pmatrix}$. This indicates that the rotational symmetry of the light source is quite good, and that correlation introduced in diagonal directions is low. The focus point for each wavelength was obtained by fitting a quadratic to each dataset and finding its turning point. The results of this process are summarised in Table 5.4, along with the chosen value used for the remainder of the experiments. The error estimates in these results are calculated from the covariance of the quadratic fit. The optimum focus points found to minimize spread in both x and y directions agree to within error for both blue and red illumination, but differ for green. In this case, a value which minimises the vertical spread was chosen. Of interest also at this

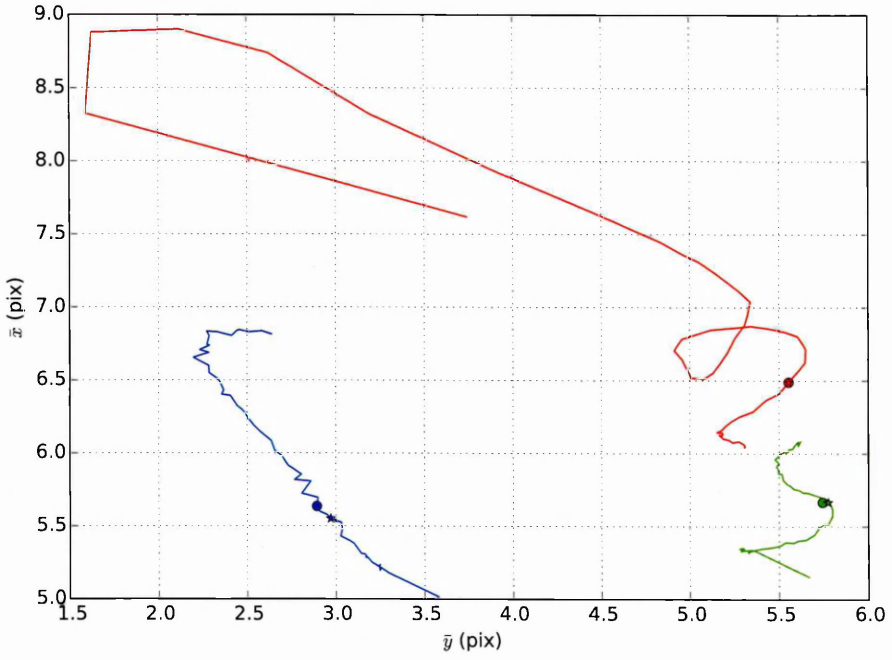

Figure 5.20: Movement of spot centroids during focussing. Spots indicate location of best horizontal focus, stars indicate location of best vertical focus. Colours indicate illumination wavelength (see Table 5.3).

stage is the fact that the blue and green spots are significantly more anisotropic than the red, as should be expected if the brighter-fatter effect is in operation. However, the anisotropy is in the opposite direction for the blue illumination ($\sigma_y > \sigma_x$) than for the green illumination ($\sigma_x > \sigma_y$). A possible explanation for this effect is the differing centroid positions at the focus point. As the positioning stage is moved through the z axis, the spread of the spots change, but also the centroid position. The movement of centroid positions throughout the focussing experiment is shown in Figure 5.20. At the optimum focus, the centroid for the blue spot is near a pixel centre in the y direction, but near a pixel boundary in the x direction. The green spot focus happened to be closer to pixel centres in both directions. Spots near pixel boundaries appear over two pixels, even for low spreads. This effect is corrected for by using a chosen (x, y) position near the centre of a pixel for the remaining experiments, and by applying more sensitive methods (such as Gaussian fitting) for relevant experiments (see Section §5.3.3). Examples of spots in optimal focus obtained during this experiment are shown in Figure 5.21.

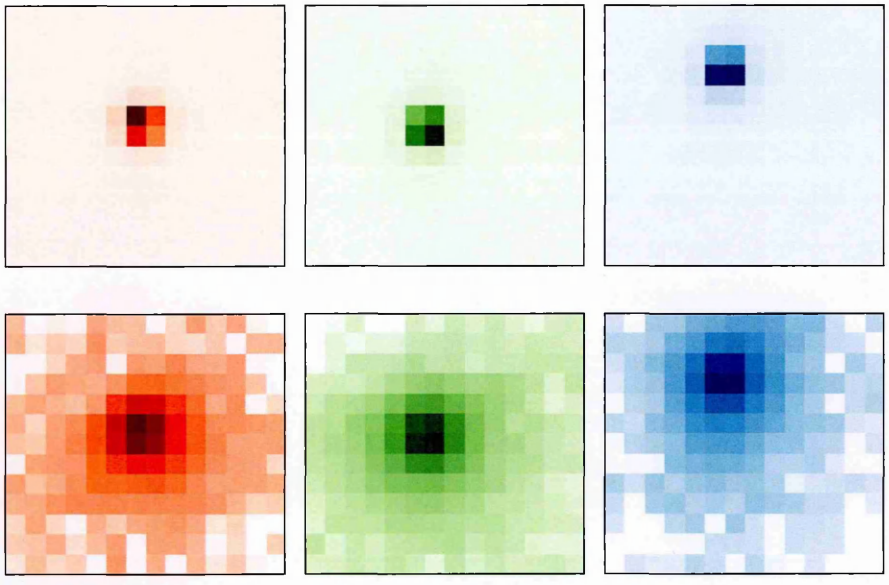

Figure 5.21: Focussed spot images in linear (top panels) and logarithmic (lower panels) colour spaces. Note that the correction for centring in the pixels has not yet been applied. Colours indicate illumination wavelengths (see Table 5.3)

5.3.2 Pixel Size

The focussed spot illumination was scanned along the x and y axes, both to find an optimum position for photon transfer analysis (near the centre of the pixel) and to check the linearity of the collection. The processing of each spot image was exactly as described in Section §5.3.1. Experiments were performed keeping the stage position in x and varying y, and vice versa. The resulting measured centroid values in both directions are shown in Figure 5.22, and the residuals after linear de-trending are given in Figure 5.23. Due to misalignment between the stage axes and the detector axes, a pure vertical movement of the stage produces a slight y axis movement of the centroid as well as x, and similarly for the horizontal movement. The value of this angle can be estimated using the ratio of the linear fit gradients for the "on-axis" (i.e. x centroid movement for vertical stage movement) to the "off-axis" (y centroid movement for vertical stage movement). Having estimated the misalignment angle χ, an estimate for the size of the pixels can be obtained using simple trigonometry. The numerical results are summarised in Table 5.5. Errors in the gradients are obtained from the fit covariance, and

the angle χ and pixel size α are calculated using:

$$\chi = \tan^{-1}\left(\frac{m_\perp}{m_\parallel}\right) \tag{5.9}$$

$$\alpha = \cos\chi\sqrt{\frac{1}{m_\perp^2}+\frac{1}{m_\parallel^2}} \tag{5.10}$$

where $m_\parallel$is the on axis gradient and $m_\perp$ is the off axis gradient. The fact that the estimates for the misalignment angle χ made using vertical and horizontal measurements differ fairly substantially (though within the quite large error margin) may indicate that there is also a misalignment in the (x,z) and (y,z) planes. The resulting estimates for pixel size are fairly consistent, though only measuring with blue light gives the value closest to the data sheet value of $\alpha = 15\,\mu$m. It is much more likely that our measurements here are confounded by (x,z) and (y,z) misalignment than that the data sheet value is incorrect - multiplied across all the pixel elements the resulting device would be of a significantly larger size than expected! It is also unlikely that we have by chance selected a particularly large pixel, since a change in gradient of the centroid lines would be observed when crossing this pixel, which is not evident in the data (see Figure 5.22). What the observed values do support, however, is that the pixel shape is square. Were this not the case, analysis of spreading of charge clouds would be complicated considerably.

Since the collecting gate is rather a small fraction of the pixel pitch, it might also be expected that systematic non-linearity in the centroid scan would be observed in the vertical direction, since positioning closer to the centre of the gate should collect charge differently than collecting far away. Against this must be set the argument that, in fact, the device is extremely thick and fully depleted: after diffusion during the long drift time, any effect due to gate width would be small. The results of the centroid scan were de-trended from the linear fit, and the residuals examined (see Figure 5.23). As is clear, it would be very difficult to claim an observable gate width effect.

5.3.3 Point Spread Function

Using the same dataset collected for the results described in Section §5.3.2, it is possible to obtain a measurement of the PSF of the pixel. The method is somewhat analogous to that described by [10] where the MTF (which is the Fourier Transform partner of the PSF) is derived using a projected image of a slit, slightly tilted with respect to the pixel axes. The

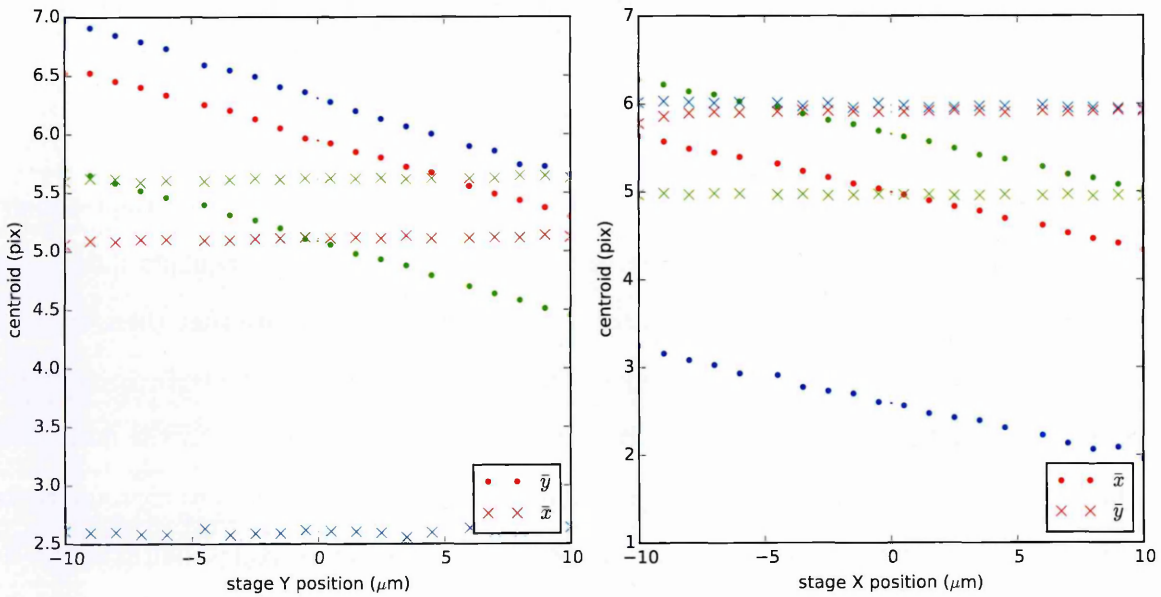

Figure 5.22: Centroid scan results. Colours indicate illumination wavelength (see Table 5.3)

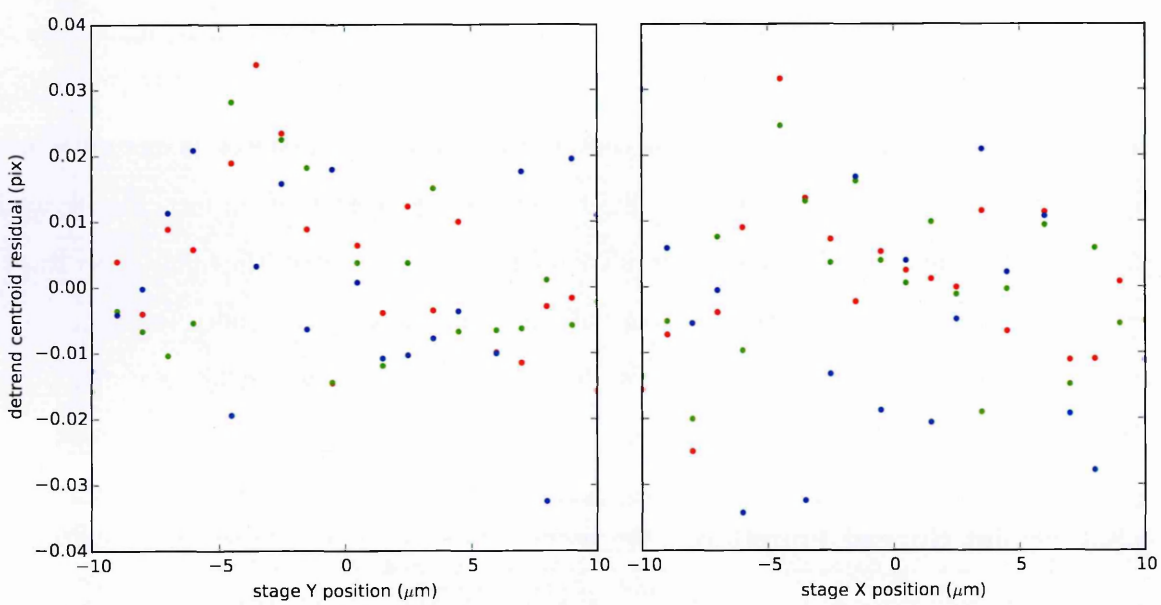

Figure 5.23: Centroid scan linear residuals. Colours indicate illumination wavelength (see Table 5.3)

	$m_{\parallel}(\text{mm}^{-1})$		$m_{\perp}(\text{mm}^{-1})$		χ (°)	
Light Colour	V	H	V	H	V	H
red	63.8 ± 0.8	64.8 ± 0.5	2.3 ± 0.4	3 ± 1	2.1 ± 0.4	2.7 ± 0.9
green	63.1 ± 0.5	63.3 ± 0.5	1.6 ± 0.4	1.0 ± 0.3	1.5 ± 0.4	0.9 ± 0.3
blue	67.1 ± 0.6	62.3 ± 1	1.8 ± 0.9	3.8 ± 0.6	1.5 ± 0.8	3.5 ± 0.6

	pixel size (μm)	
Light Colour	V	H
red	15.7 ± 0.2	15.4 ± 0.1
green	15.8 ± 0.1	15.8 ± 0.1
blue	14.8 ± 0.1	15.0 ± 0.2

Table 5.5: Pixel size measurements from centroiding

result is as though a point source was scanned along a direction, its centre being progressively more displaced with each row (for a nearly vertical slit) or each column (for a nearly horizontal slit). By displacing the measurement of each row (or column) by its measured centroid position and superimposing, a representation of the oversampled PSF is obtained. The method described here is to directly scan the point source by moving it, rather than simulating it using the slit. In fact, the slit method is much more convenient because only a single image is required for the measurement of PSF in each direction. However, the spot method has the advantage that we may obtain the position of the spot from the positioning stages, rather than having to rely on the fact that the spot centroid is a true representation of the actual spot position[2]. Any finitely-sampled detector imparts an intrinsic reduction in spatial resolution. The simplest model for this phenomenon is that the "true" PSF of the image is convolved with a top-hat function having the shape of the pixel. When measuring MTF, the standard practice is to correct for this by dividing it out of the measured MTF - implying (cf. the Convolution theorem) de-convolving from the measured PSF. When the aim of the experiment is to measure PSF, it is more convenient to simply fit a suitable function (including the sampling convolution) to the data directly. Assuming the true point source image $f(x)$ is Gaussian in shape:

$$f(x) = A \cdot \exp\left(-\frac{(x-\bar{x})^2}{2\sigma_x^2}\right) \tag{5.11}$$

[2]An assumption which, in practice, is actually rather reliable (see Section §5.3.2)

where A and σ_x are constants to be found and $\bar{x}$ is the stage position, and that the pixel is uniform in sensitivity and thus the sampling function $h(x)$ is a top-hat:

$$h(x) = \begin{cases} 1 & |x| < \frac{\alpha}{2} \\ 0 & \text{otherwise} \end{cases} \tag{5.12}$$

where α is the pixel pitch, the resulting measured image $g(x)$ will take the form:

$$g(x) = (f * h)(x) \tag{5.13}$$

$$\Rightarrow g(x) = \int_{-\infty}^{\infty} f(x)\, h(x-t)\, dt \tag{5.14}$$

where $*$ is the convolution operator and t is a dummy variable. Substituting the forms for $f(x)$ and $h(x)$ we find:

$$g(\bar{x}) = A \int_{-\frac{1}{2}}^{\frac{1}{2}} \exp\left(\frac{(x-\bar{x})^2}{2\sigma_x^2}\right) dx. \tag{5.15}$$

Performing the variable substitution:

$$s = \frac{x - \bar{x}}{\sqrt{2}\sigma_x} \tag{5.16}$$

then leads to:

$$g(\bar{x}) = \frac{A\sqrt{2\sigma_x \pi}}{2} \cdot \frac{2}{\sqrt{\pi}} \int_{\frac{1-2\bar{x}}{\sqrt{2}\sigma_x}}^{\frac{1+2\bar{x}}{\sqrt{2}\sigma}} \exp\left(-s^2\right) ds \tag{5.17}$$

and recalling the definition of the error function:

$$\operatorname{erf}(x) = \frac{2}{\sqrt{\pi}} \int_0^x \exp\left(-s^2\right) ds \tag{5.18}$$

yields:

$$g(\bar{x}) = A\frac{\sqrt{2\sigma_x \pi}}{2} \left(\operatorname{erf}\left(\frac{1+2\bar{x}}{\sqrt{2}\sigma_x}\right) - \operatorname{erf}\left(\frac{1-2\bar{x}}{\sqrt{2}\sigma_x}\right)\right) \tag{5.19}$$

which can be specified as a fitting function using a Levenberg-Marquadt fitting procedure with the free parameters being A and σ_x. To reduce the coupling between the fit parameters, typically the constant $\frac{\sqrt{2\sigma_x \pi}}{2}$ is subsumed into the free parameter A. Though qualitatively the expression (5.19) looks very similar to a Gaussian, the measured value for σ_x differs substantially when using (5.11) vs (5.19) in a fitting procedure. The PSF measurements for $V_{\mathrm{BS}} = -70\mathrm{V}$ are shown in Figure 5.24, and the fitting results summarized in Table 5.6.

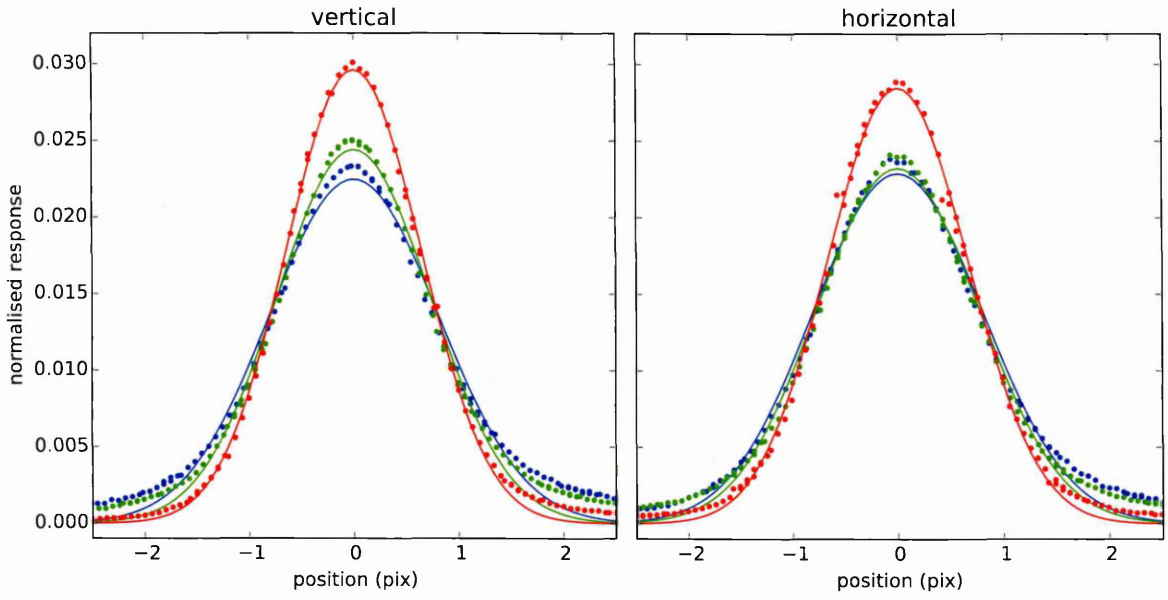

Figure 5.24: Normalised PSF measurements. The red, green and blue data designate the different wavelengths of illumination (see Table 5.3). Note that the normalisation is such that the sum of all measured pixel values is unity.

colour	horizontal PSF (pix)	vertical PSF (pix)
red	0.637 ± 0.002	0.661 ± 0.003
green	0.731 ± 0.005	0.767 ± 0.005
blue	0.803 ± 0.006	0.803 ± 0.005

Table 5.6: PSF Gaussian fitting results

Though the fit is quite good, the shape of the PSF has wider wings than the error function fit, as is expected from the numerical models (see Chapter 4). The same fitting procedure is used for the PSF measurements described in Section §5.7.

5.4 Electro-Optical Measurements

In this section, the procedures followed to optimise the device operation and measure some important parameters are presented. At all points, unless otherwise stated, the CCD261 was operated under the bias conditions shown in Table 5.7.

5.4.1 Channel Potential

The maximum potential in the buried channel $V_{\max}$ is (as has been seen in Section §3.2.2) an extremely important parameter in determining CCD performance. $V_{\max}$ is affected by many variables, including buried channel depth, doping concentrations, and applied voltages. Moreover, correctly operating a CCD requires knowledge of $V_{\max}$ as a starting point for selecting

Name	Symbol	DC level (V)	High Value (V)	Low Value (V)
Output Drain	V_{OD}	29		
Guard Drain	V_{GD}	26		
Output Gate	V_{OG}	3.2		
Reset Drain	V_{RD}	17		
Reset Clock	$V_{\Phi R}$		9.8	0
Image Clocks	$V_{I\Phi}$		9.2	0
Serial Clocks	$V_{R\Phi}$		9.8	0
Transfer Gate	V_{TG}		9.8	0

Table 5.7: Operating points used for the CCD261 experiments

clock voltages [54]. In the present work, the quantity $V_{\max}$ is of particular interest, because it can be measured experimentally and allows some refinement of the modelling with respect to the buried channel characteristics. In fact, it is the only non-destructive experimental measurement possible in the device giving direct information about the buried channel doping. In a deep depletion CCD such as the CCD261, the measurement and interpretation of $V_{\max}$ may be complicated by the "guard ring" (a term which refers to the guard drain positioned around the entire perimeter of the imaging area - see Section §3.4) which is held at V_{GD} - it is conceivable that a different channel potential could be present in the output circuitry of the device and the main imaging area. For this reason, the channel potential was verified by multiple methods.

We first follow the method of charge injection at the output node as described by Janesick [54, 1.4.3]. With the backside bias set to $V_{\mathrm{BS}} = 0V$, the reset reference voltage V_{RD} was swept through a range of values for different values of the output gate bias V_{OG}, and the mean signal measured at the output was recorded. V_{RD} reverse biases the pn junction of the buried channel (see Figure 5.2) and therefore forms a depletion region. At some point, V_{RD} will become equal to the channel potential V_m, at which point the depletion depth extends entirely to the buried channel junction, and further depletion is then controlled only by the gate voltages (and V_{BS} in the deep depletion case). With V_{RD} set below this level, electrons are injected from the sense node rather than drained. The difference between V_{RD} and the output gate voltage V_{OG} at this point is known as the Effective Threshold Voltage V_{EFF} [54]:

$$V_{\mathrm{EFF}} \approx V_{\mathrm{RD}} - V_{\mathrm{OG}} - V_{FT} \tag{5.20}$$

where V_{FT} is the reset feed-through voltage[3]. V_{EFF} is related to the channel potential maxi-

[3]The relationship is still approximate because to be accurate one must also include thermal barrier effects in transferring charge out of the sense node. This is possible to model given full details of the device design,

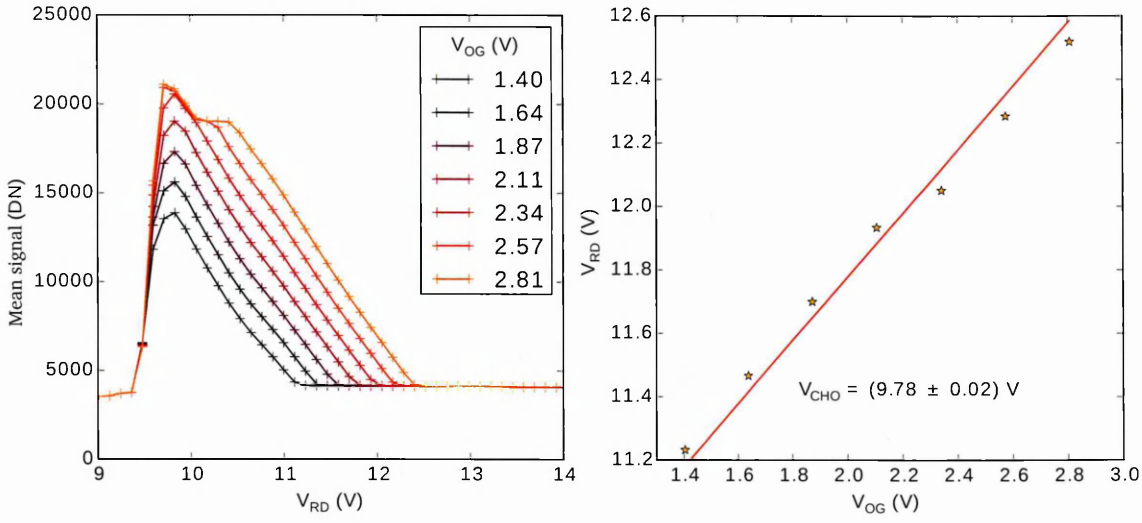

Figure 5.25: Channel parameter measurement. Sweeping V_{RD} for different V_{OG} (left), and plotting the resulting points of charge injection onset (right)

mum $V_{\max}$ for an applied gate voltage V_G by:

$$V_{\max}(V_G) = V_{\mathrm{EFF}} + V_G. \tag{5.21}$$

As V_{RD} is reduced below the threshold, charge injection is evident by the onset of an increasing mean signal (see Figure 5.25). A reasonably accurate estimate of the threshold is obtained by performing the V_{RD} sweep for multiple values of V_{OG}, finding the injection onset point at each value, and fitting a straight line with unity gradient. The intercept of this line on the V_{RD} axis gives an estimate of V'_{EFF}, which after subtracting the feed-through voltage (measured as $V_{FT} = (0.67 \pm 0.02)$ V - see Figure 5.26, and using propagation of errors) gives V_{EFF}. An estimate of the error is given by the covariance of the line fit. The threshold voltage for the device measured was found to be :

$$V_{\mathrm{EFF}} = (9.11 \pm 0.04) \text{ V}. \tag{5.22}$$

5.4.2 Full Depletion Measurement

At low applied biases V_{BS}, the active silicon of the sensor is not fully depleted of majority carriers, and a field-free region forms in part of the device. When traversing this field free region, charge carriers experience motion due only to diffusion, with no drift component. By

but cannot be independently measured experimentally

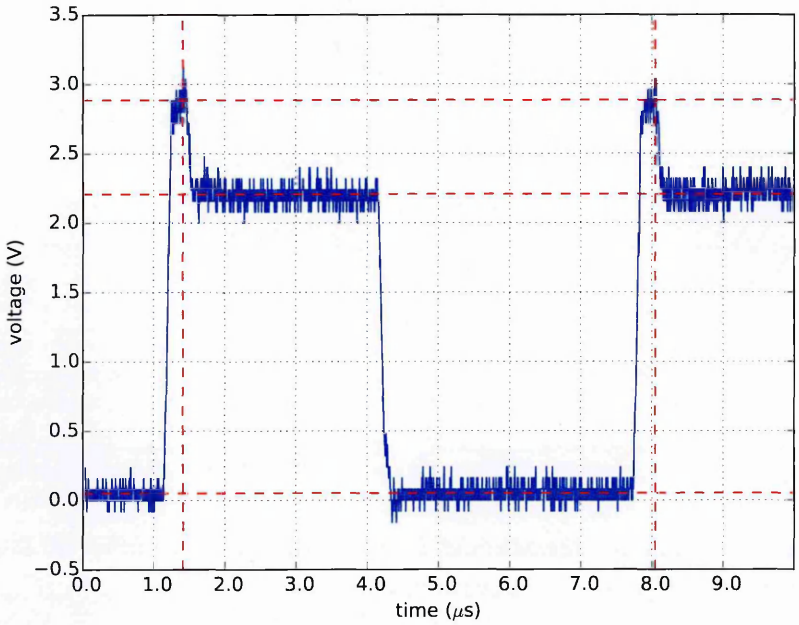

Figure 5.26: CCD output signal trace (after head board pre-amplifier) at $T = 153\,\mathrm{K}$, around 70% of full well signal.

the time the carriers are collected, they have experienced significant excess lateral spreading over the fully depleted case. As V_{BS} becomes more negative, the field free region becomes thinner, until it vanishes and full depletion is achieved. The point of onset of full depletion V_{FD} is a useful parameter because it can both indicate the region inside which we expect modelling assuming full depletion to be valid, and give a rough estimate of the resistivity of the silicon used in the device.

After full depletion has been achieved, decreasing V_{BS} continues to reduce spreading due to the increased field experienced by the carriers, and ergo reduced drift time.

An experiment was carried out varying V_{BS} between 0V and -70V, recording a spot image for each colour with 10s integration time. The images were pre-processed as described in Section §5.3.1. A straight line was fitted to the initial slope of the curve and extrapolated to the $\sigma_{xx} = 0$ to obtain a value for V_{FD}. Error estimates are obtained from the fit covariance. The results are shown in Figure 5.27. As expected, the value of V_{FD} is seen to decrease with increasing photon wavelength - this is due to longer wavelengths having a larger absorption length, and on average "seeing" less of the field free region. More unexpected are the absolute values of V_{FD} observed - in all cases the device appears to be fully depleted at a back side bias of less than $V_{\mathrm{BS}} = -10\mathrm{V}$. This does roughly agree with the depletion depth results on a CCD261 presented by Robbins et al [85], which for their device of thickness $150\,\mu\mathrm{m}$,

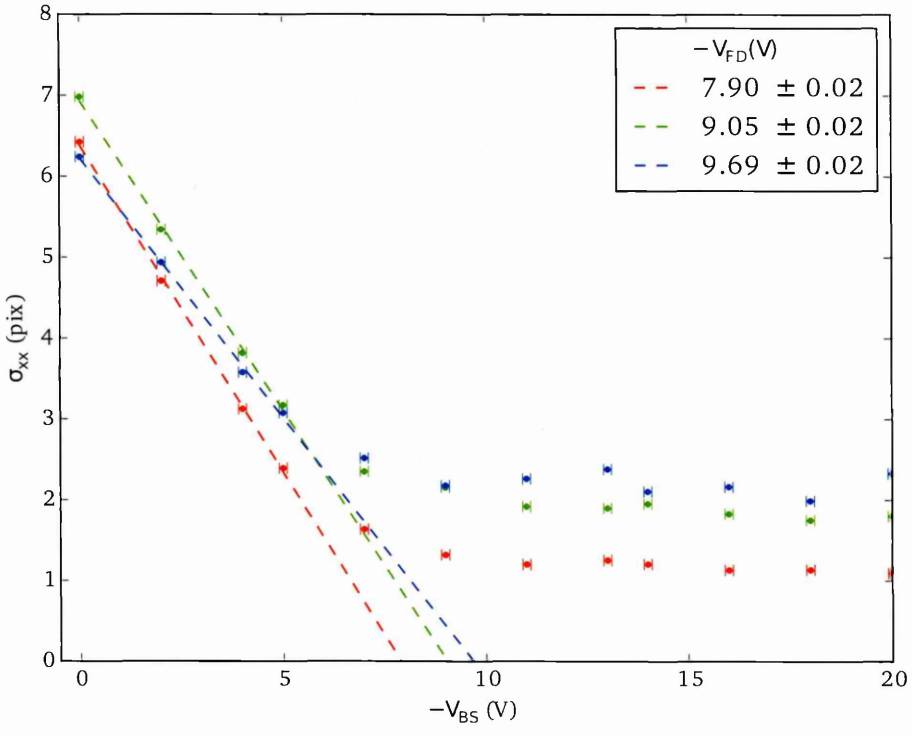

Figure 5.27: Spot size plotted for varying back side bias voltage. Colours indicate illumination wavelength (see Table 5.3)

implies that a depletion depth of 100 μm is reached at a bias somewhere between 0V and -10V. The device was operated with an image clock voltage of $V_{I\Phi} = 9.18\,\mathrm{V}$, which must be differenced from V_{BS} to obtain the full bias voltage. To estimate the substrate doping, we follow a method presented by Holland et al. [48, 30], changing the values appropriately due to their investigation of p-channel CCDs as opposed to the n-channel CCD261. The characteristic equation for estimating the channel maximum V_{max} and the substrate doping N_A is (see Section §3.2.2, particularly (3.7)):

$$V_{\mathrm{BS}} = V_{\mathrm{max}} + \frac{q_e N_A}{2\varepsilon_{\mathrm{si}}\varepsilon_0}\left(z_T - \sigma_{xx}\right)^2 . \tag{5.23}$$

Using a linear fit to this equation leads to the following estimates from the data (and assuming $z_T = 100\,\mu\mathrm{m}$ and $\alpha = 15\,\mu\mathrm{m}$ as exact values):

$$V_{\mathrm{max}} = (18.6 \pm 0.3)\,\mathrm{V} \tag{5.24}$$

$$N_A = (2.0 \pm 0.2) \times 10^{12}\,\mathrm{cm}^{-3} \tag{5.25}$$

leading to a resistivity estimate (see Section §2.4) of:

$$\rho = \left(6600^{+700}_{-600}\right) \Omega\text{cm}. \tag{5.26}$$

5.4.3 Full Well and Clock Level Optimisation

Operating the device at the correct clock levels (for both image clocks and register clocks) is necessary for precision measurements. If the energised clock level is too low, the device will exhibit a low charge handling capacity (full well) before the onset of blooming. Too high a clock level, and the stored charge packet may contact the device surface, resulting in the loss of charge into surface trapping states (a condition called "surface full well"). Increasing the clock level yet further causes greater fractions of the signal electrons to interact with the surface states, in turn causing more charge loss and reducing the charge capacity. As described in [54], the existence of these two full well possibilities implies that the optimum level to run the image clocks is that point where the blooming full well level is at a maximum, but without entering the surface full well state.

We refer to the technique which was used to optimise the clock operating levels as a flat-field Time Delay and Integration (TDI) transfer curve. More details about the PTC in general as a method of calibration are discussed later in Section §5.6. Like the "shutterless photon transfer" technique developed by Janesick [55], the transfer curve is generated rapidly (using two images of data). In contrast to shutterless photon transfer, a defocussed spot illumination is not required. The idea is that the device is exposed to flat field illumination, and lines of video are read out continuously. Each subsequent row has been exposed to a progressively longer integration time. The light source is adjusted so that full well is reached after around 2000 rows have been read out.The mean and variance of each row are calculated (as opposed to the mean and variance of a ROI as used in the "true" PTCs used for detailed investigation in Section §5.6) and used to form a PTC, an example of which is shown in Figure 5.28. The most interesting feature of this transfer curve which departs from the traditional PTC behaviour, is that the usual dominant noise source of shot noise at low levels and Fixed Pattern Noise (FPN) at high levels is reversed - before differencing, FPN is seen at low levels and shot noise behaviour is seen at high levels. This is because of the averaging process inherent in the technique - at higher exposure times (higher row numbers), the photo-generated charge has been collected over many physical pixels, so the varying photo-response of the pixels is

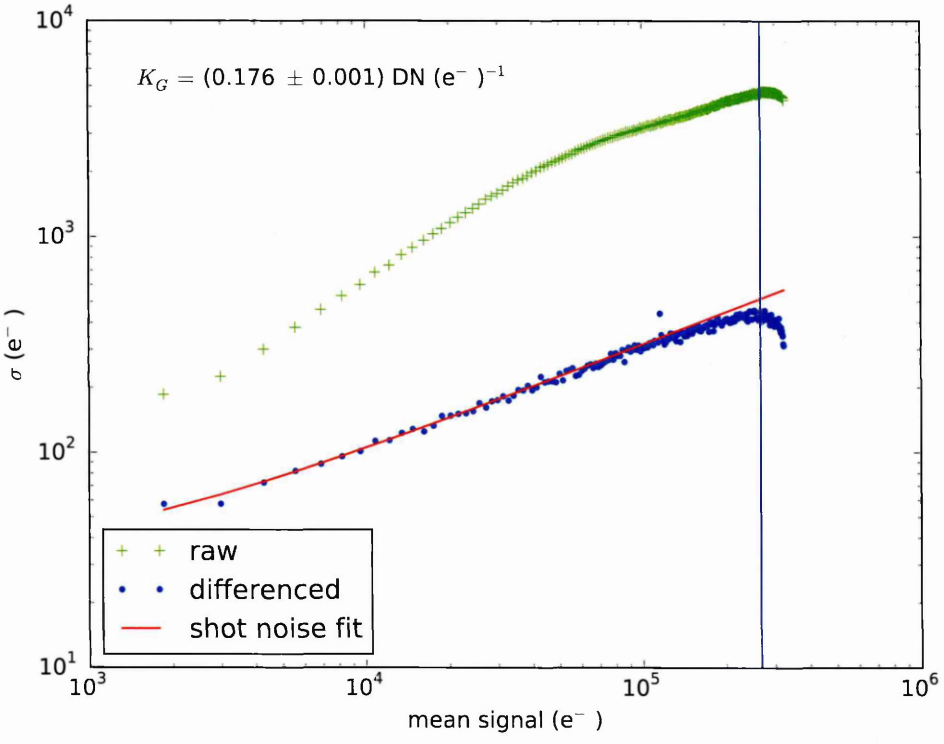

Figure 5.28: PTC generated from a single image transfer curve

averaged out, strongly suppressing FPN. The calibration value is extracted from the TDI transfer curve exactly as described later in Section §5.6, but due to the regularity of the row sampled data, a fast and robust numerical method of obtaining the full well capacity is also available - the row number vs variance data is simultaneously smoothed and differentiated using a Savitzky-Golay filter [86], and the turning point is found numerically.

As seen in the device specifications (Table 5.1), the specified charge handling capacity in the register cells is greater than that in the image area pixels; it is likely that this is simply due to the larger area of the register cells compared to the pixels. This is often the case with scientific CCDs, to allow binning of multiple pixels. Unlike a conventional PTC, the full well point (rather, the bloomed full well specifically) of the device does correspond to a visible feature in the mean vs row number plot. When parallel blooming occurs, extra charge collected from pixels "behind" the row being currently read out can spill into the current row, resulting in what appears to be a sharp increase in the rate of charge collection, which is evident in the left panel of Figure 5.29. In all cases, the highest value subsequently reached represents the full well of the register or the output node (whichever is lower): clearly neither change with $V_{\mathrm{I}\Phi}$. Conversely, for fixed $V_{\mathrm{I}\Phi}$, adjusting $V_{\mathrm{R}\Phi}$ shifts the register full well capacity up until the output node capacity is reached, beyond which further increasing $V_{\mathrm{R}\Phi}$ has no

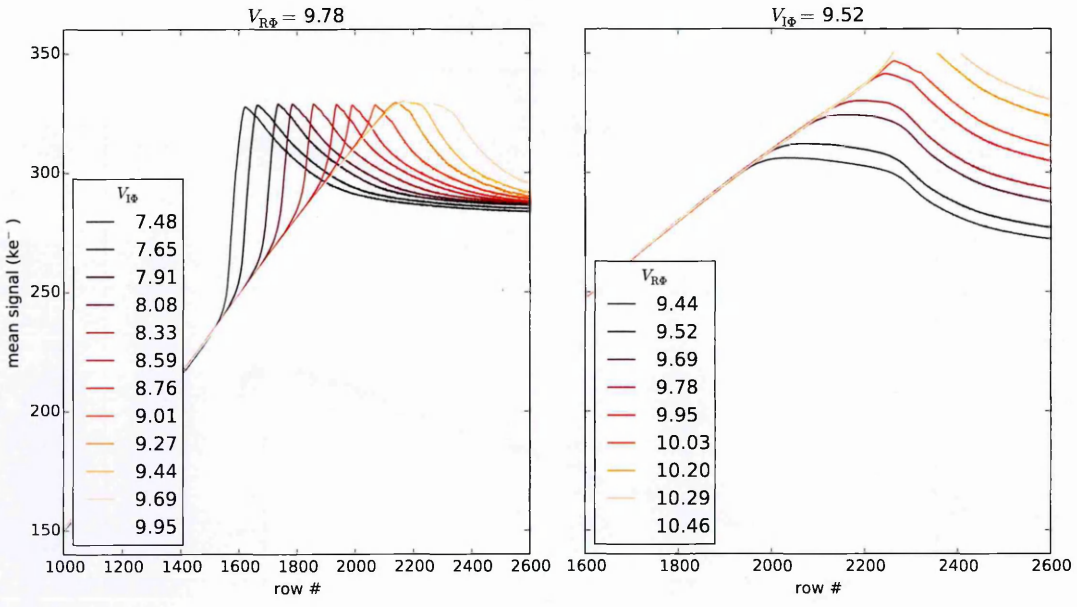

Figure 5.29: Line profiles from single image transfer curves for varying $V_{I\Phi}$ and $V_{R\Phi}$

effect (see right panel of Figure 5.29). This plot can also be used to adjust the CDS timings (see Section §5.2.3) - specifically the dual slope integration time - so that the output of the CDS circuit at the point of maximum node capacity can be adjusted to be close to the ADC full scale.

Plotting the observed full well signal against clock voltage allows the determination of the optimum clock operating point (see Figure 5.30). Note that making V_{BS} more negative increases the full well capacity but does not appear to move the position of the optimum clock operating point.

5.4.4 Inter-phase Capacitance

As mentioned in Section §5.1, the CCD261 device has a large inter-phase capacitance C_{IP} = 22nF, which leads to transient spikes being coupled into adjacent image clocks during switching (see upper panel of Figure 5.31). These transients are a problem, especially during time when the phase is high, because the excess voltage may cause the gate voltage to briefly exceed the threshold for the stored charge packet to meet the surface, allowing surface states to spuriously trap and/or inject charge leading to an excess noise source. Given the specified electrical parameters of the device (see Table 5.1), a simplified lumped element model of the gate drive conditions is constructed (see Figure 5.32). The resistor R_{IN} is part of the XCAM drive electronics and has a default value of $R_{IN} = 33\Omega$. The capacitor C_{IN} was added to the headboard to combat the transients. Figure 5.33 shows the output of transient simulations

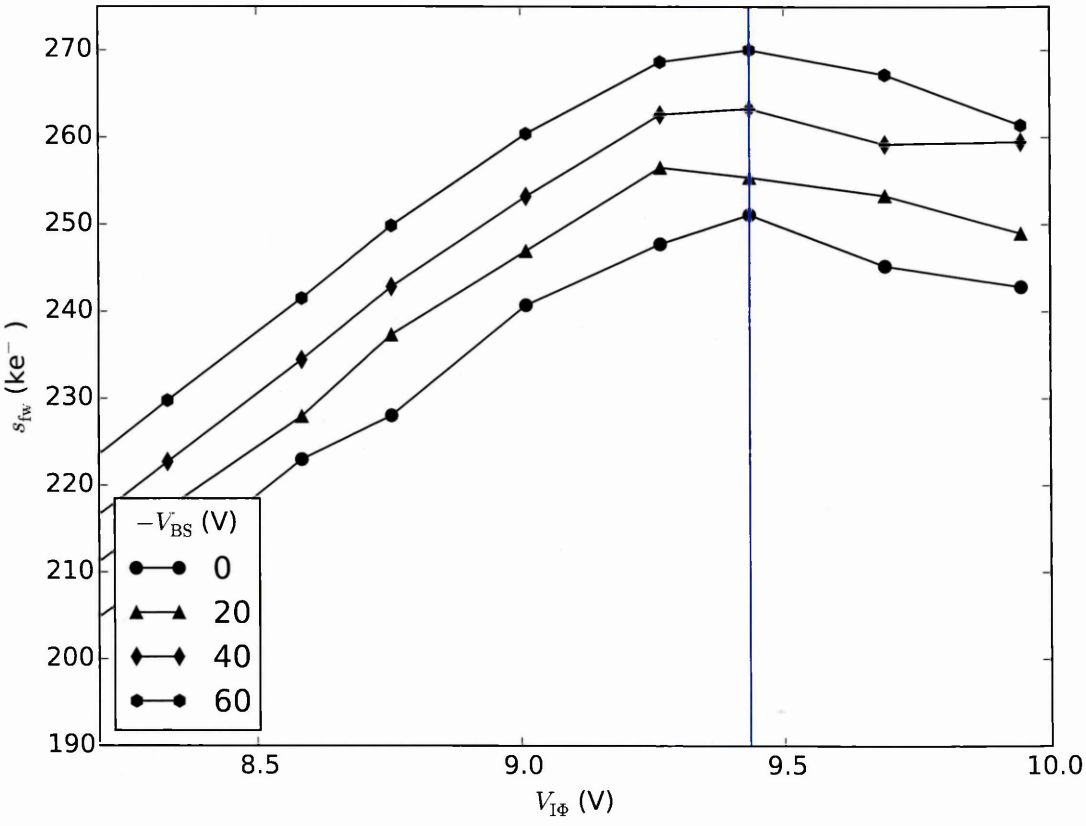

Figure 5.30: Clock level optimisation using full well measurements.

from this simplified model performed using the GNU Circuit Analysis Package (GNUCAP) circuit simulation program (a Simulation Package with Integrated Circuit Emphasis (SPICE)-like program). The phenomena exhibited clearly qualitatively match the observed behaviour of the image clocks quite well. Adding a large (C_{IN} = 100nF) capacitor helps to tame the transients somewhat, but also effective is reducing the overlap time of the clocks (see lower panel of Figure 5.33). The added capacitance means that the rise time of the signal is within allowable specifications whilst retaining imaging performance. As seen in the bottom panel of Figure 5.31, adding C_{IN} and decreasing the clock overlap time significantly helped to improve the quality of the image clock waveforms. The top panel of Figure 5.31 shows the condition with maximal clock overlap, whereas the bottom panel shows nearly synchronous clocking, with the overlap reduced to a minimum, whilst retaining charge transfer.

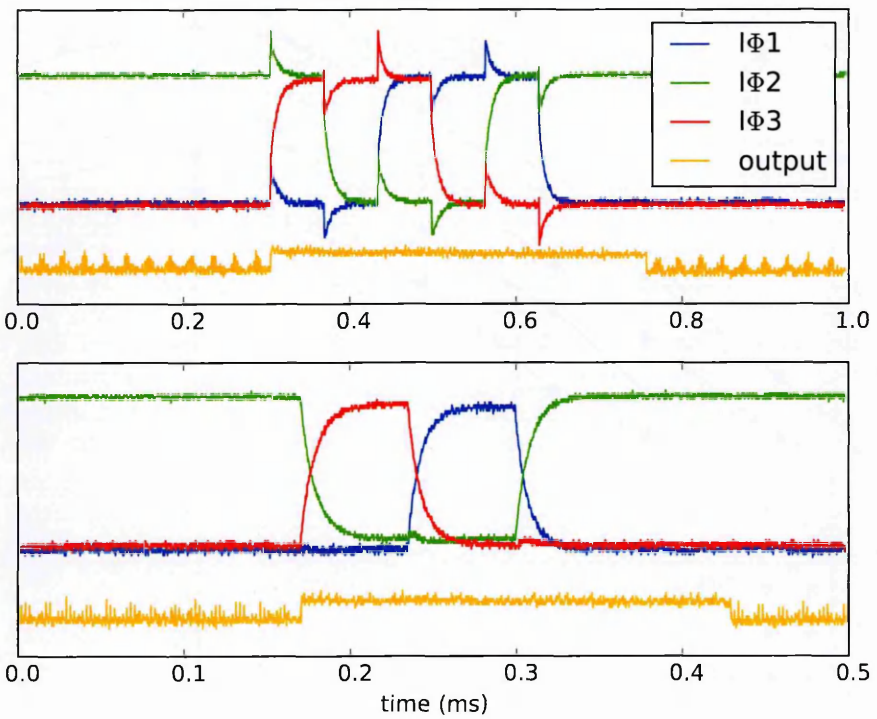

Figure 5.31: Measured CCD Image clock waveforms - fully overlapped (top panel) and synchronous (bottom panel) operation.

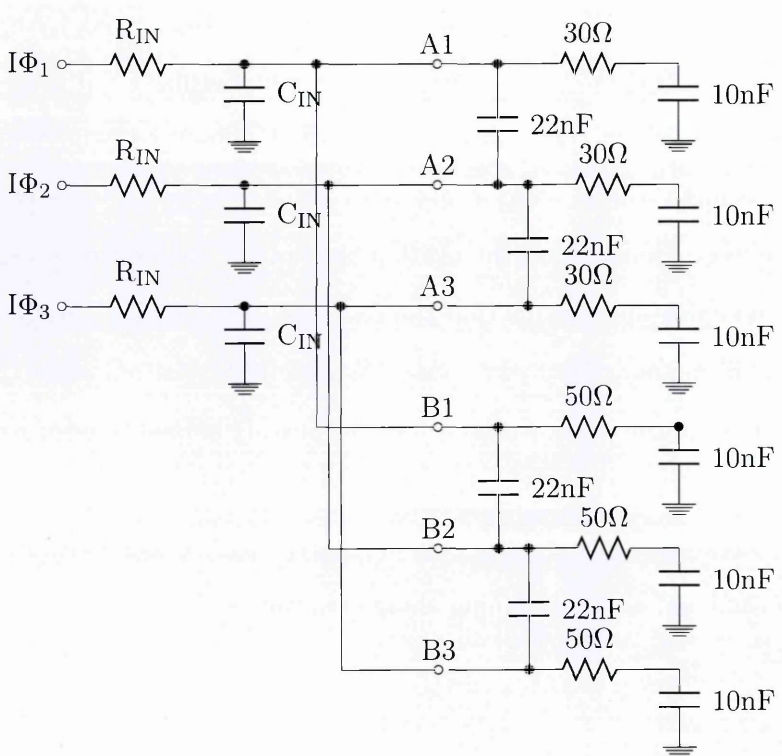

Figure 5.32: Lumped element model of CCD phases

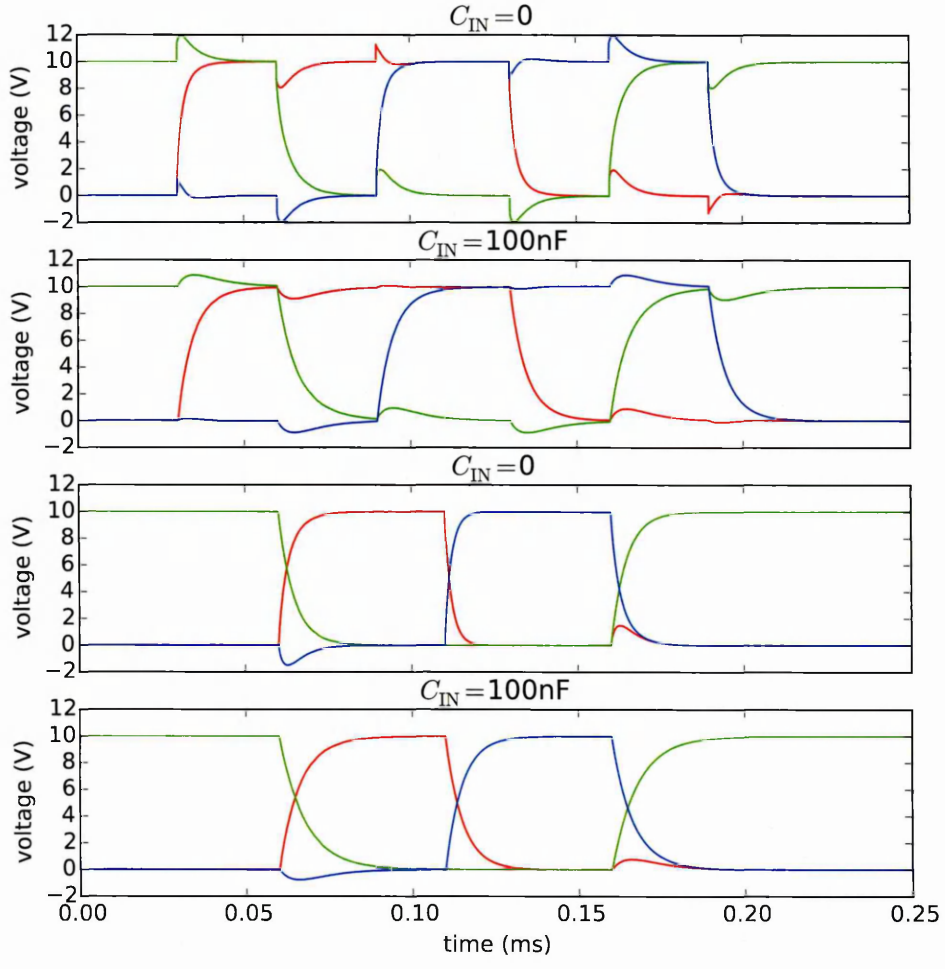

Figure 5.33: CCD image clock waveforms simulated using SPICE, with $C_{IN} = 0$ (top panel), $C_{IN} = 100$nF(upper centre panel) reduced overlaps (lower centre panel) and reduced overlaps with $C_{IN} = 100$nF (lowest panel)

5.5 Edge Distortion

Thick, deep depletion CCDs (and indeed any CCD with a guard drain structure) have been observed to exhibit distortions at the edge of the image [7]. In particular, an investigation using a scanned spot near the edge of a candidate LSST detector has been recently published [77]. That work identified that the effect is related to charge redistribution either during collection or subsequently, but ruled out a local variation in sensitivity. Other tests on the same sensor model (a similar device to the CCD261) have shown a similar effect due to the guard ring structure [26]). Here we show that the same effect due to the guard ring structure used in deep depletion devices is exhibited in the CCD261. As described in Section §3.4, deep depletion operation of a thick CCD is achieved by using a high resistivity substrate, and

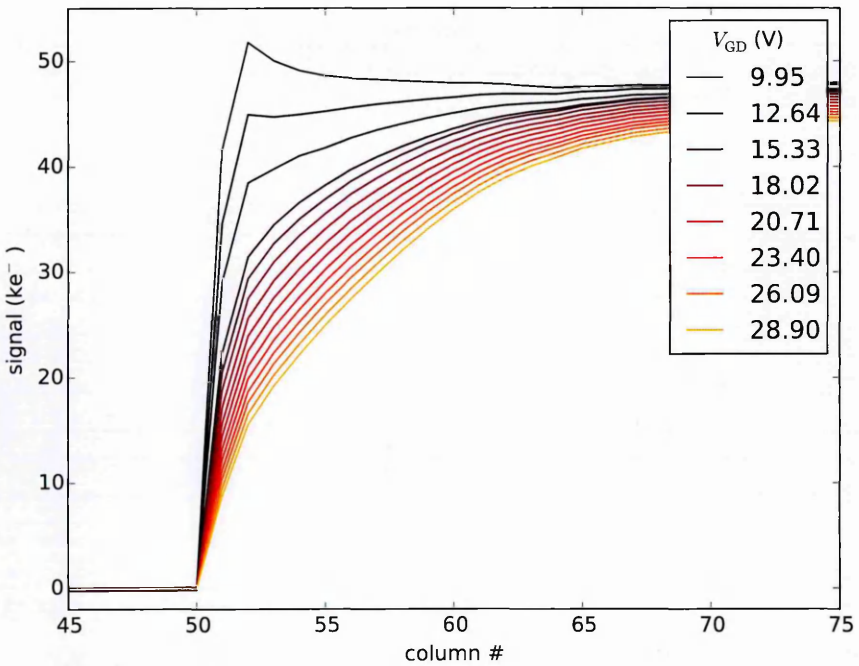

Figure 5.34: averaged row plot at the edge of the CCD for $V_{BS} = 0V$

applying a bias potential using a contact at the back surface. Though a detailed model of the phenomenon is beyond the scope of this thesis, we show in this section that there is a clear relationship between the degree of edge distortion observed and the bias applied to the guard ring, the possible explanation being that a fringing field resulting from the potential difference between the guard ring drain and the collecting gates causes charge to migrate beyond the edge of the device during collection, and be lost through the guard drain.

A flat-field illumination of $\approx 45ke^-$ was applied to the CCD261 using blue light (for the electron unit calibration details see Section §5.6) and images were obtained for varying guard ring bias voltages V_{GD} and back side biases. After overscan subtraction, the mean of the image was taken column wise (over the 500 rows read out in each image) to eliminate cosmic rays and reduce noise. The result of an experiment at back side bias $V_{BS} = 0V$ is shown in Figure 5.34. It is immediately clear that the edge distortion effect increases with V_{GD}, and also that it is in fact possible to reverse the effect (from "roll-off" to "roll-in") by applying a sufficiently low V_{GD}. Extreme care must be taken whilst operating a deep depletion device under these conditions - the point of the guard drain is to prevent excessive currents flowing between the front and backside bias contacts, and with too low a value for V_{GD} combined with a large potential difference between V_{FS} and V_{BS} will cause permanent damage to the device for this reason. Therefore it is probably inadvisable to attempt to correct edge distortion entirely using

guard drain adjustments, especially when very negative back bias potentials are to be used. It seems that the recommended operating point in the CCD261 data sheet of $V_{\mathrm{GD}} = 29\,\mathrm{V}$ may be chosen rather conservatively. The device used in these experiments was the thinnest available (at $z_T = 100\,\mu\mathrm{m}$) and operated at quite low bias voltages (V_{BS} is specified for operation up to $V_{\mathrm{BS}} = -120\,\mathrm{V}$). With those caveats, we were still able to successfully acquire images from the device running at guard drain voltages as low as $V_{\mathrm{GD}} = 9.95\,\mathrm{V}$ with no signs of excessive substrate current. The image clocks for this experiment were operated at $V_{I\Phi} = 9.52\,\mathrm{V}$, and it seems (curiously) that the edge distortion has disappeared and even reversed before V_{GD} has been lowered to this level, which implies that there is likely some complication beyond the naive assumption that the guard drain is simply dragging electron drift trajectories beyond the device edge. In any case, the effect can clearly be made to extend over 10s of pixel distances, making it substantially longer range than the brighter-fatter effect in all but the most extreme instances. On the other hand, the shape of the distortion profile gives further evidence that charge is displaced during collection rather than afterwards - if redistribution of charge were happening, we would likely expect some slight enhancement of the signal in pixels near the edge (i.e. the guard drain is "dragging" the charge towards the edge), rather than the uniform roll-off that is observed, which implies more that the carriers are lost completely during collection. A recommendation for future investigation would be to perform the experiment using dark-signal generated charge, which if the hypothesis of a purely collection-related effect were true, would exhibit much less distortion that in illuminated images.

The variation in distortion against V_{GD} was found to be reasonably well characterised as an exponential expression having the form:

$$S(y) = K_{ER}\left(1 - e^{-\gamma y}\right) \tag{5.27}$$

where $S(y)$ is the signal value observed at the distance from the edge y, K_{ER} is the flat field signal value and γ is an empirical constant. The value of γ was studied against varying values of V_{GD} and V_{BS}, the results being shown in Figure 5.35. A clear dependence on V_{BS} as well as V_{GD} indicates yet further that edge distortion is caused during collection, since the field properties at the storage region are very little affected by the value of V_{BS}. Indeed, it is plausible that a full understanding and detailed modelling of the edge distortions may prove a very useful tool in studying other collection related effects.

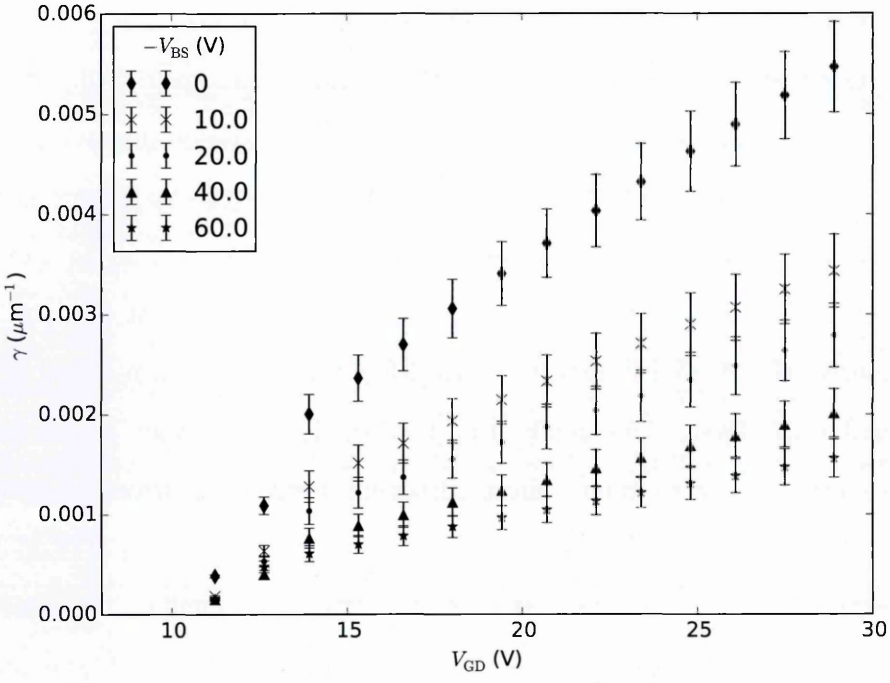

Figure 5.35: Degree of edge distortion γ with varying bias conditions

5.6 Flat-field Photon Transfer Curve

The flat-field PTC is the standard method used to calibrate imaging sensors from arbitrary digital number units to physical units of electrons. The validity of the PTC method relies on three assumptions:

1. Photon arrival obeys Poisson statistics in the temporal domain.

2. Each incoming photon causes a single electron hole-pair to be released - therefore electron arrival obeys the same statistics as photon arrival

3. The charge to voltage conversion and all subsequent amplification stages are linear.

Of these conditions, the third is the most often violated in practice, and in some cases linearity can be affected by the output amplifier. In other cases (i.e. APS detectors), the non-linearity arises from active components local to the pixel, and must be dealt with using a non-linear fitting method (as first described for this application by [78] and detailed for practical application in [91]). This type of non-linearity is easy to identify, if not always easy to correct for. The second condition is always true for optical illumination - there is insufficient energy for an incoming photon to generate multiple electrons. The first condition is satisfied for all uncorrelated light sources (indeed for all forms of "classical" light [33]), but given special

conditions can be violated, even using only common LEDs and simple equipment, as demonstrated by [46]. Luckily, it is very difficult to stumble into sub-Poisson light emission using normal operating conditions at room temperature, so we can be fairly well assured that the light sources used here are Poisson limited. Poisson arrival statistics implies a very simple relationship between the mean number of photons $\bar{s}$ observed in a time interval δt, and the variance σ_s^2 of that number [83]:

$$\sigma_s^2 = \bar{s} \tag{5.28}$$

$$\Rightarrow \sigma_s = \sqrt{\bar{s}}. \tag{5.29}$$

The standard deviation σ_s is also referred to as the noise, and the noise characteristic described by equation (5.29) is referred to as "shot noise". In a well designed imaging sensor, the minimum noise achievable is limited by the charge to voltage conversion stage. This noise is the read noise (as described in Section §5.2.4), σ_r, and is observed at zero signal. Increasing the signal level, a point is reached where the shot noise of the signal begins to dominate. The averages are usually taken spatially over a single image, allowing very high statistics to be obtained using a single image (assuming perfect flat field illumination). At a certain point, the noise caused by response differences between pixels becomes larger than the shot noise. This noise is referred to as FPN, and in typical thick CCDs it is much larger than shot noise for most values of signal. FPN is in general proportional to the signal level sampled, and so grows faster than the shot noise, but can be eliminated completely by using differenced pairs of images to calculate the variance. This technique relies on consistent illumination levels between exposures. A schematic representation of an ideal PTC can be seen in Figure 5.36.

Most importantly, the knowledge that equation (5.29) applies when the units of σ_s and $\bar{s}$ are in physical units allows calculation of the conversion factor from the measured units (digital numbers) to physical units of electrons. After elimination of FPN using differencing, following Janesick [55], the relationship between the measured signal variance and mean can be written as:

$$\sigma_s^2\,[\mathrm{DN}] = \frac{\bar{s}\,[\mathrm{DN}]}{K_G} + \sigma_r^2\,[\mathrm{DN}] \tag{5.30}$$

where the [DN] suffix denotes a quantity measured in digital numbers. The quantity K_G is

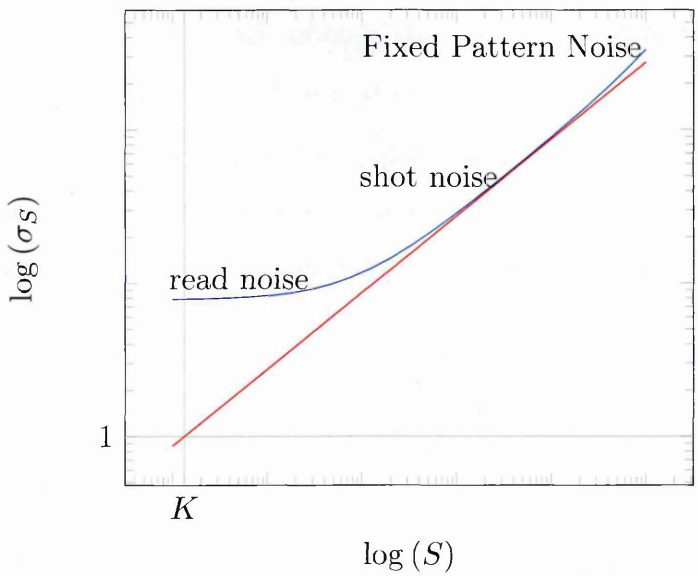

Figure 5.36: Cartoon diagram of photon transfer curve analysis. The red line indicates the shot noise relationship

known as the camera gain, and relates the arbitrary units to physical units through:

$$s\left[e^{-}\right] = s\left[\mathrm{DN}\right] K_G. \tag{5.31}$$

Assuming that the read noise is negligible compared to the shot noise (taking $\sigma_r = 0$), and taking logarithms of equation (5.30), it is found that:

$$\log\left(\sigma_s\left[\mathrm{DN}\right]\right) = \frac{1}{2}\log\left(\bar{s}\left[\mathrm{DN}\right]\right) - \frac{1}{2}\log\left(K_G\right). \tag{5.32}$$

Traditionally, the value of K_G is found by fitting a straight line to the portion of a log-log graph between σ_s and $\bar{s}$ where the slope is $\frac{1}{2}$. The intercept of this line at the point $\sigma_s\left[\mathrm{DN}\right] = 1$ then gives the value of K_G after re-arrangement. As was first pointed out by Downing et al. in 2006 [27], thick back illuminated devices cannot be accurately calibrated this way, due to the non-linearity of the PTC even in cases where the mean vs integration time curve appears linear, due to correlated charge collection. Instead, as suggested by [94], the mean-variance curve should be fitted with a quadratic equation, and the value of the linear term (i.e. the tangent to this curve at low signal levels) should be used for K_G. The equation that is fitted is thus:

$$\sigma_s^2\left[DN\right] = \beta\bar{s}^2\left[\mathrm{DN}^2\right] + \frac{\bar{s}\left[\mathrm{DN}\right]}{K_G} \tag{5.33}$$

and the fitting is performed in linear space rather than log-space. This method was used to

calibrate all PTCs in the present work. The non-linearity coefficient β is considered dimensionless, despite the form of (5.33). To see the reason, consider converting the units of (5.33) to physical units using (5.31):

$$\sigma_s^2 \left[\mathrm{DN}^2\right] K_G^2 = \beta \bar{s}^2 \left[\mathrm{DN}^2\right] K_G^2 + \bar{s} \left[\mathrm{DN}\right] K_G \tag{5.34}$$

$$\Rightarrow \sigma_s^2 \left[\left(\mathrm{e}^-\right)^2\right] = \beta \bar{s}^2 \left[\left(\mathrm{e}^-\right)^2\right] + \bar{s} \left[\mathrm{e}^-\right] \tag{5.35}$$

It is clear that fitting the quadratic form to either the raw (digital number units) or calibrated (electron units) results in the same measure of non-linearity. Flat field PTCs were taken changing either integration time or illumination level. These results are described in detail in the text that follows, but to summarize from the relevant point of view of camera gain calculation, the calculated values for K_G are shown for all experiments in Figure 5.37. The value of K_G is seen to systematically increase by around 10% when the back bias voltage is changed from $V_{BS} = 0\,\mathrm{V}$ to $V_{BS} = -70\,\mathrm{V}$. This indicates that the backside bias is either reducing the capacitance of the sense node, increasing the gain of the output amplifier stage, or both. A similar result was found on tests of the CCD261 previously published [85]. There, the variation was attributed mostly to the effect of the back bias on the sense node capacitance.

For the CCD261, flat field PTCs were taken for all three available wavelengths at bias voltages ranging from $V_{\mathrm{BS}} = 0\,\mathrm{V}$ to $V_{\mathrm{BS}} = -70\,\mathrm{V}$. An example of the results obtained is shown in Figure 5.38. As can be seen from the upper left panel, the consistency of illumination between the first and second illuminated flats was good up until beyond the onset of full well for all wavelengths. As previously observed, the green and blue LEDs provide a much higher output than the red. Note that the point at which the drop-off in mean vs. integration time occurs (in fact, the signal is spilling into the overscan, resulting in lower values after subtraction) is beyond the full well value found from the photon transfer curve (right panel) of $s_{\mathrm{FW}} \approx 2 \times 10^5\,\mathrm{e}^-$. This is as expected after optimization of the image and register clock levels (see Section §5.4.3). The bottom left panel of Figure 5.38 indicates that the linearity of the device is reasonable, the residual remaining within $\pm 1\%$ of the linear fit across the whole signal range. This was found to be typical of PTCs taken at all values of $\mathrm{V_{BS}}$. There is a discontinuity in the linearity residuals, which was an occurrence observed in several of the measured PTC experiments, which is likely attributable to long term instabilities in the light source, though the cause was not ascertained with certainty. The non-linearity of the PTC itself remains, however, as is clear from the right hand panel. As reported by Guyonnet et al.

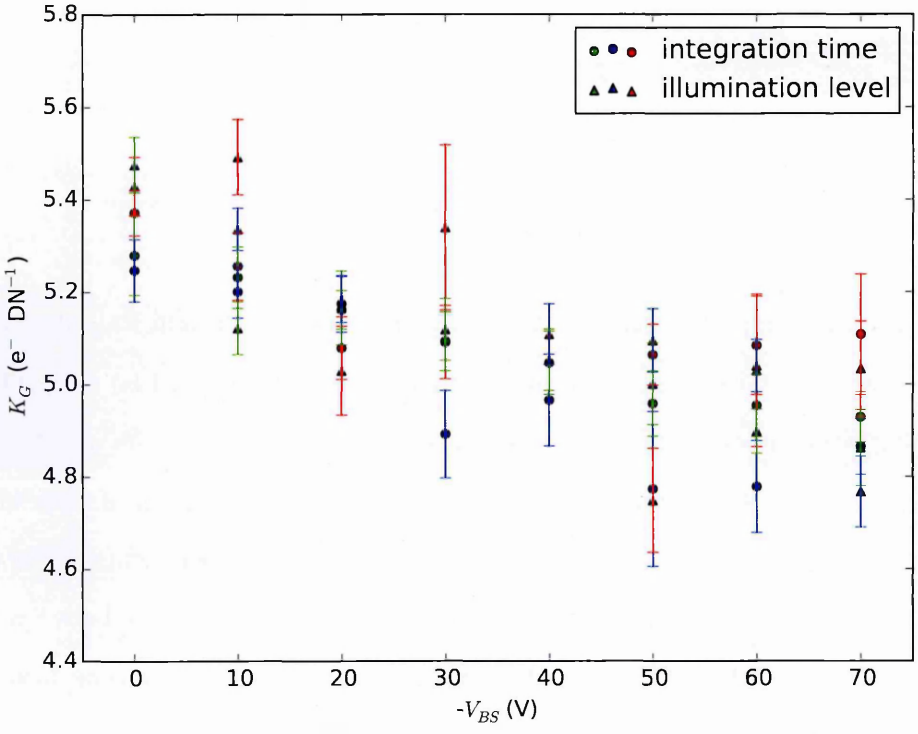

Figure 5.37: Camera gain measured vs back bias voltage V_{BS} for the CCD261. Colours indicate illumination wavelength (see Table 5.3)

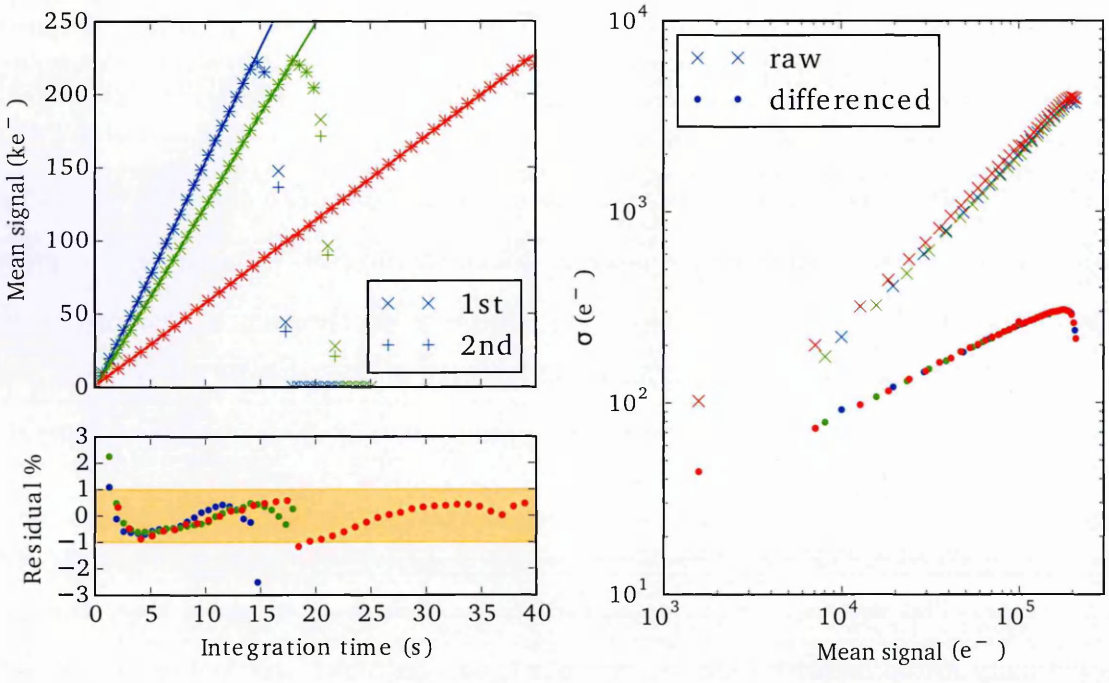

Figure 5.38: Photon transfer curves and linearity plots for $V_{\mathrm{BS}} = -60$V. The camera gains for the colours shown are $K_{\mathrm{red}} = (5.0 \pm 0.25)$ e$^-$ DN^{-1}, $K_{\mathrm{green}} = (5.0 \pm 0.5)$ e$^-$ DN^{-1}, $K_{\mathrm{blue}} = (4.8 \pm 0.2)$ e$^-$ DN^{-1}. The illumination wavelengths are given in Table 5.3

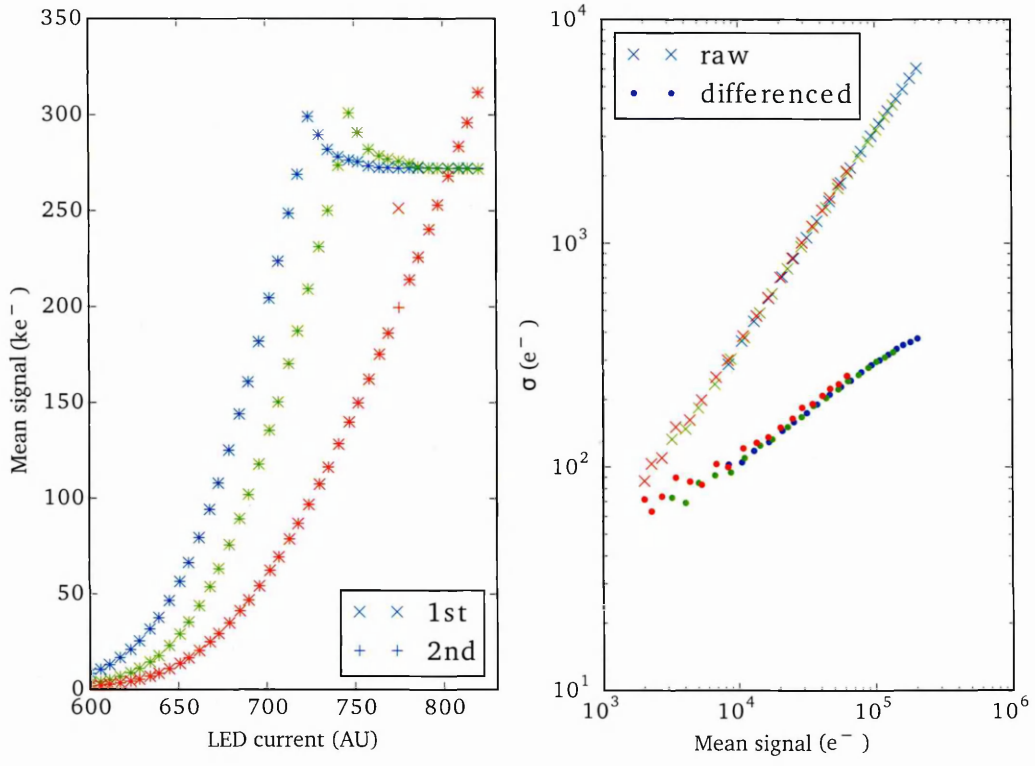

Figure 5.39: PTC obtained by altering LED brightness, for $V_{\mathrm{BS}} = -70\mathrm{V}$. The camera gain constants found are $K_{\mathrm{red}} = (5.0 \pm 0.5)\ \mathrm{e}^{-}\,\mathrm{DN}^{-1}$, $K_{\mathrm{green}} = (5.0 \pm 0.3)\ \mathrm{e}^{-}\,\mathrm{DN}^{-1}$, $K_{\mathrm{blue}} = (5.0 \pm 0.2)\ \mathrm{e}^{-}\,\mathrm{DN}^{-1}$. Illumination wavelengths are given in Table 5.3

[42] but differing from Stefanov [94], no clear chromaticity is observed.

PTCs were also taken where the change in signal was achieved by altering the brightness of the LED source, rather than the integration time. An example is shown in Figure 5.39. The form of the PTC is similar to that seen in Figure 5.38, though the non-linearity of the current mirror circuit used to adjust the LED brightness (see Figure 5.18) causes the equivalent of the linearity plot for this transfer curve to exhibit extremely non-linear behaviour at low values.

K_G was again found by quadratic fitting to the mean and variance. Examples of this process for different values of V_{BS} are shown in Figure 5.40. Again, any systematic difference in the degree of non-linearity with different wavelengths is absent, but there is, as predicted by models of the BFE a large change with V_{BS}. The non-linearity is characterised by the quadratic term used in the fit, β . The measured values for β across different wavelengths and bias voltages are shown in Figure 5.41. The linearity of the PTC is shown to be gradually recovered as the electric field across the device is increased, as expected. There also appears to be no significant difference between the PTCs collected by varying integration time and those collected by varying LED flux at fixed integration time. At the condition $V_{\mathrm{BS}} = -10\,\mathrm{V}$, the

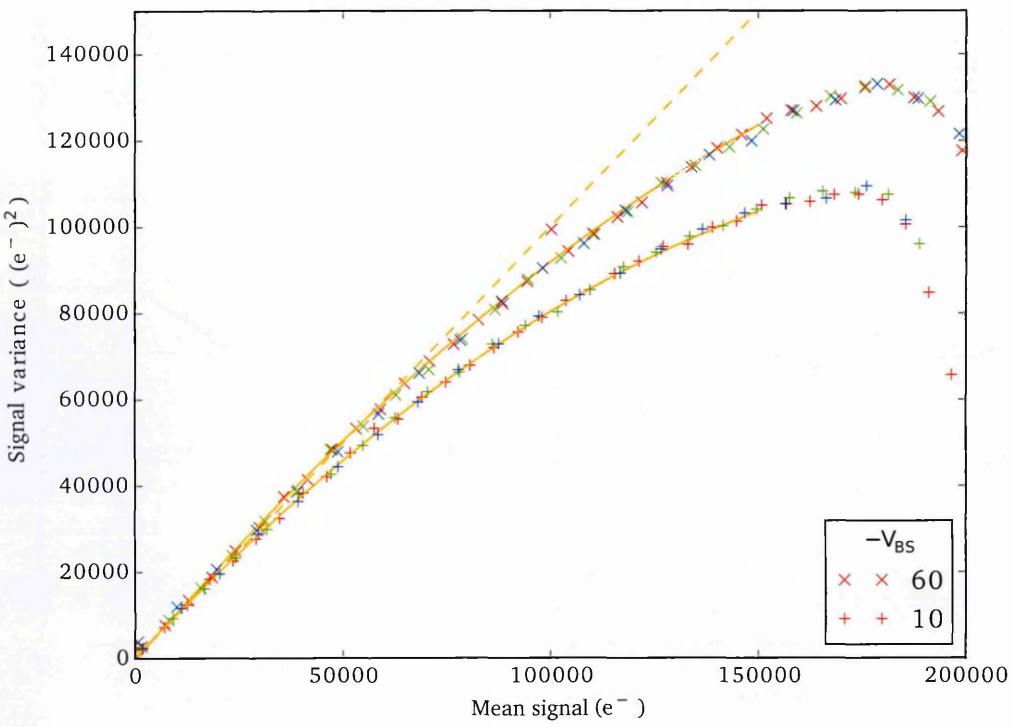

Figure 5.40: Mean-Variance curves for differing V_{BS} showing non-linearity. The solid lines are average quadratic fits, the dashed line indicated the mean=variance line. Colours indicate different wavelengths of illumination. The gain constants found are $K_{60} = (4.8 \pm 0.2)$ e$^-$ DN^{-1}, $K_{10} = (5.3 \pm 0.3)$ e$^-$ DN^{-1}. These constants are an average of the individual gain constants for each wavelength. The wavelengths used are shown in Table 5.3

device is nearing or has already reached full depletion (see Section §5.4.2). From Figure 5.41, there is some evidence that reducing the applied back bias below this level does begin to recover some linearity, which we attribute to the mechanism of an increasing field-free region being present in the device, extending from the back surface. This phenomenon was discussed in Section §4.5. An interesting avenue for future study would be to attempt collection measurements at fine steps for V_{BS} in the incomplete depletion regimen, possibly using lower values for V_G also to investigate the situation where a large field-free region exists. Investigations on front-faced devices and / or lower resistivity substrates would also help to increase understanding of the behaviour.

5.7 Point Source Illumination

Using spot illumination, two experiments were performed: measurements of a static spot at different integration times (similar to a PTC), and measurement of the PSF (as described in Section §5.3.3). In the case of the former, the size of the spots were estimated using the

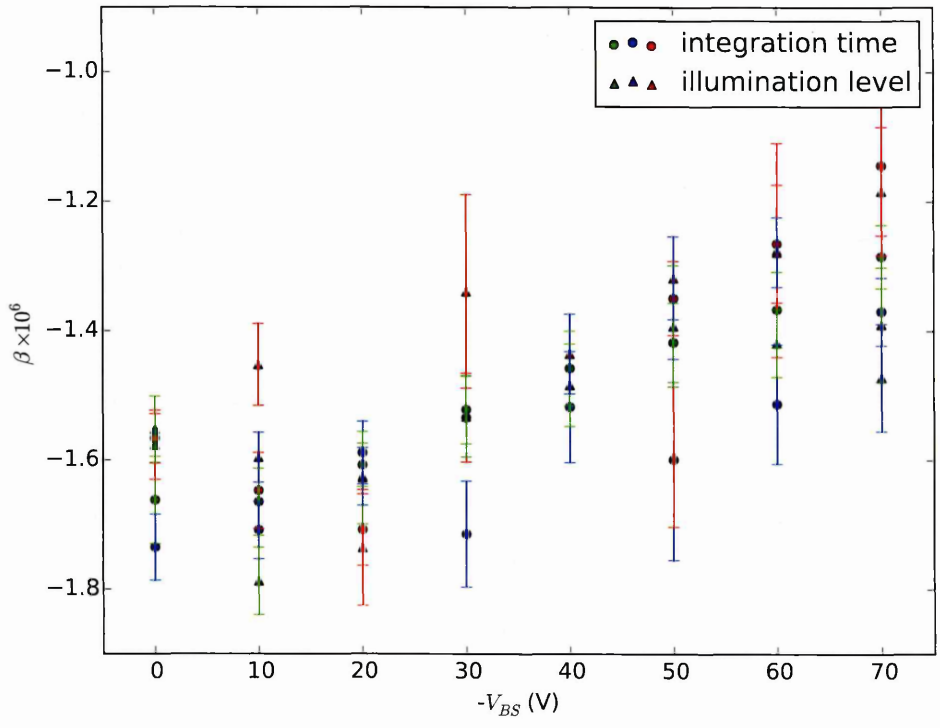

Figure 5.41: Size of quadratic term in mean-variance fit varied over V_{BS}. Colours represent illumination wavelength (see Table 5.3)

method of moments (see Section §5.3.1). For each value of spot volume (which is found using the product $M_{00}K_G$ for a pixel region of 30×30 pixels), the median of 9 images was used to reduce influence by cosmic rays and read noise. As expected, the spot size increases with volume, with the values for σ_{xx}^2 (vertical) being systematically greater than σ_{yy}^2 (horizontal). We define the quantity eccentricity, η, by:

$$\eta = \sqrt{1 - \frac{\lambda_+}{\lambda_-}} \tag{5.36}$$

$$\text{with} \quad \lambda_\pm = \frac{s_{02} + s_{20}}{2} \pm \frac{\sqrt{4s_{11}^2 + (s_{20} - s_{02})^2}}{2}. \tag{5.37}$$

An eccentricity equal to 0 corresponds to a circular spot, whilst a value near unity represents a highly elongated spot. The measured relationship between measured eccentricity and spot volume is shown in Figure 5.42, along with the relationship connecting the value in the spot's central pixel and the total spot volume. The latter is found to be approximately linear until the central pixel's signal reaches a value near full well. As described in the literature [5, 42], we find that the eccentricity generally gradually increases with volume. An anomalous result is noted (decreasing eccentricity) for the red illumination at $V_{\mathrm{BS}} = -50\,\mathrm{V}$. The eccentricity

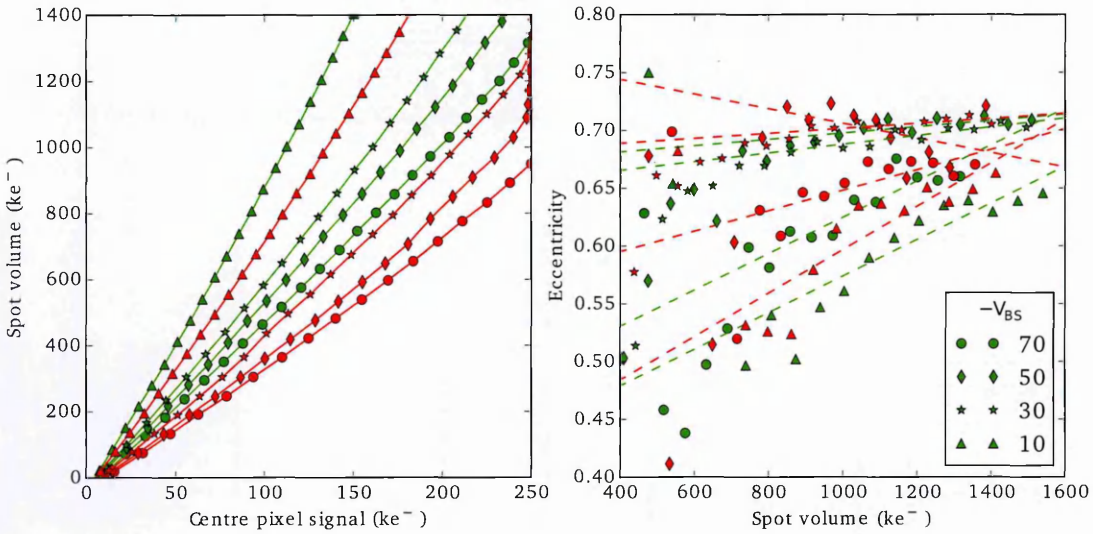

Figure 5.42: Measured spot eccentricity (defined in (5.36)) against volume. The colour of the symbols show measurements at different wavelengths (see Table 5.3).

against volume curves were fitted against a linear function, which shows reasonable agreement, though nowhere nearly as well-conditioned as the results reported on the CCD250 for a similar experiment [42]. The reason for this is unknown, though it is feasible that improved flat-fielding correction might correct for the problem somewhat. This would require large amounts of extra calibration data using flat fields to be collected - it would be insufficient to flat field correct using only a few calibration frames at high exposure (as described in [54]), because the extra shot noise implied by such a correction would likely dwarf the signal added by the point source illumination, especially away from the centre of the spot. We call the gradient of the eccentricity vs volume curve the "eccentricity slope", and the fitting results are plotted in Figure 5.43. The quality of the collected data leaves much to be desired - with only 11 images taken for each data point, the statistical errors implied are high. Future work should repeat a similar investigation using much higher statistics and eliminating fixed pattern noise using extensive flat-fielding. Though the condition of the fits is not as good as might be, it is very interesting to note that the eccentricity slope starts high at low back bias (as expected - all BFE related effects are generally enhanced at low back bias), decreases to a low value, and then appears to recover at high back bias voltages. The reason for this is unknown, and should be a priority for future experimental studies, since it may represent an important consideration in optimising device operation to reduce dynamic collection effects.

The oversampled PSF was measured for several bias voltages and integration times, with the results being shown in Figure 5.44. The spot volumes in electron units were calculated by

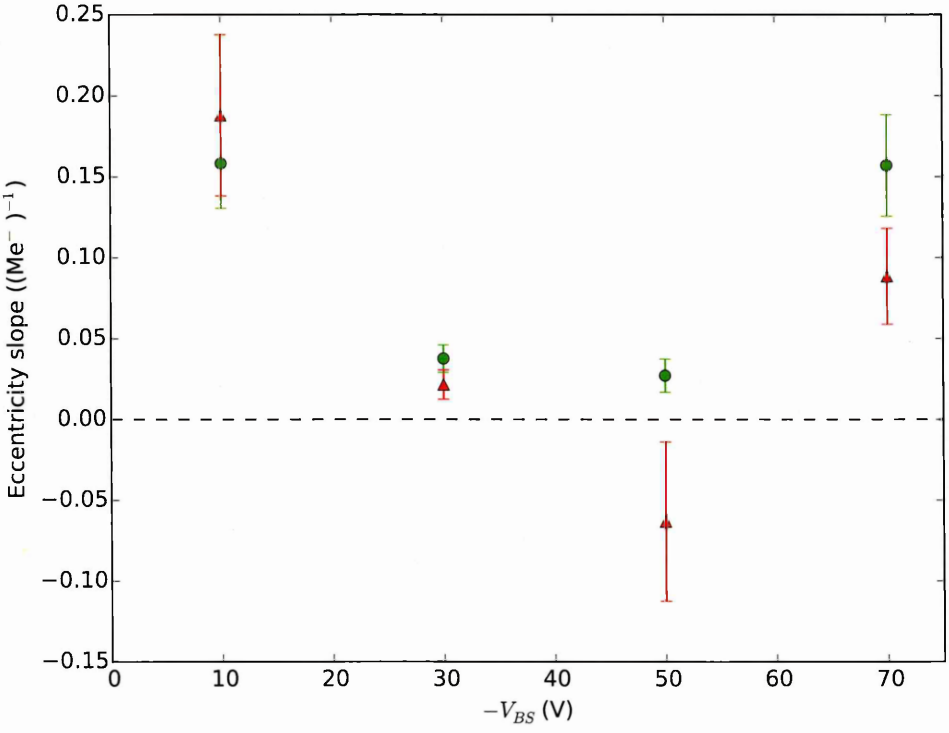

Figure 5.43: Relationship between fitted eccentricity slope (fitted line slopes in (5.42)) and back bias voltage. Colours indicate illumination wavelengths (see Table 5.3)

multiplying the volumes in DN units by the relevant camera gain constant found using flat field exposure. Since no cross correlation measurement equivalent to s_{11}^2 is available for these measurements, we measure the anisotropy ratio $\frac{\sigma_x}{\sigma_y}$ rather than η to characterize the degree of shape change due to the BFE. The variation of this anisotropy ratio against signal volume and bias voltage is shown in Figure 5.45. The expected trends (increasing anisotropy with longer integration time, decreasing anisotropy as applied V_{BS} becomes more negative) are observable, though not strikingly clear. Despite large experimental errors, we find agreement with the literature [42, 4, 73] that the increase in anisotropy is on the order of 2% across the signal range. The first reasonably clear evidence of chromaticity is found here, though: the anisotropy ratio from the shorter wavelength blue light is consistently higher than that for the longer wavelengths. The anisotropy ratios for shorter wavelengths are not only observed to be systematically higher (which is as expected for a BFE which operates as described by the model in Chapter 4), but also to increase more rapidly against spot volume.

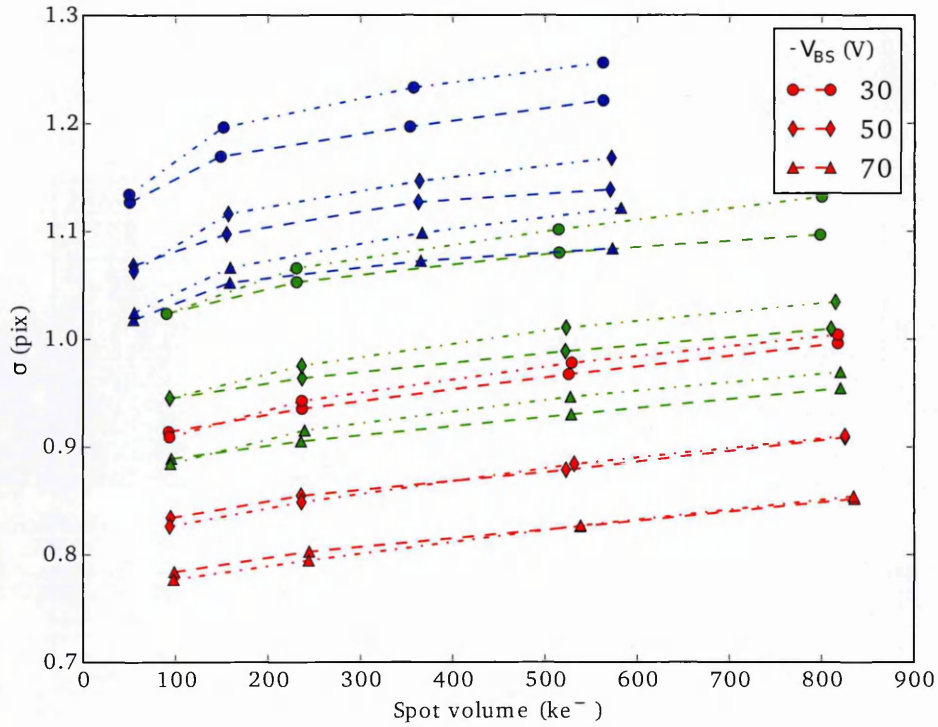

Figure 5.44: PSF measurements with varying spot volume and V_{BS}. The dotted lines represent σ_x values, and the dashed lines σ_y. Colours show different illumination wavelengths (see Table 5.3)

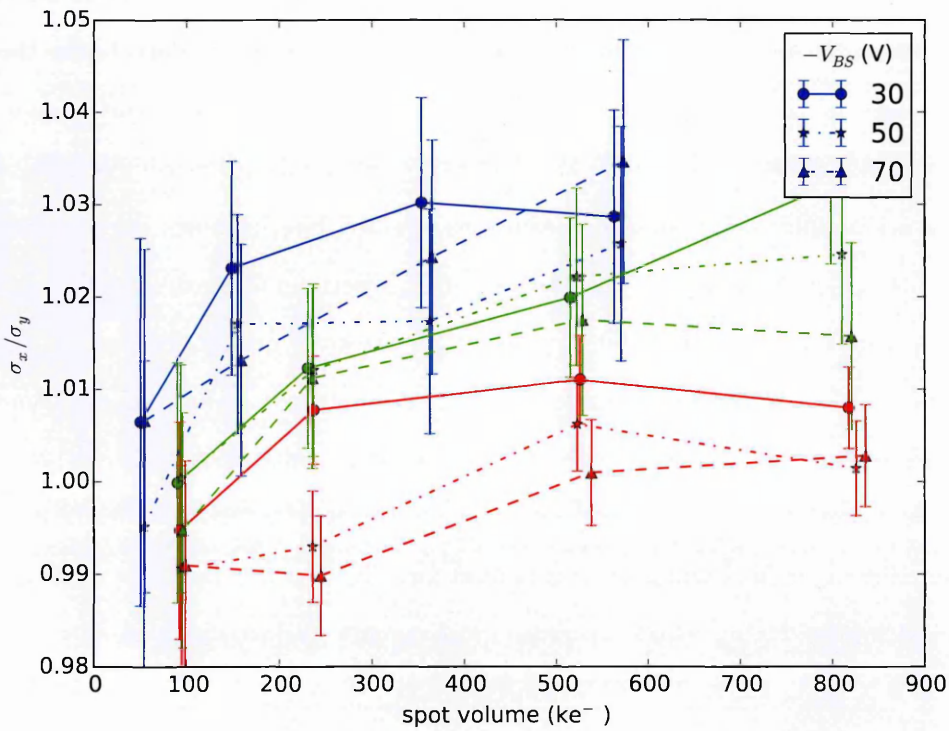

Figure 5.45: Anisotropy of PSF (σ_x/σ_y) whilst varying integration time and V_{BS}. Colours show different illumination wavelengths (see Table 5.3)

5.8 Dark Current Photon Transfer

Due to both the stray light issues mentioned earlier (in Section §5.2.6) and an instability problem in the interface between the camera and experimental computer causing occasional lost data, a traditional measurement of the dark current transfer up to significant fractions of the full well capacity using extremely long exposures was not possible. However, a nearly analogous test can be performed by adjusting temperature rather than integration time - note that as discussed in Section §2.4, the carrier mobility changes with temperature, so during this experiment estimates using that quantity cannot be sensibly made, given that in our experiment temperature was not automatically logged along with the image data. The system was set to capture pairs of exposures as in conventional flat field photon transfer (see Section §5.6), but instead of changing integration time (which was kept constant at 1s), subsequent image pairs were simply captured with a time delay between them. After starting the experiment, the cooling system was de-activated, causing the temperature of the device to gradually rise, from its measured starting point of $T = 153\,\mathrm{K}$ to an end point measured some time after the completion of the experiment of $T = 291\,\mathrm{K}$. The exponential dependence of thermal carrier generation with temperature means that even a very short integration time at room temperature overwhelms the charge handling capacity of the pixels with dark current. The resulting photon transfer curve is plotted in Figure 5.46, showing reasonably good linearity except for at low signal values, where the rate of change of dark current generation rate over time is large compared with its value. The linear axis mean - variance curve is shown in Figure 5.47, from which it is immediately clear that, excluding the anomalous non-linearity at low signal values, the plot is strikingly linear as compared with those found in flat-field photon transfer (see Figure 5.40); the effects of correlated charge collection are seemingly all but completely absent. Attempting to fit the central portion of the mean variance curve quadratically, we find that $\beta = (-7.0 \pm 0.2) \times 10^{-7}$, significantly smaller in magnitude than any non-linearity measured for illuminated experiments. The value of the camera gain is found to be $K_G = (4.3 \pm 0.2)\ \mathrm{e^-\,DN^{-1}}$, larger than any value measured for the illuminated tests (see Figure 6.16). This is attributed to the fact that the gain changes with temperature, and much of the dark current transfer curve was obtained at a temperature higher than the $T \approx 150\,\mathrm{K}$ used for the rest of the experimental work. The sensitivity decrease with increasing temperature has been remarked on previously in the literature on thick, back biased CCDs [85]. As was described in Section §3.5, this is expected since dark signal is generated evenly

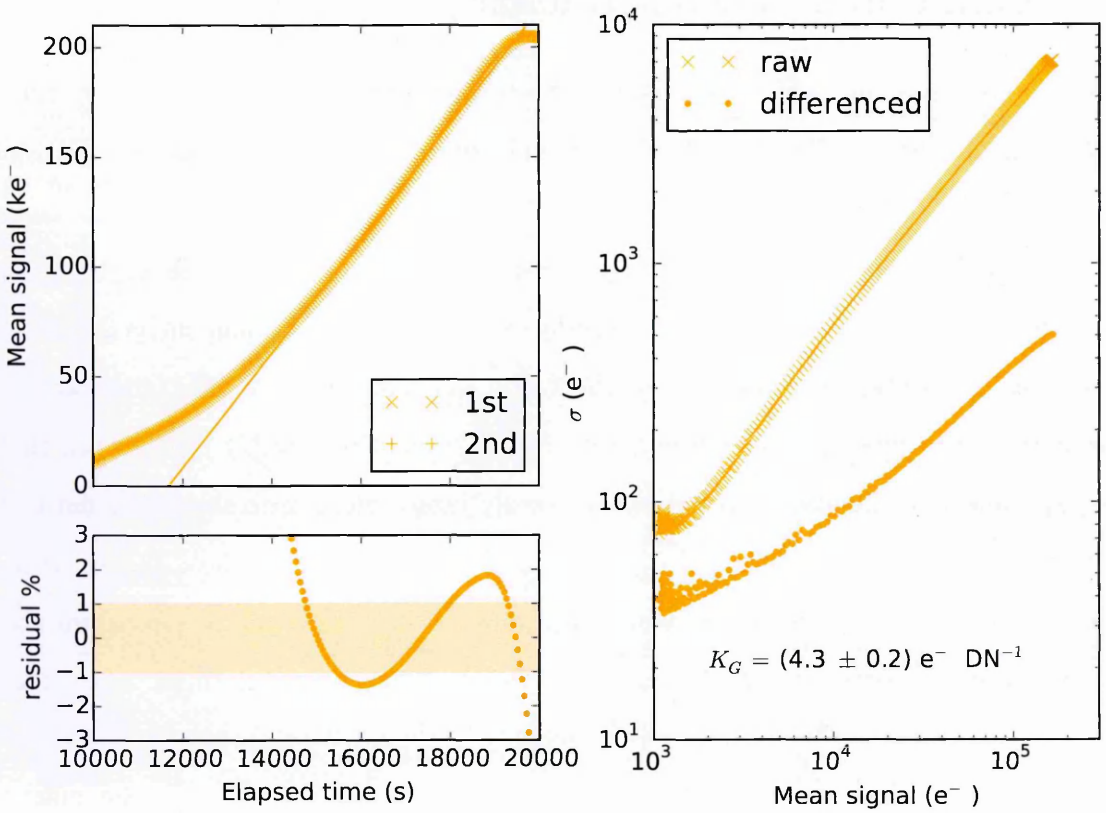

Figure 5.46: Photon transfer curve generated using dark current

throughout the device thickness (for bulk dark current) or at the device surface (for surface dark current), and therefore does not have to drift all the way to collection from near the back surface. As was described in Section §3.5, the surface component of dark signal usually dominates. In light of this, it is a logical conclusion of this experiment to recommend that, where practical, devices being affected by the BFE should obtain absolute gain calibration from dark current transfer rather than photon transfer. This could be performed at fixed temperature, given the experimental availability of long exposure times.

5.9 Summary

Selected electro-optical measurements on the CCD261 device have been presented, along with some electrical measurements on the laboratory equipment used to drive the device. The chief issue that arose when driving the large area, deep depletion CCD261 device was the large inter-phase capacitance, which was reduced by adjusting the clock overlaps and reducing the slew rate by adding extra capacitance off-chip. The operation of the CCD was optimised using full well transfer.

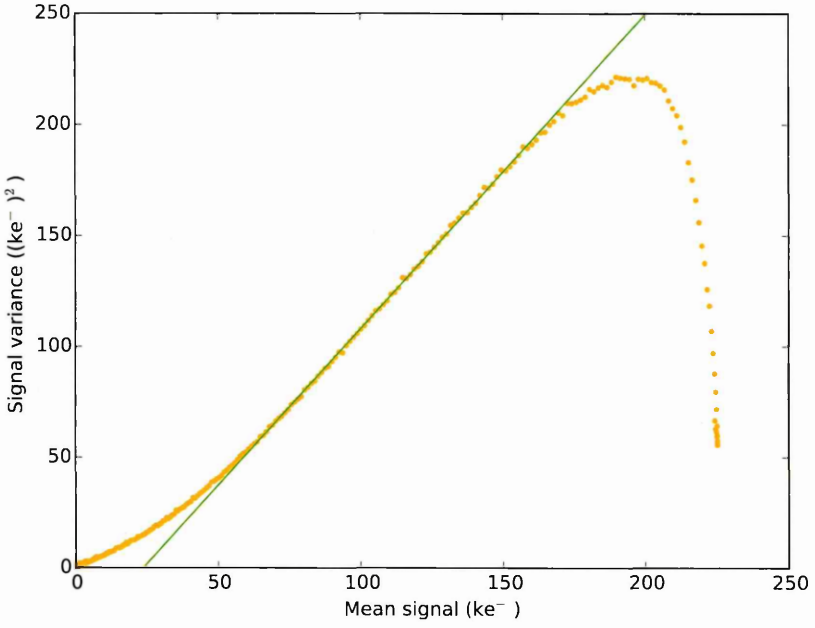

Figure 5.47: Mean-variance curve generated using dark current. The green line shows the shot noise fit.

Photon transfer measurements were performed using both flat field and point source illumination stimuli, and the non-linearities introduced by the BFE were clearly observed. A photon transfer curve generated using dark current did not exhibit non-linearity.

Chapter 6

Validation of Dynamic Charge Collection Models

> Photography as a fad is well-nigh on its last legs, thanks principally to the bicycle craze.
>
> Alfred Stieglitz, 1897

In this chapter we present several attempts at validating the simulation approach to dynamic charge collection that was presented in Chapter 4, by comparison to experimental data and with finite element calculations.

6.1 Finite Element Simulations

The Silvaco ATLAS [69] device simulation program was used to compare solutions for potential found in Chapter 4 with finite element simulations. A single CCD pixel was modelled with the same geometric parameters as described in Chapter 4 (see Table 4.1) which are similar to the CCD261 described in Chapter 5, though not intended to be identical. Of particular interest is testing the validity of the charge storage model (described in Section §4.2), and comparing the potential profiles (and hence fields) predicted. Apart from these investigations, two major sources of possible inaccuracy in the analytical model present themselves: the use of the depletion layer approximation, and the shape of the fixed charge distribution used for the buried channel implant. The former has been addressed in the literature for the specific case of a buried channel CCD [20], and a detailed discussion is not included here. The latter question of how best to "translate" between a block buried channel model and a more realistic distribution is open for discussion: either the potential maxima predicted by the block model

can be matched to the realistic doping profile by adjusting the junction depth z_J (in which case the potential profile matches well), or the total integrated charge can be matched between the two situations, in which case the charge storage depth is well matched. For the purpose of this work, we choose to attempt to match potential maxima, because this parameter is experimentally accessible (see Section §5.4.1). We justify the usage of a block doping model - even though, as seen in Section §4.1.2, a more complicated description is feasible - because the doping profiles of devices are generally proprietary information.

One of the main technical complications with modelling buried channel CCDs using Technology Computer Aided Design (TCAD) software is that (as described in Section §3.2.2) the buried channel must be depleted of majority carriers prior to imaging use. Two approaches are possible within Silvaco: either to add explicitly to the model a drain contact, or to manipulate the Quasi-Fermi Level (QFL) for the buried channel majority carriers (in this case electrons), solve Poisson's equation, then perform a short transient simulation including the continuity equations such that the carriers disappear. Manipulation of the QFL is preferred due to not requiring a change to the device mesh, but it can introduce convergence problems in the solution and is somewhat inconvenient due to the inability to command ATLAS to automatically "sweep" a range of solutions. The pixel was simulated with a mesh point spacing of $0.1\,\mu$m near the storage region, rising to $0.5\,\mu$m at the back surface. All simulations were all performed in two dimensions. For a back bias $V_{BS} = -70\,$V, potential and electric field contours for the parallel direction near to the collection area are plotted in Figure 6.1 and for the serial direction in Figure 6.2.

6.1.1 Potentials

Empty well conditions were simulated for a series of V_{BS} values from -5V to -70V. Cut lines through the z direction at $(x, y) = (0, 0)$ and the x and y directions for $z = 0.5\,\mu$m are shown in Figure 6.3. The height of the maximum channel potential is seen to decrease as V_{BS} is made more negative, though its location in depth remains constant. The width of the confining potential in both the lateral dimensions also increases with increasingly negative V_{BS}. Neither of these effects is predicted by the potential model presented in Chapter 4, though both effects are relatively small - the channel maximum increases by $1V$ over the whole range, and the width of the confining potentials changes by less than $1\,\mu$m over the same range.

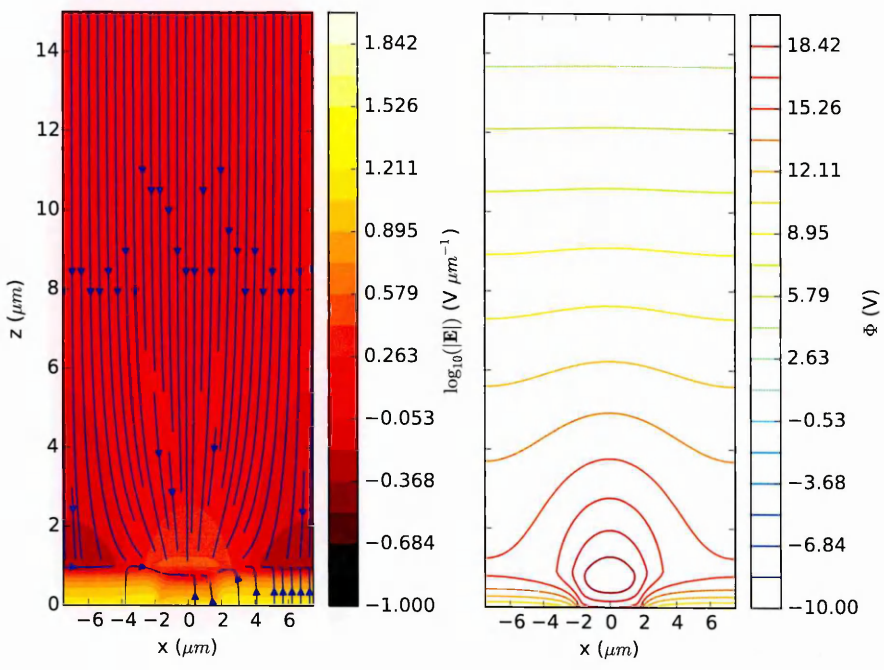

Figure 6.1: Finite Element Simulation of potential (right panel) and electric field (left panel) for the parallel direction.

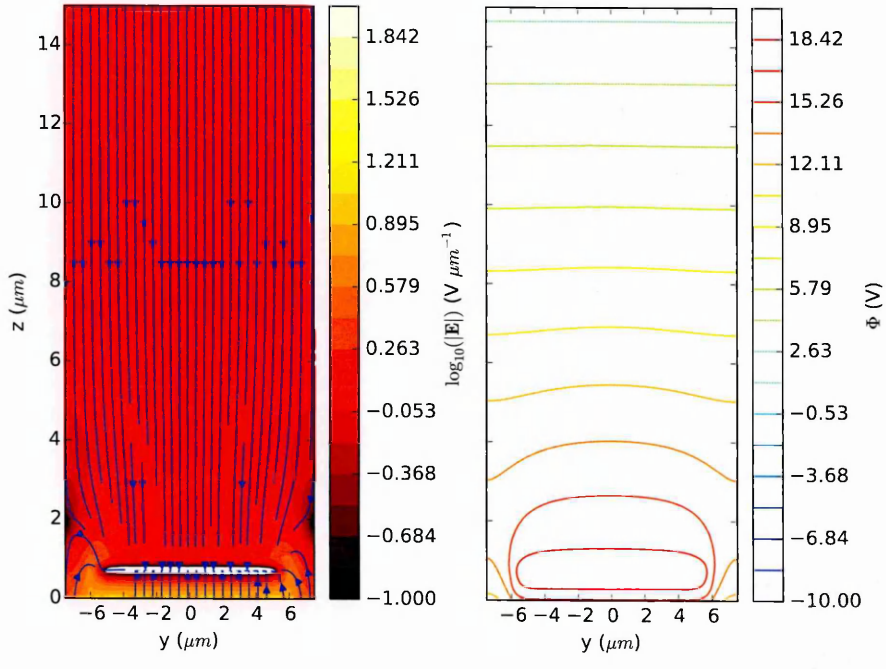

Figure 6.2: Finite Element Simulation of potential (right panel) and electric field (left panel) for the serial direction

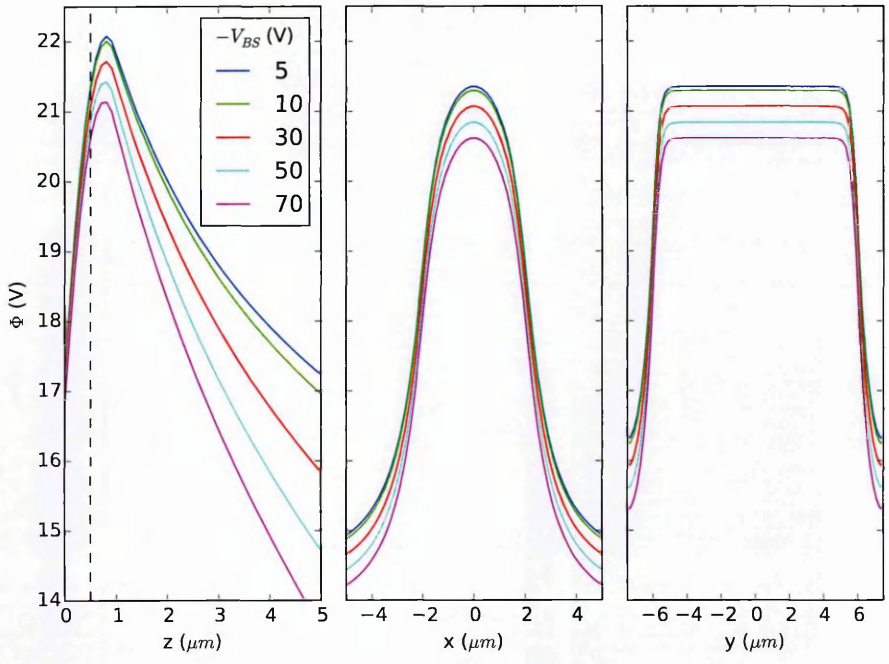

Figure 6.3: Potential cut lines through Silvaco simulations for different back biases

Potentials and fields calculated from Silvaco are compared with those calculated from our analytical model in Figure 6.4, for $V_{\mathrm{BS}} = -30\,\mathrm{V}$ and $V_{\mathrm{BS}} = -70\,\mathrm{V}$. The shape of the potentials agree fairly well, though the analytical potentials are underestimated at low depths, and slightly overestimated at high depth. The slope of the corresponding field is well matched, though the field is overall slightly over-estimated by the analytical model. One possible explanation is the existence of free charge within the substrate, which might screen the field somewhat. The right hand panel of Figure 6.4 shows the electron concentration from the Silvaco simulations against depth. At the back surface, a build up of electrons occurs. The concentration at the back surface approaches $n \approx 10^6\,\mathrm{cm}^{-3}$, and increases more rapidly at $V_{\mathrm{BS}} = -70\,\mathrm{V}$ than $V_{\mathrm{BS}} = -30\,\mathrm{V}$. In a real device, it is likely that the nature of this concentration depends on the back surface treatment applied during manufacture. As expected, the electric field magnitude for $V_{\mathrm{BS}} = -70\,\mathrm{V}$ approaches $1\,\mathrm{V}\,\mu\mathrm{m}^{-1}$ near the surface, well into the regimen of relevance for velocity saturation.

6.1.2 Charge Storage

As the electron QFL $\phi_{f,n}$ moves from low to high voltage, the amount of charge stored in the pixel decreases, until complete depletion is reached at a value of around $\phi_{f,n} = 20\,\mathrm{V}$. The total charge Q stored in the pixel is found by integrating the electron concentration over the device mesh between over the range $x = -5\,\mu\mathrm{m}$ to $x = 5\,\mu\mathrm{m}$, $z = 0\,\mu\mathrm{m}$ to $z = 2\,\mu\mathrm{m}$. The

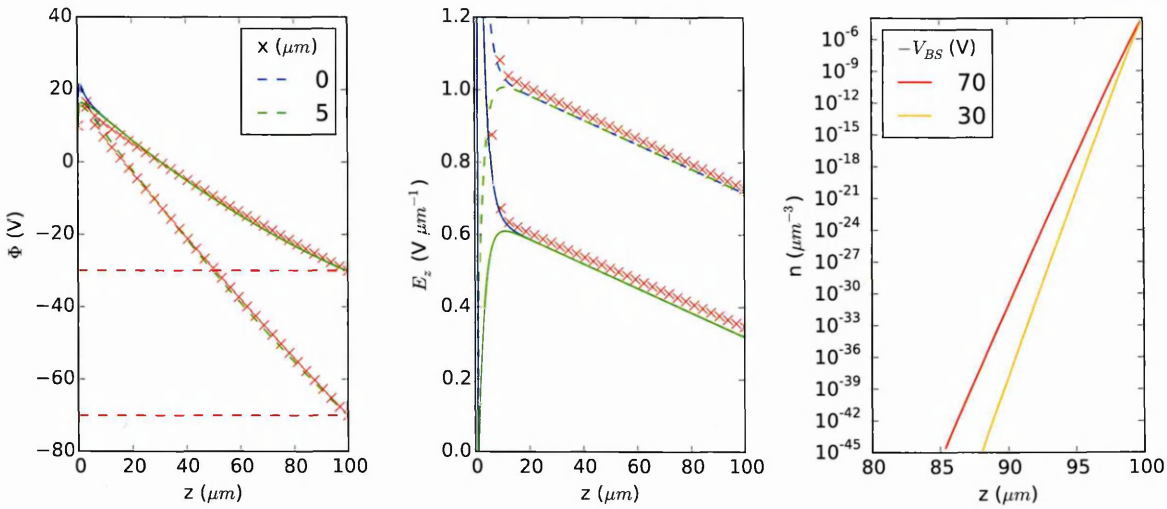

Figure 6.4: Comparison of potentials and fields calculated by Silvaco and by analytical model.

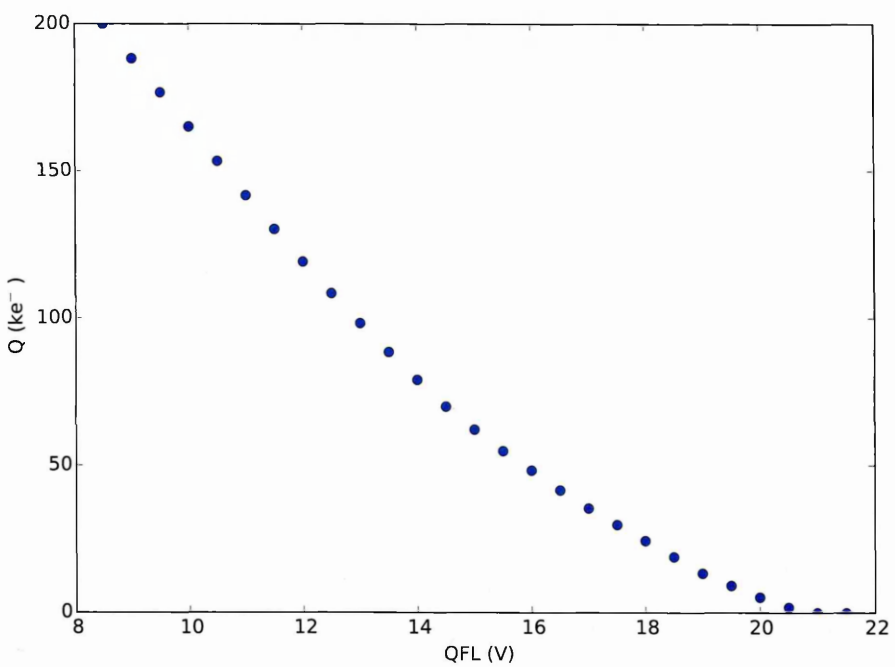

Figure 6.5: Charge stored in simulated pixel for varying electron QFL

results (for $V_{\mathrm{BS}} = -70\,\mathrm{V}$) are shown in Figure 6.5. Thus, varying the QFL is a convenient way to efficiently simulate the charge storage properties of a pixel - the alternative being to start with an empty pixel and progressively add charge via photo-generation, which requires transient simulations. This approach is not useful, however, for simulating dynamic charge collection itself.

It is informative to examine the electron distribution and potential profiles produced at different values of the QFL. Examples are plotted in Figure 6.6. From the electron concentration vs depth plot (upper left panel), we see that electrons begin to contact the

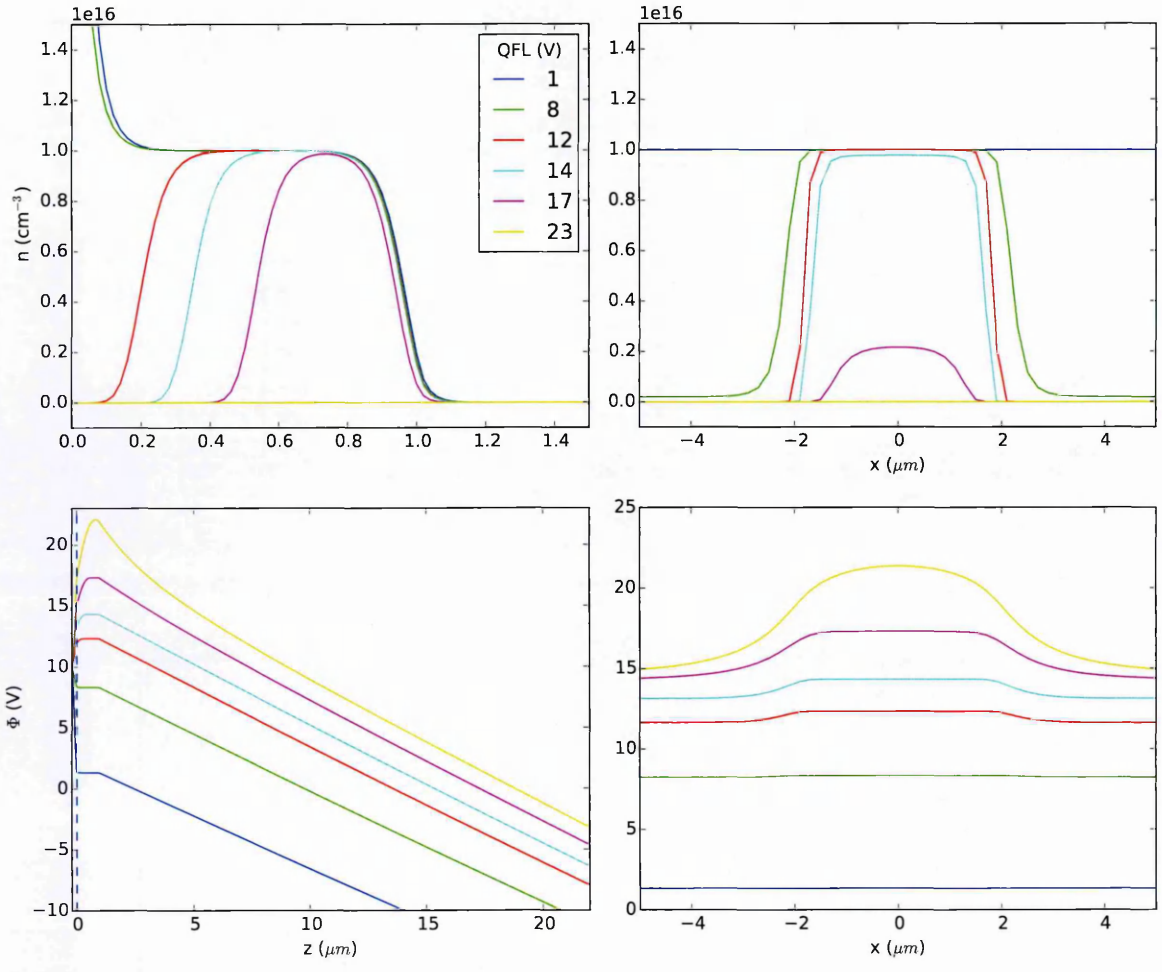

Figure 6.6: Electron concentration (upper panels) and potential (lower panels) profiles for varying electron QFL. The back side bias is set at $V_{BS} = -70\,\mathrm{V}$, the collecting phase voltage is $V_G = 10\,\mathrm{V}$, and the barrier phase voltage is $V_T = 0\,\mathrm{V}$. The plots show cut lines through the planes $x = 0\,\mu\mathrm{m}$ (left panels) and $z = 0.5\,\mu\mathrm{m}$ (right panels).

surface at a QFL value somewhere between 8V and 12V, corresponding to a stored pixel charge between $Q \approx 210\,\mathrm{ke}^-$ and $Q \approx 160\,\mathrm{ke}^-$, which is a significant under-estimate compared to our full well measurements on the CCD261 (Section §5.4.3) This is to be expected given the narrower collecting gate width of the simulation vs the real CCD261. The pixel charge density vanishes at a QFL value between 17V and 23V, which agrees well with the operating point used in the CCD261 for the reset drain $V_{RD} = 17\,\mathrm{V}$. The channel parameter of the model (measurable from the lower left panel of Figure 6.6) is $\phi_{ch} = 11\,\mathrm{V}$, somewhat higher than that measured for the CCD261 (see Section §5.4.1).

The Silvaco simulation was used also to test our assumption in Section §4.2 that the width of the stored charge packet is the same as that of the collecting gate. Of all the simplifications that were made in developing our dynamic charge collection model, this is perhaps the least well justified. An example electron distribution from the finite element simulation is shown

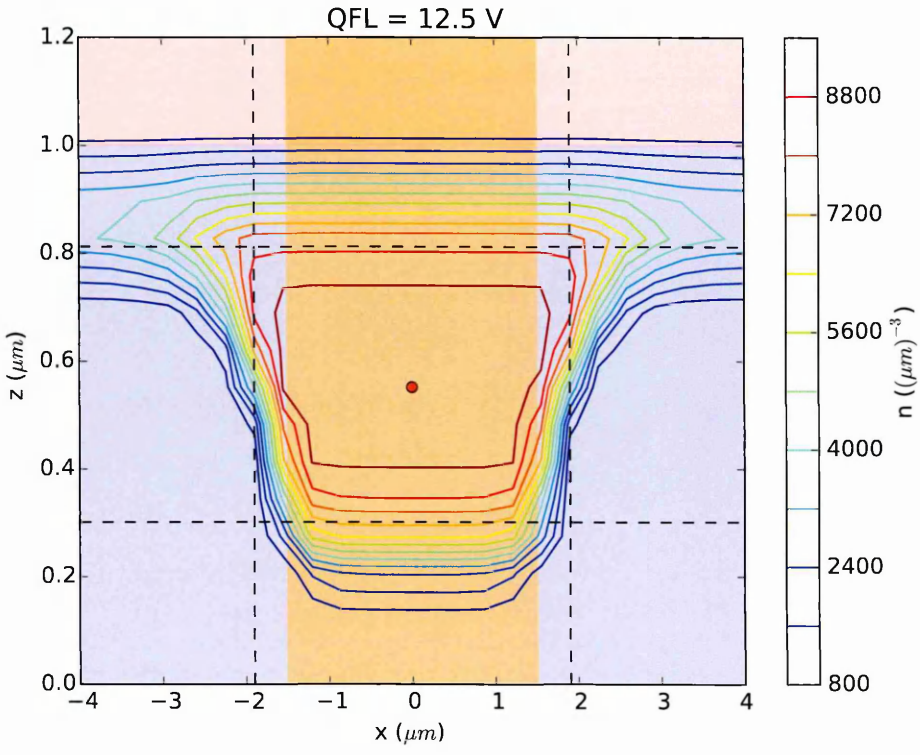

Figure 6.7: Stored charge density in a pixel. The geometric width of the collecting gate is indicated by the shaded orange region. The n-type region below the junction depth z_T is indicated by the blue shaded region, and the p-type substrate region is indicated by the red shaded region. The located charge density maximum is marked by a red circle. The black dashed lines indicate the located FWHM planes.

in Figure 6.7. Clearly, the stored charge distribution is neither perfectly cuboid nor limited in extent to the width of the collecting gate. However, the charge density is quite uniform and drops off rapidly at its edges. We compare the charge storage in the finite element simulation to the 1D storage model described in Section §4.2 by locating the position of the maximum charge density, and the positions where the distribution drops to half of its maximum value. The result of repeating this process over different stored charge values is shown in Figure 6.8. Note the accuracy of the locations is limited to the nearest mesh points. The storage depths predicted by the 1D volume model agree well, but it is again clear that the width assumption is invalid. Nevertheless, the charge distribution does reach a stable width at a signal level of around $60\,\mathrm{ke}^-$.

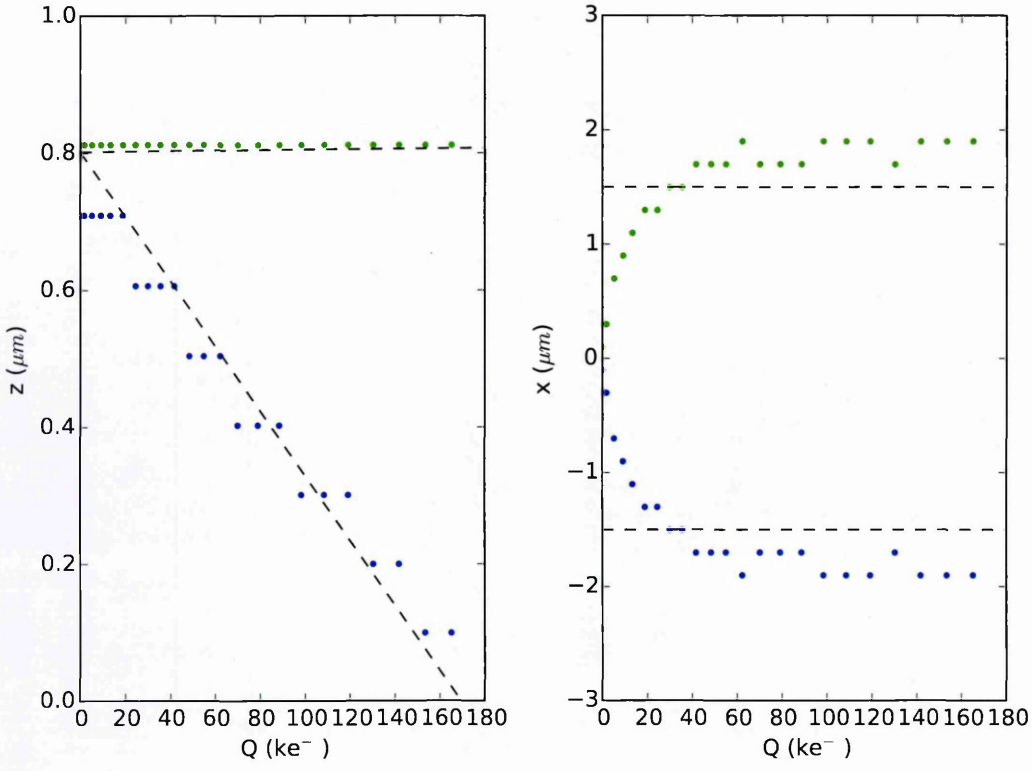

Figure 6.8: Change in charge packet size with signal level. The dashed black lines indicate the predictions of the 1D analytical storage model

6.2 e2v CCD261

One of the principle experimental effects of the BFE is to cause correlations between values in nearby pixels [27]. The correlation coefficients R_{ij} are defined, for an image I_{ij} as:

$$R_{ij} = \frac{\mathrm{cov}\left(I_{00}, I_{ij}\right)}{\sigma_{00}\sigma_{ij}} \tag{6.1}$$

where σ_{ij} is the standard deviation in the measured value at pixel (i, j). For a perfect flat field illumination, the values of σ_{ij} should be the same for all pixels, reducing (6.1) to:

$$R_{ij} = \frac{\mathrm{cov}\left(I_{00}, I_{ij}\right)}{\sigma_{ij}^2}. \tag{6.2}$$

Note that, in an image which has been affected by the BFE the values of variance actually vary with position, but following the convention of previous investigations [81, 68, 27] we still use this condition, chiefly because it is convenient to normalise the R_{ij} values with a number that can be measured from a single image (namely, the spatial variance of the image). Using individual variances for pixel positions requires a lot more data to be captured. Using the

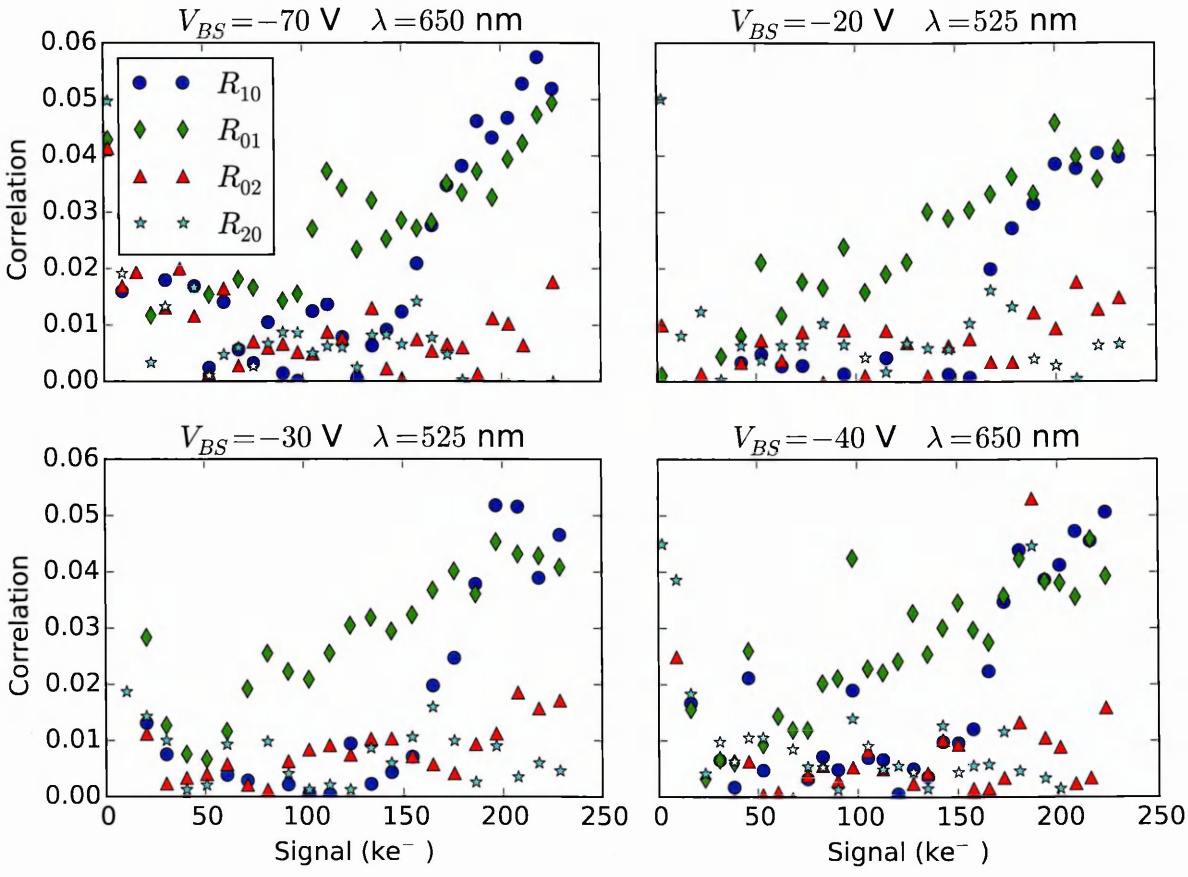

Figure 6.9: Measured flat-field correlation coefficients for the CCD261

single variance normalisation requires in principle only the same dataset as for a flat-field PTC curve to derive the values for R_{ij}. The calculation of correlation coefficients can be performed very efficiently using the Wiener-Khinchin theorem [83], stating that the autocorrelation of a function is equivalent to the square magnitude of its power-spectral density.

Previous publications have reported linearly increasing correlation values with increasing stored signal in a CCD, with the nearest-neighbour vertical coefficient R_{01} being systematically much larger than the other coefficients. Whilst results on the CCD261 largely agree with this assessment, we find that the nearest neighbour horizontal coefficient R_{10} remains small until a threshold of around 150 ke$^-$, where it rapidly increases to approximately match the value of R_{01}. This behaviour is observed across all values of V_{BS} (see Figure 6.9), but is not predicted by any model of the BFE known to the author, including the dynamic model presented in Chapter 4. To speculate, it is possible that the shape of the buried channel implant in the serial direction is involved in this phenomenon. After implantation and thermal drive-in, the depth profile of the n-type material forming the channel is not completely vertical: it extends under the masked channel stop regions slightly due to diffusion during the process. Then, a

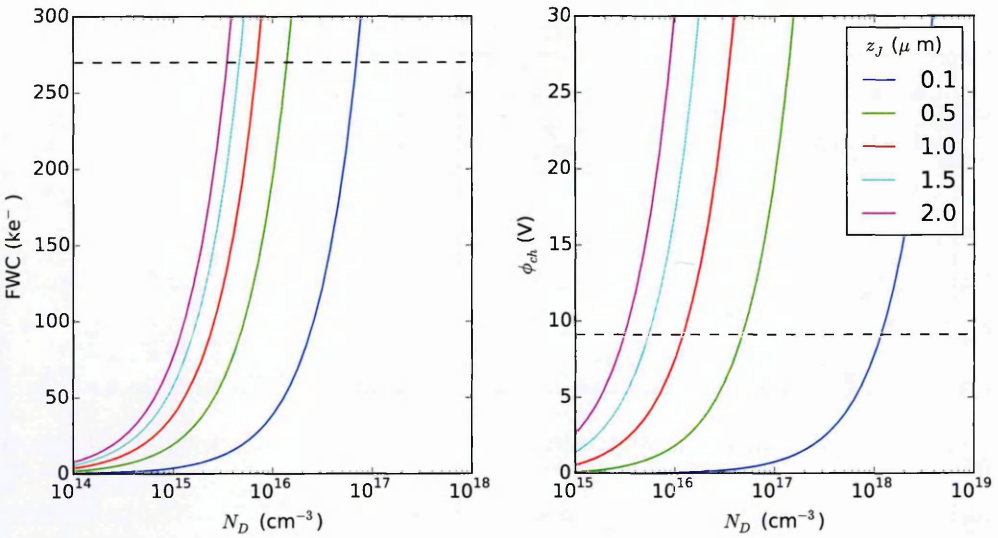

Figure 6.10: Parameter space graphs for estimating z_J and N_D. The dashed lines show the empirically measured values for full well capacity (left panel) and channel potential (right panel). The solid lines represent solutions from the 1D charge storage model.

charge packet may gradually extend into the channel stop region, slightly reducing the channel stop confinement and allowing the correlations to increase. Future work should concentrate on discovering whether this effect can be replicated in other sensors by varying operating conditions, and finding the mechanistic cause, since this reduction in correlation may be very useful in operating thick sensors to combat the BFE.

To proceed with attempting to match simulation with experiment, it is necessary to choose values for the free parameters in the simulation, namely: the gate width L, the oxide thickness d_{ox}, the doping densities N_A and N_D, the device thickness z_T, the junction depth z_J, the pixel pitch α and the distance to the channel stops y_B. For the CCD261, we know from the data sheet $\alpha = 15\,\mu m$ and $z_T = 100\,\mu$m. In the operating conditions used in our experiments (using the widest collecting gate during integration), $L = 5\,\mu$m. As representative (though not necessarily completely accurate values), we choose $d_{\text{ox}} = 0.1\,\mu$m and $y_B = 6.5\,\mu$m. A value for N_A was measured in Section §5.4.2, and found to be $N_A = (2.0 \pm 0.2) \times 10^{12}\,\text{cm}^{-3}$.

The remaining free parameters z_J and N_D are estimated with the assistance of the 1D charge storage model presented in Section §4.2. Using (4.91), we have a relationship between the minimum of the stored charge packet, and the amount of charge stored in the pixel. When the stored charge is equal to the full well capacity, assuming the device is set up to reach surface full well conditions, the value of the minimum charge packet depth will be $z_0 = 0$. Having measured full well capacities for the CCD261 (see Section §5.4.3), we

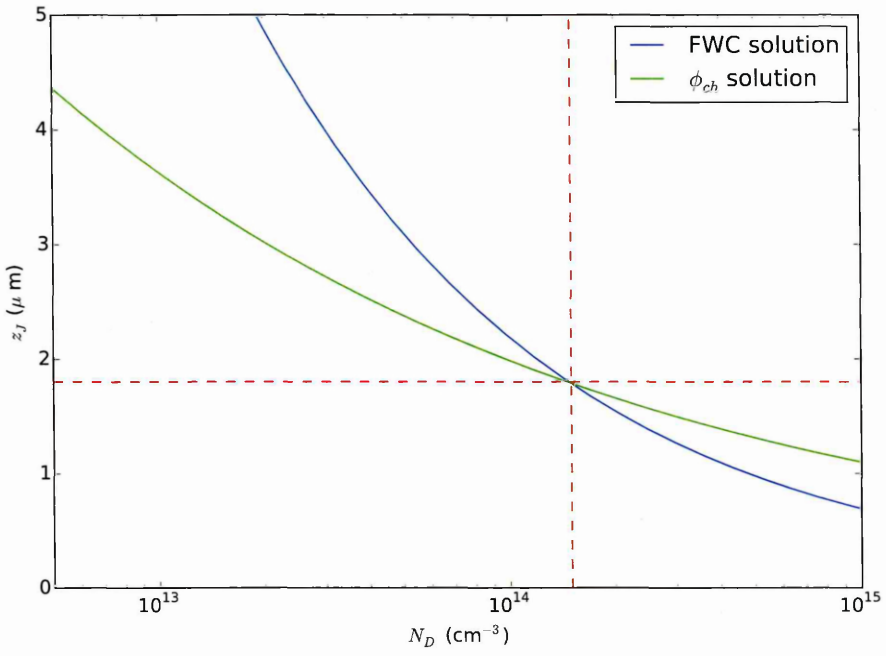

Figure 6.11: Graphical fit to find the most suitable values of N_D and z_J for simulation

can use (4.91) to constrain the sensible values for z_J and N_D. In addition, (4.93) gives a relationship between z_J, N_D and the maximum channel potential. Having measured the channel parameter of the CCD261 (see Section §5.4.1), we also have an empirical value to insert into this equation. Representations of these equations using the parameters described so far are shown in Figure 6.10. Solving the two equations simultaneously for the two unknowns yields values for z_J and N_D. For a range of values for N_D, we find using Brent's method the value of z_J which satisfies the empirically measured value. The point where the solutions for (4.93) and (4.91) coincide is the estimate for the parameters used in modelling. The solution is illustrated graphically in Figure 6.11. We find that values of $N_D = 1.5 \times 10^{14}\,\mathrm{cm}^{-3}$ and $z_J = 1.8\,\mu\mathrm{m}$ satisfy both constraints.

Mean-variance simulations (as described in Section §4.5) were performed using the estimated parameters, for a representative wavelength of $\lambda = 550\,\mathrm{nm}$ and a range of values for V_{BS}. For each simulation, a quadratic was fitted to the mean-variance curve as described in Section §5.6. The value of the quadratic coefficient β for the simulated and measured values is shown in Figure 6.12, and found to be in reasonably good agreement. However, the simulation does systematically over-estimate the degree of non-linearity (note that the more non-linear a mean-variance curve, the more negative the value of β). It is unlikely that this is related to the phenomena of the rapidly rising R_{01} correlation coefficient described previously, since in that case we would expect to under-estimate the non-linearity. As noted in Section §4.5, the

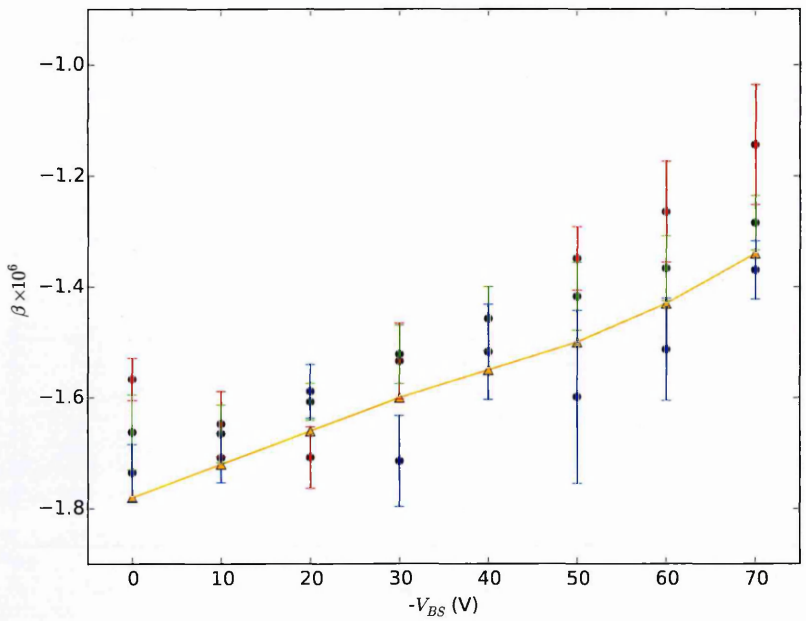

Figure 6.12: Flat field non-linearity of CCD261 PTC compared with simulation. The red, green and blue points represent measurements at different wavelengths (see Table 5.3). The orange points and line represent the simulated solution for $\lambda = 550\,\mathrm{nm}$.

expected recovery of linearity near $V_{\mathrm{BS}} = 0\,\mathrm{V}$ due to incomplete depletion is arguably evident in the experimental data, but not modelled by the simulation.

6.3 e2v CCD250 candidate LSST detector

The e2v CCD250 sensor was designed specifically for the LSST telescope. It is a deep depletion 4k×4k format device, with active thickness $z_T = 100\,\mu\mathrm{m}$ and pixel dimension $\alpha = 10\,\mu\mathrm{m}$ [59]. PTC data taken at a temperature of $T = -100°\mathrm{C}$ over a range of backside bias voltages between $V_{\mathrm{BS}} = 0\mathrm{V}$ and $V_{\mathrm{BS}} = -70\mathrm{V}$, and at two incident wavelengths $\lambda = 827\,\mathrm{nm}$ and $\lambda = 546\,\mathrm{nm}$ was kindly provided by Dr. Ivan Kotov at Brookhaven National Laboratory. Some results of our analysis of this data have been previously published [104].

For each backside bias voltage and wavelength, a PTC was taken, consisting of 30 pairs of images at differing exposure times, which were subtracted to eliminate FPN. For each experiment, 6 bias frames at zero exposure time were also taken. The illumination for the detector consisted of a broadband emission source followed by a monochromator tuned to the appropriate wavelength. Apart from V_{BS} , all voltages were held constant for all runs. The operating voltages are shown in Table 6.1. The CCD250 is readout through two registers at opposite sides of the device, each with an output tap in 8 locations, giving 16 total outputs

Name	Symbol	DC level (V)	High Value (V)	Low Value (V)
Output Drain	V_{OD}	29.5		
Guard Drain	V_{GD}	26		
Output Gate	V_{OG}	4		
Reset Drain	V_{RD}	18		
Reset Clock	$V_{\Phi R}$		12	0
Image Clocks	$V_{I\Phi}$		9	0
Serial Clocks	$V_{R\Phi}$		9.5	0.5

Table 6.1: Operating conditions for the e2v CCD250 test

per device. This architecture is necessary to achieve the high readout rate demanded by the LSST application [3], without introducing too much readout noise, which is specified as $5\,e^-$ [59].

On initial examination of the data, it was found that some variances of difference images were extremely high, severely affecting the stability and accuracy of the PTC fitting procedure. These points seem to be dispersed fairly uniformly, though at random, throughout the dataset. The culprit of these spurious variances was found to be the reliability of the mean level. An example linearity plot is shown in Figure 6.13, where despite generally good linearity, a clear discontinuity can be seen at a certain integration time. These discontinuities appear throughout the data set, and are not consistent in which value of exposure time is affected, leading us to suspect a problem with the stability of illumination rather than the repeatability of integration times. When the mean illumination level changes in between two pairs of a flat field measurement, the result is that the subtraction of the two images does not cancel FPN, causing the anomalous variances observed. This can be clearly seen in Figure 6.14 which plots the mean and variance of the raw frames before differencing for a single PTC acquisition. Though the points clearly lie on the same (non-FPN corrected) mean-variance curve, the resulting differenced image is essentially useless from the shot noise measurement point of view.

We proceeded with the data analysis by implementing a rolling local variance filter on the differenced PTC curves. Any point which was further than 5σ outside the variance of the neighbouring 7 points was discarded from analysis. This procedure allowed the recovery of some useful data, but the reduction in precision due to the temporally inconsistent illumination is likely still the largest source of error, especially when it comes to the measurement of correlation coefficients.

As reported by other published results on the CCD250 sensor [42], individual calibration of the channels shows that the non-linearity of the mean-variance curve expressed in units

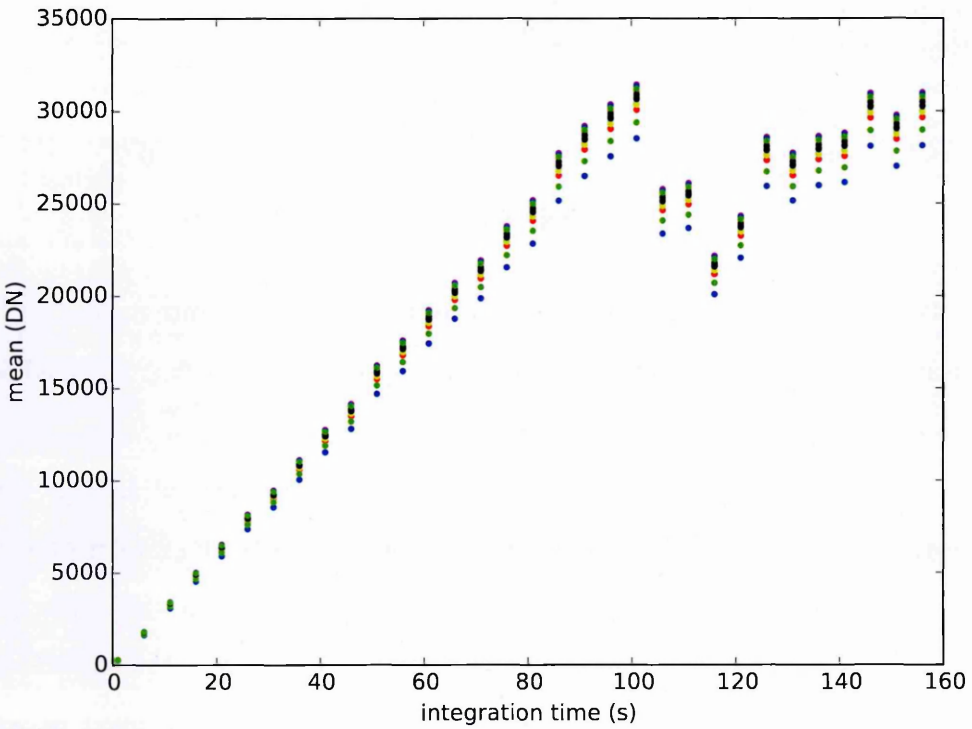

Figure 6.13: Example CCD250 linearity plot. Each colour represents a different CCD output. The sharp discontinuity at around $t_{\text{int}} = 6s$ reveals a major issue with the reliability of either the exposure time or the incident illumination level.

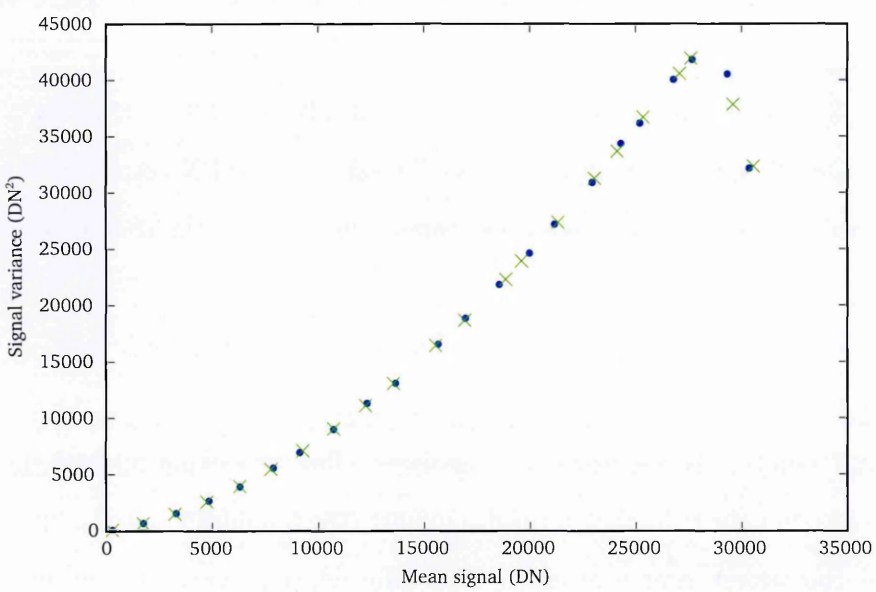

Figure 6.14: Example problematic raw mean-variance curve showing the first images (dots) and the second images (crosses) taken at the same integration time.

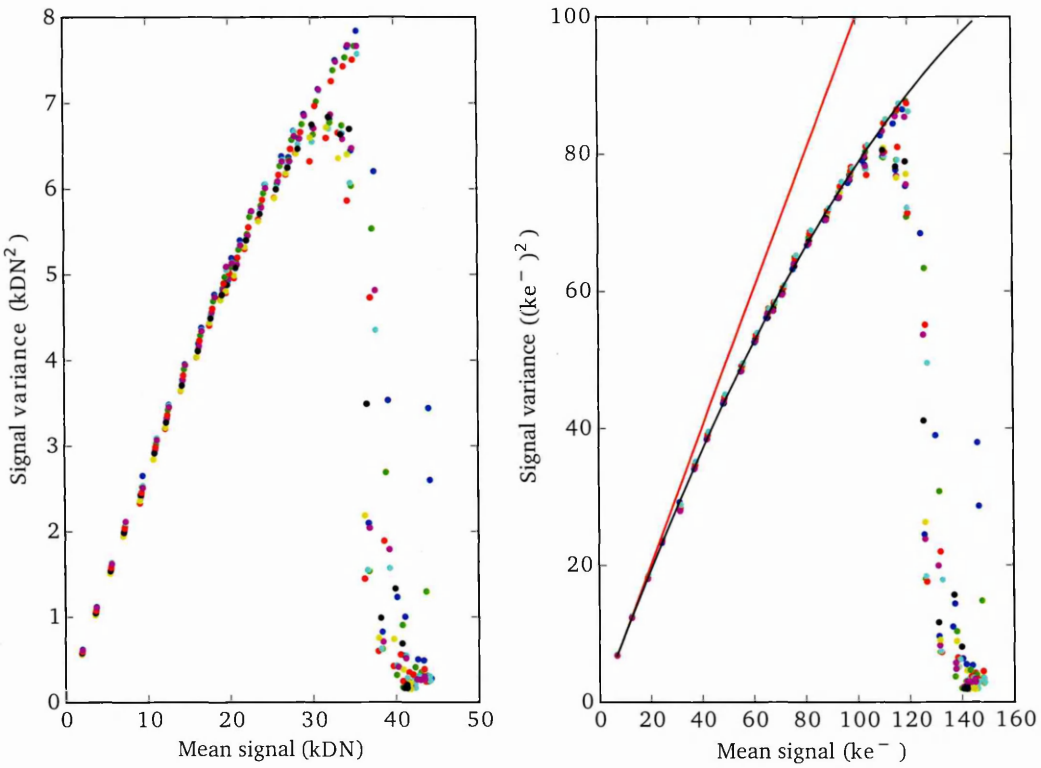

Figure 6.15: Mean-variance curves for $\lambda = 546\,\text{nm}$, $V_{BS} = -40\,V$, before (left panel) and after (right panel) per-channel calibration. The red plotted line indicates the shot noise condition.

of electrons is equal throughout the device (see Figure 6.15). We note that the full well capacity found in this dataset ($\approx 110\,\text{ke}^-$) is somewhat lower than that reported by previous studies. Whether this is due to different operating voltages or a different clocking sequence (the CCD250 has four image phases) is unknown, though one reported measurement [42] was taken at $V_G = 10\,\text{V}$, as opposed to the $V_G = 9.5\,\text{V}$ reported here. The camera gain for the sensor overall was found to be around $0.29\,\text{DN}\,(e^-)^{-1}$, with four channels (channels 8, 9, 10 and 11) exhibiting anomalous measurements. On inspection of images, these channels were visibly non-uniformly illuminated, and were not used for any further analysis. The gain measurements across all data are summarised in Figure 6.16.

The read noise of the device was assessed using the standard deviation of differenced bias frames. Apart from channels 8 and 9, the readout noise of the device was found to be mostly within the specified $5e^-$ value (see Figure 6.17).

In order to attempt to match charge collection simulations with the CCD250 data, relevant values for geometric and doping parameters must again be chosen. The pixel pitch is known as $\alpha = 10\,\mu\text{m}$, and the collecting gate width for the experiments presented here is $L = 3\,\mu\text{m}$. Again, we choose reasonable values of $d_{\text{ox}} = 0.1\,\mu\text{m}$ and $y_B = 4.5\,\mu\text{m}$. The device

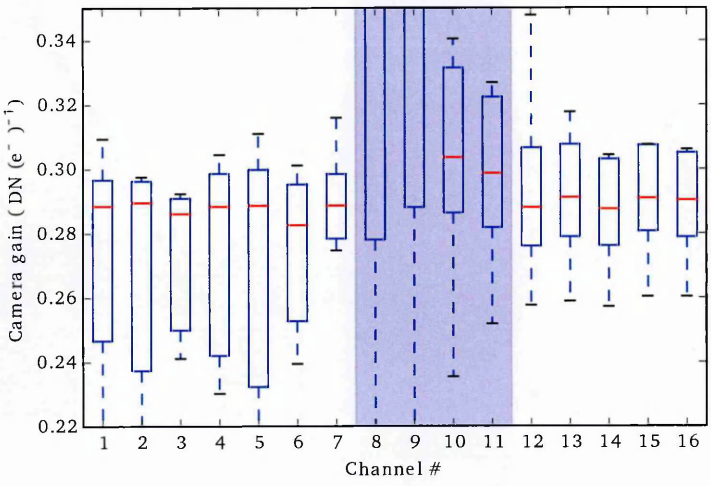

Figure 6.16: Summary statistics for camera gain measurements across the detector channels. Channels 8, 9, 10 and 11 (shaded) were not used in data analysis

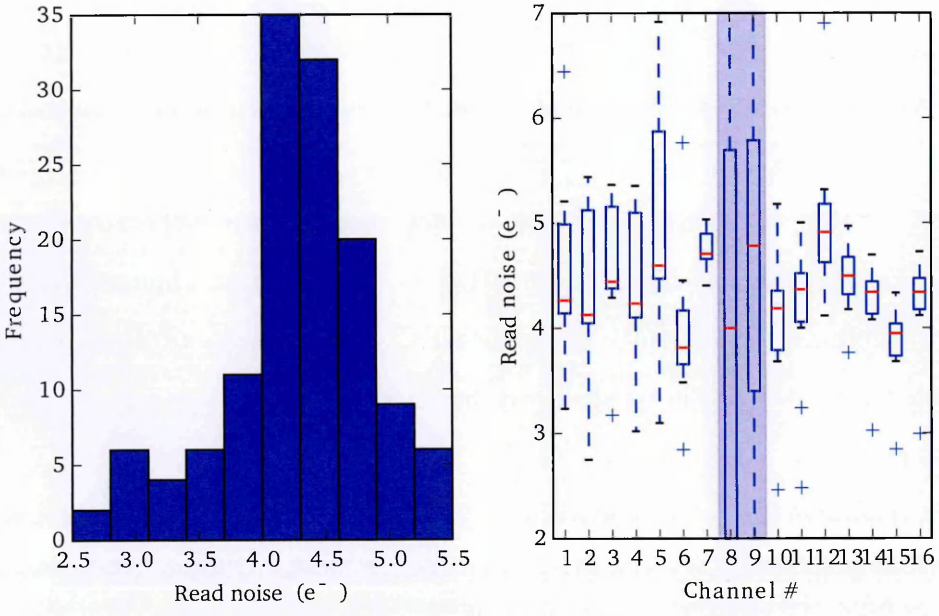

Figure 6.17: Analysis of CCD250 read noise using bias frames. A histogram of all read noise measurements from each differenced bias frame (left panel), and box plots of the read noises of each channel (right panel). Channels 8 and 9 (shaded) show particularly high variability in the read noise measured.

thickness is known as $z_T = 100\,\mu$m. Without access to experimental data for channel potential measurements, it is hard to justifiably choose values for the remaining parameters N_A, N_D and z_J. For N_A, we note that a depletion depth measurement similar to that given in in Section §5.4.2 has been presented in the literature for the CCD250 [26], in comparison with sensors from other vendors. Though an analysis of substrate resistivity was not performed by the original authors, from their Figure 4 it is estimated that the CCD250 they tested became fully depleted at a back side bias voltage of at most $V_{BS} = -10\,$V, implying that the substrate doping corresponds at least roughly to a similar resistivity to that measured for the CCD261, and is indeed quoted in the specifications as being $\geq 5000\,\Omega cm^{-1}$. Therefore, the CCD261 measured value $N_A = 2 \times 10^{12}\,\mathrm{cm}^{-3}$ is taken as being a relevant estimate. Remaining to be obtained are values for N_D and z_J.

In electrostatic point charge simulations of the BFE, it has been reported [5] that a storage depth of $2.5\,\mu$m fitted the experimental results very well. Though the nature of simulations using point charge should differ somewhat from our simulations using a solid block of charge, it is likely that the optimum storage depth is similar between the two situations, though as noted in Section §4.5 it is likely that the point source model over-estimates somewhat. It is also noted that, given the reported full well capacity of the CCD250 as $\sim 150\,\mathrm{ke}^-$ [26], the stored charge per unit collecting area is:

$$\rho_{\mathrm{coll}} = \frac{150}{3 \times 9} \approx 5.6\,\mathrm{ke}\,\mu\mathrm{m}^{-2} \tag{6.3}$$

which may (somewhat crudely) be compared to the value for the CCD261 of $\approx 3.7\,\mathrm{ke}^-\,\mu\mathrm{m}^{-2}$. These values are both under-estimates, given that charge storage width is in fact slightly wider than the collecting gate, as shown in Section §6.1. Nevertheless, the significantly higher per-area storage capacity of the CCD250 implies that its buried channel must have a correspondingly higher channel potential, and hence either a higher dopant density N_D, or a deeper storage depth z_J, or both. After some experimentation, it was found that values of $N_D = 2 \times 10^{15}\,\mathrm{cm}^{-3}$ and $z_J = 2\,\mu$m worked reasonably well. It is presumed that the low full well value measured in the CCD250 data set presented here is due to a lower collecting gate voltage V_G than presented in the literature. The effect of this should be to increase the non-linearity beyond our simulation's predictions. However, since we have chosen N_D and z_J to match quite well, rather than on the basis of direct experimental tests, it is likely that in fact any major under-estimate is incorporated into our chosen values for these parameters.

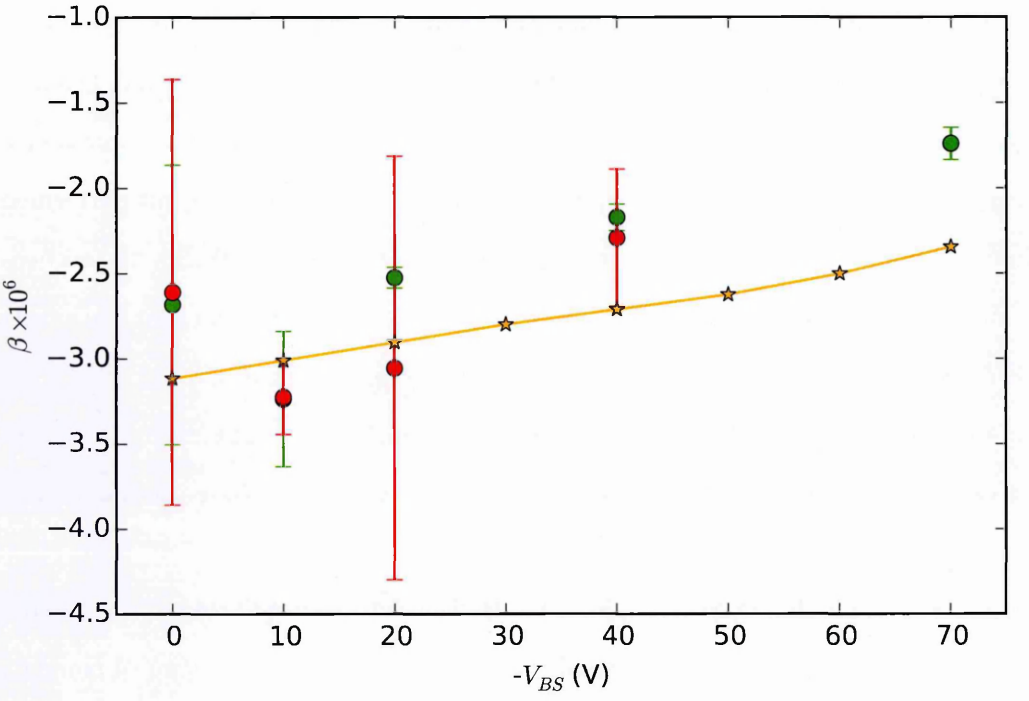

Figure 6.18: Measured and simulated flat field non-linearity of CCD250. Colours show the different incident wavelengths ($\lambda_{\text{red}} = 827\,\text{nm}$, $\lambda_{\text{green}} = 546\,\text{nm}$)

The measured non-linearities from our CCD250 dataset are plotted along with the simulation predictions for a range of V_{BS} values and the two wavelengths in Figure 6.18. In fact, the simulation tends to over estimate the degree of non-linearity, as found with the CCD261. In general the measured (and simulated) mean-variance curves for the CCD250 show that it exhibits much more non-linearity than the CCD261. This is expected due to its smaller pixel size as compared with the device thickness: the magnitude of the collecting fields applied is broadly speaking very similar between the two devices, so the movements of the boundary field lines in physical units should also be quite similar. Then, the measured correlations between pixels is roughly scaled by the pixel size. Very crudely, we note that the measured non-linearity of the CCD261 at $V_{BS} = -70\,\text{V}$ is $\beta \approx -1.3 \times 10^{-6}$. The corresponding value for the CCD250 is $\beta \approx -2.0 \times 10^{-6}$. This gives a ratio of ≈ 1.5, which is the same ratio as that between the pixel pitches.

From the CCD250 flat field data set, correlation coefficients were also measured. An example for a single wavelength and V_{BS} is shown in Figure 6.19. As reported by other authors [5], the "early" increase in R_{10} which was observed in the CCD261 is not present in the CCD250. Using the statistical precision accorded by combining all 16 channels of the CCD250, the correlation coefficients measured are quite well behaved, and amenable to

fitting using a linear function. These so-called "correlation slopes" are integral to a correction strategy using ancillary pixel data (described in Section §6.4). The observed variation in the correlation slopes for R_{10}, R_{01}, R_{20} and R_{02} with V_{BS} is presented in Figure 6.20, along with estimates from our simulations (which are obtained from the same run as for the mean-variance non-linearity values, just as for a real experiment, where both measurements are obtained from a single flat-field illuminated dataset). The general trend of the results is quite well matched for R_{10} and R_{20}, though the simulation systematically over-estimates the degree of correlation, and this is particularly pronounced for R_{01}. This is especially true at low bias, where effects due to incomplete depletion (not included at all in the simulations) are likely to become important. The expected linearity recovery at low bias is not clearly seen in the non-linearity of the mean-variance curves (Figure 6.18), but it seems likely that this is causing the disagreement with simulation in the R_{01} value. Note that, in common with previous studies [42], it is found that the value of R_{10} (the nearest neighbour horizontal correlation) actually becomes an anti-correlation for less negative V_{BS}, and that our simulation does predict this to some degree. The explanation is that the BFE causes the shift of pixel boundaries out to a fairly large radius - when the effect is strong (i.e. at low back bias), both boundaries of neighbouring pixels in the horizontal direction are "pulled" towards a pixel containing higher charge. This means that the effective collecting area of these pixels may actually also reduce rather than increase due to being near a pixel with high stored charge, and thus exhibit both a measured anti-correlation at high charge values, and a negative correlation slope. This effect is visible in the boundary shift illustration shown in Section §4.4 (see Figure 4.27). The boundary shift in the vertical direction is much larger in magnitude, but drops off more quickly, changing substantially even between the nearer boundary of the neighbour pixel and the further. Thus, even the nearest neighbour pixels in the vertical direction generally experience an increased effective collecting area due to the BFE.

6.4 Ancillary Pixel Data

An approach to correction of science frames has been recently advanced [42] which can successfully recover the linearity of mean-variance curves and restores the shape of point sources. The method is used empirically to gather "ancillary pixel coefficients" from flat-field calibration data, and using an iterative re-distribution method to reverse the effects of the BFE. We briefly recount the method here, following the same logic used by Antilogus et al [5], before

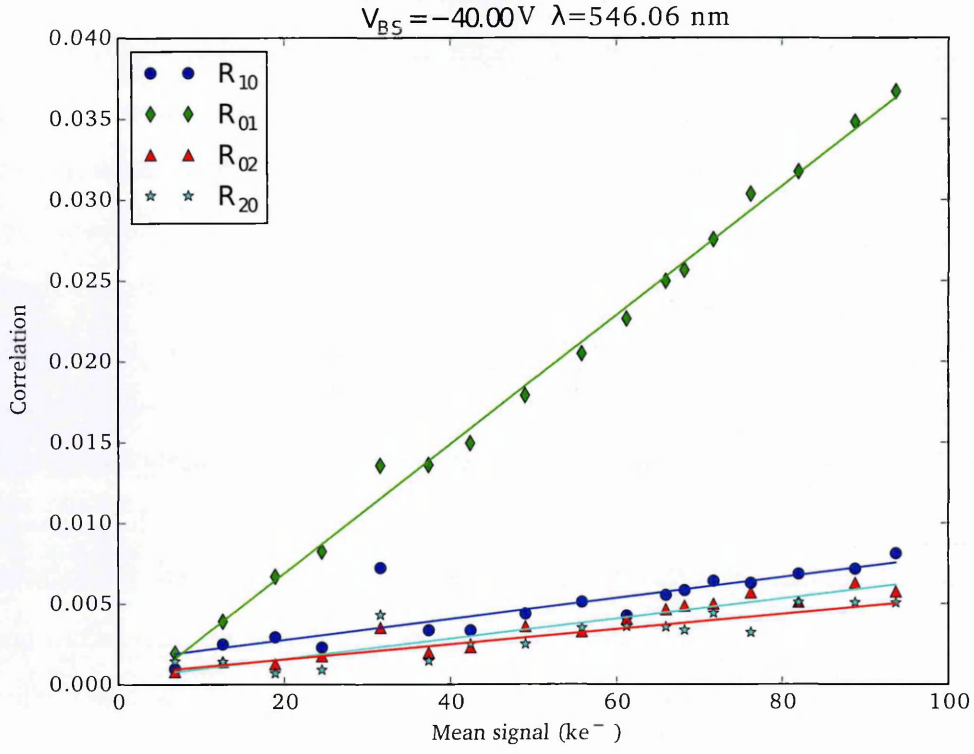

Figure 6.19: Example measured correlation coefficients for the CCD250

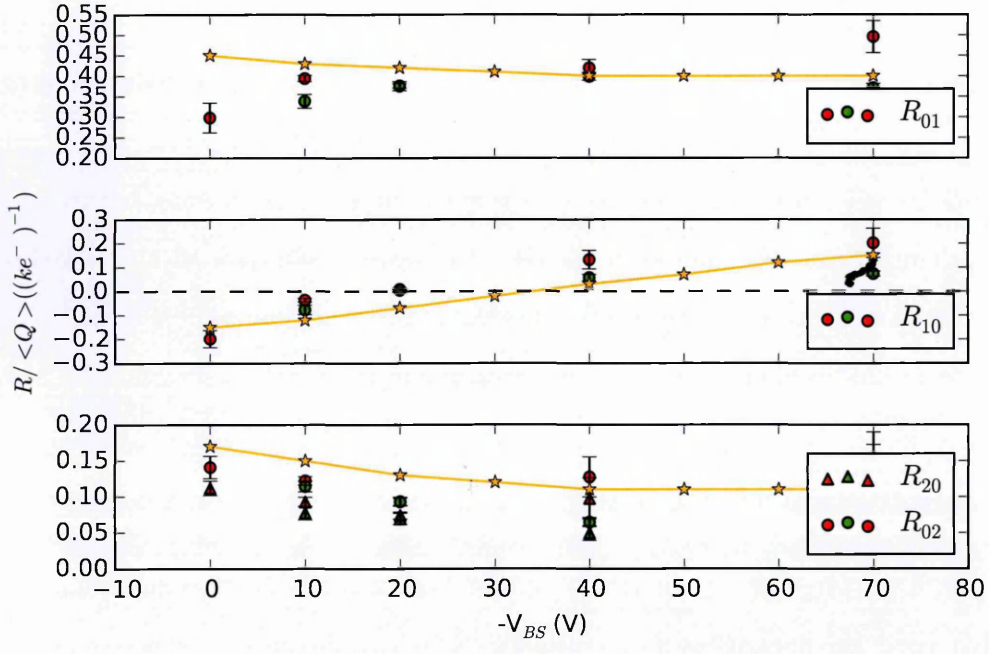

Figure 6.20: Measured correlation coefficient slopes against back bias voltage compared with simulation predictions (orange lines). Colours show the different incident wavelengths (λ_{red} = 827 nm, λ_{green} = 546 nm)

demonstrating the estimation of the ancillary pixel data from our own modelling.

Since the non-linear PTC caused by the BFE is very well fitted using a quadratic function (see Section §5.6), it seems a fair assumption that the effect can be well modelled using first order perturbations. Approximating that the pixel boundary distortion due to a perturbing field is directly proportional to that field, and given that a perturbing field magnitude is directly proportional to its source charge, the following relationship is posited:

$$\delta_{ij}^{X} = \frac{\alpha}{2} \sum_{kl} a_{ij}^{X} Q_{kl} \tag{6.4}$$

where α is the pixel size (as throughout Chapter 4), Q_{ij} is the signal charge in the pixel at position (i,j), δ_{ij}^{X} is the shift in the boundary of pixel (i,j) in direction X (measured in physical distance units), and a_{ij}^{X} are the ancillary pixel coefficients. The index X runs over the four possible 2D boundary directions. (6.4) shows that, in principle, the boundary δ_{ij}^{X} depends on the charges in all nearby pixels. Considering a particular boundary displacement, the amount of signal charge which is "moved" by the BFE from pixel (i,j) to a neighbour over boundary X is:

$$\Delta Q_{ij}^{X} = \frac{\delta_{ij}^{X}}{\alpha} \frac{\left(Q_{ij} + \vec{Q}_{ij}^{X}\right)}{2} \tag{6.5}$$

where the notation $\vec{Q}_{ij}^{X}$ means "the signal in the pixel to the neighbour of (i,j) in the direction X" . The assumption here is that charge is stored perfectly uniformly throughout the entire pixel area, so that a movement of a boundary results in the re-distribution of an amount of charge which is the mean average of the total charges in the pixels, weighted by the amount of boundary shift. This is illustrated in Figure 6.21. The total charge in a pixel (i,j) after re-distribution is :

$$Q'_{ij} = Q_{ij} + \sum_{X} \Delta Q_{ij}^{X} \tag{6.6}$$

and, substituting using (6.4) and (6.5) leads to:

$$Q'_{ij} = Q_{ij} + \frac{1}{4} \sum_{X} \sum_{k,l} a_{kl}^{X} Q_{kl} \left(Q_{ij} + \vec{Q}_{ij}^{X}\right). \tag{6.7}$$

Next, the covariance of two observed pixel values is constructed:

$$\operatorname{cov}\left(Q'_{ij}, Q'_{kl}\right) = \operatorname{cov}\left(Q_{ij} + \Delta Q_{ij}, Q_{kl} + \Delta Q_{kl}\right) \tag{6.8}$$

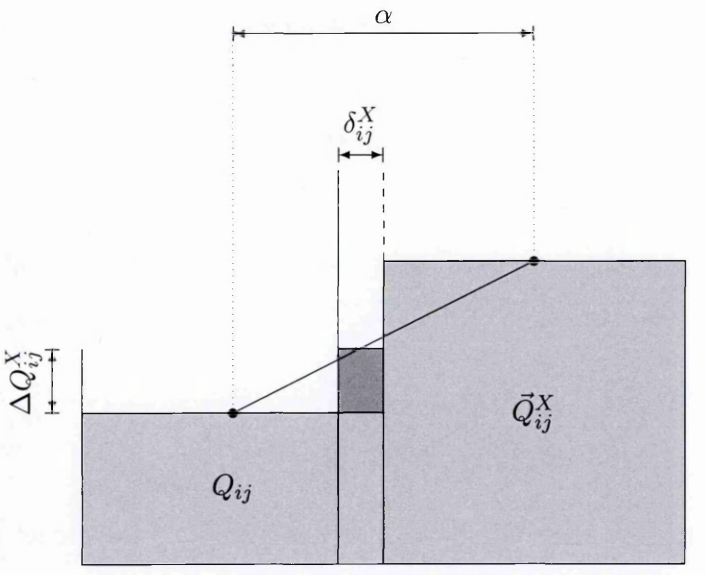

Figure 6.21: Illustration of charge re-distribution due to boundary shift in the ancillary pixel data model. An induced boundary shift of δ_{ij}^X between pixel (i,j) and its neighbour in direction X causes a redistribution of an amount of charge ΔQ_{ij}^X from the pixel with the higher charge to the pixel with lower charge, which is the mean average of the charges Q_{ij} and $\vec{Q}_{ij}^X$ weighted by the boundary shift.

where $\Delta Q_{ij} = \sum_X \Delta Q_{ij}^X$ for brevity. This expression can be expanded using the covariance's distributive property:

$$\begin{aligned} \mathrm{cov}\left(Q'_{ij}, Q'_{kl}\right) &= \cancel{\mathrm{cov}\left(Q_{ij}, Q_{kl}\right)} + \mathrm{cov}\left(Q_{ij}, \Delta Q_{kl}\right) \\ &\quad + \mathrm{cov}\left(Q_{kl}, \Delta Q_{ij}\right) + \cancel{cov\left(\Delta Q_{ij}, \Delta Q_{kl}\right)} \qquad (6.9) \\ \therefore \mathrm{cov}\left(Q'_{ij}, Q'_{kl}\right) &= 2\mathrm{cov}\left(Q_{ij}, \Delta Q_{kl}\right) \qquad (6.10) \end{aligned}$$

where the first term on the right hand side of (6.9) is dropped because the incident illumination is spatially uncorrelated (for a good flat field), and the final term is dropped because we are working to first order perturbation. (6.10) then follows from a symmetry argument. The covariance in (6.10) can be explicitly written down using the bilinear distributive properties of the covariance operation:

$$\begin{aligned} \mathrm{cov}\left(Q'_{ij}, Q'_{kl}\right) &= 2\mathrm{cov}\left(\mathrm{Q_{ij}}, \frac{1}{4}\sum_{\mathrm{X}}\sum_{\mathrm{m,n}} \mathrm{a_{mn}^X Q_{mn}}\left(\mathrm{Q_{kl}} + \tilde{\mathrm{Q}}_{\mathrm{kl}}^{\mathrm{X}}\right)\right) \qquad (6.11) \\ \Rightarrow \mathrm{cov}\left(Q'_{ij}, Q'_{kl}\right) &= \frac{1}{2}\sum_X \sum_{m,n} a_{mn}^X \mathrm{cov}\left(Q_{ij}, Q_{mn}\left(Q_{kl} + \vec{Q}_{kl}^X\right)\right). \qquad (6.12) \end{aligned}$$

On the assumption that the true light field is spatially uncorrelated, the covariance between any two "true" pixel values vanishes, i.e. $\mathrm{cov}\left(Q_{ij}, Q_{mn}\right) = 0$, except when $(i,j) = (m,n)$.

Therefore:

$$cov\left(Q'_{ij}, Q'_{kl}\right) = \frac{1}{2}\sum_X a_{ij}^X \mathrm{cov}\left(Q_{ij}, Q_{ij}\left(Q_{kl} + \vec{Q}_{kl}^X\right)\right). \tag{6.13}$$

Using the familiar rule that:

$$\mathrm{cov}\left(A, B\right) = \langle AB\rangle - \langle A\rangle\langle B\rangle \tag{6.14}$$

where $\langle A\rangle$ represents the expectation value of variable A, the covariance (6.12) may be further simplified:

$$\mathrm{cov}\left(Q'_{ij}, Q'_{kl}\right) = \frac{1}{2}\sum_X a_{ij}^X \left(\langle Q_{ij}^2 Q_{kl}\rangle + \left\langle Q_{ij}^2 \vec{Q}_{kl}^X\right\rangle - \langle Q_{ij}\rangle\left(\langle Q_{ij}Q_{kl}\rangle + \left\langle Q_{ij}\vec{Q}_{kl}^X\right\rangle\right)\right). \tag{6.15}$$

In the case when the pixels (i, j) and (k, l) are not nearest neighbours, then the independence of all expectation values allows simplification of (6.15) to:

$$\mathrm{cov}\left(Q'_{ij}, Q'_{kl}\right) = \frac{1}{2}\sum_X a_{ij}^X \left(\langle Q_{ij}^2\rangle - \langle Q_{ij}\rangle^2\right)\left(\langle Q_{kl}\rangle + \left\langle \vec{Q}_{kl}^X\right\rangle\right) \tag{6.16}$$

$$\mathrm{cov}\left(Q'_{ij}, Q'_{kl}\right) = \frac{1}{2}\sigma_Q^2 \sum_X a_{ij}^X \left(\langle Q_{kl}\rangle + \left\langle \vec{Q}_{kl}^X\right\rangle\right) \tag{6.17}$$

where σ_Q^2 is the "true" (as opposed to measured) signal variance. Then, under perfect flat field conditions, the average value for each pixel is the same. This implies translational symmetry, such that without loss of generality the value Q'_{kl} can be replaced with Q'_{00} and all co-ordinate values become relative. In addition, the expectation values for any given pixel are the same, yielding:

$$\mathrm{cov}\left(Q'_{ij}, Q'_{00}\right) = \sigma_Q^2 \langle Q\rangle \sum_X a_{ij}^X \tag{6.18}$$

which is the expression connecting the ancillary pixel data values to measurable quantities (namely, the covariance between pixel values in a flat field image). The quantity$\langle Q\rangle$ is the true signal mean. The expression arising from (6.15) for the case when the pixels are nearest neighbours (such that $\vec{Q}_{kl}^X = Q_{ij}$ for some value of X) is more complicated, and explored in full by Antilogus [5]. After some additional algebra, under the flat field condition the result ends up being the same as (6.18). The connection between the correlation coefficients R_{ij} and the ancillary pixel data follows immediately from equation (6.18):

$$R_{ij} = \frac{\mathrm{cov}\left(Q'_{ij}, Q'_{00}\right)}{\sigma_Q^2} = \langle Q\rangle \sum_X a_{ij}^X \tag{6.19}$$

indicating that the ancillary pixel data can be derived from the slope of the correlation coefficient against signal. The variance is a special case of(6.19):

$$\mathrm{cov}\left(Q'_{00}, Q'_{00}\right) = \langle Q \rangle \sigma_Q^2 \sum_X a_{00}^X \tag{6.20}$$

which is not quite the correct expression for the measured variance, because in the derivation we began with a perfect shot noise limited flat-field and "shuffled" it - the variance of the pixel value given by (6.20) only includes variance which is introduced by this re-distribution. The experimental variance is calculated using many pixels, each of which is subject to the re-distributive variance and the true shot-noise variance σ_Q^2 in addition. So, the measured variance is actually:

$$\mathrm{var}\left(Q'_{00}\right) = \sigma_Q^2 \left(1 + \langle Q \rangle \sum_X a_{00}^X\right) \tag{6.21}$$

$$\Rightarrow \mathrm{var}\left(Q'_{00}\right) = \langle Q \rangle \left(1 + \langle Q \rangle \sum_X a_{00}^X\right) \tag{6.22}$$

which, by comparison to the non-linear fitted mean-variance equation (5.35) shows that the non-linearity parameter β is given by:

$$\beta = \sum_X a_{00}^X. \tag{6.23}$$

Despite the simplicity of equation (6.19), actually obtaining the values for a_{ij}^X from calibration experiments remains a fairly involved procedure. A multidimensional non-linear fitting method is used to fit a trial functional form for the ancillary pixel coefficients by Guyonnet et al [42]. They report that a reasonably well-fitting functional form is the exponential integral form:

$$a_{i,j}^X = p_0 \mathrm{Ei}\left(p_1 r_{ij}\right) \cos\theta_{ij}^X \tag{6.24}$$

where r_{ij}^X is the radial distance to the pixel boundary, θ_{ij}^X is the angle between the boundary normal and the radial vector, p_0 and p_1 are fitting parameters, and:

$$\mathrm{Ei}\left(x\right) = -\int_{-x}^{\infty} \frac{e^{-t}}{t} dt \tag{6.25}$$

is the Exponential Integral. This functional form is fitted to measured correlation coefficients. There has not been scope available in the present work to attempt to derive ancillary pixel data

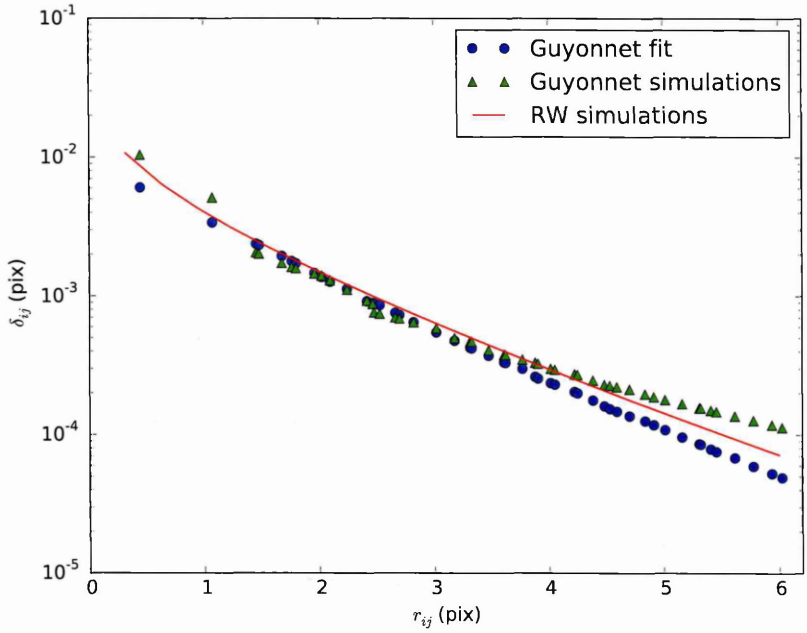

Figure 6.22: Comparing simulated boundary shift data for the e2v CCD250 (red line) to published measurements [42] (blue points), and published electrostatic simulation data (green triangles)

from the experimental correlation coefficient measurements previously presented. However, from equation (6.4) it is clear that the pixel boundary shifts δ_{ij}^X can easily be obtained from a_{ij}^X. Values for the boundary shifts are readily available from our simulation (see Section §4.4). Though we do not precisely know the details of the buried channel and channel stop implants for the device in question, as seen previously (in Section §6.3), the calculated data from our simulation nevertheless agrees well with the published data for boundary shifts derived from ancillary pixel data (see Figure 6.22), and indeed is slightly closer in estimating the fitted boundary shift values than the point charge simulations presented in the original work [42]. This should probably be taken more as an endorsement of Guyonnet et al's pixel data model than a validation of the accuracy of our simulation strategy, since as described the relevant free parameters were chosen by us to match quite closely the measured values.

In contrast to the experimental case, it is clear that the ancillary pixel data a_{ij}^X can be obtained from pixel boundary simulations very simply. Consider a pixel grid where only one (central) pixel contains charge and every other pixel is completely empty. This pixel is given

the co-ordinate $(0,0)$. Then, (6.4) reduces to:

$$\delta_{ij}^{X} = \frac{\alpha}{2} a_{ij}^{X} Q_{00} \tag{6.26}$$

$$a_{ij}^{X} = \frac{2}{Q_{00}\alpha} \delta_{ij}^{X} \tag{6.27}$$

so that the ancillary pixel coefficients can, in principle, be extracted from a single simulation using the boundary calculations (see Section §4.4). Since the ancillary pixel data approach is a first order perturbation, this is not completely correct. A useful addition to the ancillary pixel data scheme might be to introduce signal-dependent coefficients $a_{ij}^{X}(Q)$, which could be extracted from simulations using equation (6.27). This is not pursued further in the current work, though we now demonstrate the application of the combined simulation and ancillary pixel data approach to investigate the behaviour of the mean-variance non-linearity with pixel size.

A square grid with dimensions of 5×5 pixels was simulated, at varying values of pixel size α, collecting gate L and channel stop distance y_B. The gate bias was set as $V_G = 10\,\mathrm{V}$, the back bias at $V_{\mathrm{BS}} = -70\,\mathrm{V}$. The wavelength used was $\lambda = 550\,\mathrm{nm}$. All other geometrical and doping parameters were taken to be equal to the values obtained for the CCD261. For each value, the central pixel was initially filled with a charge $Q = 80\,\mathrm{ke}^{-}$. The boundary shifts δ_{ij}^{X} were directly calculated using the method described in Section §4.4, and then (6.27) was used to derive the ancillary pixel data (200 a_{ij}^{X} coefficients in total for each simulation). The values for a_{00}^{X} were then used to obtain the non-linearity parameter as shown by (6.23). This approach has a great deal of speed advantage as compared with tracing electron trajectories, though may suffer somewhat in accuracy. The results of this calculation are shown in Figure 6.23. As discussed in Section §4.5, the non-linearity is seen to increase both with pixel pitch and gate width. At smaller pixel pitches, the change of non-linearity with pixel pitch is nearly linear (as expected from the theoretical discussion in Section §4.5). As the pixel pitch becomes large compared with gate width, the rate of decrease of non-linearity slows. This might be justified by considering the fact that a very narrow gate width simulation should appear (in terms of the stored charge potential, though not the homogeneous component) like a point charge. As previous simulation efforts [5] have shown, significant non-linearity is evident when the stored charge is represented as a point charge. Further experimental investigation of this property is required - in particular with the anisotropy of point sources - according to our simulation, changing gate width affects the boundaries in the serial direction indirectly (as shown in

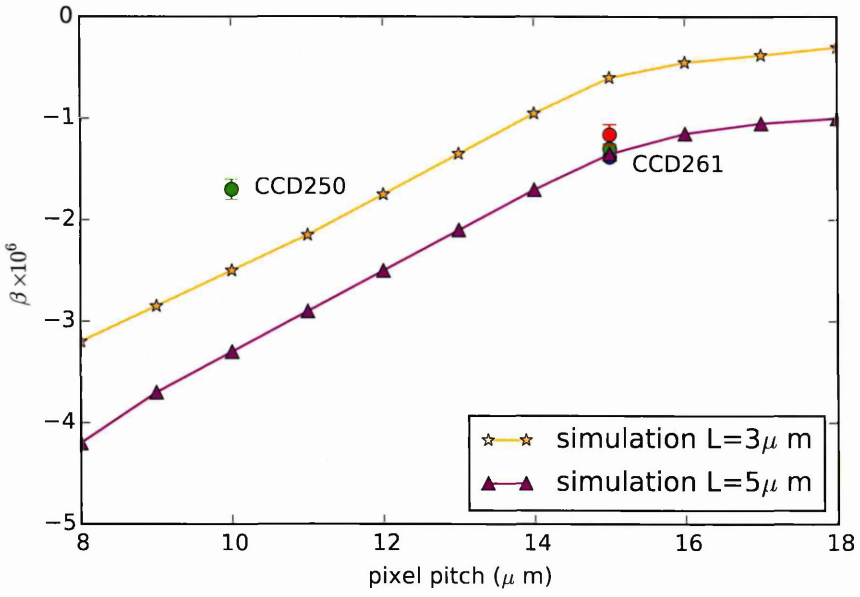

Figure 6.23: Simulated non-linearities for varying pixel pitch and gate width. Experimental points for both CCD250 and CCD261 are shown by the round points. Colours indicate (roughly) colours of light used.

Section §4.4), which might indicate selection of gate width against channel stop distance as a very important design parameter for future devices.

6.5 Summary

The extent to which some of the main assumptions made in constructing the Poisson's equation solution used to simulate the BFE in this work are valid has been examined by comparison to finite element simulations using Silvaco. In general, it was found that agreement between predicted electric field values and potentials was good, but that the charge storage model might benefit from improvement using more realistic assumptions.

Predictions from our model were compared against flat-field derived experimental datasets from both the e2v CCD261 and the e2v CCD250, and found to generally over-estimate the measured non-linearity slightly. A comparison to the measured correlation coefficients of the CCD250 was also made, where the simulation was generally found to re-produce at least qualitatively the main features.

We found that the relationship between the measured non-linearity co-efficients of the devices was roughly in the same ratio as their pixel pitches, and simulation using the ancillary pixel data approach supported the assertion that this relationship is to some degree linear.

Chapter 7

Conclusions and Further Work

> If we knew what it was we were doing, it would not be called research, would it?
>
> Albert Einstein

In this thesis, an account has been made of dynamic charge collection effects as they apply to thick, back illuminated CCD sensors.

A theoretical approach for simulating these effects has been advanced, experimental measurements have been described for two specific sensors (the CCD261 and the CCD250), and the model results have been compared against these experiments. In general, a good agreement has been found between simulation and experiment, though quantitative agreement could be substantially improved, and a rich parameter space of possible factors which affect the nature of dynamic charge collection remains to be investigated, both numerically and experimentally.

The approach presented in this work represents, to the author's knowledge, the first effort to model dynamic correlated charge collection effects starting from physical principles and including some realistic assumptions which does not use finite element based numerical calculations. The closest previous work in the literature used a point charge model to represent the stored charge, and did not include the effects of the buried channel doping on either collection or storage [5]. Thus, though that model had only one free parameter (the storage depth), the parameter itself had to be chosen to match experiments manually. In contrast, our approach can provide some predictive power: starting from known values or measurements for the physical device parameters (channel potential, resistivity, operating voltages, etc.) we are able to reasonably well re-produce the values for the PTC non-linearity, and (in the case of the CCD250) the spatial correlation co-efficients.

The general approach of our model can be readily extended for utility beyond the specific effects examined in this work. In particular, electron tracing using random walks has a wide variety of possible uses in calculating collection properties of semiconductor detectors (for example, X-ray PSF). In these cases, the semi-analytical potential calculations we have presented could be replaced by interpolations of pre-calculated finite element meshes. On the other hand, our approach has a fundamental advantage over any finite element method for dynamic charge collection simulations: the coupling between the charge storage model and the potential requires the frequent re-calculation of the latter whilst adding stored charge. The semi-analytical calculation method scales linearly with the spatial fidelity of the mesh, and is constant time for any stored charge distribution. The much more data-parallel nature of the formulation as compared with a numerical finite element simulation offers performant implementation opportunities (e.g. GPU computing) which are more difficult for finite element methods.

In this chapter, the main points arising from the thesis are summarized, along with suggestions for future work in both theoretical and experimental directions which have arisen along the way.

7.1 Dynamic Models for Charge Collection

In Chapter 4, an approach for solving Poisson's equation in a fully depleted CCD was described, utilising the linearity of the equation to split the solution into components due to the collecting gates, the back substrate contact, the substrate doping, the channel stop implants and the stored charge. At each stage, limitations and simplifications were described. Some of these assumptions can be changed or relaxed, and investigating these possibilities could be useful for understanding the varying size of the BFE in different devices. We now address some of these points in turn:

- Incomplete depletion - at low back bias voltages, the substrate in a thick sensor is not fully depleted, and some of the volume consists of a field free region. Incorporating full details of incomplete depletion into the modelling approach here is impossible, because it would require a full solution of the drift-diffusion equations. However, a simplified form of incomplete depletion could be readily added, treating the field free region using a "block" approach similar, for example, to that used by Pavlov and Nousek [79] in the case of CCDs used for X-ray detection. This would extend the validity of the model for

use in sensors which are not back biased, but which nevertheless exhibit the BFE. A particular example for which this approach might be suited is the CCD273 used in the Euclid mission [4].

- Improved charge storage model - a simple 1D analytical charge storage model based on work by previous authors was presented in Section §4.2. As shown in Section §6.1, this model is at least slightly inaccurate when compared with finite element simulations. The model used in this work was, in effect, a "constant density" model in the taxonomy presented by Clarke et al [17]. The use of a model (probably fitted to finite element simulations) which uses non-constant density would be a useful avenue of investigation.

- Realistic doping profile - The doping profile used was based on an abrupt junction block approximation. There is nothing in the solution of the Poisson equation described which mandates this, though it was well justified on the grounds that it is the simplest assumption, with parameters that can be matched to experiment, and was also required for consistency by the simple 1D charge storage model. Improving the charge storage model would allow for more realistic doping profiles (perhaps motivated by process simulation) to be used.

- Recombination at the back surface - the conditions at the back surface of the device were assumed to be perfectly conducting, and having zero recombination velocity for electrons. The treatment of the back surface in a real device might affect the BFE significantly, because either or both of these assumptions may be invalid. A detailed investigation into the magnitude of the effect of relaxing these assumptions would be illuminating, and within the scope of the basic modelling framework already presented with only slight modifications.

As was mentioned in Section §4.4, the field dependent mobility model which was used does not change the overall direction of drift field lines, only the collection time for electrons. This is a consequence of the simplicity of the model used. More sophisticated approaches to field dependent mobility which vary also with the orientation of the crystal axes could be included in the simulations, and might affect the predictions about charge collection.

There remains enormous scope to implement the models in a much more computationally efficient manner, which has already been described in the relevant sections. Improved calculation time will allow more extensive investigations of the limits of applicability of the model

and the effect of other parameters, and a very fast (possibly GPU-based) implementation would likely allow CCD designs to be evaluated for dynamic charge collection very rapidly.

Those parameters which likely affect dynamic charge collection but which have not received detailed attention in this work include: temperature, applied collecting gate bias, substrate resistivity, channel doping, device thickness and buried channel depth. Of these parameters, all are in principle amenable to investigation using the model presented without further modification.

Temperature and gate bias are, in addition, directly accessible experimentally using a single device. The effects of biases and temperature, in particular, are very important from an operational point of view: it might be that the mitigation of dynamic charge collection effects adds an extra consideration into the determination of these parameter choices in future projects. Using simulations of boundary shifts, we also found that our simulation predicts a significant change in both the magnitude and anisotropy of the BFE based on the collecting gate width. This parameter is experimentally accessible by integrating under different sets of collecting gates.

It was found that the model agreed well with flat field non-linearity measurements on both CCD250 and CCD261 when reasonable physical parameter estimates were used. This is an encouraging result from the point of view of further work based on the model presented. In addition, we found that inclusion of diffusion was necessary to include in modelling, otherwise the collection statistics for a particular image would depend on not only the incident distribution of photons, but the exact order in which they arrive, a situation which seems not to be the case empirically. We wish to emphasize this result as perhaps one of the most important we have obtained throughout this work - though it is widely acknowledged that the phenomenon of excess diffusion contributes only a small portion of the BFE, the inclusion of diffusion in electron tracing simulations.

Qualitatively, most features of the observed BFE are well predicted by the potential model, including the lack of non-linearity from signal generated by dark current and the increased boundary shift (and therefore correlation) in the vertical direction as compared with the horizontal. The model was also able to re-produce published measurements of CCD250 boundary shifts with reasonable accuracy. We predict that the dependence of the effects on wavelength should be measurable, and the data presented in this thesis gives some indication of chromaticity (chiefly in the anisotropy measurements of the CCD261), though the strength of this is not convincing enough to be conclusive. Fully determining whether a wavelength depen-

dence needs to be included in correction strategies for the BFE is crucial, because for schemes like the ancillary pixel data approach (discussed in Section §6.4), chromaticity would imply separate sets of correction coefficients are needed for every filter set used in collecting science frames.

7.2 Experimental Charge Collection Measurements

Measurements of flat field and point source illumination were made on the CCD261, and in most cases the results were found to agree with past results on thick CCDs - non-linearity of the PTC decreases as V_{BS} becomes more negative, as does the anisotropy of spot illuminations. Mean-variance curves generated from changing illumination level were found to behave identically to those generated by changing exposure time to within experimental error. The mean-variance curve generated using dark current does not exhibit significant non-linearity, again as expected. The nearest neighbour flat-field correlation coefficient measured from the CCD261, however, was found to have an anomalous increase at a threshold significantly lower than the device full well capacity.

In terms of driving the CCD261, it was found that large spikes in the image clock shapes were due to inter-phase capacitance, and were reduced by a combination of additional capacitance and reduced clock phase overlap.

Analysis of flat field measurements were also presented for the CCD250 device. Despite significant problems due to inconsistent illumination level in the dataset, it was possible to verify that the read noise achieved was within the specification for LSST. A similar behaviour to the CCD261 was found for non-linearity of mean-variance curves, though the absolute values were around 50% greater for the CCD250. This is in direct relationship to the pixel size ratio between the two devices, and simulations corroborated the argument that the decrease in the magnitude of dynamic collection effects should be roughly linear as pixel size increases.

The experience gained from our experimental investigations enable us to make some recommendations for device calibration: since the BFE's effect on dark current is much less than that for photo-generated signal, a robust gain calibration can be obtained using dark current transfer, rather than photon transfer. A method for characterising the transfer function of a CDS system using only the same equipment used for CCD image capture was also presented.

An experiment on the guard ring of the CCD261 was performed through which we were able to show that the observed "roll-off" at the edge of the device is well characterised by

an exponential decay. The variation of this roll-off was studied with changing guard drain voltage and back side bias. We found that the recommended operating guard drain voltage from the sensor manufacturer might be specified rather conservatively, though extreme care should be exercised in optimising this parameter to avoid damaging the device.

At this stage, the relationship between the BFE and back bias voltage is well established, though there remains the question of to what extent partial depletion might become important. For the devices investigated in this work, full depletion occurs at a comparatively low back bias ($V_{\mathrm{BS}} \approx 10\,\mathrm{V}$). In the non fully-depleted case, a recovery of linearity should be observed, the justification for which was given in detail (see Section §4.5). The effect of gate voltage has been examined by previous authors [5]. The most obvious parameters for future experimental investigations should be the collecting gate width and operating temperature, which would establish in particular to what degree the value of the mobility in silicon affects dynamic charge collection (mobility being the only related material parameter which changes over a large range for relevant operating temperatures). This might open up new possibilities for correction of the BFE in future device designs.

Bibliography

[1] Elsamuko. URL `https://www.flickr.com/people/28653536@N07`.

[2] Tactic electronics. URL `http://www.tacticelectronics.com`.

[3] Paul A. Abell, Julius Allison, Scott F. Anderson, John R. Andrew, J. Roger Angel, Lee Armus, David Arnett, S. J. Asztalos, Tim S. Axelrod, Stephen Bailey, et al. LSST science book, version 2.0. *arXiv preprint arXiv:0912.0201*, 2009.

[4] Edgar A. H. Allanwood, Neil J. Murray, Konstantin D. Stefanov, David J. Burt, and Andrew D. Holland. Point-spread function and photon transfer of a CCD for space-based astronomy. *Proc. SPIE*, 8860:88600I–88600I–9, 2013. doi: 10.1117/12.2024263.

[5] P. Antilogus, P. Astier, P. Doherty, A. Guyonnet, and N. Regnault. The brighter-fatter effect and pixel correlations in CCD sensors. *Journal of Instrumentation*, 9(03):C03048, 2014. URL `http://stacks.iop.org/1748-0221/9/i=03/a=C03048`.

[6] Neil W. Ashcroft and David N. Mermin. Solid state physics. *Saunders, Philadelphia*, page 293, 1976.

[7] P. Astier. An introduction to some imperfections of CCD sensors. *Journal of Instrumentation*, 10(05):C05013, 2015. URL `http://stacks.iop.org/1748-0221/10/i=05/a=C05013`.

[8] Brooks Automation. *Polycold Compact Cooler (PCC) With PT Refrigerand Blends - Operating Manual*, rev C edition, 2006.

[9] G.M. Bernstein and M. Jarvis. Shapes and shears, stars and smears: Optimal measurements for weak lensing. *The Astronomical Journal*, 123(2):583, 2002.

[10] Glenn D. Boreman. *Modulation transfer function in optical and electro-optical systems*, volume 4. SPIE Press Bellingham, WA, 2001.

[11] Willard S. Boyle and George E. Smith. Charge coupled semiconductor devices. *Bell System Technical Journal*, 49(4):587–593, 1970.

[12] Willard S. Boyle and George E. Smith. Buried channel charge coupled devices, February 12 1974. US Patent 3,792,322.

[13] Geoffrey Brooker. *Modern classical optics*, volume 8. Oxford University Press, 2003.

[14] George W. Burns, M. G. Scroger, G. F. Strouse, M. C. Croarkin, and W. F. Guthrie. Temperature-electromotive force reference functions and tables for the letter-designated thermocouple types based on the ITS-90. *NASA STI/Recon Technical Report N*, 93, 1993.

[15] C. Canali, G. Majni, R. Minder, and G. Ottaviani. Electron and hole drift velocity measurements in silicon and their empirical relation to electric field and temperature. *Electron Devices, IEEE Transactions on*, 22(11):1045–1047, Nov 1975. ISSN 0018-9383. doi: 10.1109/T-ED.1975.18267.

[16] James E. Carnes, Walter F. Kosonocky, and E.G. Ramberg. Free charge transfer in charge-coupled devices. *Electron Devices, IEEE Transactions on*, 19(6):798–808, Jun 1972. ISSN 0018-9383. doi: 10.1109/T-ED.1972.17497.

[17] A.S. Clarke, D.J. Hall, A. Holland, and D. Burt. Modelling charge storage in euclid CCD structures. *Journal of Instrumentation*, 7(01):C01058, 2012.

[18] TUFNOL corporation. *TUFNOL Grades 10G/40 10G/41 10G/42 and 10G/44 Data Sheet.*

[19] Merton H. Crowell and Edward F. Labuda. The silicon diode array camera tube. *Bell System Technical Journal*, 48(5):1481–1528, 1969.

[20] B. Dale. The validity of the depletion approximation applied to a bulk channel charge-coupled device. *IEEE Journal of Solid-State Circuits*, 11(1):207–214, Feb 1976. ISSN 0018-9200. doi: 10.1109/JSSC.1976.1050699.

[21] K.M. De Meyer and G.J. Declerck. A new method for the two-dimensional calculation of the potential distribution in a buried-channel charge-coupled device: Theory and experimental verification. *Electron Devices, IEEE Transactions on*, 28(3):313–321, Mar 1981. ISSN 0018-9383. doi: 10.1109/T-ED.1981.20334.

[22] John E. Dennis Jr and Robert B. Schnabel. *Numerical methods for unconstrained optimization and nonlinear equations*, volume 16. Siam, 1996.

[23] R. Devanathan, L.R. Corrales, F. Gao, and W.J. Weber. Signal variance in gamma-ray detectors - A review. *Nuclear Instruments and Methods in Physics Research Section A: Accelerators, Spectrometers, Detectors and Associated Equipment*, 565(2): 637 – 649, 2006. ISSN 0168-9002. doi: 10.1016/j.nima.2006.05.085. URL `http://www.sciencedirect.com/science/article/pii/S0168900206009089`.

[24] Analog Devices. AD829 high speed, low noise video op amp. URL `http://www.analog.com/en/products/amplifiers/operational-amplifiers/low-noise-amplifiers-lessthanequalto-10nv/ad829.html`.

[25] R.E. Thomas D.M. Caughey. Carrier mobilities in silicon empirically related to doping and field. *Proceedings of the IEEE*, 55(12):2192–2193, Dec 1967. ISSN 0018-9219. doi: 10.1109/PROC.1967.6123.

[26] Peter E. Doherty, Pierre Antilogus, Pierre Astier, James Chiang, Kirk D. Gilmore, Augustin Guyonnet, Dajun Huang, Heather Kelly, Ivan Kotov, Petr Kubanek, Andrei Nomerotski, Paul O'Connor, Andrew Rasmussen, Vincent J. Riot, Christopher W. Stubbs, Peter Takacs, Anthony J. Tyson, and Kurt Vetter. Electro-optical testing of fully depleted CCD image sensors for the large synoptic survey telescope camera. *Proc. SPIE*, 9154:915418–915418–17, 2014. doi: 10.1117/12.2056733.

[27] Mark Downing, Dietrich Baade, Peter Sinclaire, Sebastian Deiries, and Fabrice Christen. CCD riddle: a) signal vs time: linear; b) signal vs variance: non-linear. *Proc. SPIE*, 6276:627609–627609–11, 2006. doi: 10.1117/12.671457.

[28] e2v technologies. Technical note on the MTF of CCD sensors. Technical Report A1A-CCDTN105, e2v technologies limited, June 2003. URL `http://www.e2v.com/shared/content/resources/File/documents/imaging-space-and-scientific-sensors/Papers/ccdtn105.pdf`.

[29] Tom E. Faber. *Fluid dynamics for physicists*. Cambridge University Press, 1995.

[30] Jessamyn A. Fairfield, Donald E. Groom, Stephen J. Bailey, Christopher J. Bebek, Stephen E. Holland, Armin Karcher, William F. Koble, Wolfgang Lorenzon, and Na-

talie A. Roe. Reduced charge diffusion in thick, fully depleted CCDs with enhanced red sensitivity. *Nuclear Science, IEEE Transactions on*, 53(6):3877–3881, 2006.

[31] U. Fano. Ionization yield of radiations. ii. the fluctuations of the number of ions. *Physical Review*, 72(1):26, 1947.

[32] Mark Fox. *Optical properties of solids*, volume 3. Oxford university press, 2001.

[33] Mark Fox. *Quantum Optics: An Introduction*. OUP Oxford, 2006.

[34] I.L. Fujimori and C.G. Sodini. Temporal noise in CMOS passive pixels. In *Sensors, 2002. Proceedings of IEEE*, volume 1, pages 140–145 vol.1, 2002. doi: 10.1109/ICSENS.2002.1037005.

[35] Brian Gough. *GNU scientific library reference manual*. Network Theory Ltd., 2009.

[36] J. Gow, N. J. Murray, A. D. Holland, D. Burt, and P. Pool. A comparative study of proton radiation damage in p and n channel CCDs. *Proc. SPIE*, 7435:74350F–74350F–8, 2009. doi: 10.1117/12.826866.

[37] Martin A. Green. Self-consistent optical parameters of intrinsic silicon at 300K including temperature coefficients. *Solar Energy Materials and Solar Cells*, 92(11):1305 – 1310, 2008. ISSN 0927-0248. doi: http://dx.doi.org/10.1016/j.solmat.2008.06.009. URL `http://www.sciencedirect.com/science/article/pii/S0927024808002158`.

[38] D. Gregor and Matthias Troyer. The boost MPI library, 2012.

[39] C.V. Griffith, S.D. Bongiorno, D.N. Burrows, A.D. Falcone, and Z.R. Prieskorn. Characterization of an x-ray hybrid cmos detector with low interpixel capacitive crosstalk. In *SPIE Astronomical Telescopes+ Instrumentation*, pages 84530F–84530F. SPIE, 2012.

[40] Don Groom. Cosmic rays and other nonsense in astronomical CCD imagers. *Experimental Astronomy*, 14(1):45–55, 2002.

[41] H.K. Gummel. A self-consistent iterative scheme for one-dimensional steady state transistor calculations. *Electron Devices, IEEE Transactions on*, 11(10):455–465, Oct 1964. ISSN 0018-9383. doi: 10.1109/T-ED.1964.15364.

[42] A. Guyonnet, P. Astier, P. Antilogus, N. Regnault, and P. Doherty. Evidence for self-interaction of charge distribution in charge-coupled devices. *Astronomy & Astrophysics*, 575:A41, 2015.

[43] Erika T. Hamden, Frank Greer, Michael E. Hoenk, Jordana Blacksberg, Matthew R. Dickie, Shouleh Nikzad, D. Christopher Martin, and David Schiminovich. Ultraviolet antireflection coatings for use in silicon detector design. *Appl. Opt.*, 50(21):4180–4188, Jul 2011. doi: 10.1364/AO.50.004180. URL `http://ao.osa.org/abstract.cfm?URI=ao-50-21-4180`.

[44] H.W. Hanneman and L.J.M. Esser. Field and potential distributions in charge-transfer devices. *Philips research reports*, 30(1):56–72, 1975.

[45] P. J. Hayman, N. S. Palmer, and A. W. Wolfendale. The rate of energy loss of high-energy cosmic ray muons. *Proceedings of the Royal Society of London A: Mathematical, Physical and Engineering Sciences*, 275(1362):391–410, 1963. ISSN 0080-4630. doi: 10.1098/rspa.1963.0176. URL `http://rspa.royalsocietypublishing.org/content/275/1362/391`.

[46] T. Hirano and T. Kuga. Generation of weak sub-poissonian light by a high-efficiency light-emitting diode. *IEEE Journal of Quantum Electronics*, 31(12):2236–2240, Dec 1995. ISSN 0018-9197. doi: 10.1109/3.477752.

[47] Michael Paul Hobson, George P. Efstathiou, and Anthony N. Lasenby. *General relativity: an introduction for physicists.* Cambridge University Press, 2006.

[48] Stephen E. Holland, Donald E. Groom, Nick P. Palaio, Richard J. Stover, and Mingzhi Wei. Fully depleted, back-illuminated charge-coupled devices fabricated on high-resistivity silicon. *Electron Devices, IEEE Transactions on*, 50(1):225–238, 2003.

[49] G.C. Holst and T.S. Lomheim. *CMOS & CCD sensors and camera systems.* SPIE Press Monographs Series. JCD Publishing, 2011. ISBN 9780819486530.

[50] S.M. Hong and C. Jungemann. A fully coupled scheme for a Boltzmann-Poisson equation solver based on a spherical harmonics expansion. *Journal of Computational Electronics*, 8(3-4):225–241, 2009. ISSN 1569-8025. doi: 10.1007/s10825-009-0294-y.

[51] G.R. Hopkinson and D.H. Lumb. Noise reduction techniques for CCD image sensors. *Journal of Physics E: Scientific Instruments*, 15(11):1214, 1982. URL `http://stacks.iop.org/0022-3735/15/i=11/a=020`.

[52] Paul Horowitz, Winfield Hill, and Thomas C. Hayes. *The art of electronics*, volume 2. Cambridge University Press Cambridge, 1989.

[53] John David Jackson. *Classical electrodynamics.* Wiley, 1999.

[54] James R. Janesick. *Scientific charge-coupled devices.* SPIE Press, Bellingham, Wash, 2001. ISBN 0819436984.

[55] James R. Janesick. *DN to λ.* Press Monographs. SPIE, 2007. ISBN 9780819467225.

[56] P. Jerram, D. Burt, N. Guyatt, V. Hibon, J. Vaillant, and Y. Henrion. Back-thinned cmos sensor optimisation. volume 7598 of *Proc. SPIE*, pages 759813–1, 2010.

[57] David V. Jordan, Andrea S. Renholds, John E. Jaffe, Kevin K. Anderson, L. Rene Corrales, and Anthony J. Peurrung. Simple classical model for Fano statistics in radiation detectors. *Nuclear Instruments and Methods in Physics Research Section A: Accelerators, Spectrometers, Detectors and Associated Equipment*, 585(3):146 – 154, 2008. ISSN 0168-9002. doi: 10.1016/j.nima.2007.11.009. URL `http://www.sciencedirect.com/science/article/pii/S0168900207023285`.

[58] Paul R. Jorden, Mark Downing, Andrew Harris, Andrew Kelt, Pritesh Mistry, and Pash Patel. Improving the red wavelength sensitivity of CCDs. *Proc. SPIE*, 7742: 77420J–77420J–11, 2010. doi: 10.1117/12.862435. URL `http://dx.doi.org/10.1117/12.862435`.

[59] Paul R. Jorden, Doug Jordan, Paul A. Jerram, Jerome Pratlong, and Ian Swindells. e2v new CCD and CMOS technology developments for astronomical sensors. *Proc. SPIE*, 9154:91540M–91540M–15, 2014. doi: 10.1117/12.2069423.

[60] A. Jungel. *Transport Equations for Semiconductors.* Lecture Notes in Physics. Springer, 2009. ISBN 9783540895251. URL `http://books.google.co.uk/books?id=d6YIyevAQG4C`.

[61] Wayne S. Kendal and Bent Jørgensen. Tweedie convergence: A mathematical basis for taylor's power law, $1/f$ noise, and multifractality. *Phys. Rev. E*, 84:066120, Dec 2011. doi: 10.1103/PhysRevE.84.066120. URL `http://link.aps.org/doi/10.1103/PhysRevE.84.066120`.

[62] W. H. Kent. Charge distribution in buried-channel charge-coupled devices. *The Bell System Technical Journal*, 52(6):1009–1024, July 1973. ISSN 0005-8580. doi: 10.1002/j.1538-7305.1973.tb02000.x.

[63] Jirayr Kevorkian. *Partial differential equations: Analytical solution techniques*, volume 6. Springer Science & Business Media, 2000.

[64] D.B.M. Klaassen. A unified mobility model for device simulation i. model equations and concentration dependence. *Solid-State Electronics*, 35(7):953 – 959, 1992. ISSN 0038-1101. doi: http://dx.doi.org/10.1016/0038-1101(92)90325-7. URL `http://www.sciencedirect.com/science/article/pii/0038110192903257`.

[65] Gregory F. Lawler and Vlada Limic. *Random walk: a modern introduction*, volume 123. Cambridge University Press, 2010.

[66] T. P. Lester and D.L. Pulfrey. A new method based on the superposition principle for the calculation of the two-dimensional potential in a buried-channel charge-coupled device. *Electron Devices, IEEE Transactions on*, 31(7):999–1001, Jul 1984. ISSN 0018-9383. doi: 10.1109/T-ED.1984.21647.

[67] David Levin. Development of non-linear transformations for improving convergence of sequences. *International Journal of Computer Mathematics*, 3(1-4):371–388, 1972. doi: 10.1080/00207167308803075.

[68] Bin Ma, Zhaohui Shang, Lifan Wang, Yi Hu, Qiang Liu, and Peng Wei. The nonlinear photon transfer curve of CCDs and its effects on photometry. *Proc. SPIE*, 9154:91541U–91541U–10, 2014. doi: 10.1117/12.2055430.

[69] ATLAS User's Manual. Silvaco. *Santa Clara, CA*, 2010.

[70] J. McKenna and N.L. Schryer. The potential in a charge coupled device with no mobile minority carriers and zero plate separation. *Bell System Technical Journal*, 52(5):669–696, 1973.

[71] Paul Monckton. World's most powerful camera will map the universe, August 2015. URL `http://www.forbes.com/sites/paulmonckton/2015/08/31/worlds-most-powerful-camera/`.

[72] Ramakrishnan Mukundan and K.R. Ramakrishnan. *Moment functions in image analysis: theory and applications*, volume 100. World Scientific, 1998.

[73] N.J. Murray, E.A.H. Allanwood, B.J. Dryer, D.P. Weatherill, K.D. Stefanov, A.D. Holland, and D.J. Burt. Comparison of point spread function in p- and n-channel

CCDs. *Journal of Instrumentation*, 10(08):C08007, 2015. URL http://stacks.iop.org/1748-0221/10/i=08/a=C08007.

[74] E.H. Nicollian and J.R. Brews. *MOS /metal oxide semiconductor/ physics and technology.* 1982.

[75] P.J.W. Noble. Self-scanned silicon image detector arrays. *Electron Devices, IEEE Transactions on*, 15(4):202–209, Apr 1968. ISSN 0018-9383. doi: 10.1109/T-ED.1968.16167.

[76] H. Nyquist. Thermal agitation of electric charge in conductors. *Phys. Rev.*, 32:110–113, Jul 1928. doi: 10.1103/PhysRev.32.110. URL http://link.aps.org/doi/10.1103/PhysRev.32.110.

[77] P. O'Connor. Spot scan probe of lateral field effects in a thick fully-depleted CCD. *Journal of Instrumentation*, 9(03):C03033, 2014. URL http://stacks.iop.org/1748-0221/9/i=03/a=C03033.

[78] Bedabrata Pain and Bruce R. Hancock. Accurate estimation of conversion gain and quantum efficiency in CMOS imagers. *Proc. SPIE 5017, Sensors and Camera Systems for Scientific, Industrial, and Digital Photography Applications IV*, pages 94–103, 2003. doi: 10.1117/12.483900.

[79] George G. Pavlov and John A. Nousek. Charge diffusion in CCD x-ray detectors. *Nuclear Instruments and Methods in Physics Research Section A: Accelerators, Spectrometers, Detectors and Associated Equipment*, 428(2-3):348–366, 1999. ISSN 0168-9002. doi: 10.1016/S0168-9002(99)00045-5. URL http://www.sciencedirect.com/science/article/pii/S0168900299000455.

[80] James C. Phillips and Leonard Kleinman. New method for calculating wave functions in crystals and molecules. *Physical Review*, 116(2):287, 1959.

[81] A. Rasmussen. Pixel area variations in sensors: a novel framework for predicting pixel fidelity and distortion in flat field response. *Journal of Instrumentation*, 9(04):C04027, 2014. URL http://stacks.iop.org/1748-0221/9/i=04/a=C04027.

[82] Andrew Rasmussen, Pierre Antilogus, Pierre Astier, Chuck Claver, Peter Doherty, Gregory Dubois-Felsmann, Kirk Gilmore, Steven Kahn, Ivan Kotov, Robert Lupton, Paul O'Connor, Andrei Nomerotski, Steve Ritz, and Christopher Stubbs. A framework for

modeling the detailed optical response of thick, multiple segment, large format sensors for precision astronomy applications. *Proc. SPIE*, 9150:915017–915017–13, 2014. doi: 10.1117/12.2057411.

[83] Kenneth Franklin Riley, Michael Paul Hobson, and Stephen John Bence. *Mathematical methods for physics and engineering: a comprehensive guide.* Cambridge University Press, 2006.

[84] Michael Riordan and Lillian Hoddeson. *Crystal fire: the invention of the transistor and the birth of the information age.* WW Norton & Company, 1997.

[85] Mark S. Robbins, Pritesh Mistry, and Paul R. Jorden. Detailed characterisation of a new large area CCD manufactured on high resistivity silicon. *Proc. SPIE*, 7875:787507–787507–12, 2011. doi: 10.1117/12.876627.

[86] Abraham Savitzky and Marcel J.E. Golay. Smoothing and differentiation of data by simplified least squares procedures. *Analytical chemistry*, 36(8):1627–1639, 1964.

[87] D.L. Scharfetter and H.K. Gummel. Large-signal analysis of a silicon read diode oscillator. *Electron Devices, IEEE Transactions on*, 16(1):64–77, Jan 1969. ISSN 0018-9383. doi: 10.1109/T-ED.1969.16566.

[88] Will Schroeder, Ken Martin, and Bill Lorensen. The visualisation toolkit. *Kitware, ISBN*, pages 1–930934, 2002.

[89] D. H. Seib. Carrier diffusion degradation of modulation transfer function in charge coupled imagers. *IEEE Transactions on Electron Devices*, 21(3):210–217, Mar 1974. ISSN 0018-9383. doi: 10.1109/T-ED.1974.17898.

[90] John Singleton. *Band theory and electronic properties of solids*, volume 2. Oxford University Press, 2001.

[91] M. Soman, K. Stefanov, D. Weatherill, A. Holland, J. Gow, and M. Leese. Non-linear responsivity characterisation of a CMOS active pixel sensor for high resolution imaging of the jovian system. *Journal of Instrumentation*, 10(2), February 2015. URL `http://oro.open.ac.uk/42227/`.

[92] Matthew Soman. *High-resolution detectors for soft X-ray spectroscopy.* PhD thesis, The Open University, 2014.

[93] K. D. Stefanov. Digital CDS for image sensors with dominant white and 1/f noise. *Journal of Instrumentation*, 10(4), April 2015. URL http://oro.open.ac.uk/42476/. 18 pp.

[94] K.D. Stefanov. A statistical model for signal-dependent charge sharing in image sensors. *Electron Devices, IEEE Transactions on*, 61(1):110–115, Jan 2014. ISSN 0018-9383. doi: 10.1109/TED.2013.2291448.

[95] Bjarne Stroustrup. *The C++ programming language*. Pearson Education, 2013.

[96] M. Szafraniec, S.M. Niemi, D. Walton, and M. Cropper. On-ground characterization of the euclid low noise CCD273 sensor for precise galaxy shape measurements. *Journal of Instrumentation*, 10(01):C01030, 2015. URL http://stacks.iop.org/1748-0221/10/i=01/a=C01030.

[97] Simon M. Sze. *Physics of semiconductor devices*. Wiley-interscience, 2006.

[98] Nobukazu Teranishi, Akiyoshi Kohono, Yasuo Ishihara, Eiji Oda, and Kouichi Arai. No image lag photodiode structure in the interline CCD image sensor. In *Electron Devices Meeting, 1982 International*, volume 28, pages 324–327. IEEE, 1982.

[99] Y.P. Varshni. Temperature dependence of the energy gap in semiconductors. *Physica*, 34(1):149–154, 1967. ISSN 0031-8914. doi: http://dx.doi.org/10.1016/0031-8914(67)90062-6. URL http://www.sciencedirect.com/science/article/pii/0031891467900626.

[100] Dragica Vasileska and Stephen M. Goodnick. *Computational electronics*, volume 1. Morgan & Claypool Publishers, 2005.

[101] Philip Russell Wallace. *Mathematical analysis of physical problems*. Courier Corporation, 1972.

[102] N.R. Waltham, M. Prydderch, H. Mapson-Menard, P. Pool, and A. Harris. Development of a thinned back-illuminated CMOS active pixel sensor for extreme ultraviolet spectroscopy and imaging in space science. *Nuclear Instruments and Methods in Physics Research Section A: Accelerators, Spectrometers, Detectors and Associated Equipment*, 573(1–2):250–252, 2007. ISSN 0168-9002. doi: 10.1016/j.nima.2006.10.259. URL http://www.sciencedirect.com/science/article/pii/S0168900206021991. Proceedings of the 7th International Conference on Position-Sensitive Detectors.

[103] Xinyang Wang, P.R. Rao, A. Mierop, and A.J.P. Theuwissen. Random telegraph signal in CMOS image sensor pixels. In *Electron Devices Meeting, 2006. IEDM '06. International*, pages 1 –4, dec. 2006. doi: 10.1109/IEDM.2006.346973.

[104] Daniel P Weatherill, Konstantin D Stefanov, Andrew D Holland, Douglas Jordan, and Ivan V. Kotov. Models for dynamic correlated charge collection effects in thick CCDs. In *SPIE Optical Engineering+ Applications*, pages 96020M–96020M. International Society for Optics and Photonics, 2015.

[105] D.P. Weatherill, K.D. Stefanov, A.D. Holland, and D.Jordan. Analytical investigation of correlated charge collection in CCDs. *Journal of Instrumentation*, 10(02):C02002, 2015. URL `http://stacks.iop.org/1748-0221/10/i=02/a=C02002`.

[106] G.P. Weckler. Operation of p-n junction photodetectors in a photon flux integrating mode. *Solid-State Circuits, IEEE Journal of*, 2(3):65–73, 1967. ISSN 0018-9200. doi: 10.1109/JSSC.1967.1049795.

[107] Ralf Widenhorn, Morley M. Blouke, Alexander Weber, Armin Rest, and Erik Bodegom. Temperature dependence of dark current in a CCD. *Proc. SPIE*, 4669:193–201, 2002. doi: 10.1117/12.463446.

[108] Charles Sumner Williams and Orville A. Becklund. *Introduction to the optical transfer function*, volume 112. SPIE Press, 1989.

[109] Y. Yin and Jr. Cooper, J.A. Simple equations for the electrostatic potential in buried-channel MOS devices. *Electron Devices, IEEE Transactions on*, 39(7):1770–1772, Jul 1992. ISSN 0018-9383. doi: 10.1109/16.141247.

[110] Peter Yu, Manuel Cardona, and Lu Sham. Fundamentals of semiconductors: physics and materials properties. *Physics Today*, 50:76, 1997.

Then, as his planet killed him, it occurred to Kynes that his father and all the other scientists were wrong, that the most persistent principles of the universe were accident and error.

Frank Herbert, in *Dune Messiah*